Review of the National Ignition Campaign 2009-2012

John Lindl, Otto Landen, John Edwards, Ed Moses, and NIC Team

Review of the National Ignition Campaign 2009-2012

John Lindl,[1] Otto Landen,[1] John Edwards,[1] Ed Moses,[1] and NIC Team[1,2,3,4,5,6,7,8]

[1]*Lawrence Livermore National Laboratory, Livermore, California 94550, USA*
[2]*Laboratory for Laser Energetics, University of Rochester, Rochester, New York 14623, USA*
[3]*Los Alamos National Laboratory, Los Alamos, New Mexico 87545, USA*
[4]*Sandia National Laboratory, Albuquerque, New Mexico 87123, USA*
[5]*General Atomics, San Diego, California 92186, USA*
[6]*Plasma Science and Fusion Center, Massachusetts Institute of Technology, Cambridge, Massachusetts 02139, USA*
[7]*Atomic Weapons Establishment, Aldermaston, Reading, Berkshire RG7 4PR, United Kingdom*
[8]*CEA, DAM, DIF, F-91297 Arpajon, France*

The National Ignition Campaign (NIC) was a multi-institution effort established under the National Nuclear Security Administration of DOE in 2005, prior to the completion of the National Ignition Facility (NIF) in 2009. The scope of the NIC was the planning and preparation for and the execution of the first 3 yr of ignition experiments (through the end of September 2012) as well as the development, fielding, qualification, and integration of the wide range of capabilities required for ignition. Besides the operation and optimization of the use of NIF, these capabilities included over 50 optical, x-ray, and nuclear diagnostic systems, target fabrication facilities, experimental platforms, and a wide range of NIF facility infrastructure. The goal of ignition experiments on the NIF is to achieve, for the first time, ignition and thermonuclear burn in the laboratory via inertial confinement fusion and to develop a platform for ignition and high energy density applications on the NIF. The goal of the NIC was to develop and integrate all of the capabilities required for a precision ignition campaign and, if possible, to demonstrate ignition and gain by the end of FY12. The goal of achieving ignition can be divided into three main challenges. The first challenge is defining specifications for the target, laser, and diagnostics with the understanding that not all ignition physics is fully understood and not all material properties are known. The second challenge is designing experiments to systematically remove these uncertainties. The third challenge is translating these experimental results into metrics designed to determine how well the experimental implosions have performed relative to expectations and requirements and to advance those metrics toward the conditions required for ignition. This paper summarizes the approach taken to address these challenges, along with the progress achieved to date and the challenges that remain. At project completion in 2009, NIF lacked almost all the diagnostics and infrastructure required for ignition experiments. About half of the 3 yr period covered in this review was taken up by the effort required to install and performance qualify the equipment and experimental platforms needed for ignition experiments. Ignition on the NIF is a grand challenge undertaking and the results presented here represent a snapshot in time on the path toward that goal. The path forward presented at the end of this review summarizes plans for the Ignition Campaign on the NIF, which were adopted at the end of 2012, as well as some of the key results obtained since the end of the NIC. © 2014 AIP Publishing LLC. [http://dx.doi.org/10.1063/1.4865400]

NATIONAL IGNITION CAMPAIGN TEAM

Members of the National Ignition Campaign Team who contributed to advances in target fabrication, laser capability, diagnostics, target design, and experimental platforms as well as the integration of all these into the sequence of experiments covered in this review are cited below.

J. Adams, P. A. Amendt, N. Antipa, P. A. Arnold, R. C. Ashabranner, L. J. Atherton, D. Barker, M. A. Barrios, I. Bass, S. H. Baxamusa, P. M. Bell, L. R. Benedetti, D. L. Berger, L. Bernstein, L. Berzins, S. D. Bhandarkar, T. Biesiada, R. M. Bionta, D. L. Bleuel, E. J. Bond, M. Borden, M. W. Bowers, D. K. Bradley, S. G. Brass, E. Bruce, G. K. Brunton, J. Bude, S. C. Burkhart, R. F. Burr, B. Butlin, J. A. Caggiano, D. A. Callahan, W. Carr, D. T. Casey, C. Castro, P. M. Celliers, C. J. Cerjan, J. Chang, M. Chiarappa-Zucca, C. Choate, D. S. Clark, S. J. Cohen, G. W. Collins, A. Conder, W. H. Courdin, J. R. Cox, P. S. Datte, E. L. Dewald, P. Di Nicola, J. M. Di Nicola, L. Divol, S. N. Dixit, T. Doeppner, V. Draggoo, O. Drury, R. Dylla-Spears, E. G. Dzenitis, J. M. Dzenitis, M. J. Eckart, M. J. Edwards, D. C. Eder, J. H. Eggert, R. B. Ehrlich, G. V. Erbert, J. Fair, D. R. Farley, B. Felker, R. Finucane, D. N. Fittinghoff, J. Folta, R. J. Fortner, S. Frieders, G. Frieders, S. Friedrich, J. Gaylord, P. Geraghty, S. M. Glenn, S. H. Glenzer, W. Gourdin, G. Gururangan, G. Guss, S. W. Haan, B. J. Haid, B. Hammel, A. Hamza, E. P. Hartouni, R. Hatarik, S. P. Hatchett, R. Hawley, C. Haynam, J. Heebner, G. Heestand, M. R. Hermann, D. G. Hicks, D. E. Hinkel, D. D. Ho, J. P. Holder, J. Honig, J. Horner, N. Izumi, M. C. Jackson, K. S. Jancaitis,

M. Johnson, O. S. Jones, D. H. Kalantar, R. L. Kauffman, L. Kegelmeyer, J. R. Kimbrough, R. Kirkwood, J. J. Klingman, J. A. Koch, T. R. Kohut, K. M. Knittel, B. J. Kozioziemski, K. Krauter, G. W. Krauter, A. Kritcher, J. Kroll, W. L. Kruer, G. LaCaille, K. N. La Fortune, L. J. Lagin, T. A. Land, O. L. Landen, A. B. Langdon, S. H. Langer, D. W. Larson, D. A. Latray, T. Laurence, S. LePape, Z. Liao, J. D. Lindl, R. R. Lowe-Webb, T. Ma, B. J. MacGowan, A. J. Mackinnon, A. G. Macphee, K. Manes, E. R. Mapoles, M. M. Marinak, C. D. Marshall, D. Mason, D. G. Mathisen, I. Matthews, G. N. McHalle, M. McNaney, N. B. Meezan, J. Menapace, P. Michel, P. Miller, J. L. Milovich, M. Mintz, J. D. Moody, M. J. Moran, R. Montesanti, M. Monticelli, J. Moreno, E. I. Moses, D. H. Munro, B. Nathan, R. Negres, M. Norton, M. Nostrand, M. O'Brien, Y. P. Opachich, C. Orth, E. S. Palma, J. N. E. Palmer, T. G. Parham, H.-S. Park, M. V. Patel, P. K. Patel, R. W. Patterson, J. E. Peterson, R. Prasad, K. Primdahl, R. Qiu, J. E. Ralph, F. Ravizza, B. Raymond, B. A. Remington, J. Reynolds, M. J. Richardson, B. Rittman, H. F. Robey, J. S. Ross, J. R. Rygg, R. A. Sacks, J. T. Salmon, J. D. Salmonson, J. D. Sater, R. L. Saunders, K. Schaffers, D. H. Schneider, M. B. Schneider, S. M. Sepke, R. Seugling, M. J. Shaw, N. Shen, N. Simanovskaia, V. Smalyuk, M. Spaeth, B. K. Spears, P. T. Springer, W. Stoeffl, M. Stadermann, C. Stolz, E. Storm, D. J. Strozzi, T. Suratwala, L. J. Suter, J. Taylor, C. A. Thomas, R. Tommasini, R. P. J. Town, B. Vanwonterghem, R. Von Rotz, R. J. Wallace, C. F. Walters, A. Wang, S. Weaver, S. V. Weber, P. J. Wegner, B. Welday, K. Widmann, C. C. Widmayer, E. A. Williams, P. K. Whitman, L. Wong, R. D. Wood, S. Yang, C. Yeamans, B. K. Young, B. Yoxall, and R. A. Zacharias (Lawrence Livermore National Laboratory, Livermore, California 94551, USA).

T. R. Boehly, D. H. Edgell, V. Y. Glebov, M. Hohenberger, J. P. Knauer, P. McKenty, S. P. Regan, C. Sangster, and C. Stoeckl (Laboratory for Laser Energetics, University of Rochester, Rochester, New York 14623, USA).

S. Batha, G. P. Grim, N. Guler, H. W. Herrmann, J. L. Kline, G. A. Kyrala, R. J. Leeper, F. E. Merrill, R. E. Olson, M. D. Wilke, and D. C. Wilson (Los Alamos National Laboratory, Los Alamos, New Mexico 87545, USA).

G. A. Chandler, K. D. Hahn, and C. L. Ruiz (Sandia National Laboratory, Albuquerque, New Mexico 87123, USA).

N. Alfonso, E. Alger, L. Carlson, K. C. Chen, N. Dorsano, M. Emerich, M. Farrell, E. Giraldez, D. Hoover, M. Hoppe, H. Huang, J. D. Kilkenny, M. Mauldin, A. Nikroo, S. Woods, and K. Youngblood (General Atomics, San Diego, California 92186, USA).

J. A. Frenje, M. G. Johnson, R. D. Petrasso, H. Rinderknecht, M. Rosenberg, F. H. Sequin, and A. Zylstra (Plasma Science and Fusion Center, Massachusetts Institute of Technology, Cambridge, Massachusetts 02139, USA).

W. Garbett, P. Graham, T. Guymer, and A. S. Moore (Atomic Weapons Establishment, Aldermaston, Reading, Berkshire RG7 4PR, United Kingdom).

P. Gauthier, J.-P. Leidinger, L. Masse, and F. Phipppe (CEA, DAM, DIF, F-91297 Arpajon, France).

I. INTRODUCTION

The National Ignition Campaign (NIC) was a multi-institution effort under the National Nuclear Security Administration of DOE in 2005, prior to the completion of the National Ignition Facility (NIF). The scope of the NIC was the planning and preparation for the execution of the first 3 yr of ignition experiments as well as the development, fielding, qualification, and integration of the wide range of capabilities required for ignition.[1] Besides the operation and optimization of the use of NIF, these capabilities included over 50 optical, x-ray, and nuclear diagnostic systems, target fabrication facilities, experimental platforms, and a wide range of NIF facility infrastructure including the cryogenic target positioner (Tarpos) required for fielding implosions with cryogenic fuel layers. Partners in the NIC were Lawrence Livermore National Laboratory, Los Alamos National Laboratory, Sandia National Laboratory, the University of Rochester's Laboratory for Laser Energetics, and General Atomics, Other key contributors included Massachusetts Institute of Technology, Lawrence Berkeley Laboratory, Duke University, the British AWE, and the French CEA. The members of the NIC team cited in this review contributed to advances in target fabrication, laser capability, diagnostics, target design, and experimental platforms as well as the integration of all these into the sequence of ignition campaign experiments addressed in this review. The NIC in total covered a much wider range of technology development and involved a much larger team of scientists, engineers, technicians, and other staff members, than those involved directly in the ignition experiments.

The goal of ignition experiments on the NIF is to achieve, for the first time, ignition and thermonuclear burn in the laboratory via inertial confinement fusion (ICF) and to develop a platform for ignition and high energy density (HED) applications on the NIF. The goal of the NIC was to develop and integrate all of the capabilities required for a precision ignition campaign and, if possible, to demonstrate ignition and gain by the end of FY12. Ignition on the NIF is a grand challenge undertaking and the results presented here represent a snapshot in time on the path toward that goal. The path forward presented at the end of this review summarizes plans for the Ignition Campaign on the NIF which were adopted at the end of 2012, as well as some of the key results obtained since the end of the NIC.

The NIC team developed an approach to the ignition campaign on the NIF, shown in Fig. 1, which evolves from requirements established by the Point Design Target, to system capabilities, to implosion optimization platforms and experiments, and finally to integrated platforms and implosion output performance experiments. To set the point design requirements for the NIC, we used numerical algorithms and databases integrated into models which have been extensively tested on more than three decades of experiments on the Nova and Omega lasers and laser systems leading up to these facilities. These requirements were used to establish system capabilities for the Laser, Targets, Diagnostics, and Facility Infrastructure. Using these system capabilities, we identified a sequence of experimental platforms designed to measure and optimize (or tune) a variety of physical
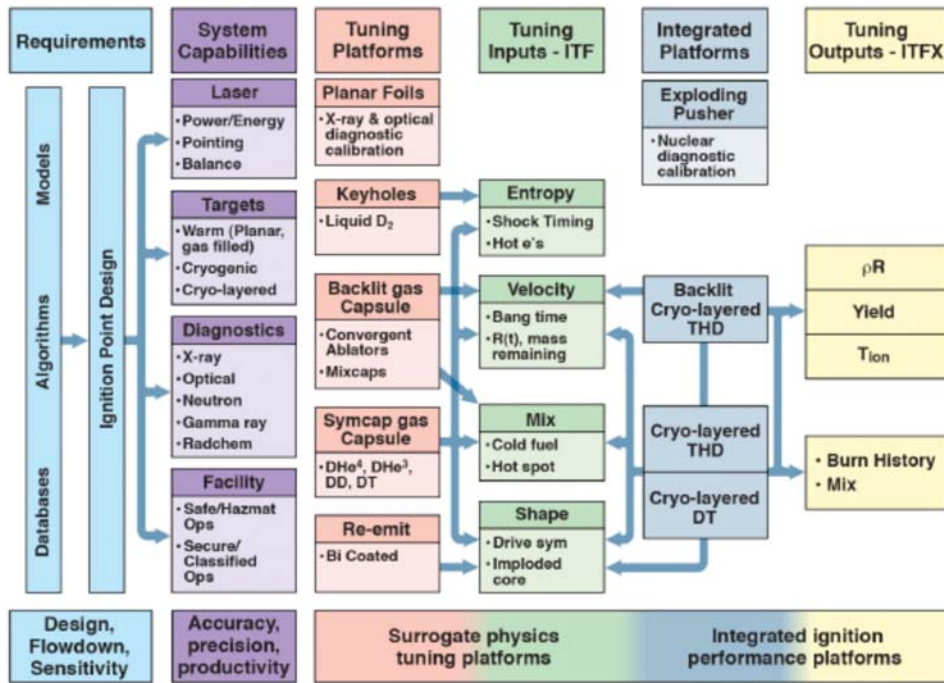
FIG. 1. The NIC framework—Requirements established by the point design determine the required system capabilities. These capabilities enable the development of implosion optimization platforms and the fielding of implosion optimization (tuning) experiments. The tuning experiments yield optimized laser and target parameters for the integrated implosion platforms whose output performance is measured with a wide array of diagnostics.

parameters needed to optimize the implosion of the fuel. Finally, these optimized target and laser parameters were applied to cryo-layered implosions whose performance was assessed using a variety of diagnostics that measured the implosion outputs.

The design of the NIF was optimized for Indirect Drive ICF[2] and that was the focus of the NIC although initial experiments have been carried out to begin testing the feasibility of using the NIF beam geometry for Polar Direct Drive (PDD).[3] In the indirect drive approach, the 192 high-energy NIF[4,5] laser beams enter a high-z cylinder, called a hohlraum, through entrance holes (LEHs) on the ends of the cylinder. The hohlraum for the CH ablator point design target used in experiments in 2011–2012 is shown in Figure 2. There are 192 beams in NIF, which enter the target chamber in 48 "quads." For most purposes, a quad can be considered as a single ∼f/8 beam. These beams are arrayed in 8 cones,
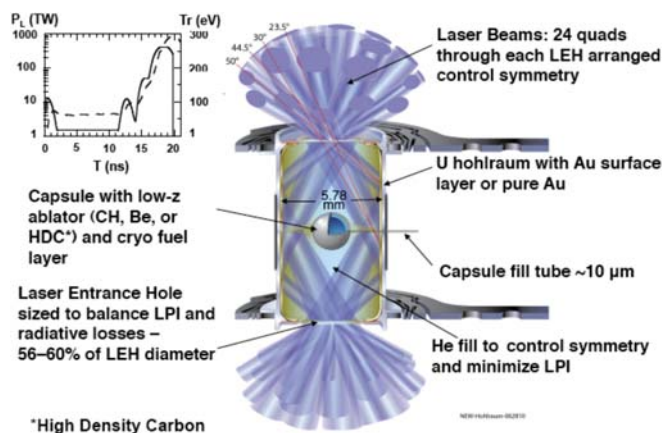

FIG. 2. Schematic of ignition target design, highlighting key features and options for hohlraum and capsule materials. Also indicated is the laser pulse shape showing the laser power in TW and the radiation temperature reached at that power versus time in ns.

forming angles with the hohlraum axis of 23.5°, 30°, 44.5°, and 50° from each side. These cones of beams contain 4, 4, 8, and 8 quads, respectively, on each side. Beams coming in along 23.5° and 30° have a wavelength or color that differs by a few angstroms and a pulse shape that differs from the color and pulse shape for the 44.5° and 50.0° beams. The 23.5° and 30° beams can also have different wavelength. The relative brightness of the two sets of cones allows time-dependent control of the symmetry of the x-rays irradiating the capsule. The slightly different color of the different cones makes it possible to transfer energy from one set of beams to another, providing an additional technique for controlling long wavelength radiation flux symmetry. The hohlraum is filled with He gas which is confined by a ∼0.5 μm thick window of polyimide over the LEHs.

The x-rays that result from heating the high-z walls of the hohlraum ablate material from the spherical shell surrounding the fuel, which is mounted in the center of the hohlraum. The resulting implosion compresses and heats the central fuel to fusion conditions. The central capsule containing the fuel is made up of thin concentric spherical shells. The outer shell can be CH plastic or Be, high-density carbon (HDC or nano-crystalline diamond) or another low-Z material, called the ablator. The layers of the shell must be very smooth, to minimize seeds of hydrodynamic instabilities. In order to minimize instability growth at the interface between the ablator and fuel layer, the ablator includes concentric layers of mid-Z dopant. These layers absorb preheat x-rays, thereby tailoring the temperature profile and hence the density of the ablator near the interface with the cryogenic fuel. The ablator encloses a spherical shell of DT fusion fuel, kept solid by keeping the entire assembly at cryogenic temperatures near the triple-point of the fuel mixture. The interior of the shell contains DT vapor in equilibrium with the solid fuel layer. The capsule is supported in the hohlraum between two films of Formvar that is 15–100 nm thick. The DT filling the

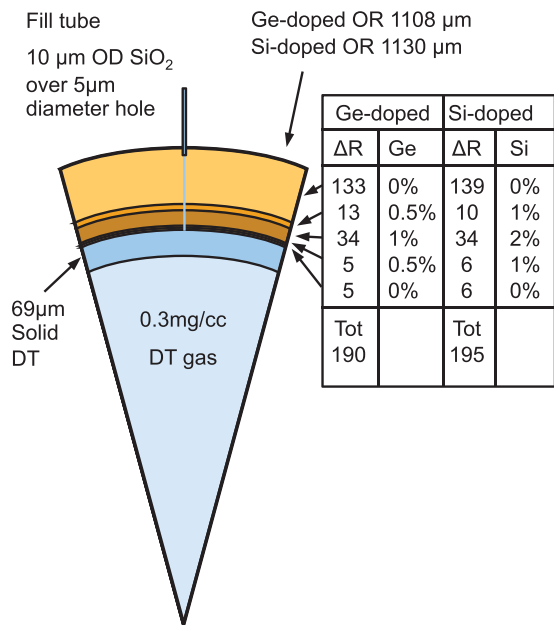| Ge-doped		Si-doped	
ΔR	Ge	ΔR	Si
133	0%	139	0%
13	0.5%	10	1%
34	1%	34	2%
5	0.5%	6	1%
5	0%	6	0%
Tot 190		Tot 195	

FIG. 3. CH point design capsule. Variants have been tested with both Ge and Si dopants with point design dimensions as shown. Experiments have been carried out with variations in thickness, dopant profiles, and dopant concentrations

capsule is fed through a $10\,\mu m$ diameter fill tube and hole through the ablator. The NIC utilized a CH ablator, doped with either Si or Ge for preheat protection. Dimensions and other features of the capsules with the two different dopants are shown in Figure 3. The initial CH point design capsule with Ge preheat dopant was used in the NIC campaign until August 2011. Si doped capsules were found to be more efficient as described in the discussion of experiments below and were used after August 2011. Experiments have tested different thickness ablators as well as different dopant concentrations and profiles as part of the optimization process.

The x-rays heat the hohlraum to a peak radiation flux temperature (Tr) that can range from 270 eV to above 300 eV, depending on the laser power, the hohlraum design, the

capsule design, and the ablator material. The CH capsules shown in Figure 3 were designed to operate at about 300 eV. The drive pulse, as shown in Fig. 2, has four precisely controlled steps. Also indicated in Figure 2 are the laser power in terawatts (TW) and the hohlraum temperature Tr in eV generated by this power versus time in nanoseconds (ns). This shape is necessary to compress the DT fuel without generating unacceptable shock preheat and entropy in the fuel. The DT fuel must be quite close to Fermi degenerate to minimize the pressure required for a given compression. The fuel is initially compressed by three shocks, followed by nearly adiabatic compression. Maintaining adequately low entropy for the entire fuel volume requires that each shock be carefully controlled in strength and launch time: no shock may overtake its predecessor in the solid fuel, and the shocks must be sufficiently closely timed that no substantial rarefaction occurs between breakout of one shock and the compression by the following shock. Each of the first three shocks is launched by a well-defined pulse in laser power, as evident in Fig. 2.

The key challenges for the ignition campaign are:

(1) Designing a laser/target system that can achieve fusion ignition and burn propagation
(2) Developing the capabilities needed to achieve the conditions required for ignition in the presence of uncertainties in the physics models, and
(3) Gauging progress and advancing toward those conditions as we progress through the ignition campaign.

These challenges and the response to them define the framework of the NIC. Addressing these questions and developing the answers to them and providing the capabilities to achieve the subsequent requirements on the laser, target fabrication, and experiments has been the focus of research in ICF for more than four decades.

One of the key advances in forwarding this strategy is developing an approach to reducing the effective dimensionality of the ignition campaign. This is shown schematically in Fig. 4. There are hundreds of actionable quantities that affect an ICF implosion. These can be binned by the physical
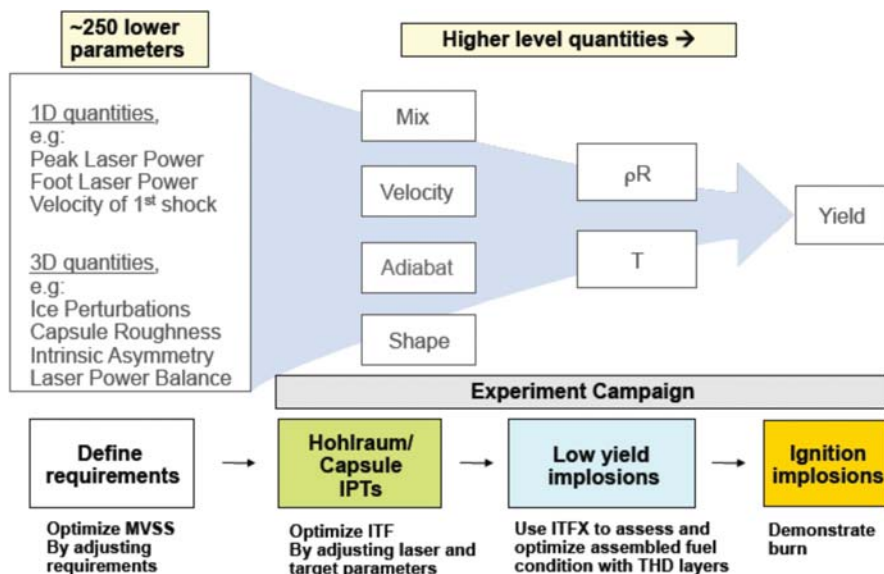

FIG. 4. Schematic of the NIC campaign methodology designed to reduce the dimensionality of the experimental campaign from initially ~250 target and laser parameters to four primary input variables: velocity, adiabat, hotspot shape, and fuel/ablator mix, and an ITF based on those variables. These four variables in turn together determine the total fuel ρR, hotspot ρR, and temperature of the hotspot, an output parameter ITFX based on those quantities as well as a Generalized Laswon Criterion (GLC), and ultimately the fusion yield.

instantiation of the laser and target configuration along with specifications and allowable variations in experiments. Or these quantities can be binned into 1-dimensional variables (e.g., capsule dimensions and dopants, laser power, and shock timing precision) or 3-dimensional variables (e.g., ablator/fuel roughness, pointing errors, and beam-to-beam power balance).

These variables can be mapped onto the principal in-flight parameters of the implosion process to address challenge (1) above by optimizing the implosion velocity (V), the fuel entropy or adiabat (α), the hotspot shape (S), and the mix of ablator into the fuel (M). For a given ablation pressure, simple analytical models[6,7] show that the two key inputs to an implosion that determine the total ρR and hotspot conditions in 1D are the implosion velocity (V) of the fuel and its adiabat (α) or entropy. The velocity provides the kinetic energy for compression and heating. The adiabat—the ratio of the pressure required to reach a given density compared to that required for a Fermi degenerate compression—determines how efficiently that kinetic energy can be used to generate the required total ρR and hotspot conditions. Velocity and adiabat, modified by the 3D effects from an imperfect spherical shape and from mix form the basis for a metric that we call the Ignition Threshold Factor (ITF)[8–13] for setting specifications on the laser, targets, and experiments, required for ignition. The target platforms developed to achieve the specifications on these key input parameters, and the experimental measurements on these platforms,[14] allow us to address question (2) above. The principal outputs required to address question (3) above are reduced to a set of performance metrics. One metric is a Generalized Lawson Criterion (GLC)[15,16] for ICF which depends on the product Pτ of the hot spot pressure P and the confinement time τ, and the ion temperature T. A second metric that we call ITFX[17] depends on a measurement of the neutron yield (Y) and the fraction of those neutrons down scattered (DSR) by the surrounding cold fuel in an implosion with a cryo fuel layer. The yield is a measure of the hotspot performance, and the DSR is a measure of the total ρR of the fuel, which determines confinement time. As discussed below, both ITF and ITFX are equivalent to the GLC for a wide range of implosions but serve complementary purposes.

The basic requirements for ignition of DT fuel in an inertially confined implosion have been known for decades:[18] a central hotspot of 4–5 keV with a size comparable to the range of an alpha particle $\sim$0.3 g/cm^2, surrounded by a confining layer with a ρR > 1 g/cm^2 to provide adequate confinement. These are the conditions for the compressed state of the fuel, the endpoint or outputs of a properly tuned implosion. These conditions are similar to the nτ and T specified by the Lawson Criterion in magnetically confined fusion plasmas. Under these conditions, the alpha heating can generate a self-sustaining burn wave, with no external energy input, which heats the fuel surrounding the hotspot to 10s of keV. The thermonuclear burn generated by such a burn wave can exceed 1000 times the kinetic energy initially imparted to the fuel in the capsule implosion process or a factor of 10 or more times that of the energy in the laser pulse used to heat the hohlraum and drive the implosion. In discussing the definition of ignition the 1997 NRC report[19] commented:

"The definition of ignition, while seeming straightforward at first glance, is not necessarily a point of consensus within the community of ICF researchers. Therefore the committee has adopted an operative definition for the purposes of this report. The shape of the yield curve is cliff-like, in that fusion yield increases very rapidly, from near zero to its full value, over a relatively small range of incident energy. A plot of fusion yield as a function of other relevant drive parameters (such as laser uniformity or capsule surface finish) would exhibit a similar structure. This curve leads to the operative definition of ignition adopted by the committee: gain greater than unity.

However, there are two diagnosable milestones on the yield curve. At a gain of about 0.1, energy deposited by fusion alpha particles is sufficient to double the central temperature. At a gain of about 0.3, fusion reactions occur over a sufficient region to induce propagation of the thermonuclear burn into the denser, colder, outer fuel."

This burn wave is well established by the time yields reach an energy equal to the input laser energy or yields of about 1 MJ, and this level of performance, as recommended by the 1997 NRC review of NIF has been adopted as the working definition of ignition for the National Ignition Campaign. At this yield, the thermonuclear energy amplification produced as a result of alpha heating is typically 70–100 times the yield that would be produced by heating from PdV work alone without alpha deposition. There is a continuum of effects from alpha heating as the yield and fuel ρR increase toward ignition and beyond to high gain. For the first time in laboratory ICF, the hot spot ρr in the NIF implosions is sufficient to stop the alpha particles being produced by the thermonuclear reactions occurring within that hot spot. With the compressions currently being achieved in the NIC implosions, as described below, the ρr of the hot spot is about 0.1 g/cm^2 which is sufficient to stop the alpha particles at the $\sim$3 keV temperature of the hot spot. As described below, a yield of $\sim$2 kJ as achieved on the better implosions during the NIC is about equal to the compressive work done on the central hot spot in those implosions. The alpha particle energy is 20% of the thermonuclear (TN) yield or 400 J from 2 kJ of yield. The heat capacity of the DT fuel is about 100 J/keV/μg. Since the hot spot mass in a typical implosion is $\sim$5–10 μg, deposition of 400 J of alpha particles would be enough to raise the hot spot temperature nearly $\sim$0.5–1 keV. However, thermal conduction transports much of this energy to material beyond the initial hot spot, and the calculated temperature change is only about 100 eV. We calculate that it takes a yield from PdV work of 7–10 kJ or 1.4–2 kJ of alphas to produce an ion temperature increase of about 0.5 keV, sufficient to double the yield as a result of alpha heating. This is a yield from PdV work that is about a factor of 3–5 greater than the best performing experiments during the NIC. Beyond this point, the thermonuclear burn is alpha dominated and the yield becomes a very rapidly increasing function of the conditions reached in the compressed fuel.

If we follow temperature versus time in an igniting capsule, the central temperature reaches 10–12 keV at a yield of 100–150 kJ for a NIF ignition capsule. At this temperature, the burn rate is sufficient to initiate a self-sustaining burn

wave that requires no additional heating beyond that provided by the alphas to propagate the burn. This is the definition of ignition adopted by Lindl[20] and by Atzeni and Meyer-ter-Vehn.[21] However, the degree of burn propagation depends on the relative fraction of the total confinement time required to get to 10–12 keV central temperature compared to the time remaining for burn propagation.

Progress on the NIC experimental campaign[22,23] has gone hand in hand with advances in NIF capabilities since the start of the NIC experimental campaign. A key element in the progress toward ignition has been integration into the experimental platforms of a wide range of improvements in the technological capabilities of the NIF laser, the targets, and the diagnostics including:

- Steady advances in laser performance enabled the longer pulses requiring increased laser energy used in the recent experiments:

  - During the March and April 2012 experiments, the NIF laser routinely delivered pulse energies of 1.45–1.7 MJ with powers over 400 TW. In July 2012, NIF delivered an ignition pulse with the full NIF design energy and power of 1.8 MJ and 500 TW.

- A steady increase in the number of diagnostics and their performance. Approximately 60 diagnostic systems are now in use.
- Significant advances in the characterization and precision of targets used for these experiments.

Progress in the NIC experimental campaign can be summarized as follows:

- Diagnostics, targets, and laser capabilities have reached the levels of performance needed for a systematic optimization of ignition-scale experiments.
- Peak hohlraum temperatures have been achieved which exceed the 300 eV point design goal with nearly constant laser energy coupling of 84 ± 2% for energies from 1.2 to 1.7 MJ. The use of higher *albedo* Au-lined U hohlraums has further improved peak temperatures by ∼10 eV to above 320 eV.
- Hot spot symmetry, which meets ignition specifications, has been achieved using a combination of power balance and wavelength shifts between the inner and outer beams and an additional wavelength shift between the two cones of inner beams.
- Shock timing experiments have demonstrated the accuracy needed to achieve the point design adiabat.
- The dependence of implosion velocity on ablated mass has been accurately measured and is consistent with code simulations within the error bars, over a range of peak inferred fuel velocities up to velocities approaching the point design velocity of 370 km/s.
- By systematically optimizing the shock timing and peak power part of the laser pulse shape, the NIC experiments have demonstrated a fuel areal density $\rho r \sim 1.25$ g/cm^2 which is about 85% of that specified for the point design. The total areal density of the imploded core is in excess of 1.7 g/cm^2 when the ρr of the remaining ablator is included.

- As the NIC experiments have moved toward implosions with optimized shock timing and extended drives to achieve higher pressure and higher fuel ρr, the observed levels of hot spot mix become significant. For the "no coast" implosions, which achieve the highest pressure, GLC, and ITFX, the threshold for significant mix occurs at a velocity of about 300 km/s, below the 370 km/s velocity of the point design. One of the key research efforts moving forward in the ignition program is experiments to provide the data needed to understand this difference and to develop a path forward to higher velocity.
- 1D Calculations predict pressures about 2-3× higher than observed experimentally. Large amplitude low mode asymmetry not included in these calculations, or hydrodynamic instability effects larger than calculated are leading candidates to explain at least some of the reduced pressure seen in the experiments. Experiments to better understand the source of low mode asymmetry and measures to mitigate it in the implosions, as well as experiments to directly measure instability growth rates and initial amplitudes are two of the key focus areas for experiments going forward.

The rest of this review of the NIC is organized as follows: Section II discusses the various ignition metrics and their uses. Section III discusses the role of modeling in the ignition campaign, Sec. IV discusses the approach taken by the ignition campaign to optimize ignition implosions, Sec. V is an extensive discussion of results obtained in the ignition campaign to date, and Sec. VI addresses the path forward.

II. IGNITION METRICS AND THEIR APPLICATION IN SETTING SPECIFICATIONS AND EVALUATING PROGRESS TOWARD IGNITION

Over the past 15 years, a wide variety of metrics has been developed to both guide approaches to ignition and to gauge progress. One approach to developing these metrics has grown out of efforts to set specifications on the laser, targets, diagnostics, and the experimental campaign. A second approach has grown out of an effort to identify metrics for progress toward ignition from the results of experiments. All of these metrics have a common origin in the Lawson Criterion.

A general Lawson Criterion can be obtained by setting the energy gain from alpha deposition equal to the energy loss from the central hot spot. This is a condition that is sufficient for the energy deposited from thermonuclear burn to overcome the energy losses, assuming the hot spot has a ρr equal to or greater than the range of an alpha particle so that the alpha kinetic energy is largely deposited in the hotspot. The hot spot gain Q is given by

$$Q = \frac{Y_N E_a / \tau_{TN}}{\frac{3}{2} PV / \tau_E} \simeq \frac{Y_N E_a}{\frac{3}{2} PV}, \tag{1}$$

using $\tau_{TN} \sim \tau_E$ where τ_{TN} is the thermonuclear burn width and τ_E is the energy confinement time, P is the hot spot pressure, V is the hot spot volume, Y_N is the total neutron yield, and E_α is the alpha particle energy. The yield in Eq. (1) is

from a "no-burn" calculation in which the energy from the alphas generated is not used to provide any additional self-heating or boot-strapping of the temperature obtained by PdV work on the hot spot. This metric is designed to be a measure of the hydrodynamic performance of the implosion in the absence of alpha heating. These conditions can be approximated by using low tritium content mixtures of tritium, hydrogen, and deuterium (THD) fuel compositions. For a yield of 1 MJ, adopted as the working definition of ignition on the NIF as described above, we expect to require that the alpha deposition be equal to some fraction f of the PV work done on the hot spot, where f is near unity. This will define a GLC for ignition on the NIF. Using

$$Y_N = n_D n_T \langle \sigma v \rangle V \tau_{TN} = \frac{1}{4} n_i^2 \langle \sigma v \rangle V \tau_{TN} \qquad (2)$$

for 50/50 DT, where Y is the number of neutrons produced, n_i is the ion number density in particles per cm^3, and $\langle \sigma v \rangle$ is the thermally averaged reaction rate[24]

$$\langle \sigma v \rangle (\mathrm{cm}^3/\mathrm{s}) = 9.1 \times 10^{-16} \exp\left(-0.572 \left| \ln \frac{T}{64.2} \right|^{2.13}\right) \qquad (3)$$

for T in keV. Using total particle density (ions and electrons)

$$n_p = 6.02 \times 10^{23} \frac{z+1}{A} \rho = 2.4 \times 10^{23} \rho$$

and

$$P(\mathrm{Gbar}) = 0.96 \frac{Z+1}{A} \rho T(\mathrm{keV}) = 0.768 \rho T(\mathrm{keV}), \qquad (4)$$

where ρ is in g/cm^3, we can write

$$GLC = \left[9.11 \times 10^{16} \frac{\langle \sigma v \rangle}{fT^2}\right] P \tau_{TN} = \frac{P \tau_{TN}}{(P\tau)_{IGN}}, \qquad (5)$$

where τ_{TN} is in ns and we have set

$$P\tau_{IGN}(\mathrm{GBar} - \mathrm{ns}) = \frac{fT^2}{9.11 \times 10^{16} \langle \sigma v \rangle}. \qquad (6)$$

The neutron production in Eq. (2) is the integral over space and time of the reactions occurring in an evolving density and temperature profile. However, the simple formulae above using burn averaged measured values give the pressure to a few percent when benchmarked against two and three dimensional radiation hydrodynamic calculations.[25,26]

The burn averaged ion temperature of the deuterium-tritium plasma is determined by neutron time of flight measurements. The neutrons produced by thermonuclear reactions have an energy spread around the narrow 14.1 MeV fusion peak due the thermal motions of the deuterons and tritons. The energy spread turns into a temporal spread at the detector that can be converted to a burn averaged and volume averaged temperature using the formula of Brysk[27]

$$\mathrm{For\ DT}: \ \Delta t = 0.122 d\sqrt{T_i}$$

and

$$\mathrm{For\ DD}: \ \Delta t = 0.778 d\sqrt{T_i},$$

where Δt is in ns, d is in m, and T_i is in keV.

Hydrodynamic motion of the hot spot during burn can introduce an uncertainty in the estimated temperature but estimates indicate that this is generally a small effect that can be checked by examining angular isotropy of the temporal spread of neutrons in detectors at different locations. The burn time is inferred from the x-ray pulse width in the x-ray band near 10 keV or from the temporal width of the gammas produced by the DT reactions. The 10 keV x-ray production closely mimics the neutron production as a function of density and temperature and is only weakly attenuated in the matter surrounding the hot spot.

Since $\langle \sigma v \rangle \sim T^2$ between 10 and 20 keV, $P\tau_{IGN} \sim$ constant $= 8 - 10$ Gbar $-$ ns (*or* atmos $-$ s) for $f = 1$. This is the classical Lawson Criterion used in magnetic fusion energy (MFE) in which a near steady state plasma is confined at 10–20 keV. In ICF, however, the PdV compression of an imploding shell of fuel typically reaches burn averaged temperatures of 3–4 keV without alpha deposition. Alpha deposition is then relied upon to heat the fuel to temperatures in excess of 10 keV for efficient thermonuclear burn. Since the cross section decreases faster than T^2 below 10 keV, an ICF implosion must achieve a $P\tau > 10$ gigabars-ns to allow enough time for heating to these higher temperatures needed for efficient burn. At 4 keV, $P\tau_{IGN} \sim 29.6f$ Gbar $-$ ns while at 3 keV, $P\tau_{IGN} \sim 54f$ Gbar $-$ ns.

The pressure achieved in an implosion can be obtained from measured quantities[26] using Eq. (2)

$$P(\mathrm{GBar}) = 2 \times 10^{-19} \sqrt{\frac{Y_N T^2}{\langle \sigma v \rangle V \tau_{TN}}}, \qquad (7)$$

where V is the hot spot volume in cm^3 and the units of the other quantities were specified above.

The pressure (Eq. (7)) and ignition metric (Eq. (5)) can also be evaluated from synthetically derived measurement quantities provided by simulations. Specifically, the value of Eq. (5) as an ignition metric is clear from the grouping by yield within a large data set of nearly 2000 2D calculations[28] shown in Figure 5. Each of the dots is the result of a 2D calculation whose inputs spanned a range of calculated performance from near 1D with yields approaching 20 MJ to calculated performance with yields of only a few kJ. These calculations were carried for the Ge-Doped CH capsule shown in Fig. 3(b) using variations in the pulse shape (including peak power as well as shock timing and strength), radiation flux asymmetry, and capsule specifications (including low mode and high mode capsule characteristics and cryo-fuel layer low mode and high-mode characteristics). These calculations are carried out using a similar computational methodology to computational data sets discussed in Haan *et al.*[8] and Edwards *et al.*,[17] but include a wider range of variations in symmetry and pulse shape. However, the 2D calculations discussed in this section have not included very large low mode asymmetries or high levels of mix from the ablator into the hot spot as seen in many current experiments. The impact such large perturbations on the performance of cryo-layered implosions is discussed in Sec. V C

The curve in Figure 5 is given by Eq. (6) with $f = 0.75$. As shown, this curve passes through the points with a 50%
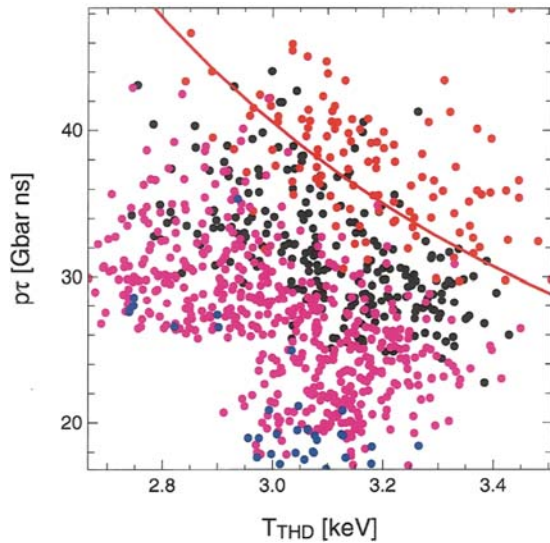
FIG. 5. $P\tau$ and T for each dot in the figure are the result of a 2D calculation of the Ge-doped CH capsule using a THD fuel mixture. Yields indicated are the result of a companion calculation using DT fuel. Performance variations are the result of variations in the laser pulse shape, the radiation flux asymmetry, and the capsule specifications including variations in the surface roughness of the ablator and the ice layer. Red, black, magenta, and blue represent yields >1 MJ, 0.1–1 MJ, 30 kJ–100 kJ, and <30 kJ. As shown, the contour for implosions with a 50% probability of 1 MJ yield is well fit with the red curve specified by Eq. (6) with $f = 0.75$.

probability of having a yield of 1 MJ or more. The temperature and $P\tau$ plotted in this figure are obtained from calculations with THD fuel mixtures having 2%D, 24%H, and 74%T (referred to as 2% THD in the following discussion) while the yields are obtained from calculations in which the fuel was a 50/50 mixture of DT. The THD fuel mixture is chosen so that it has the same density as a 50/50 mixture of DT and so behaves hydrodynamically the same.[17] Using THD layers, as indicated above, the PdV yields are low enough to ensure that the capsule performance is purely a measure of the hydrodynamic quality of the implosion. However, there are surrogacy offsets between a THD implosion and a DT cryo-layered implosion. These surrogacy issues arise because of a different stoichiometry in the THD central gas than in the surrounding fuel layer, specifically

more H-rich. This leads to a higher particle density in the THD central gas fill relative to that for DT at the same vapor pressure. The results of calculations that used a 50/50 DT mixture are shown in Figure 6. The points plotted are for the same calculations used for Fig. 6 with the sole exception of the fuel composition. The temperatures and hydrodynamic yields used for the axes in this figure are obtained from calculations with no alpha deposition, while the yields including alpha-deposition are obtained from companion calculations with alpha deposition. As shown, the hydrodynamic temperatures in the DT implosions are about 13% higher on average than temperatures from a similar series of THD implosions, and the hydrodynamic yields are about 30% higher on average. For the DT calculations, this shifts the locations of the ignition boundary in a plot of $P\tau$ versus T to the curve given by Eq. (6) with $f = 0.85$ as shown in Fig. 7. As expected from Fig. 6, the temperatures for the DT (no-burn) calculations are shifted upward at a given $P\tau$ by $\sim$0.3–0.4 keV from those calculated from otherwise hydrodynamically equivalent calculations with a 2% THD fuel mixture. Because of the slightly higher temperature achieved in the DT implosions, they have to perform somewhat better to achieve the equivalent quality hydrodynamic implosion. This is shown by the fact that the curve passing through the 1 MJ yield points requires a higher $P\tau$ and T compared to the equivalent THD implosion. Based on these results, we can define a GLC for a yield of 1 MJ as

$$GLC \equiv \left(\frac{P\tau(THD)}{T^2/1.21 \times 10^{17}\langle\sigma v\rangle} \right) = \left(\frac{P\tau(DT - no\ alpha)}{T^2/1.07 \times 10^{17}\langle\sigma v\rangle} \right).$$

(8)

In practice, most of the NIF cryo-layered implosions use 50/50 DT because it has proven easier to obtain high quality layers with this fuel mixture. Even at yields as low as a few kilojoules, the yields of DT implosions on NIF are affected by alpha deposition and this introduces an additional surrogacy issue. After the discussion of alternate metrics for assessing the quality of an implosion, we will come back to these surrogacy issues and introduce modifications to the ignition metrics that can be used in the presence of alpha deposition effects.
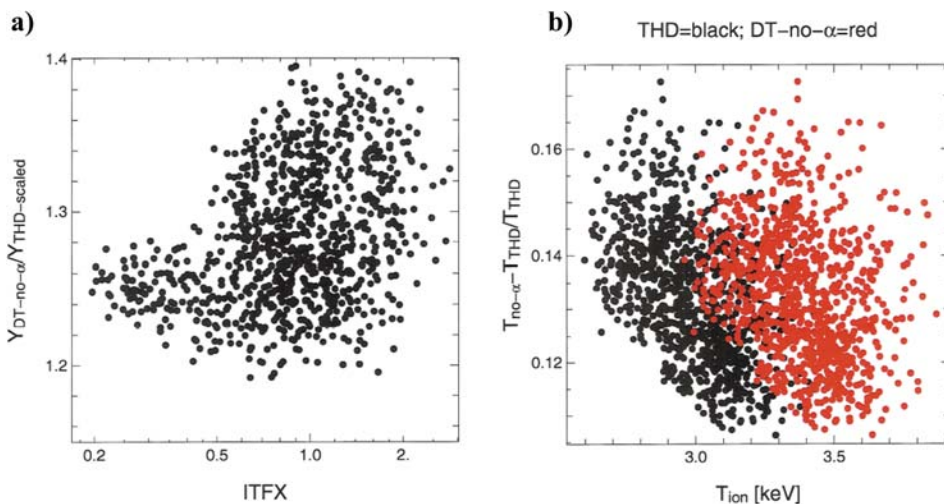

FIG. 6. Yields (a) for a given ITFX are about 30% higher than a yield scaled by the ratio of $N_D N_T$ for a 50/50 DT implosion vs a 2% THD fuel mixture. We find that Y(DT-no alpha) $\sim$22 Y(2% THD) rather than $\sim$17Y(2% THD) expected from the D and T fractions. Temperatures (b) are 13%–14% higher or 400–500 eV higher for a DT implosion vs a 2% THD implosion.

Hydrodynamic models of an ICF implosion can also be used to express the hot spot energy gain Q in Eq. (1) in terms of the hot spot temperature and the main fuel ρr (Betti's X discussed below), the main fuel ρr and the hot spot yield (ITFX), or the implosion velocity and main fuel adiabat (ITF). Each of these formulations has their utility and limitations.

Instead of utilizing the measured hot spot quantities described above to obtain $P\tau$ directly, Zhou and Betti used a hydrodynamic model[29] to obtain a generalized Lawson Criterion, which they called X, based on the hot spot temperature and the main fuel ρr.[15] This was later generalized to incorporate 3D effects from distortions of the hot spot due to hydrodynamic instability.[16]

Following Ref. 16, a simplified implosion model to obtain $P\tau$ relates the PdV work on the hot spot to the imploding shell energy

$$\frac{3}{2}PV = \frac{1}{2}\eta M_{Shell}v_{imp}^2 \quad \text{or}$$

$$P = (\eta\psi)\rho\Delta r_{shell}\left(\frac{v_{imp}^2}{r}\right) \approx (\eta\psi)(\rho r)_{total}\left(\frac{v_{imp}^2}{r}\right), \tag{9}$$

where M_{shell} is the mass of fuel in the imploding shell, Δr is the thickness of the fuel shell surrounding a hot spot of radius r, η is the fraction of the imploding shell energy contained in the hotspot, and ψ is a correction to a thin shell model for the mass of the main fuel. Since the imploded fuel region is nearly isobaric, η is the ratio of the hot spot volume to the volume of the total compressed fuel. For a uniform density shell surrounding the hot spot, η and ψ depend on the aspect ratio $A = r/\Delta r$ of the shell of cold fuel surrounding the hot spot and are given by

$$\eta = (1 + A^{-1})^{-3} \quad \text{while} \quad \psi = \left(1 + A^{-1} + \frac{1}{3}A^{-2}\right).$$

The implosion time τ is estimated from

$$M_{shell}\ddot{r} = 4\pi r^2 P.$$

Using Eq. (9) to obtain P/M_{shell} gives the implosion time as

$$\tau = \sqrt{\frac{r}{\ddot{r}}} = \sqrt{\frac{M_{shell}}{4\pi Pr}} = \frac{r}{v}\eta^{-0.5}. \tag{10}$$

Equations (9) and (10) together give

$$P\tau = \sqrt{\eta}\psi(\rho\Delta r)v_{imp}.$$

The product $\sqrt{\eta}\psi \sim 0.8 - 0.9$ for $1 < A < 4$, which is typical for the imploded fuel region. If we set $\rho\Delta r \sim (\rho r)_{total}$ and put in units, we have

$$P\tau(\text{Gbar} - \text{ns}) = 85(\rho r)_{total}\frac{v(\text{cm/s})}{10^8}. \tag{11}$$

We can relate ρr and v to T_i, fuel adiabat α, and yield through hydrodynamic relationships developed by Zhou and Betti[29] for a 1D implosion in which the hot spot and main fuel are compressed to a near isobaric final state that efficiently converts the fuel kinetic energy into fuel

compression. The relevant relationships, normalized for the NIF ignition scale implosions, are

$$\rho r = \left(\frac{\alpha}{1.5}\right)^{-0.54}\left(\frac{v}{3.7\times10^7\,\text{cm/s}}\right)^{0.06}\left(\frac{E_{fuel}}{2.5\,\text{kJ}}\right)^{0.33}, \tag{12}$$

$$\frac{T}{3.8} = \left(\frac{\alpha}{1.5}\right)^{-0.15}\left(\frac{v}{3.7\times10^7\,\text{cm/s}}\right)^{1.25}\left(\frac{E_{fuel}}{2.5\,\text{kJ}}\right)^{0.07}, \tag{13}$$

$$Y_{15} = 6.5\left(\frac{M}{0.17\,\text{mg}}\right)\left(\frac{\rho r}{1.5\,\text{g/cm}^2}\right)^{0.56}\left(\frac{T}{3.8\,\text{keV}}\right)^{4.7}. \tag{14}$$

Using Eqs. (12) and (13) to replace velocity in Eq. (11), we obtain Zhou and Betti's 1D ignition metric

$$GLC \approx \chi = \left(\frac{\rho R}{1.5}\right)^{0.8}\left(\frac{T}{3.8}\right)^{1.8}. \tag{15}$$

In obtaining Eq. (15), we have also approximated $T^2/\langle\sigma v\rangle \sim T^{-1}$ for the temperature range of interest. Using Eq (14), we can rewrite Eq. (15) to obtain an ignition metric that depends on yield and ρr instead of temperature and ρr. This form of the ignition metric is closely related to ITFX[17,30]

$$GLC = \left(6.5\left(\frac{\rho r}{1.5}\right)^{1.6}\left(\frac{Y_{15}}{M/0.17\text{mg}}\right)\right)^{0.375} \sim (ITFX)^{0.375}. \tag{16}$$

We can also use Eqs. (12) and (13) to write Eq. (15) in terms of the velocity, adiabat, and the peak fuel kinetic energy

$$GLC = \left(\left(\frac{\alpha}{1.5}\right)^{-1.8}\left(\frac{v}{370\,\text{km/s}}\right)^{5.8}\left(\frac{E_{fuel}}{6\,kJ}\right)\right)^{0.387}$$

$$= \left(\frac{E_{fuel}}{E_{fuel-ign}}\right)^{0.387}, \tag{17}$$

where $E_{fuel-ign}$ is given by

$$E_{fuel-ign}(\text{kJ}) = 6\left(\frac{\alpha}{1.5}\right)^{1.8}\left(\frac{v}{370\,\text{km/s}}\right)^{5.8} \sim E_{ign-HTL}.$$

This formulation recovers the ignition threshold factor of Herrmann-Tabak-Lindl (HTL)[11] at constant pressure at the fuel/ablator interface that was an assumption in the derivation of Eqs. (12) and (13).

If we write the fuel kinetic energy in terms of the fuel mass and velocity, Eq. (17) can be re-written as

$$GLC = \left(2\left(\frac{M}{0.17\,\text{mg}}\right)\left(\frac{\alpha}{1.5}\right)^{-1.8}\left(\frac{v}{370\,\text{km/s}}\right)^{7.8}\right)^{0.387}$$

$$\sim (ITF)^{0.387}. \tag{18}$$

This formulation is closely related to the Ignition Threshold Factor ITF[8] in 1D. Finally, if we use

$$\frac{\tau}{P\tau_{ign}} \sim \frac{r_{hs}/v_{imp}}{T^2/\langle\sigma v\rangle} \sim r_{hs}, \qquad (19)$$

we obtain a formulation of the ignition threshold factor which depends on the pressure and the hot spot radius

$$GLC \approx \left(\frac{P}{375\,\text{Gbar}}\right)\left(\frac{r_{hs}}{25\,\text{microns}}\right). \qquad (20)$$

We can also combine Eqs. (18) and (20) to relate adiabat and velocity to pressure and hot spot radius

$$\left(\frac{P}{375\,\text{Gbar}}\right)\left(\frac{r_{hs}}{25\,\mu\text{m}}\right) \approx 2\left(\frac{\alpha}{1.5}\right)^{-0.7}\left(\frac{v}{370}\right)^3. \qquad (21)$$

A similar relationship can be obtained from a simple model of the implosions. The pressure at stagnation will scale approximately as $\rho_{if}v^2$ where ρ_{if} is the in-flight density of the DT fuel at peak velocity and v its velocity. For a given adiabat, α, the fuel pressure in-flight is given by $P_{if} \sim \alpha\rho_{if}^{5/3}$ or $\rho_{if} \sim (P_{if}/\alpha)^{3/5}$. The implosion velocity scales approximately as gt, where g is the shell acceleration and t is the time over which the acceleration occurs. Thus, from Eq. (10), the implosion velocity scales as $v \sim P_{if}^{1/2}$ or $P_{if} \sim v^2$. Hence, $\rho_{if} \sim \alpha^{-0.6}v^{6/5}$ and $P_{stag} \sim \rho_{if}v^2 \sim \alpha^{-0.6}v^{3.2}$. If the ablation pressure is not maintained until the capsule begins its stagnation phase without experiencing decompression from rarefaction waves, an additional factor must be introduced to account for this. Experiments with various degrees of "coasting" after the end of the laser pulse observe this effect as described in Sec. V C.

Instead of relating all of the ignition criteria to $GLC = P\tau/P\tau_{ign}$, we can relate them to the ratio of the fuel kinetic energy achieved to that required for ignition

$$\left(\frac{E_{fuel}}{E_{ign-HTL}}\right) \approx ITFX \approx ITF \approx \left[\left(\frac{P}{375\,\text{Gbar}}\right)\left(\frac{r_{hs}}{25\,\text{microns}}\right)\right]^{\frac{8}{3}}$$

$$\approx \left(\frac{P\tau}{P\tau_{IGN}}\right)^{\frac{8}{3}} = GLC^{\frac{8}{3}}. \qquad (22)$$

Viewed this way, we can see that ITF and ITFX are linear in the ratio of fuel kinetic energy achieved to that required for ignition. The ignition margin is determined by the ratio of the fuel mass or fuel kinetic energy above the minimum required to achieve ignition. We can write

$$E_{fuel} = \eta_{hydro}E_{cap} = \eta_{hohlraum}\eta_{cap}E_{laser},$$

where E_{cap} is the capsule absorbed energy, η_{hydro} is the hydrodynamic efficiency between capsule absorbed energy and fuel kinetic energy, E_{laser} is the laser energy into the hohlraum, and $\eta_{hohlraum}$ is the efficiency of transfer of laser energy to the capsule absorbed energy, and n_{cap} is the fraction of the energy absorbed by the capsule that ends up in the fuel. Written this way, the ignition threshold factors are
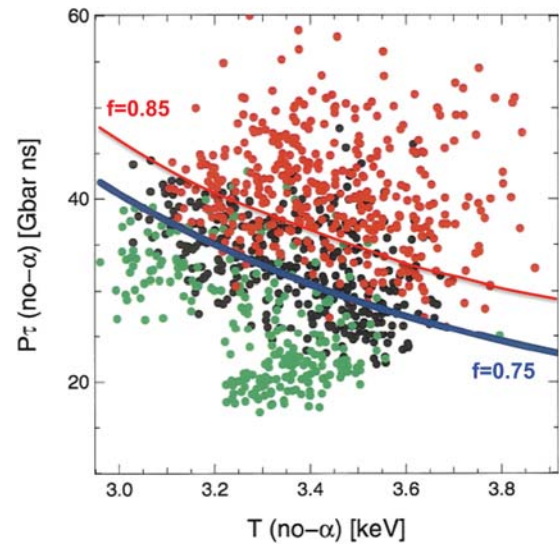

FIG. 7. $P\tau$ and T for each dot in the figure are the result of a 2D calculation of the Ge-doped CH capsule using a DT fuel mixture without alpha deposition. Yields indicated are the result of a companion calculation using DT fuel with alpha deposition. Red, black, and green represent yields >1 MJ, 0.1–1 MJ, and <100 kJ. As shown, the contour for implosions with a 50% probability of 1 MJ yield is well fit with the red curve specified by Eq. (6) with f = 0.85. Blue curve represents f = 0.75 which was appropriate for a 2% THD fuel mixture.

linearly related to the laser energy that is the ultimate constraint for the ignition campaign.

The relationships in Eqs. (15)–(22) and their extension to include 3D effects can be compared to the results of the large ensemble of 1D and 2D calculations whose results are shown in Figs. 5–7. We obtain ITFX and ITF from this computational data base by finding a best fit to a power law in DSR and yield for ITFX and to velocity and fuel adiabat for ITF. In obtaining this fit, we find that yield amplification rather than yield itself is better fit. Yield amplification is defined as the ratio of yield that would be obtained using burn-on calculations with alpha deposition to the yield that would be obtained with no alpha deposition, i.e., the yield due to heating from PdV compression alone. Since these metrics are related to the GLC which is derived from a ratio of energies, this is not a surprising finding in hindsight. However, this realization resulted in a somewhat different approach than that followed by Haan *et al.* and Edwards *et al.*, which focused on finding a best fit to yields very near the ignition threshold of 1 MJ yield. Both approaches work equally well near yields of 1 MJ, but we find that yield amplification is much better correlated with ITFX or ITF at low yields. The difference in these two relationships is shown in Fig. 8. Fig. 8(a) shows yield amplification vs ITFX and Fig. 8(b) shows yield vs ITFX. The "no-alpha" yield for this figure is taken from calculations with 2% THD fuel so that the level of alpha deposition is negligible. The burn-on yield is from a companion calculation in which all aspects of the implosion except the fuel composition were identical. The THD yields in Fig. 8 have been adjusted for the surrogacy effects relative to a 50/50 DT fuel mixture shown in Fig. 6 so that the yield ratio goes to one for low values of ITFX. Fig. 8(b) shows the growing spread in yield vs ITFX for values of ITFX well below ignition. The blue points in
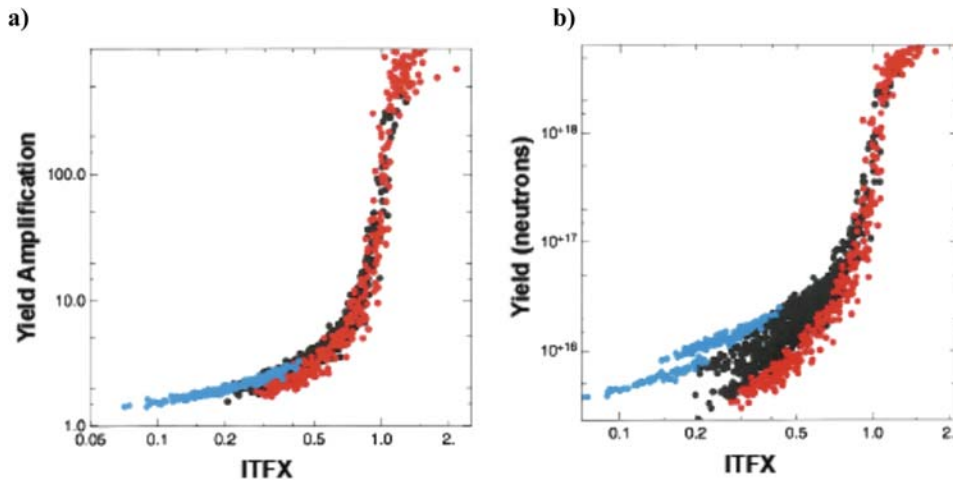
FIG. 8. (a) Yield (burn)/Y_{THD} (yield amplification) is generally better correlated with ITFX than (b) yield (burn) itself. Each point is the result of a 2D calculation. The colors represent calculations with different combinations of Yield and DSR. The blue points are the highest velocity lowest DSR implosions, while the red points have relatively lower velocity and higher DSR. The black points have intermediate values of both. At a given value of ITFX, particularly for low values of ITFX, we find that higher velocity implosions have higher yield. However, when we look at yield amplification, which depends on the fuel ρr or DSR as well as yield, we find that the higher velocity implosions have the same yield amplification at a given ITFX as somewhat lower velocity implosions with a greater fuel ρr. The THD yields have been adjusted for surrogacy effects relative to a 50/50 DT mixture so that the yield amplification goes to unity for low values of ITFX.

Fig. 8(b) have high velocity and low compression or low DSR. They have high power and poor shock timing. The red points have lower velocity and higher DSR. They have good shock timing but lower power. The black points are intermediate. The blue points get to higher yield because of the strong dependence of implosion velocity on temperature as seen in Eq. (13) and the strong dependence of yield on temperature as seen in Eq. (14). Said differently, they have lower ITFX for a given yield because of reduced ρr. Moreover, because of the reduced ρr and reduced confinement time, those implosions would be just as far from ignition and have comparable yield amplification to the red points. We find that the best fit functional form for ITFX normalized to values at 1 MJ yield is given by

$$ITFX = \left(\frac{Y^{THD}_{13-15\,MeV}}{1.8 \times 10^{14}}\right)\left(\frac{DSR_{10-12\,MeV}}{0.067}\right)^{2.1}$$

$$= \left(\frac{Y^{DT}_{13-15\,MeV}}{4 \times 10^{15}}\right)\left(\frac{DSR_{10-12\,MeV}}{0.067}\right)^{2.1}. \qquad (23)$$

In Eq. (23), Y is the primary neutron yield from 13 to 15 MeV. The formula for a THD implosion is based on a fuel mixture of 2%D, 24%H, and 74%T, while the formula for a DT implosion is for a 50/50 mixture of DT. The ratio of the yields between the THD and DT implosions accounts for the 30% surrogacy offset between a DT implosion and a THD implosion discussed above. For the DT implosions, these yields would be from calculations without alpha deposition. DSR is the ratio of neutrons downscattered to 10–12 MeV to those in the primary peak from 13 to 15 MeV. The relationship between the fuel ρr and DSR for neutrons in these energy bands is approximately given by $\rho r(g/cm^2) = 20$ DSR. Equation (23) has a somewhat stronger dependence on the fuel ρr or DSR than the analytic model given by Eq. (16).

Fig. 9 is a plot of the GLC ($= P\tau/P\tau_{ign}$) vs ITFX. Fig. 9(a) is a plot for a wide range of 1D calculations with varying x-ray powers and pulse shapes. Fig. 9(b) includes a wide range of 2D calculations in which the imploded shape and surface roughness of the CH shell and cryogenic fuel layer is varied. For both the 1D and 2D calculations, we find

$$GLC = IFTX^{0.45}_{1D} = ITFX^{0.45}_{2D}. \qquad (24)$$

Equation (24) is close to the relationship found in Eq. (16) from the 1D analytic implosion model and we find that this relationship works equally well in 2D without modification. The primary effect of the varying surface roughness is to reduce the hot spot yield as cold fingers of the main fuel penetrate and cool the outer regions of the hot spot. The implications of this and the reasons for the broad applicability of ITFX are discussed further below in relation to the scaling of ITF from 1D to 2D.

For an ignition metric based on the fuel adiabat and implosion velocity, we find the best fit functional form normalized to values along the 1 MJ yield contour in 1D to be given by

$$ITF(CH-1D) = 3.85\left[\frac{M_{DT}}{0.17mg}\right]\left[\frac{v}{370\,km/s}\right]^8\left[\frac{\alpha}{1.4}\right]^{-2.6}.$$

$$\qquad (25)$$

In obtaining Eq. (25), we used the same data set used to obtain ITFX in Eq. (23). The normalization constants in the velocity and adiabat term are chosen to be the nominal values for the ignition point design.[8] As was the case for ITFX, ITF has a somewhat stronger dependence on the fuel adiabat than predicted by Eq. (18). The formulation of ITF also has a weaker dependence on fuel adiabat than an earlier publication[8] on ITF which utilized a set of calculations with a smaller range of variation in the fuel adiabat near the ignition threshold. From Eqs. (16) and (18), we expect ITF(1D) and
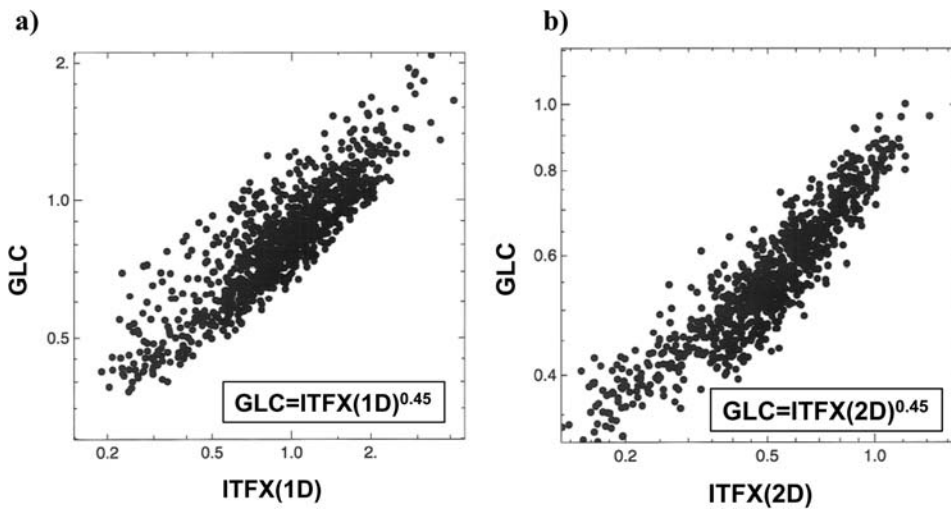
FIG. 9. We find that GLC ($P\tau/P\tau_{\text{ign}}$) versus ITFX closely follows the relationship expected from hydrodynamic scaling for both (a) 1D and (b) 2D for implosions perturbed by surface roughness and flux asymmetry.

ITFX(1D) to be linearly related. This is indeed what we find as shown in Fig. 10(a).

As indicated by Eq. (22), ITF is a measure of the ignition margin of an implosion, where we define margin as ITF-1. The ignition margin is determined by the ratio of the fuel mass or fuel kinetic energy above the minimum required to achieve ignition. If the implosion achieved the values indicated for the velocity and adiabat terms, with no degradation from the 3D terms, the ignition margin for the baseline optimized 1D Si-doped CH point design is approximately 3 as indicated by Eq. (25). As discussed extensively in the article by Haan *et al.*, we have used ITF to set specifications on the laser, targets, and experiments in order to maximize the margin available for dealing with all the various factors which degrade an implosion from an idealized 1D calculation.

To extend ITF to include 2D and 3D effects, we have incorporated three additional terms in ITF. We find that a wide range of effects from the surface roughness of the CH shell and cryogenic fuel layer as well as variations in the radiation flux from laser power imbalance and pointing errors can be incorporated by the addition of a shape term

(S) which accounts for the variation in the effective size of the hot spot as cold fuel fingers from growth of hydrodynamic instabilities penetrates into the hot spot. These cold fingers cool the outer regions of the hot spot and reduce the yield of the hot spot. Levedahl and Lindl[9] proposed that the correction needed to account for this cooling amounted to a rescaling of the implosion to recover a hot spot size equal to that which existed before the perturbations were imposed. Kishony and Shvarts[12] extended this analysis to show that perturbations with mode number of 6 or less had a reduced impact on the degree to which the hot spot had to be rescaled. In this context, "shape" includes such long wavelength shape variations as those from intrinsic hohlraum variations and pointing errors as well as shorter wavelength variations such as those caused by ablator and ice surface roughness. Because of thermal conduction driven ablation at the hotspot/cold fuel interface, perturbations at this interface are dominated by modes of $\ell = 30$ or less. There is an implicit assumption that the shape of the main fuel is sufficiently spherical that the principal effects of asymmetry are captured by looking at the shape of the hot spot. For implosion calculations near ignition, this is generally a good
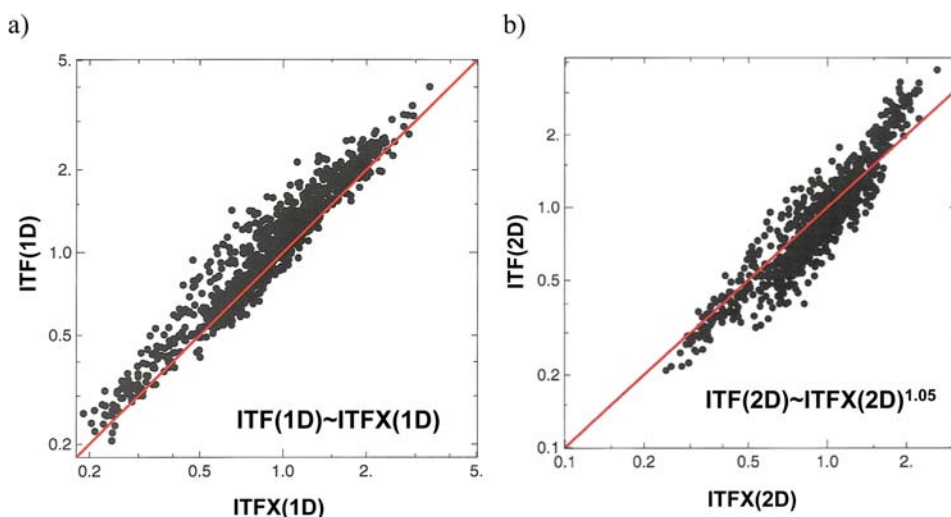

FIG. 10. ITF is approximately linear in ITFX in both (a) 1D and (b) 2D as expected from hydrodynamic scaling.

assumption. However, as discussed in Sec. V, it is possible to have implosions in which the fuel has large long wavelength mass variations while the hot spot is nearly spherical. It is necessary to have adequate diagnostics to avoid or correct implosions of this type. We find a best fit to the 1 MJ contour for the 2D calculations with a wide range of ablator surface and fuel roughness is given by

$$ITF(CH) = 1.6 \left[\frac{M_{DT}}{0.17\,\mathrm{mg}} \right] \left[\frac{v}{370\,\mathrm{km/s}} \right]^8 \left[\frac{\alpha}{1.5} \right]^{-2.6}$$
$$\times \left[\frac{1 - \frac{\Delta \mathrm{R}_{RMS-hotspot}}{R_{hotspot}}}{0.815} \right]^{3.3}. \quad (26)$$

The normalization constant for the shape term gives a factor of 2 reduction in ITF. Specifications on the capsule and radiation flux are set to achieve this level of shape distortion or less. The definition of the hot spot used in obtaining Eq. (26) is that developed by Clark,[13] but uses the distortion at the time the 2D calculation reaches 12 keV for capsules which burn, or the time of peak burn for those which do not ignite. Clark used the distortion from the 2D calculation but used the time at which the 1D calculation reached 12 keV. The result given here is closer to what one would measure in an experiment and has a physical interpretation very close to that of Levedahl and Lindl. If the exponent in Eq. (26) were exactly 3, the correction for the hot spot distortion would be equal to the volume change needed to recover the original yield and volume of the hot spot. This correction is consistent with the fact that the form of ITFX does not need to be changed in going from 1D to 2D since ITFX naturally accounts for the impact of reduced yield from distortions of the hot spot. Betti has used this yield correction to generalize his ignition criterion to 3D by setting

$$X(3\mathrm{D}) = X(1\mathrm{D}) \left(\frac{Y}{Y(1\mathrm{D})} \right)^{0.4} = X(1\mathrm{D}) YOC^{0.4},$$

where YOC is defined to be the ratio of the yield obtained in an experiment to that calculated for a 1D implosion. This relationship is expected from the relationship between X and ITFX in Eqs. (15) and (16) as a result of the fact that ITFX is unchanged between 1D and 2D/3D for the range of implosions discussed above. As a performance metric, this modification now makes X dependent on an accurate knowledge of what the 1D implosion for a given experiment would have been if there had been no degradation from 3D effects.

With the shape term in ITF given by Eq. (26), we find that ITFX and ITF are also linearly related in 2D as shown in Fig. 10(b). Equation (26) does not yet include the effects of the degradation in performance that results from the mix (M) of ablator into the cryogenic fuel layer or of ablator material that makes its way to the hot spot. Haan *et al.*[8] set specifications on the magnitude of these effects from capsule surface imperfections. When these effects are a small perturbation on capsule performance, we can modify Eq. (26) as follows to account for them:

$$ITF = 1.2 \left[\frac{M_{DT}}{0.17\,\mathrm{mg}} \right] \left[\frac{v}{370\,\mathrm{km/s}} \right]^8 \left[\frac{\alpha}{1.5} \right]^{-2.6} \left[\frac{1 - \frac{\Delta \mathrm{R}_{hotspot}}{R_{hotspot}}}{0.815} \right]^{3.3}$$
$$\times \left[\frac{\frac{M_{clean}}{M_{DT}}}{0.7} \right]^{0.5} \frac{[1 - M_{HS-mix}]}{0.9}. \quad (27)$$

In this equation, M_{clean}/M_{DT} is the fraction of the DT fuel layer which contains less than 5% by mass of ablator material. This mix term accounts for the fact that the cold DT fuel layer, which becomes the piston for forming the hot spot, is less compressible and acts as a less efficient piston when mixed with ablator material. Mix of ablator into the outside of the main fuel effectively raises the average main fuel adiabat. The term M_{HS-mix} is a measure of the hotspot mix. As the level of higher-z material from the ablator or from He resulting from T decay increases in the hot spot, the radiative losses from the hot spot increase making ignition more difficult. The added mass in the hot spot also increases its heat capacity, but the dominant effect is the increased radiative loss.

For the temperature and densities of the Si-doped CH capsule near ignition, M_{HS-mix} is given by

$$M_{HS-mix} = \left[\frac{M_{HSmixCHS}}{700\,\mathrm{ng}} \right] + \left[\frac{M_{HSmixSi}}{150\,\mathrm{ng}} \right] + \left[\frac{DT_{age}}{900\,\mathrm{h}} \right]. \quad (28)$$

The equivalent mass[8] for Ge-doped CH would be about 120 ng. These mix masses are to be compared to the typical hot spot mass which is $\sim 10\,\mu g$. Most of the mix mass from the ablator will be CH because the dopant fractions for Si or Ge are at atomic percent levels. These approximations for the effects of mix break down for levels of mix at which their impact becomes a dominant factor in ITF.

The shape and adiabat terms in ITF can largely be optimized without directly affecting the velocity or mix terms. However, the velocity and mix terms are strongly connected. Because of the strong velocity dependence of ITF and the relatively weak dependence on mix for small levels of mix, the optimum performance will occur with as high a velocity as possible without developing catastrophic mix. Figure 11 shows the results from a high-resolution 3D calculation that included measured capsule roughness on a patch of the capsule surface.[31] Based on this type calculation and other estimates, an implosion that is driven until the mix fraction reaches $\sim 30\%$ is estimated to give the optimum performance. However, these estimates also indicate that with a mix fraction of about 40%, the amount of mass penetrating the hot spot from statistical variability in the surface will increase rapidly. There is a fine line between optimizing the velocity with acceptable mix and stepping over the boundary. This boundary will have to be determined and optimized experimentally. An extensive discussion of ITF and its use in setting specifications and optimizing the ignition point design is contained in Ref. 8 by Haan *et al.*

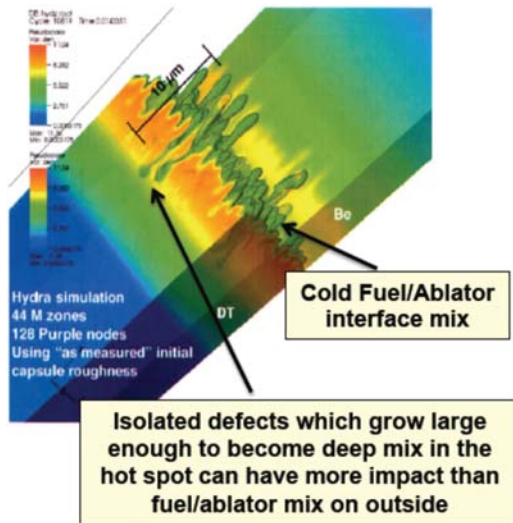From Eq. (20), we expect a linear relationship between the GLC and pressure achieved in the hot spot for constant

FIG. 11. 3D patch simulation of density profiles of cold fuel/ablator interface near peak velocity for a capsule initialized with as-measured initial surface roughness.

hot spot radius. Since capsules in the NIF ignition campaign have largely been the same size, we expect the hot spot radius to be nearly constant for 1D implosions. For the same computational data base, we have been using above, Fig. 12(a) is a plot of GLC versus pressure in the hot spot for a 2% THD fuel composition. Fig. 12(b) is the GLC vs pressure for the same set of implosions but with a 50/50 DT fuel layer

and no alpha particle deposition. GLC is linear in the hot spot pressure as seen in the Fig. 12 but as indicated by Eq. (29), there is a 90 gigabars surrogacy offset for GLC = 1 between the pressure required in a THD implosion and the equivalent no-alpha pressure required with 50/50 DT fuel

$$GLC = \left(\frac{P_{THD}}{420\,\text{Gbars}}\right) = \left(\frac{P_{DT}}{330\,\text{Gbars}}\right). \quad (29)$$

For this surrogacy offset to be consistent with the earlier finding that no-alpha implosions with 50/50 DT fuel were hotter and had higher scaled hydrodynamic yield than the equivalent 2% THD implosion (Fig. 6), Eq. (7) implies that the product of the hot spot volume and the burn time in the DT implosions must be larger than that in the equivalent THD implosions. From Eq. (7), we obtain

$$\left(\frac{V_{DT}\tau_{DT}}{V_{THD}\tau_{THD}}\right) = \left(\frac{r_{hs-DT}^3\tau_{DT}}{r_{hs-THD}^3\tau_{THD}}\right)$$
$$= \frac{Y_{DT}/Y_{THD}}{\left(P_{DT}^2 T_{DT}^{1.5}\right)/\left(P_{THD}^2 T_{THD}^{1.5}\right)} = 1.75,$$

where we have used $\langle\sigma v\rangle \sim T^{3.5}$ in the relevant temperature range and $P_{DT} = 0.79 P_{THD}$, $Y_{DT} = 1.3 Y_{THD}$, and $T_{DT} = 1.13 T_{THD}$. From Eq. (10), we expect the burn width to scale approximately as the hot spot radius, since the implosion velocities are nearly identical. We then expect $r_{hs-DT} \simeq$
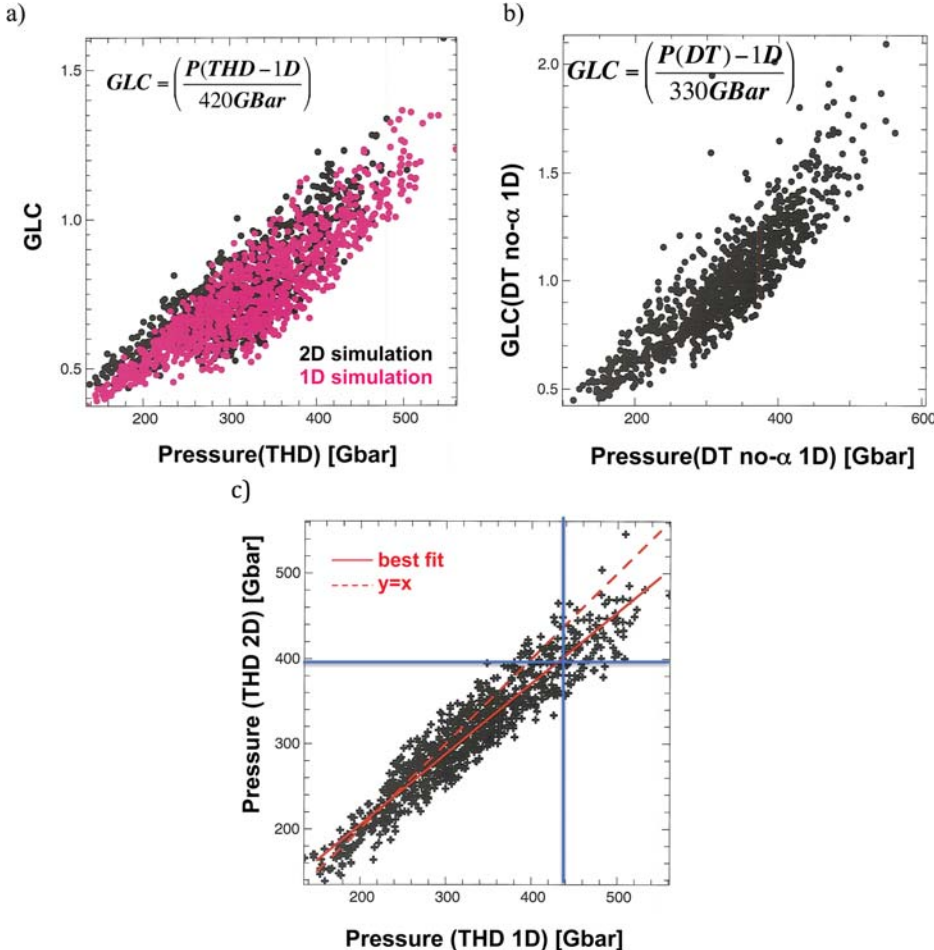

FIG. 12. GLC is linear in the hot spot pressure. Implosions (a) with a 2% THD fuel mixture require a higher pressure than implosions (b) with a 50/50 DT fuel at a given GLC (420 gigabars vs 330 gigabars at GLC = 1 in 1D). Implosion in 2D (a) require a slightly lower pressure at a given GLC than implosions in 1D (395 gigabars vs 420 gigabars at GLC = 1) because the clean hot spot temperature in the 2D implosions is slightly higher. This partially compensates for the fact that the hot spot pressure in 2D (c) is slightly lower for a given implosion velocity and adiabat than the comparable 1D implosion as a result of hydrodynamic instabilities.

$1.15r_{hs-THD}$ and $\tau_{DT} \simeq 1.15\tau_{THD}$. These are close to the values we find from our numerical data base which gives mean values for the radius and burnwidth as $r_{hs-DT} \simeq 1.16r_{hs-THD}$ and $\tau_{DT} \simeq 1.11\tau_{THD}$. Since the hot spot temperature is greater in the DT implosions than in the THD implosions, thermal conduction during the final compression process creates a larger hot spot with longer burn times and higher yield at lower pressure than is the case for the equivalent implosion with a THD fuel mixture.

The linear relationship between GLC and pressure also holds for the 2D calculations although there are a couple of differences from 1D that are worth noting. Fig. 12(c) is a plot of the hot spot pressure for the 2D THD data base versus the 1D THD hot spot pressure. The 2D data base was generated as indicated above by applying different levels of surface roughness to the 1D implosion data set. The surface roughness is sufficient to generate rms variations in the hot spot of up to 30%. As shown, the hot spot pressure generated in 2D is somewhat lower than that generated in 1D. However, the hot spot pressure required for a given GLC is slightly reduced for the 2D implosions relative to that required in the 1D implosions. This can be seen in Fig. 12(a) which includes data points for both the 1D and 2D calculations. For this data set, the pressure required for GLC = 1 is reduced from 420 gigabars in 1D to 395 gigabars in 2D. This slight reduction occurs because the hot spot temperatures in the 2D calculations are slightly higher than those in the equivalent 1D implosions. $P\tau_{ign}$ is therefore reduced. Although the 2D implosions have reduced size hot spots as a result of the growth of perturbations on the outer boundary of the hot spot, the remaining hot spot is hotter on average because the hot spot temperature increases toward the center of the implosion.

Since GLC is linear in pressure, we expect Pressure to scale as $\text{ITF(1D)}^{0.45}$ as indicated in Eq. (24). From Figure 13, for 1D implosions having a 50/50 DT fuel mixture with variations in fuel adiabat and implosion velocity, we find

$$\left(\frac{P}{330\,\text{Gbars}}\right) = 1.85\left(\frac{v}{3.7 \times 10^7\,\text{cm/s}}\right)^{3.7}\left(\frac{\alpha}{1.4}\right)^{-1.15},$$

(30)

which is within a couple of percent of $\text{ITF}^{0.45}$.

Based on the above analysis, we expect

$$ITFX \approx ITF \approx \left(\frac{E_{fuel}}{E_{ign-HTL}}\right) \approx \left(\frac{P_{DT}}{330\,\text{Gbars}}\right)^{2.2} \approx (GLC)^{2.2}$$

(31)

to be equally good, and complementary, metrics for characterizing the performance of an implosion. Fig. 14 is a plot of the yield amplification versus each of these metrics for the data base of calculations discussed above. As seen, the yield amplification as a function of each of these metrics is a nearly universal curve. However, each of these metrics has served a different purpose in the ignition campaign. ITF was developed primarily for its utility in setting specifications on the laser, targets, and the experiments. The quantities that comprise ITF in Eq. (27) can be more readily related to the
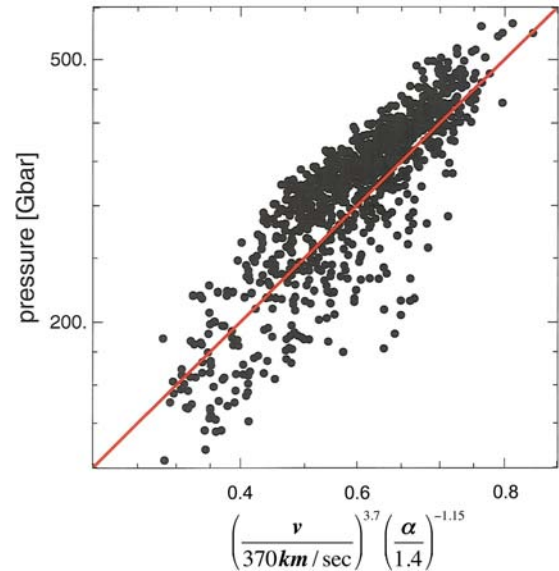

FIG. 13. The relationship between pressure and velocity follows from the relationship between pressure and ITF. The points plotted are for 1D implosions without alpha deposition having a 50/50 DT fuel mixture with variations in the fuel adiabat and implosion velocity.

many control parameters that constitute the total ignition system of physics and technology than the more integral quantities that constitute ITFX, the GLC and the hot spot pressure. For example, implosion velocity is readily related to the laser power and energy as well as to the shell thickness and composition. We have accordingly devised experiments described below that can directly measure the implosion velocity and its dependence on these variables. The hot spot shape is directly related to specifications on the hohlraum dimensions, the laser power balance, and the pointing accuracy, as well as various specifications of the target dimensions. X-ray and neutron emission experiments, as well as x-ray backlit implosions, have been developed to measure the shape of the imploding fuel. The fuel adiabat is directly related to the precision of the pulse shape as well as to hot electrons generated by laser plasma interactions (LPI). Experiments described below have been devised to optimize the pulse shaping to ensure optimal timing and strength of the various shocks generated by the laser pulse. Other experiments measure the level of hot electrons reaching the capsule. Mix is driven by the growth of hydrodynamic instabilities from seeds initially present on the capsule. Techniques have been developed to accurately characterize initial seeds for perturbation growth. Experiments have been developed to measure the growth of perturbations and to measure the amount of material mixed into the hot spot. ITFX, the GLC, and the hot spot pressure are complementary metrics for assessing the integrated performance achieved on any given cryo-layered implosion.

The threshold nature of implosions in the near vicinity of ITFX or GLC = 1 is seen clearly in Fig. 14. Fig. 15 shows more details of the implosion trajectory in the $T_{ion} - \rho R$ space for three implosions that span a range of GLC from just below 1 to about 1.5. These are the variables in Betti's 1D *X*.
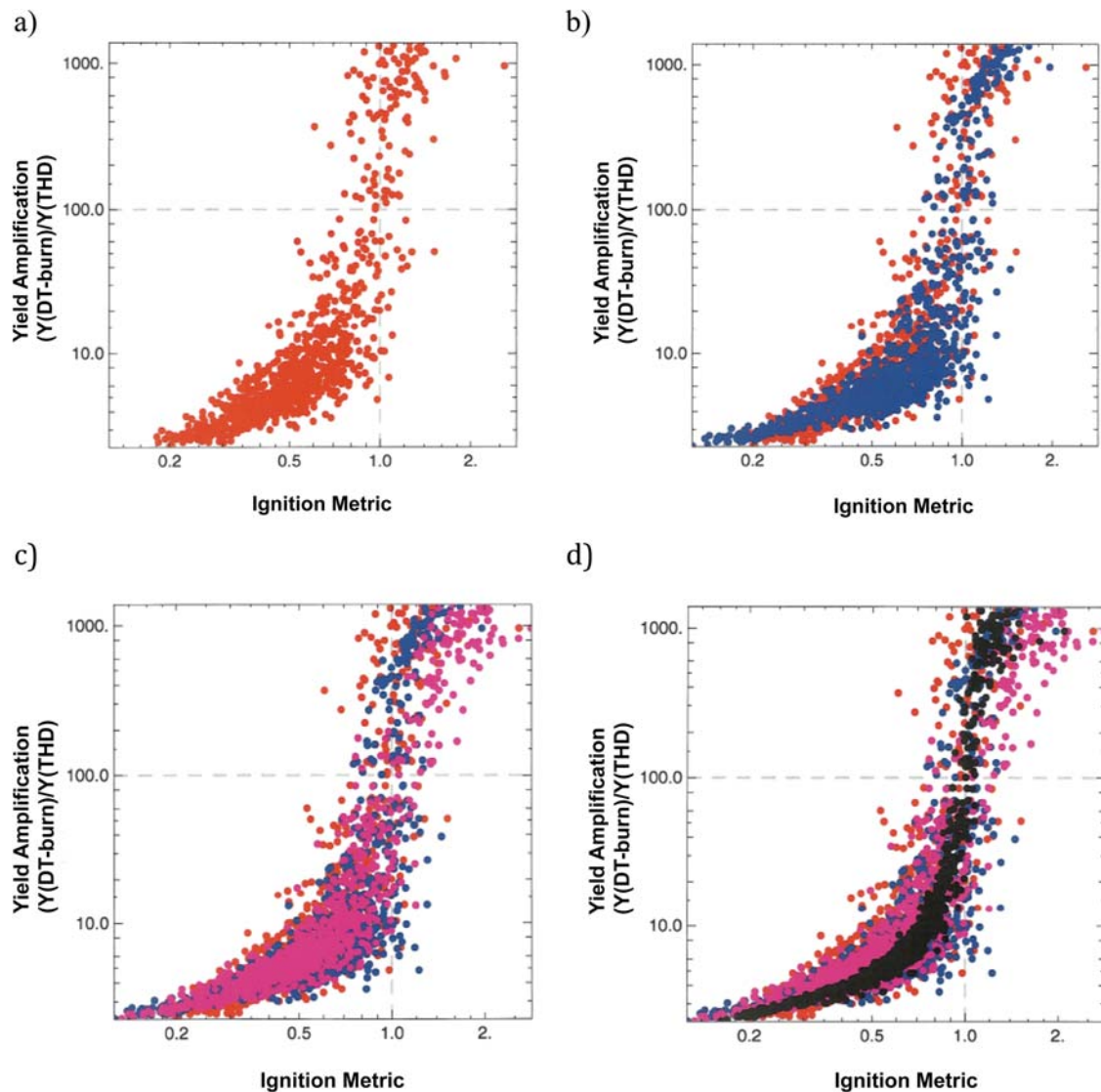
FIG. 14. Yield amplification versus ignition metric has the same functional form for several ignition metrics (a) GLC$^{2.2}$ in red, (b) pressure$^{2.2}$ in blue, (c) ITF in magenta, and (d) ITFX in black. Yields of 1 MJ occur near a yield amplification of ~100 for the Si-doped CH point design target.

Also plotted are lines of constant GLC for the case in which the yield is assumed to equal the 1D yield. Any combination of temperature and ρR along those curves would have the same GLC. Fig. 15(a) shows the trajectory in this space for an implosion with a GLC = 1.5 without alpha heating. The trajectory plotted starts at the time of peak implosion velocity when the stagnation shock has collapsed to the center and raised the hotspot temperature to about 2 keV. These are mass averaged quantities. Peak temperatures at the center of the hotspot are about twice these values. From this initial point, the kinetic energy in the imploding shell of fuel is gradually converted to internal energy over a period of about 300 ps. Points are shown along the implosion trajectory when 10% of the kinetic energy remains, at peak energy production, and at a time when the shell is expanding and again has 10% of its initial kinetic energy. In the absence of alpha heating, as the final compression proceeds, the average fuel ion temperature increases only slowly while the fuel ρR increases several fold. Hence, the initial increase in burn rate as the capsule implodes is coming primarily from the increase in

density. The slow increase in fuel temperature occurs because of thermal conduction and radiation losses of energy out of the heated central DT. It is interesting to note that the implosion follows a contour of nearly constant GLC as it approaches peak compression. Plotted in Fig. 15(b) is the companion implosion for a 50/50 DT fuel implosion. It parallels the THD implosion until alpha heating is large enough to cause a rapid heating of the fuel. This implosion is robust enough for the fuel to ignite before peak compression. It then has most of the confinement time provided by the peak ρR to burn and gets 17 MJ of yield, a burn-up fraction of about 30%. One feature evident in Fig. 15(b) is the slight offset in the temperatures of the THD and DT trajectories throughout the early phase of the implosion. This arises because of the disparity in composition of the central gas and cryo-layer in the THD implosion as described above.

Fig. 15(c) shows similar trajectories for a capsule with a GLC = 0.85 and a yield of about 40 kJ. There is some alpha heating in the DT and an associated measurable rise in fuel temperature, but the heating is insufficient to raise the fuel
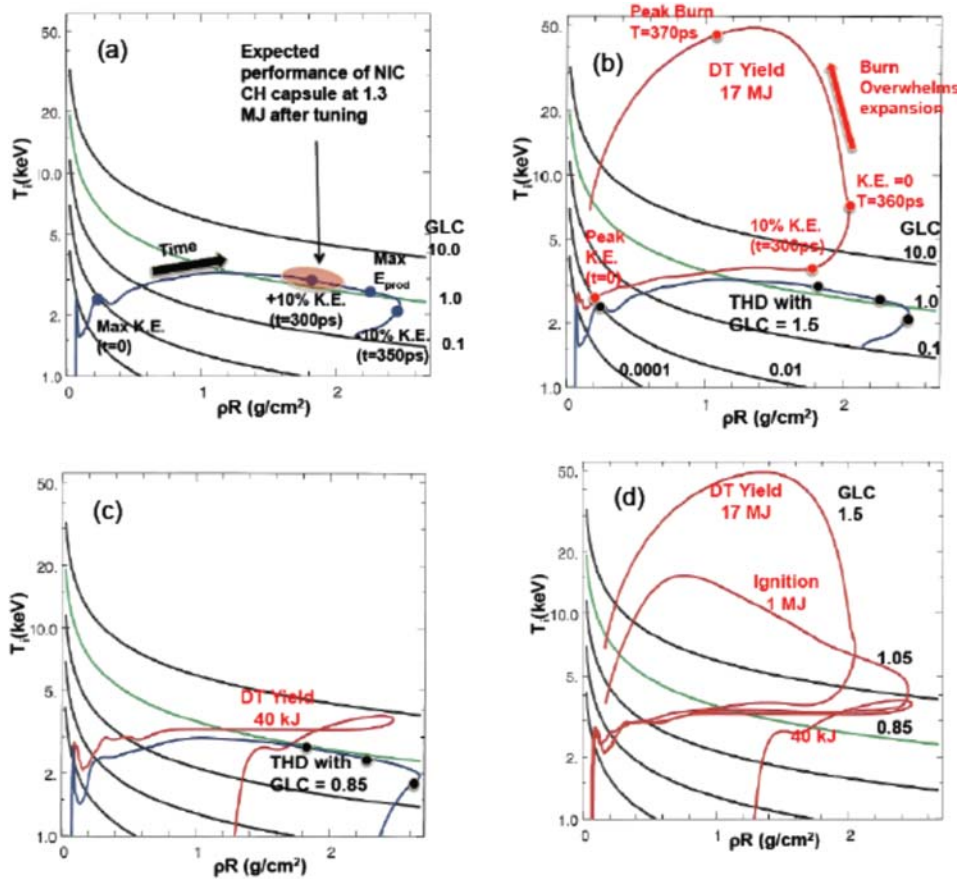
FIG. 15. Trajectories (in red) in $T_{ion} - \rho R$ space showing the threshold behavior of ignition near GLC or ITFX equal unity. Contours (in black) of GLC (THD) on all plots range from 10^{-3} to 10. The offset between the THD and DT curves in temperature is due to surrogacy effects between the two fuel compositions. (a) Trajectory of a THD capsule with GLC = 1.5 during the compression of the fuel starting at the time of peak kinetic energy. Points along the curve mark the time of peak kinetic energy, as well as 10% K.E., peak burn rate, and −10% K.E. (expansion). (b) The companion 50/50 implosion with GLC = 1.5 shows the rapid heating due to alpha particle deposition as the implosion approaches maximum compression. (c) The THD and equivalent DT implosion trajectories for an implosion with GLC = 0.85. Although there is some alpha heating, it is not rapid enough to heat the fuel to ignition conditions. (d) An implosion with a GLC = 1.05 has just enough alpha heating power to continue heating during the initial phases of expansion and reach ignition conditions.

temperature to ignition conditions before it starts cooling from expansion. Fig. 15(d) shows the previous DT trajectories along with the trajectory for an implosion with a GLC = 1.05, just above the ignition threshold. This implosion has a yield of 1 MJ and the alpha heating is just sufficient to continue heating as the capsule begins expanding. This capsule would burn well if it had more confinement time but the yield is terminated by expansion at about 1 MJ.

In principle, the computational equivalence between ITF, ITFX, and GLC gives us a sequence of complementary metrics for use in assessing the accuracy of the models in capturing the experimental performance of implosions in the ignition campaign and in assessing progress toward

implosions that meet the requirements for ignition. However, these metrics have all been developed on the basis of the purely hydrodynamic performance of an implosion without any effects from alpha deposition. This situation can be approached, as described above, by the use of THD fuel mixtures. However, these cryo-fuel mixtures are more difficult to form into high quality layers, and even with high quality layers, there are surrogacy issues with respect to DT layers that are hard to validate quantitatively. As a result, there is substantial value in an ignition metric that is applicable to a DT implosion that does not require a calculated surrogacy correction for either a different fuel composition or the effects of alpha deposition. We find that the GLC and ITFX
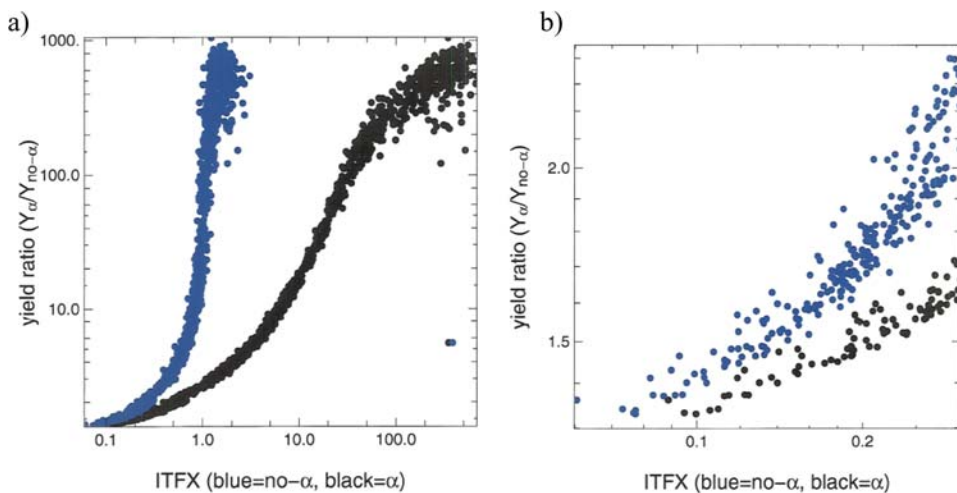

FIG. 16. (a) ITFX using burn-on quantities (black points) for DT implosions provides an equally good ignition metric for yield amplification as burn-off values (blue points). The fact that we can use burn-on quantities in ITFX means that we can use the as measured DT implosion data without requiring surrogacy corrections for THD vs DT implosions and without corrections to the data for alpha heating. (b) Blow-up of low ITFX region.
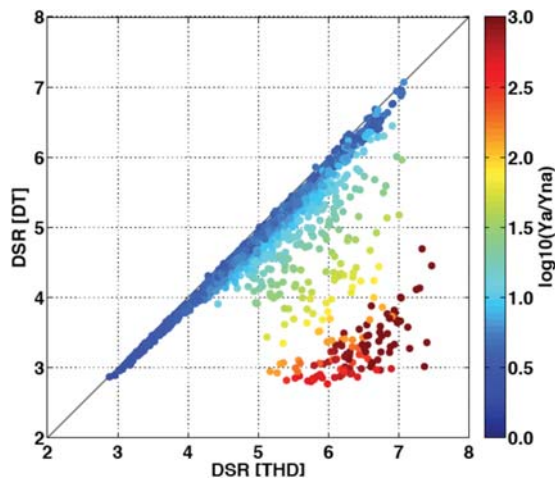
FIG. 17. Above an alpha gain of about 10, the DSR measured in a DT implosion begins dropping substantially below that which would be measured in a THD implosion or in a DT calculation without burn. This occurs because a substantial fraction of the yield occurs, while the capsule is exploding and the DSR is dropping. Nonetheless, ITFX using burn-on quantities is a good metric for yield amplification.

work equally well as a metric for yield amplification using either the no-alpha values or the burn-on values with alpha deposition in Eqs. (8) and (23). This is shown for ITFX in Fig. 16. The values for ITFX now span a much larger range because the yield is increasing from alpha deposition as the performance approaches ignition. And as shown in Fig. 17, the measured DSR begins dropping substantially for a yield amplification greater than 10 because the imploded fuel is exploding as it burns. Nonetheless, the yield amplification is still a well defined function of ITFX. The same is true for the GLC as shown in Fig. 18. Fig. 19 shows that the relationship between ITFX and the GLC given by Eq. (31) continues to be true when burn-on quantities are used. This correspondence gives us a very convenient way for expressing progress toward ignition based on the degree of yield amplification achieved. Fig. 20 is a plot of Pτ(burn-on) vs

FIG. 19. The relationship between GLC and ITFX obtained in the no-burn implosions is maintained when burn-on quantities are used.

T(burn-on) showing contours of yield amplification. These are the variables utilized in the GLC. Fig. 20 also shows the values of GLC (no-alpha) and ITFX (no-alpha) that would be required to achieve the yield amplification indicated. The best performing implosions at the end of the NIC, as discussed in Sec. V, have a GLC ~ 0.3. This figure shows that a factor of ~ 1.5 improvement in GLC would get the experiments to the alpha dominated regime with gain amplification of ≥ 2. Figure 21 is the complementary plot of Yield (burn-on) vs DSR (burn-on) showing contours of gain amplification. Plots of this type will be used in the discussion below in Sec V C on the data from layered implosions. For the computational data based used in constructing Figures 16–21, the uncertainty in the ITFX needed for a given yield amplification is approximately $\pm 10\%$. As seen in the figures, there is a larger spread of $\pm 30\%$ in the GLC needed for a given yield amplification.

FIG. 18. Yield amplification from alpha deposition versus GLC2.2 (overlaid on ITFX values of Fig. 16, with light blue and red denoting burn on and off, respectively), using burn-on quantities for DT implosions, also works equally well as an ignition metric.
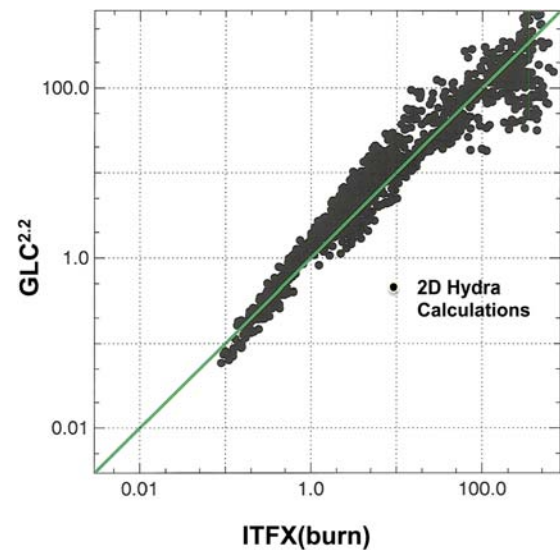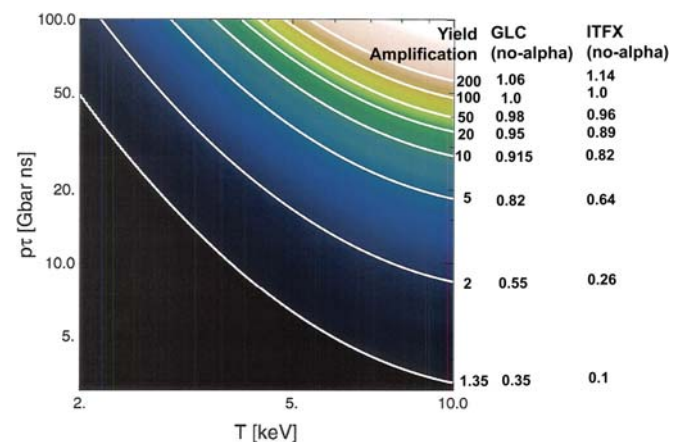

FIG. 20. A plot of Pτ(burn-on) vs T (burn-on) showing contours of yield amplification provides a convenient way of viewing progress toward ignition which does not require surrogacy corrections to the DT data. Also listed are the GLC (no-burn) and ITFX (no-burn) quantities which would produce the same yield amplification. This illustrates the large improvement in yield amplification expected for relatively small improvements in the underlying hydrodynamic parameters.

III. USE OF NUMERICAL MODELS WITHIN THE NATIONAL IGNITION CAMPAIGN

Development of the underlying science of ICF has been a multi-decade long process. By its nature, the scientific challenge of ignition requires the integration of an exceptionally wide range of physical phenomena. ICF computational models incorporate this accumulated knowledge into a system of equations, algorithms, and databases, with calculations carried out on computers[32] where the capabilities have increased more than 6 orders of magnitude in the past two decades. The two principal codes used for radiation hydrodynamics calculations on the NIF are Lasnex[33] and Hydra.[34] The principal code used for modeling LPI physics is the pF3D[35] code. The models were developed and tested using a wide range of experiments on the Nova and Omega lasers as well as other facilities. However, these experiments were carried out with nearly a factor of 100 less energy than NIF. Accordingly, these models have not been tested over the full range of spatial and temporal scales or conditions of temperature and density required for ignition experiments.

Because of the complexity of the scientific issues involved, and the difficulty of solving the equations describing these phenomena, even with today's computers these computational models necessarily involve approximate solutions of the relevant physics. While recognizing that there will inevitably be areas where the models prove inaccurate, a key challenge in the pursuit of ignition is to identify ways to utilize the models together with experimental data from the campaign, to optimize progress toward ignition. Although we expected the models to be insufficiently accurate to allow *a priori* specifications of precise details of the targets and laser pulse, the large data base acquired on all the principal ICF physics phenomena provided confidence that the specifications set by the codes are close enough to provide a good starting point for the campaign which can then iterate experimentally to the imploded fuel conditions required for ignition.

The use of the numerical models in NIC is shown schematically in Fig. 22. Prior to the start of experiments, the codes were used to set the initial laser pulse and target specifications, as well as experimental inputs including expected timing and signal levels for the various diagnostics. We also generated "playbooks" of sensitivities to adjustments to the experimental inputs that we expected to utilize in order to optimize the implosion performance. The expectation has been that in some cases, the models would prove adequate to specify experiments that would achieve the required performance in relatively few iterations. In other cases, we expected that the models might disagree with the data to a sufficient extent that additional experiments, which probed more deeply into the underlying physics, would be necessary. This approach has allowed the NIC team to move quickly through those areas of the physics where the models proved to be adequate for rapid progress while focusing resources on the areas where the data are at greater odds with the models. This approach helps identify those areas of the underlying physics where improvements would have the largest impact, both in current experiments and for future applications, where a more *a priori* predictive capability would allow more rapid convergence to the required performance. In advance of experiments, it was not possible to know which areas of the physics would prove to be the most challenging.

As data are obtained, that information is fed into the models. On a time scale of days to months, the models are adjusted to obtain better correspondence between the calculations and the observations. These adjustments are generally not unique, since a number of factors can contribute to the differences between experiment and calculation. However, this kind of adjustment of the models has been shown to be quite effective as a means for predicting the required changes to upcoming experiments in order to move the results closer to those required for ignition. Once enough experimental data have been obtained, the measured sensitivities themselves can be used for further adjustments. This process has been used to optimize symmetry, adiabat, and implosion velocity, and examples are given below.
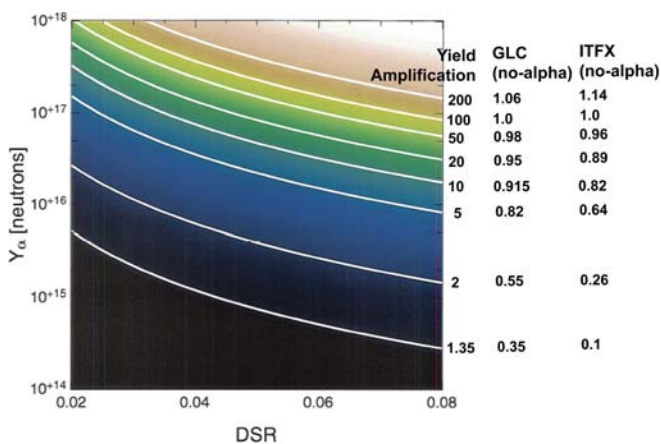

FIG. 21. Yield (burn-on) vs DSR (burn-on) showing contours of yield amplification complements the view of progress toward ignition provided by Fig. 20 plot of Pτ (burn-on) vs T (burn-on). Also listed are the GLC (no-burn) and ITFX (no-burn) quantities which would produce the same yield amplification.
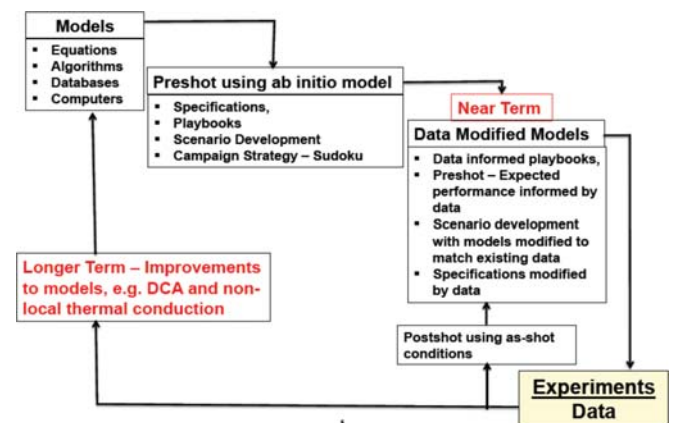

FIG. 22. Flow diagram for showing how numerical models, with years of development of the underlying physics, are used to establish starting points for the experimental campaign. In the short term, as data are acquired, inputs to the codes are modified to match measured performance and used to obtain expected performance on succeeding experiments. Over longer times, the underlying models are improved in order to enhance the *a priori* predictive capability of the codes.

To provide room for adjustment, the NIF laser was designed with about a 40% margin in power and energy above the baseline requirements for the point design target. The NIF also has substantial flexibility in pulse shaping, pointing, and beam smoothing, as well as the ability to adjust the wavelength of beams at different angles in order to adjust energy transfer between beams. The features of the targets are also very flexible and the target fabrication precision is the subject of a continuous improvement process. The differences between the models and the experiments are not an impediment to progress toward ignition as long as the differences between the models and experimental results are within the range of adjustment provided by this flexibility. On a longer time scale, which can range from months to a year or more, the underlying physics equations, algorithms, or data bases are improved as necessary to obtain a better *a priori* predictive capability. Areas in which the models need further improvements are also given below.

IV. THE APPROACH CHOSEN FOR IMPLOSION OPTIMIZATION

Many lower level variables affect the four principal quantities in ITF. However, extensive analysis of the ignition point design indicated that, given a target and laser that meet specifications, a relatively small number of high-level variables have the largest leverage in the process of optimizing the V, α, S, and M of an implosion. Based on an assessment of the variables optimized in computer simulations to achieve ignition and propagating burn, we identified an initial set of laser and target parameters, shown schematically in Fig. 23(a) which must be set precisely in pre-ignition experiments in order to optimize the imploded fuel assembly as required for ignition. Precisely setting this set of parameters in simulations was sufficient to achieve ignition, however, it was expected that experiments would uncover the necessity for a more extensive optimization of features such as the pulse shape, capsule structure, and hohlraum geometry. Optimization of these high-level variables forms the

basis for an array of basic target platforms used in the implosion optimization campaign, as well as for the measurement precision required by NIF as discussed extensively in the article by Landen *et al.*[14] The principal target platforms, Symcaps, Re-emits, Keyholes, and Convergent Ablators (ConA) are shown schematically in Figs. 23(b) and 24, and actual target pictures shown in Fig. 25. These include:

A. Hohlraums with gas-filled symmetry capsules (Symcaps)

In Symcaps, the cryogenic fuel-layer is replaced with an equivalent mass of ablator material. Hydrodynamically, these capsules are designed to have a response to long wavelength radiation asymmetry very similar to that of a cryogenic-layered target but they are simpler to field.[36–39] They are also designed for lower convergence by having an initial gas fill which is higher than that in a cryo-layered capsule. Symcaps are used to establish that (a) the required peak radiation temperature can be achieved consistent with specifications on the radiation asymmetry, (b) the level and variability of scattered laser light is acceptable, and (c) the hot electron production from LPI effects as well as the level of hot electrons transported to the capsule are at acceptable levels. Symcap targets are used to set beam smoothing characteristics of the laser including smoothing by spectral dispersion (SSD) and polarization smoothing as well as to set the hohlraum gas fill and the spot size to maximize coupling and minimize LPI effects. The level of scattered light and its variability and the hot electron fraction are not quantities that are "set" in the tuning campaign. But if they exceed levels as established in the point design specifications, it might be necessary to drop the hohlraum temperature, modify the hohlraum design, or increase the target size and laser energy to achieve ignition conditions. Symcaps are used to set the relative power in the beams and the wavelength separation between cones as required to obtain long wavelength radiation symmetry (both polar and azimuthal) integrated over the pulse. Also obtained from these targets is
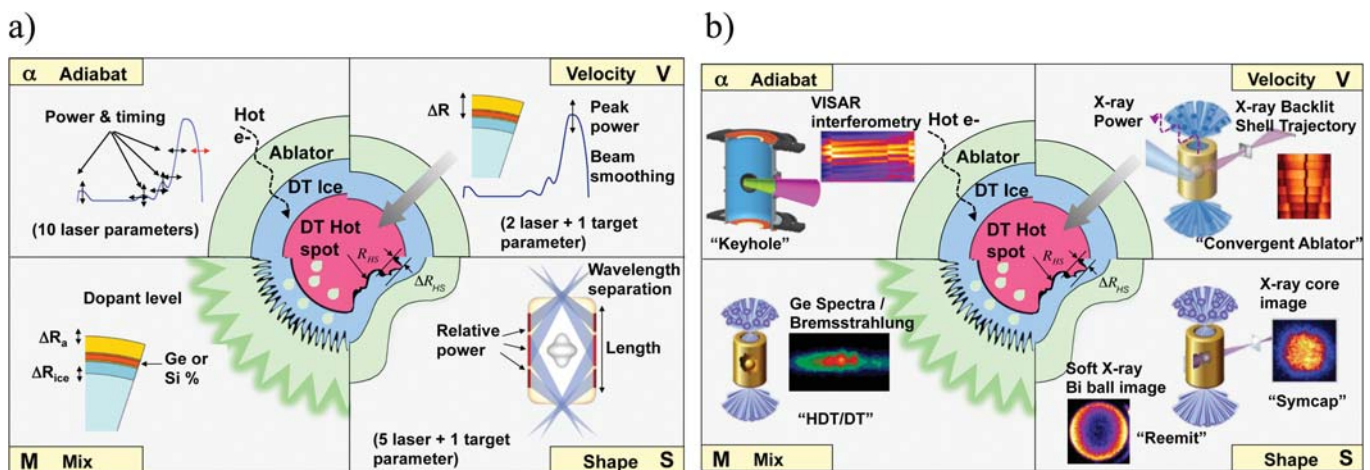

FIG. 23. (a) To compensate for physics uncertainties, the implosion optimization campaign will set a variety of pulse shape and target parameters. The 19 laser and 5 target parameters shown are indicative of the key parameters which must be set to optimize velocity (V), adiabat (α), mix (M), and shape (S) but are not comprehensive. The complete optimization is determined as the ignition campaign proceeds. (b) The principal experimental platforms and sample data required for optimizing each of the four principal implosion attributes.
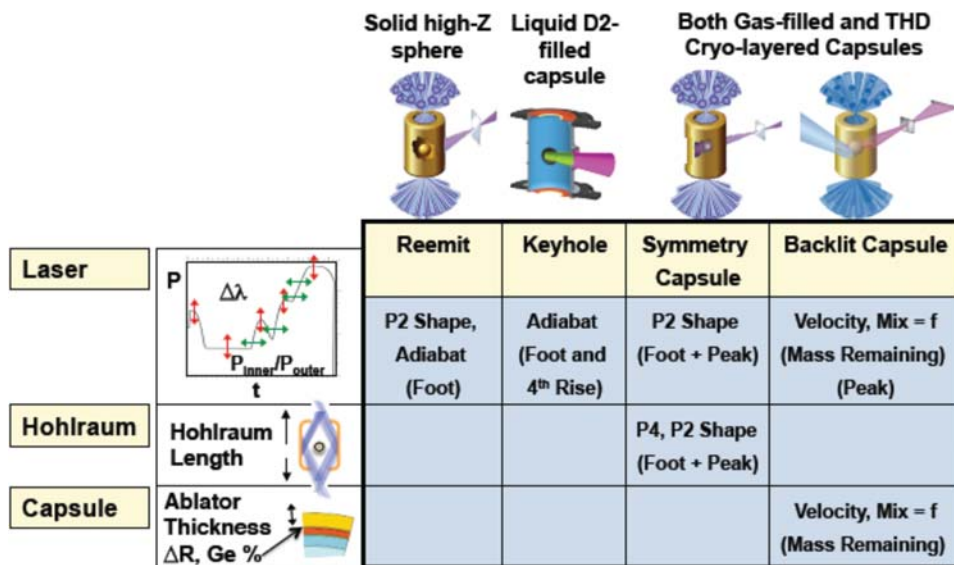
FIG. 24. Principal experimental platforms utilized in implosion optimization experiments.

the spectrum of the x-rays in the hohlraum. In particular, the fraction of x-ray energy above 1.8 keV is responsible for preheat of the ablator at the fuel/ablator interface. This measurement is used to set the ablator dopant levels as needed to control the Atwood number at the fuel/ablator interface. The hohlraum length is adjusted to optimize the P4 mode asymmetry in the radiation drive.

Fig. 26 summarizes the principal diagnostic measurements utilized to assess these performance parameters. Light from Stimulated Brillouin scatter (SBS) and Stimulated Raman Scatter (SRS) which is scattered back through the lens is measured using the Full Aperture Backscatter[40] (FABS) diagnostic on one 50° outer quad and on one 30° inner quad. SBS and SRS, which are scattered to positions near the lens, are measured using the Near Backscatter Imager[41] (NBI) on one 50°, one 30°, and one 23° quad. Soft x-ray production is measured using the Dante soft x-ray spectrometer[42] and hard x-rays are measured using the FFLEX hard x-ray

spectrometer.[43] The Static X-ray Imager (SXI)[44] provides a time integrated image of x-ray emission from the LEH. The Gated X-ray Diagnostic (GXD)[45] provides a sequence of snapshots of emission from the imploding capsule near peak compression. Separate lines of sight looking through the LEH and through diagnostic holes at the waist of the hohlraum provide equatorial and polar measurements.

B. Re-emit capsules

In these targets, a high-z sphere of Bi replaces the plastic ignition capsule.[46,47] Re-emit capsules have a high *albedo* for the radiation incident on their surface and re-emit x-rays in proportion to the incident flux. This re-emission is used to measure and set the low mode polar and azimuthal radiation flux asymmetry during the first 2 ns of the pulse. This is important for both the shape of the implosion and the entropy of the fuel.
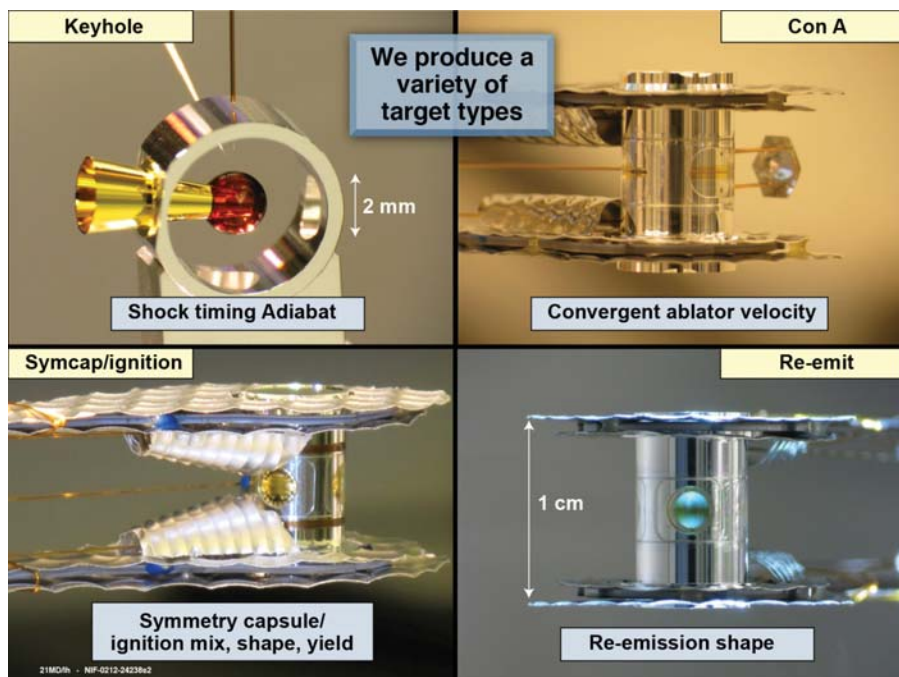

FIG. 25. Target pictures of principal experimental platforms utilized in implosion optimization experiments.
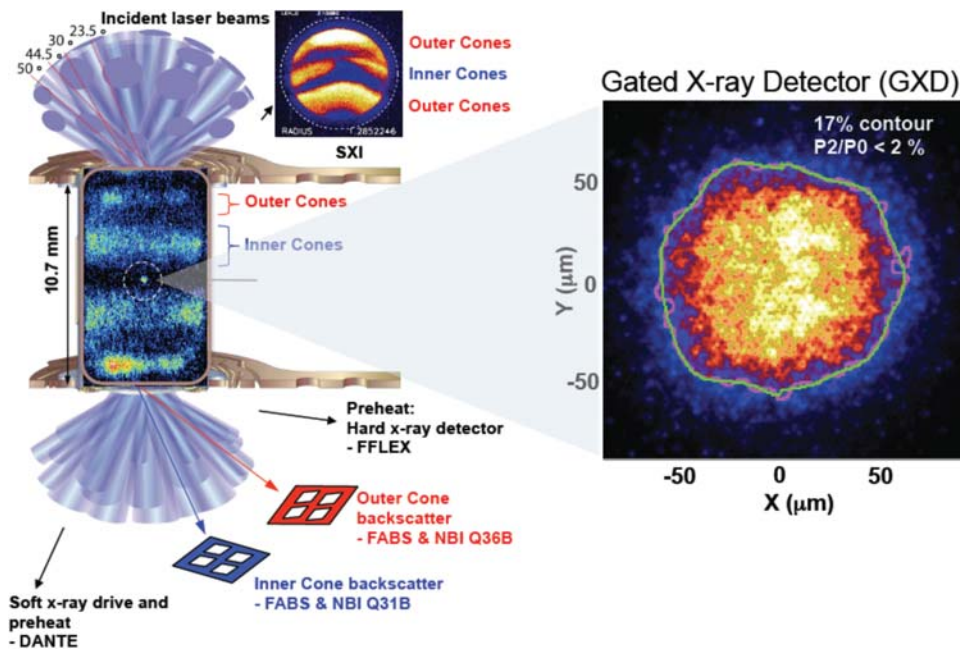
FIG. 26. Key optical and x-ray diagnostics utilized in the symcaps and other implosion experiments on the NIF.

C. "Keyhole" targets

These targets have a cone inserted through the side of the hohlraum wall and into the capsule that is filled with liquid deuterium (surrogate for frozen DT) so that an optical interferometer (VISAR)[48] can see the inside of the shell. Keyhole targets are used to measure the timing and strength of shocks launched in the ablator[49–51] They are used to set the key parameters of the pulse shape—the power levels of the initial picket and the trough following the 1st picket, the power levels of the 2nd and 3rd shocks, the timing of the 2nd, 3rd, and 4th shocks, and the rate of rise of the radiation temperature during the 4th pulse. If hot electron preheat effects from LPI meet specification, shock mistiming is the dominant source of entropy generation in the fuel. Initial keyhole experiments carried out 2010 had a single straight through line of sight through the cone that was pointed toward the waist of the hohlraum. A "mirrored" keyhole was introduced in 2011. The mirror allows the VISAR to look both at the pole and waist of the capsule in a single shot. With the mirrored keyhole, we are able to tune the P2 symmetry of shocks on the capsule as well as the strength and timing. 3-axis keyholes are now being used and designed to allow optimization of the P_4 and m_4 components of the flux on the capsule.

The data provided by the keyhole target platform are central to the ability of the NIC to achieve low entropy in the cryogenic fuel layer. As indicated above, ITF varies strongly with the fuel adiabat. To achieve the design goals of the NIC point design, pressure in the cryogenic fuel layer must be within about a factor of 1.5 of the Fermi pressure at peak implosion velocity. This requires 50 ps timing accuracy for the shocks.[8,14] Because of uncertainty over a wide range of processes which determine the timing and strengths of the shocks generated in the shell, this level of precision can only be obtained by looking on the interior of the shell directly at the shocks generated.

D. Radiography targets

1. Convergent ablator

This target (ConA) can be either a Symcap or a cryo-layered target with a slot at the waist of the hohlraum and a backlighter illuminated by two quads of NIF beams. Convergent Ablator targets are used to radiograph at 8-10 keV the position of the imploding shell radius versus time and the optical depth of the mass remaining in the ablator as it implodes.[52,53] This measurement is used to adjust the laser peak power and the shell thickness so that the implosion has both the required velocity and the required residual mass of ablator. The peak power and shell thickness along with the dopant level in the ablator must be adjusted to optimize the tradeoff between implosion velocity and mix. The position of the shell and its optical depth as it implodes can be obtained either with a framed imager or a streak camera.[54] There are a number of variants of targets that use radiography to image the state of the imploding ablator or fuel. For example, designs exist for assessing the in-flight fuel width using refraction-enhanced x-ray radiography.[55,56]

2. Mix-caps

These are a variant of symcaps with engineered surface features. The variation in optical depth of these features can be imaged during the course of an implosion using a 5–10 keV x-ray backlighter.[57,58] The growth of variations in the optical depth is used to obtain hydrodynamic instability growth rates, both from the shock phase Richtmyer-Meshkov and acceleration phase Rayleigh-Taylor instability. Mix depth is a nearly linear product of growth x amplitude of surface features on ICF capsules. Measurement of this growth determines the level of surface roughness and the level of mass ablated required to keep mix at acceptable levels. In the keyhole geometry, it is possible to look at the

growth in optical depth from inside of the shell, hence from just one side, but after less convergence. Additional targets, which would use emission or absorption spectroscopy[59] or radiochemistry[60] to more directly measure mix at the fuel ablator interface, or deep within the hotspot, are being evaluated.

3. 2D-radiography

This is a variant of the ConA target which uses a 10–20 keV backlighter and a pinhole instead of a slit to obtain a sequence of 2D images of the optical depth of the imploding shell as a function of time.[61,62] With 2D radiography, besides the 1D parameters of peak velocity, mass remaining, and shell profile, it is possible do obtain information about the spatial variation in the location of the shell as well as variations in the optical depth of the remaining mass when it is at radii of 150 to 350 μm. These variations are shown by simulations to be correlated with the final stagnated fuel configuration. The higher the backlighter photon energy the later and smaller radius it is possible to probe. Recent experiments demonstrated 0.3% efficient 12.3 keV KBr and 15 keV Zr backlighters[63] at NIF that will allow probing down to 100 μm radius.

4. Compton radiography

Information about areal density and shape of the dense cold fuel surrounding the hotspot can be obtained by active probing using an external source of hard X-rays. High-energy x-ray images[64] can be obtained using transmission Compton radiography where high energy Compton scattering is used rather than traditional photo-absorption to cast a shadow of the imploding capsule. The Compton scattering cross section is largely independent of photon energy for photon energies of 50–200 keV. As a consequence, the optical depth of the fuel of an ICF target shows a plateau above ∼50 keV, where the Compton scattering dominates. Because of the slow dependence of the Compton scattering cross section on the X-ray photon energy, the areal density of the fuel can be inferred even using a polychromatic backlighter. A broadband bremsstrahlung emitting source is adequate and the energies of the X-ray photons can be selected by a combination of a high-pass filter and the gated hard x-ray detector response[65] to optimize signal to background. The accuracy of measurements of fuel areal density depends mainly on the signal-to-noise ratio and on the contrast of the recorded radiograph, which would have 0.6 optical depth for a typical 3 g/cm^2 chord fuel areal density. In the current implementation, the backlighting source is produced by irradiating Au wires with the UV beams from two tightly focused NIF 8 TW quads. Adequate 70-ps temporal resolution is provided by a gated framing camera. When the NIF Advanced Radiographic Capability (ARC) is available, 30 ps, 1 kJ/beam ARC pulses will be used to irradiate the Au micro-wires. Accuracies between 10% and 7% for measurements of limb-averaged ρR are expected when using short-pulse NIF UV beams to generate the backlighter, and about 2% is expected when using NIF-ARC.

E. Cryo-layered implosions

The results of the implosion optimization campaign, using the surrogate targets discussed above, are used to set most details of the target and laser pulse used to drive the cryogenically layered capsules.[66] Nevertheless, some physics issues which result from the layer itself, principally instability growth at the hotspot/main fuel interface and at the ablator/main fuel interface as well as surrogacy issues arising from differences between the tuning targets and cryo-layered targets, can only be addressed with cryo-layered target experiments. The surrogacy issues include shape of the hotspot and the spatial distribution of compressed fuel in the main DT layer at the higher convergence of the cryogenic implosion, as well as the velocity and velocity profile of the imploding fuel layer. Each of these can be slightly different in a layered target. These cryo-layered targets can be designed with varying cryo-layer composition from layers for low yield using a fuel layer composition consisting mainly of tritium and hydrogen with only a few percent deuterium, referred to as THD layers above, to 50/50 DT layers. The ratio between Hydrogen, Deuterium, and Tritium in the reduced deuterium targets is generally chosen to maintain a density in the frozen fuel layer equal to that for 50/50 DT in order to retain surrogacy for hydrodynamic instability at the fuel ablator interface. By using cryo-layered targets designed for low yield, we are able to maintain the full array of diagnostics needed to optimize the fuel assembly before shifting to 50/50 DT layers to obtain higher yields and ultimately to achieve ignition.

A central goal of the THD experiments is to optimize the tradeoff between velocity and mix in ITF. This tradeoff occurs because achieving higher velocity requires ablating more mass. With less mass remaining, instabilities, which initially grow on the ablation front, imprint on the ablator/fuel interface, and provide a larger seed for growth at that interface. Since ITF depends so strongly on velocity, ITF will increase until mix begins to penetrate a significant fraction of the cryo fuel layer or until the penetration of mass from isolated defects in the ablator starts to significantly affect the hotspot as described above. The nominal values of velocity and mix penetration are chosen based on extensive computational studies as discussed by Haan *et al.*[8] We can vary the ablated mass and velocity by varying the peak laser power until we find the optimal performance. If this velocity is below the velocity needed for ignition, we can either reduce the size of perturbations by improving target fabrication or other sources of perturbation, work to reduce the growth rates which are dependent on the capsule dopant profile and the laser pulse shape or increase the laser power and energy in order to implode thicker shells and/or thicker fuel layers to higher velocity. Calculations indicate that growth during the initial picket and the several nanosecond trough that follows can vary by factors of 2-4, depending on details of the pulse. The point design is optimized to minimize this growth, but the optimum is uncertain because of equation of state (EOS) effects and radiation transport effects. Hydrodynamic instability growth during the foot of the pulse can be measured using the mix-cap targets discussed above

and optimized by modifying the initial picket and the subsequent trough.

A large number of diagnostics have been fielded to measure the performance of THD and DT implosions. As described above, the key performance metrics are the size and shape of the hot spot and main fuel, the X-ray spectrum, the neutron yield and fraction of neutrons scattered from the fuel (ρR), and the burn history. The principal diagnostics are summarized briefly below.

A key feature of the THD implosions is that the neutron yield can be controlled via the %D concentration in the fuel to optimize the diagnostics environment. X-ray imaging is feasible on NIF, without special relay optics to a shielded location, for neutron yields up to $\sim10^{15}$ using a hardened gated X-ray imager.[67,68] This provides a large number of snapshots of the implosion for hot spot size and shape. Each image integrates over $\sim$35–70 ps, and a total interval $\sim$800 ps can be covered, compared to the 100–200 ps of the THD emission time. The spatial resolution is $\sim$5–10 μm compared to the $\sim$50 μm diameter of the X-ray image at peak brightness. Different filtering can be used to provide spectral discrimination on the same shot in order to extract temperature information.[69] A similar diagnostic, being built to operate in the range of 10^{17} neutrons, must be located outside the target chamber with adequate shielding against the higher neutron environment.[70] A faster camera is under development to provide $\sim$10 ps resolution,[71] which is on the same order as the burn width of igniting targets.

A neutron imager provides time integrated spatial information of the compressed fuel.[72] The detector is a stacked fiber scintillator located 28 m from the target, imaged by two cameras to produce one image of the primary neutrons, between $\sim$13 and 20 MeV, and another gated from 10 to 12 MeV or 6 to 12 MeV showing neutrons scattered within the capsule.[73]

The neutron spectrum is measured by several diagnostics.[74] A number of neutron time of flight (nTOF) detectors[75] are used to measure the primary DT neutron yield, burn averaged ion temperature from neutron Doppler broadening, and the fraction of neutrons scattered by the fuel, which is proportional to fuel ρR. A number of detectors are required to cover the large range in neutron yields for THD and DT implosions. Several detectors are located at $\sim$4 m from the target chamber center (TCC) and measure prompt signals (Y, T_{ion}, Bang Time) for lower yield targets. An additional 2 detectors are located at $\sim$20 m from TCC. These allow the neutron signal to dilate in time making it easier to measure the spectrum for the down scattered fraction. As DT yields approach ignition levels, the close in detectors will no longer work, and the 20 m detectors will be relied on for all spectral information.

The neutron spectrum is also measured quantitatively using a magnetic recoil spectrometer (MRS), which provides an additional line of sight.[76,77] This converts the neutron signal to a proton signal via collisions in a CH target foil. The proton spectrum is then measured by dispersing the protons spatially on to CR39 using a magnet. This diagnostic has been designed to work for the entire range of neutron yields expected from NIF. It also provides absolute yields and

mean primary neutron energies for checking for residual collective hot spot velocities.[78]

Neutron activation detector[79] containing Zirconium [Zr90(n,2n)Zr89], referred to as FNADs (flange nuclear activation detectors), arrayed at several locations on the target chamber, measure yield to complement the nToF and MRS detectors. The threshold energy for activation is $\sim$12 MeV making this suitable for measuring the primary DT neutron signal. The yield is inferred by measuring absolutely the $\sim$909 keV γ-ray yield from the activated Zr nuclei. This is similar to the copper activation technique used for many years in ICF, but unlike Cu the Zr has a much longer half-life ($\sim$3 days vs 10 min)[80] making it functionally easier to implement. Variations in the primary yield measured by these Zirconium detectors are also a measure of the spatial variation in fuel ρR. These fuel ρR variations will result in variations in the number of neutrons down-scattered below the Zirconium detection threshold and hence in variations in the signal measured by the detector.

The capability to field capsules with radiochemical tracers is also being implemented on NIF. There are several potential applications, one of which is to measure the ρR of the fuel. The tracer material in this instance is ^{124}Xe loaded into the inner region of the ablator. There are two nuclear reactions of interest, the ^{124}Xe (n,2n)^{123}Xe reaction and the ^{124}Xe(n, γ)^{125}Xe reaction. The former is sensitive to neutrons with energies $\leq$10 MeV, while the latter has a threshold >11 MeV. The ratio of the two product nuclei is similar in nature to the number of primary and scattered neutrons, similar to DSR. Numerical simulations have found a very strong correlation between the ^{123}Xe:^{125}Xe ratio and DSR.

The gamma ray reaction history (GRH) or "burn history" is measured using a 4-channel gas Cherenkov γ-ray detector[81] located 6 m from TCC. The γ's impact a converter foil producing electrons, which then produce Cerenkov radiation in the gas cells. The four cells will have different gas densities to produce gamma thresholds of 3, 5, 8, and 14 MeV. Data from these signals are used to obtain the total yields and time history of three capsule gamma rays; 16.7 MeV gamma rays from a branch of the D + T reaction, 19.8 MeV from T + H reaction, and 4.4 MeV from neutrons interacting with the carbon in a plastic ablator. Neutrons passing through the Au/U/Al hohlraum wall produce a background of gamma rays delayed from the prompt signal, which must be subtracted. The time dependent ratio of the 4.4 MeV to the 16.7 MeV gammas is proportional to the carbon (or plastic) ρR. Finally, the combined information from the 16.7 MeV γ's and the 19.8 MeV γ's diagnose the H/D ratio in the burning fuel. The temporal resolution is currently limited to $\sim$100 ps by the optical diode used to resolve the Cherenkov signal, but will later be improved to $\sim$20 ps by using a streak camera.

F. Sequencing of experiments within the ignition campaign

The Ignition Campaign involves a series of iterations on implosion optimization in which the non-layered surrogate targets are interleaved with layered THD and DT targets. In

this way, we are able to determine if we achieve the expected improvement in performance as the precision of the implosion inputs improves. Although it would be ideal if we could separately fully optimize each of the key implosion attributes (velocity, adiabat, symmetry, and mix), this is not possible in practice because of coupling between them. However, we have worked hard to identify an optimal sequence in which to iteratively improve each of these attributes. As much as possible, we want to set quantities early in an optimization cycle that will primarily affect those downstream variables which have not yet been set and not those variables which have already been set. For example, optimizing the symmetry of the initial picket of the pulse by adjusting the cone balance will not be affected by subsequent adjustments to the pulse to optimize shock timing. On the other hand, even though adjustments to the capsule thickness will certainly affect shock timing and can affect symmetry, it is necessary to have good symmetry and shock timing in order to adequately explore the tradeoff between shell thickness and mix. So some iteration through the cycle of optimization is inevitable. The sequence adopted by the NIC for implosion optimization, shown schematically in Fig. 27, was developed in a year long Red-team and Blue-team assessment. In this exercise, the Blue team was responsible for optimization of implosions. The Red-team consisted of a group of experts who initially made an assessment of the likely uncertainty in the underlying physics that govern ICF. The Red team then modified the Hydra code models consistent with these uncertainties, but in ways unknown to the Blue-team. The Blue-team used its own version of the Hydra code but the

Red-team was responsible for conducting virtual experiments specified by the Blue-team using the Red-team code. The Blue-team was then given the results of those calculations in the form of synthetic data that would be obtained by the diagnostics planned for the NIF. Using that synthetic data, the Blue-team specified changes to the experiments that they judged would move performance closer to that required for ignition. The process is shown in Fig. 28. This exercise was very valuable in identifying the type of diagnostic data as well as the diagnostic precision that would be required for a successful ignition campaign in the presence of the expected physics uncertainty. Each of these iterations through the optimization sequence in general entails 20–30 shots. The findings of each of these mini-campaigns have motivated improvements to the targets, the laser performance, and the diagnostics, as well as the numerical models, which have helped advance the experimental performance toward the ignition requirements.

V. IGNITION CAMPAIGN EXPERIMENTS

Initial experiments in 2009 began with energies of about 0.5 MJ and powers up to about 300 TW. To generate ignition-like hohlraum temperatures and plasma conditions, hohlraums were employed which were reduced in scale from the ignition point design. These hohlraums were 4.58 mm in diameter and 8.45 mm in length (referred to as scale 458). Throughout 2010–2012, laser energies gradually increased from about 1 MJ to 1.8 MJ and laser powers increased from 300 TW to 500 TW. Along with this increase in power and
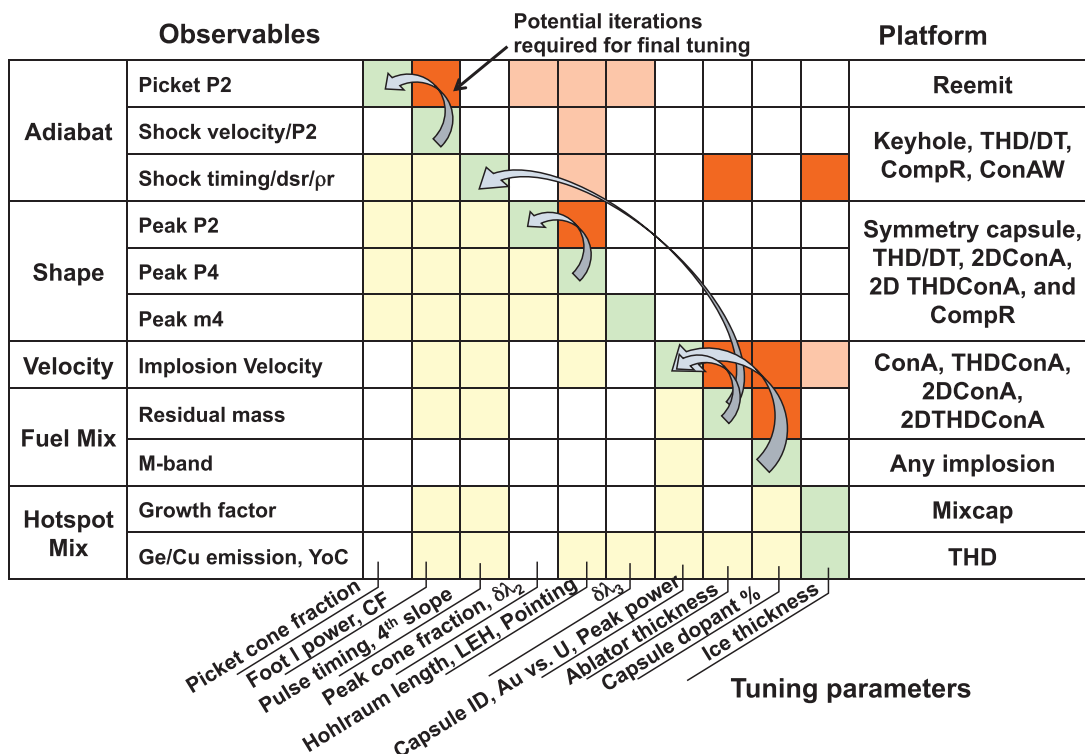

FIG. 27. Rows of observables versus columns of ignition optimization target and laser parameters. Also shown on far left and right are principal implosion attribute addressed and experimental platforms used. Green indicates the primary tuning parameter set by a particular observable. Yellow indicates coupling to parameters which are yet to be set. Orange indicates potentially strong coupling to parameters already set, while light orange indicates weaker coupling. Arrows indicate principal iterations that will in general be required.
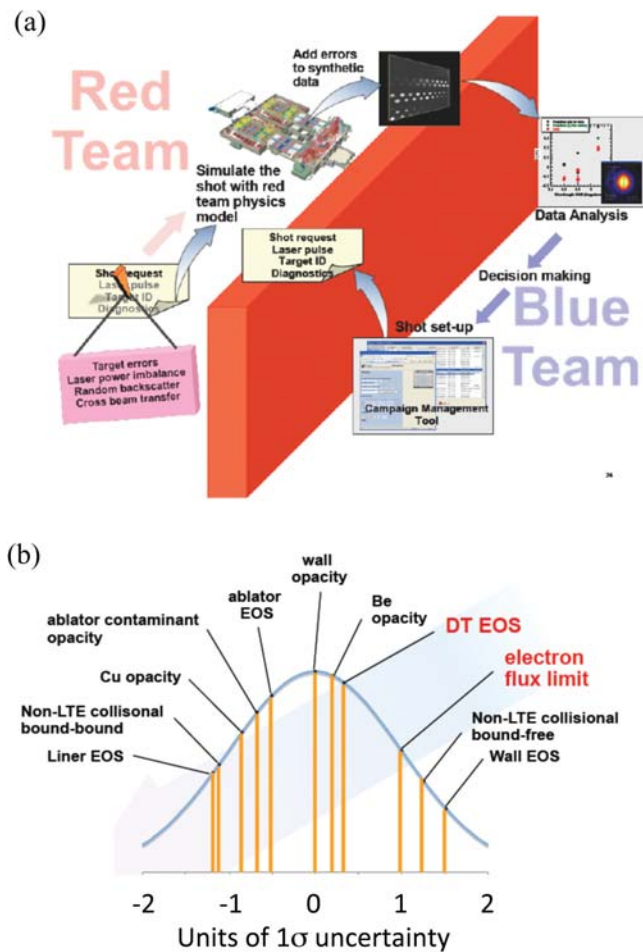
FIG. 28. (a) Schematic of simulated campaign workflow, starting with The Red Team developing a physics model consistent with current uncertainty but different from the standard Lasnex and Hydro models, and unknown to the Blue Team. The Red team ran the experiments as requested by the Blue Team with this model and sent synthetic diagnostic information to the Blue Team. The Blue Team then had to use this synthetic data, and its own model, to iterate the implosions to ignition. (b) Parameter variations from nominal physics set by Red Team by role of the dice. Typical model uncertainties are 10%–20% and 2× in NLTE collision rates and electron flux limiter.

energy, the ignition campaign moved to ignition scale hohlraums. The initial ignition hohlraum was 5.44 mm in diameter and 1.01 cm in length (referred to as scale 544). Experiments from September 2010 through July 2011 used this scale hohlraum. Based on the calculations using the improved hohlraum modeling developed in 2010, discussed below, which predicted improved symmetry control with a slightly larger diameter and shorter hohlraum, the ignition hohlraum was modified to 5.75 mm in diameter and 0.943 cm long in July 2011 (referred to as scale 575) and this has been the standard geometry since. The discussion below will cover results from all three hohlraum scales. A length scaling series, planned as part of the NIC to optimize the P4 radiation flux asymmetry, was not carried out by the official end of the NIC on September 30, 2012. However, the 2D ConA and Compton Radiography platforms designed to image the imploding shell and main fuel needed for the shape optimization were under development as part of the NIC and initial results from the 2D ConA targets obtained in October 2012 are also included in this review.

Initial experiments from August to December 2009 focused on LPI including hot electron production, as well as x-ray drive and the resulting implosion symmetry in the Symcap platform described above. Much of 2010 was devoted to installation of a wide array of nuclear, optical, and x-ray diagnostics as well as the facility infrastructure required for cryogenically layered DT implosions including the cryogenic target positioner. September 2010 through February 2011 was focused on fielding, testing, qualifying, and integrating all of the experimental platforms. May 2011 marked the beginning of the precision implosion optimization campaign.

The discussion below covers the results from 2009 that established the basic framework for the rest of the NIC campaign, and then covers the results of the precision optimization experiments from their beginning in May 2011.

A. Establishing the basic framework: Drive scaling, symmetry control, and LPI effects

A fundamental question that had to be addressed at the outset of experiments on the NIC was the following: Would LPI allow access to the long pulse length, high temperature conditions required for ignition at the megajoule scale? Achieving radiation temperatures of about 300 eV while preserving the temporal and spatial precision of x-ray production needed for shock timing and symmetry is central to achieving ignition. Although the NIC fully expected that the details of the hohlraum, capsule, and laser pulse would require successive optimization, the wide range of experiments and comparison with models carried out over more than two decades on the Nova and Omega facilities provided the basis for setting the initial specifications for the NIF experiments.[2]

Symcaps were the target platform used almost exclusively in the first NIC experiments in 2009, experiments with energies of 500 kJ to 1 MJ, a factor of 20–40 beyond that done with earlier lasers and with targets which were a factor of 3–4 larger in dimension than previously used. These experiments were very successful and established the foundation for the precision implosion optimization experiments to follow. Absorption levels were about 85%–90%, radiation temperatures achieved were close to expectations, control of long wavelength radiation asymmetry was demonstrated by tuning the wavelength separation between inner and outer beams, and hot electrons were at acceptable levels.[82–84]

Although there were evident differences between the initial calculations and the data, playbooks developed for these experiments were used to achieve symmetry at different energy levels, typically in 3 or fewer shots. This campaign was a good demonstration of the fact that the sensitivity of the numerical models to changes in key input variables can be used to guide experiments even when the absolute values deviate quantitatively from predictions at a single point. This process as applied to capsule implosion symmetry is shown in Fig. 29 for early symmetry experiments at the 500 kJ level. These experiments used hohlraums that were 4.58 mm in diameter, roughly 3 times the size of hohlraums used on Nova or the Omega laser. As indicated,
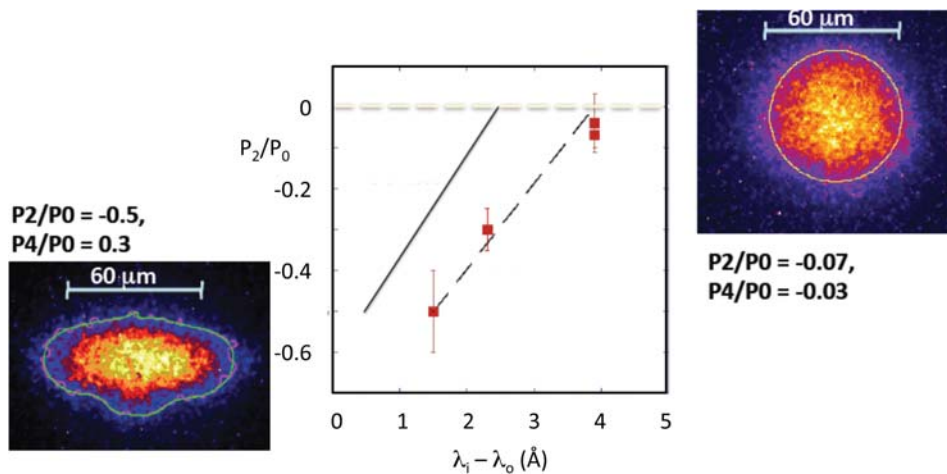
FIG. 29. Examples of measured >8 keV x-ray core shapes at peak emission listing values for extracted P2 and P4 Legendre asymmetry. In center, P2/P0 Legendre x-ray core shape asymmetry versus wavelength separation at 1ω between inner and outer cones. Red dots are data, solid and dashed lines are from old and newer simulations discussed in text.

the difference in wavelength between the inner beams and outer beams required for a symmetric implosion, predicted by the original hohlraum model, differed from that observed in the data. The black line labeled LASNEX scaling Old Model utilized the XSN opacity model and flux limited diffusion for electron transport with a flux limiter optimized to match a wide range of Nova and Omega laser data at 20–30 kJ. As discussed further below, the dashed lined labeled LASNEX scaling HFM (High Flux Model) utilizes a more sophisticated DCA (detailed configuration accounting) opacity model and a non-local electron transport model or a flux limiter which better matches the predictions of the non-local electron transport model.

However, this original model had predicted that a difference in frequency between the inner and outer beams would result in a transfer of energy and the model predicted sensitivity to changes in the wavelength separation that is very close to observations. The basic physics of this transfer is indicated in Fig. 30. Interference between quads of beams interacting near the LEH sets up density modulations that act like a plasma grating that can shift energy between quads.[85] Theoretical analysis and experiments on the Nova laser and elsewhere,[86] although not exactly analogous to the multi-quad interaction near the LEH in NIC hohlraums, provided the motivation for construction of NIF with oscillators at different frequencies for inner and outer beams. This capability and the playbooks developed based on the theoretical models for cross-beam transfer allowed the NIC campaign to achieve a symmetric hot spot in these early experiments in only three shots.

A wide range of hohlraum drive and symmetry experiments were carried out on the Nova and Omega lasers, and especially on the Omega laser whose beam geometry allowed us to replicate many aspects of the NIF beam geometry. However, deficiencies in the hohlraum modeling that showed up at the NIF scale were not as clearly evident at the Omega scale. Early work using the DCA opacity model[87] applied to NIF scale hohlraums indicated that volumetric effects in the hohlraum interior blowoff would become more important at the NIF scale than at smaller scales because of the larger volume to surface ratio in larger hohlraums. These early calculations indicated that emission from the laser

heated interior volume of the hohlraum would be larger than predicted by XSN[88] and that this emission would become a significant contributor to the energy balance in the hohlraum.[89] However, since key aspects of the DCA model necessary for modeling high-Z plasmas were in an early developmental stage at that point, and the XSN model tended to predict somewhat less radiation production, the XSN was chosen for the NIC design basis. Similarly, non-local electron conduction models were under development for several years before a modified version of the Schurtz[90,91] model was adopted for NIC. This non-local model results in thermal conduction out of the laser heated interior of the hohlraum at a rate greater than that predicted by the flux limiter initially used for NIC scale hohlraums. In addition, experiments such as x-ray emission from a uniformly heated gold sphere[92,93] done on Omega were best matched by a flux limiter which was higher than that adopted for the early NIC hohlraum calculations. The combinations of the higher x-ray emission predicted by DCA and the higher conductivity predicted by non-local electron conduction, both of which were not fully implemented into LASNEX and HYDRA until after the 2009 experiments, provide a physics model which is a better match to the data obtained on NIF.[94,95] The improvements include symmetry as shown by the dashed line in Fig. 29.

The improved model of hohlraum physics, which has been labeled the HFM provides a fairly accurate estimate of the hohlraum x-ray drive expected from a wide range of laser energies and a variety of hohlraums. The radiation temperature versus absorbed laser energy for 465 and 544 scale hohlraums is shown in Fig. 31, along with a simple Marshak scaling model[96] assuming 85% conversion efficiency to x-rays and predictions from the LASNEX code using the HFM. The improved model of hohlraum physics also improves the modeling of many aspects of the observed laser plasma interaction physics. Because the HFM lowers the temperature of the laser-heated hohlraum interior plasma, the location and density within the hohlraum where the strongest LPI effects occur is moved to lower density closer to the LEH. This changes the wavelength of the SRS, particularly on the inner beams. Because the location of the SRS changes to a location closer to the LEH, the SRS also occurs in a region with substantial overlap of several quads of NIF beams. LPI calculations which
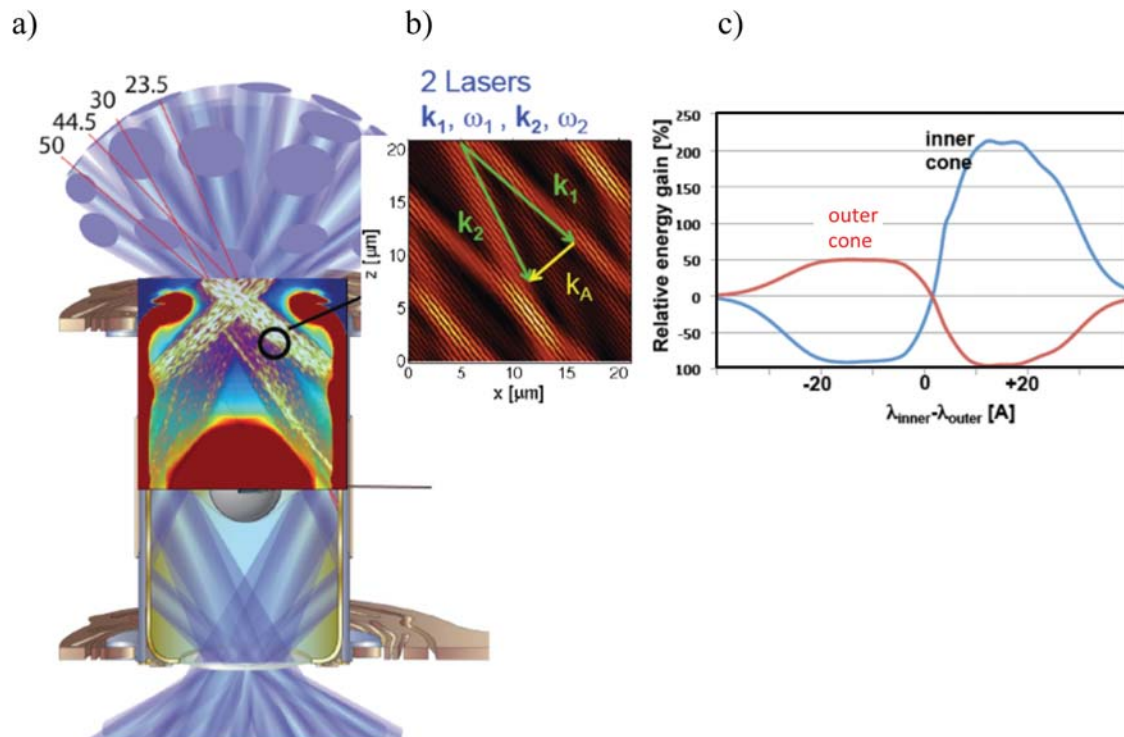
FIG. 30. (a) Cross-section of simulated density and laser intensity contours at peak power. (b) k-vector diagram for crossing beams showing interacting acoustic wave k-vector. (c) Relative energy gain versus wavelength separation between inner and outer beams at 1ω.

have been carried out using the PF3D code in the two years since the 2009 experiments which include the effects of two quads of beams in this overlap region, as well as cross beam effects, come much closer to matching the observed SRS scattering levels and scattered light wavelengths than the earlier single quad calculations using the plasma conditions predicted by the original hohlraum model.[97]

B. Precision implosion optimization experiments

Following the beginning of precision optimization implosion experiments in May 2011, a wide range of experiments addressing each of the key implosion attributes was
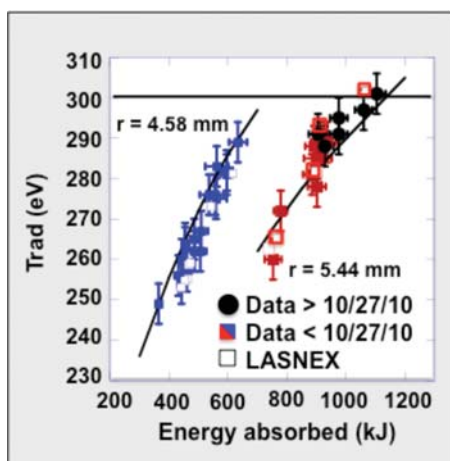
FIG. 31. The radiation temperature versus absorbed energy in two different size hohlraums. The Lasnex calculations using the HFM match the observations to about 10% in flux. Also shown is a line based on a simple Marshak scaling assuming 85% conversion efficiency to x-rays.

carried out. The discussion below summarizes drive experiments from the start of the precision tuning campaign and then summarizes results in the order identified in Fig. 27, moving sequentially through early time symmetry, shock timing, time integrated symmetry, measurements of implosion velocity and shell thickness, and mix before discussing the progress on the integrated performance obtained in cryolayered implosions.

Specifications for the accuracy with which the key variables must be established in tuning campaign surrogate targets are set by a multivariable sensitivity study (MVSS) designed to achieve a global optimization of specifications for the laser, targets, and experiments. The MVSS carried out for the ignition point design is discussed in the article by Haan *et al.*[8] These requirements, along with the experimental observables and their required measurement precision, are discussed in the paper by Landen *et al.*[14] The requirements on these measurements set the goals of the precision optimization or "tuning" campaign. Tuning requirements for each of the implosion optimization platforms are defined so that implosions meeting these requirements would meet the calculated ITF specifications set for the point design. A summary of those requirements and the precisions (shot-to-shot uncertainty in measurement) and accuracies (absolute error in measurement) that have been achieved[98] is given in Table I and is discussed in more detail in the review of the experiments below.

1. Drive

Since the start of the precision implosion optimization experiments in May 2011, the NIC has accumulated a wide range of Drive and LPI data using ignition scale hohlraums at

TABLE I. Required and achieved tuning precision and accuracies for each of the implosion optimization platforms. Color coding: met or exceeded requirement (blue), on track to meet requirement (green), and not applicable (yellow).

Platform	Key Parameter	Precision		Accuracy or Goal	
		Budget	June 2012	Spec	June 2012
Reemit	Picket Symmetry (P2)	± 3%	± 1%	± 7.5%	± 2%
Keyhole	Shock Velocities	± 2%	± 1.5-2%	± 5%	± 5%
	Shock Merge Depths	± 4 µm	± 2-5 µm	± 6 µm	± 9 µm
Backlit Capsule	Velocity (Gated)	± 5%	± 5%	± 2%	± 5%
	Velocity (Streaked)	± 1.5%	± 3%	± 2%	± 4%
	Mass Remaining	± 1.5%	± 1%	± 1.5%	± 1.5%
	Hydroinstability GF	± 20%	Designed	± 20%	
Symmetry Capsule	Hot Spot Symmetry rms	± 5 µm	± 3 µm	± 5 µm	± 5 µm
	Peak Drive (Dante)	± 5%	± 3%	± 5%	± 5%
	X-ray Bangtime	± 50 ps	± 30 ps	± 50 ps	± 50 ps, SPBT[a]
	Hot e- @ Capsule	± 50 J	± 50 J	< 100 J	< 100 J
	X-ray preheat fraction	± 10%	± 7%	± 10%	± 7%
	Hot spot mix (ng of Ge)	± 30 ng	± 20 ng	± 30 ng	± 30 ng
Cryo-Layered Capsule (THD and DT)	Yield (nToF, Activation)	± 5%	± 5%	± 10%	± 10%
	Fuel ρr (MRS)	± 10%	± 8%	± 10%	± 8%
	Tion (nToF)	± 10%	± 7%	± 10%	Bulk motion
	Nuclear Bangtime (GRH)	± 50 ps	± 20 ps	± 50 ps	± 30 ps
	Nuclear Burn Duration	± 30 ps	± 30 ps	± 30 ps	± 30 ps
	HS radius (P0) (NI)	± 5 µm	± 3 µm	± 5 µm	± 3 µm
	HS symmetry rms (NI)	± 5 µm	± 5 µm	± 7 µm	± 5 µm
	Fuel ρr rms (CR)	± 10%	± 15%, OMEGA	± 10%	± 15%

[a]SPBT stands for south pole bang time diagnostic.

energies between 1 and 1.8 MJ in scale 544 and 575 hohlraum, with Au and Au-coated U hohlraum wall material, and with 3.1 and 3.375 mm diameter LEHs. The two different scale hohlraums are shown schematically in Fig. 32. The change from the scale 544 hohlraum to the scale 575 hohlraum was made to improve symmetry control with cross beam transfer as discussed below. Since the area of the two hohlraum is very similar and the calculated plasma conditions are very similar, the drive and LPI effects were expected to be very similar. Fig. 33 shows that the absorbed laser energy defined as the incident energy minus the measured
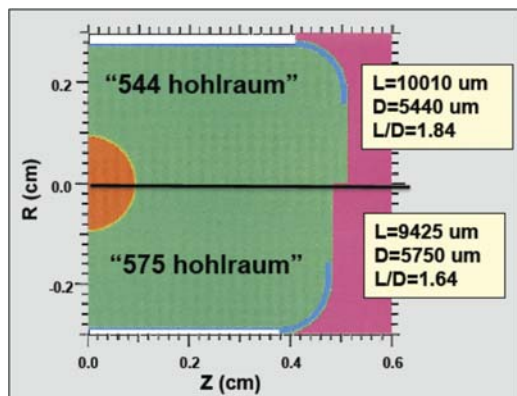

FIG. 32. Comparison of cross-sections and dimensions of original scale 544 hohlraum (top half) versus newer scale 575 hohlraum (bottom half).

backscattered and near-backscattered energy is ∼85%, independent of hohlraum scale and incident energy over the range of 1.2–1.8 MJ. About 90% of the 15% losses are from the inner cones, and of that, 80% is due to SRS during peak power. By turning off the outer cones midway through the peak power phase, the late inner cone SRS could be significantly reduced, proving such SRS occurs after cross beam energy transfer.[99]

Fig. 34(a) shows that the time-integrated LEH imaged[100] near the 3kTr peak of a 300 eV Planckian shows about 15% of LEH closure with 10% of the soft x-ray flux outside this aperture. These data are used to translate[101] the peak Dante flux into a peak internal radiation temperature as shown in Fig. 34(b) for both Scale 544 and Scale 575 hohlraums. The shorter Scale 575 hohlraums should be cooler because their LEH subtends a larger solid angle for x-ray losses. The final LEH size is ≈7%–10% larger in diameter in data than simulations and the implications of this are further discussed in this section.

In December 2011, the NIC began using U hohlraums whose inside surface is coated with 0.6 µm of Au. About 0.2 µm of Au coating is needed to prevent oxidation of the U in the current fabrication process. However, making the coating 0.6 µm has the benefit that all experiments up to the final pulse behave the same in both Au and U hohlraums, reducing the number of iterations needed for optimization, while having little impact on the expected efficiency advantage of U.
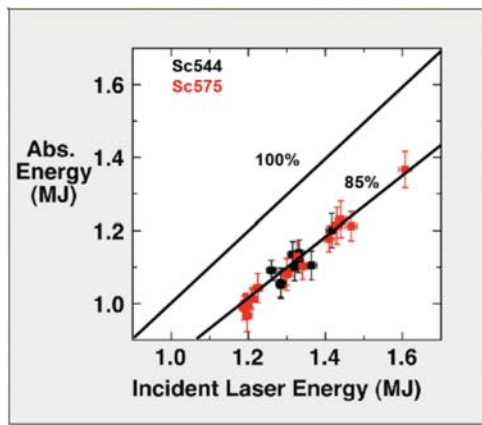
FIG. 33. Absorbed laser energy versus incident laser energy for Sc544 (black) and Sc575 (red) hohlraums equipped with 3.1 mm LEHs.
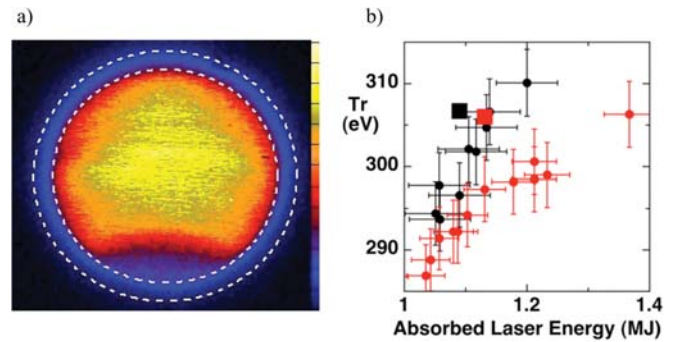

FIG. 34. (a) 870 eV time-integrated image through the LEH at an angle of 17° to the hohlraum axis. Dashed inner and outer circles show soft x-ray defined and initial LEH contour. (b) Peak internal Tr versus absorbed laser energy for Au Sc544 (black) and Sc575 (red) hohlraums equipped with 3.1 mm LEHs, showing data (circles) and simulations (squares).

Fig. 35(a) shows that the absorption has remained high and the same for Au and Au-lined U hohlraums, averaging 84% for all experiments with incident energies over 1 MJ. Internal radiation temperatures have recently been more accurately calculated by subtracting the soft x-ray halo flux observed outside the LEH[100] before dividing the measured Dante flux by the measured LEH area[102] that has closed by $\approx 200\,\mu$m in radius by peak power and finally applying an ≈ -3 eV calculated viewfactor correction to translate between fluxes measured by Dante and the flux impinging on average on the capsule.[101] Fig. 35(b) shows that the peak internal x-ray drive in the Au-lined U hohlraums has now exceeded 320 eV at 500 TW peak power.[103] The hard x-ray fraction (>1.8 keV) which dictates the level of dopant preheat shielding required is shown in Fig. 35(c), increasing with peak Tr and similar for Au-lined U vs Au hohlraum walls as expected. The data lie above or near the hard x-ray fraction expected for a pure Planckian drive at the peak Tr, corrected slightly upward for Dante Tr being 1% higher than the internal Tr. The U hohlraums do have a drive advantage, equivalent to about 3% in radiation temperature, 12% in flux, or 40 TW of laser power
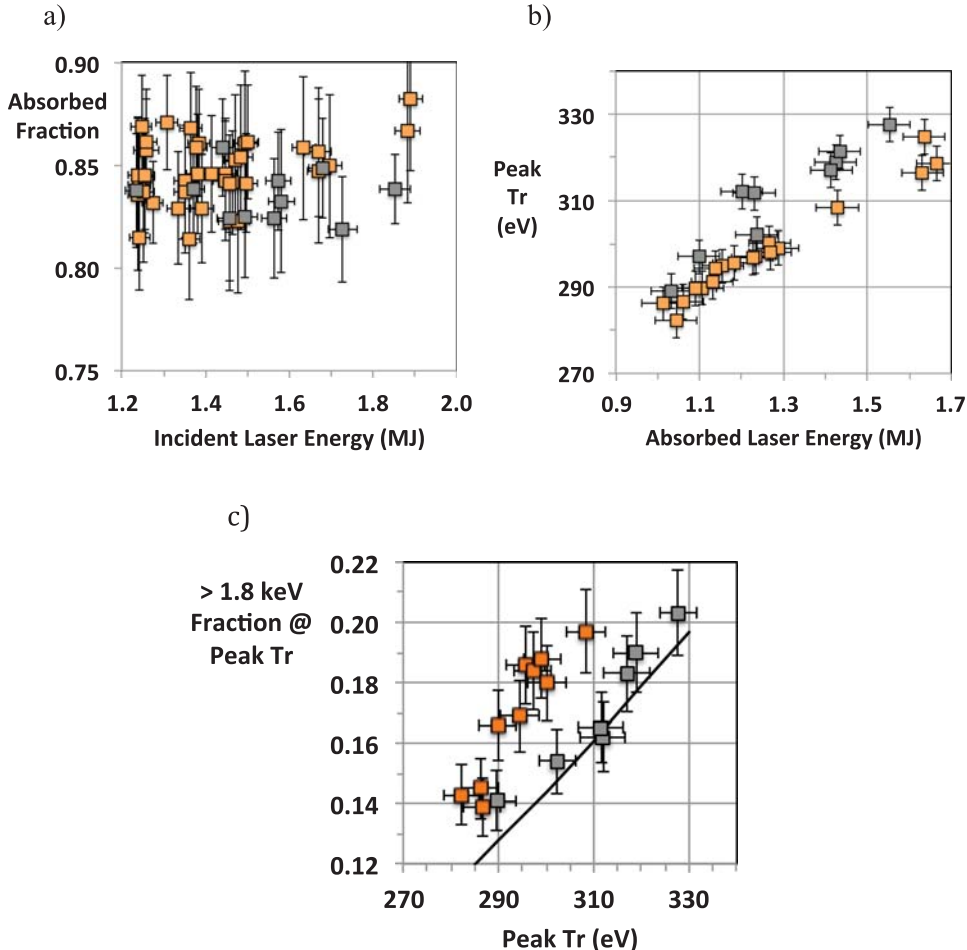

FIG. 35. (a) Absorbed fraction vs. incident laser energy. (b) Peak internal Tr vs. absorbed laser energy for >400 TW peak power, 5.75 mm-diameter, 3.1 mm-LEH hohlraums. (c) >1.8 keV fraction vs peak internal Tr for subset consisting of symcap and DT implosions. Line is expected fraction for Planckian at peak internal Tr, corrected for 1% higher Tr seen by Dante than capsule. Au and Au-lined U hohlraums are orange and gray, respectively. The data show that Au-lined U hohlraums generate about 10 eV more drive at a given laser energy relative to Au hohlraums and lower hard x-ray fraction for a given peak drive.
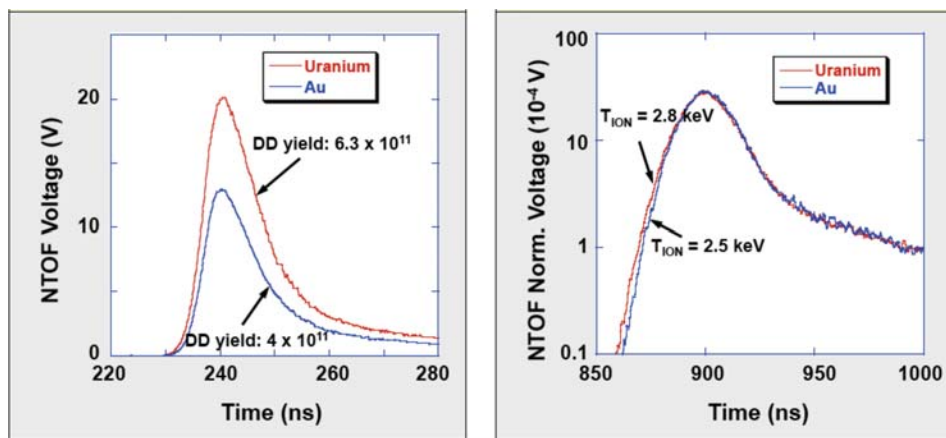
FIG. 36. Nuclear scintillator measures of yield and ion temperature from a symcap in an Au (blue) and Au-coated U hohlraum (red).

above $T_r = 300$ eV. The Uranium hohlraums also exhibit higher yields and ion temperatures consistent with this higher drive as shown in Fig. 36.

The scale 575 hohlraum has been tested with both 3.1 mm and 3.375 mm diameter LEHs. Hohlraums with larger LEHs have more clearance and allow more flexibility in pointing at the cost of larger x-ray losses. A 3.373 mm LEH has about 20% more LEH area than a 3.1 mm LEH, equal to 40–50 kJ and 4%–5% of the x-ray drive for the hohlraums tested. An objective of the larger LEH was to test if moving the pointing of the inner beams outward, away from the capsule blowoff, would result in better inner beam propagation and reduced LPI losses. However, within the range of pointing variation enabled by the LEH size, LPI effects and implosion symmetry were essentially unchanged. Following these tests, the LEH size was changed back to the original 3.1 mm diameter.

In general, the HFM does a good job of capturing the scaling of drive and symmetry. However, a more detailed comparison between the predictions of x-ray drive and the data indicate that the combination of DCA and non-local transport as currently implemented systematically overpredicts the x-ray drive by about 9% on average as indicated in Fig. 37. Some of this discrepancy is likely due to numerical zoning and convergence effects. For example, it is very difficult in 2D calculations to get adequate resolution of the x-ray conversion region that tends to occur in a region of steep temperature and density gradients. It has also proved difficult to accurately calculate the laser entrance hole closure. The

calculated time integrated hole closure is often of order 20% greater in area than that seen in experiments as shown in Fig. 38. Drive estimates based on the measured Dante flux must correct for this difference in LEH size. Work continues to better understand the differences between the drive data and the calculations. Also, as indicated in Fig. 37, matching the implosion velocity of the Si-doped ConA experiments requires a further reduction in the peak drive, of about 5% relative to the measured flux. This is discussed further below.

2. Hot electron preheat

One possible obstacle to high compression is preheat of the DT fuel by energetic electrons produced during high intensity laser-plasma interactions inside the hohlraum. Fig. 39 shows that several x-ray diagnostics provide information about hot electron production and deposition. The FFLEX provides 8 time-integrated channels ranging from 20 to 90 keV x-rays and 2 time-resolved channels centered at 150 and 250 keV x-rays using a combination of filters and fluorescers in front of scintillator-based photomultiplier tubes. The low magnification eHXI/HEMPI[104] and pHXI[105] are time-integrated high energy multipinhole, multichannel x-ray imagers located at the hohlraum equator and pole, respectively.

The hot electron energy generated by LPI processes is estimated from the high energy Bremsstrahlung spectrum.[106] A simple formula, balancing bremsstrahlung emission and stopping power for energetic electrons, is used to relate the
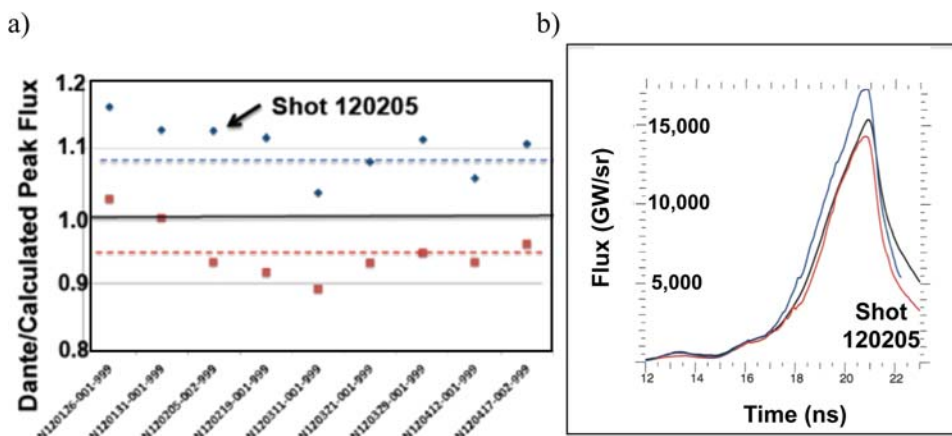

FIG. 37. (a) Ratio of measured to calculated Dante flux for 9 shots for standard Hydra calculation (blue) and calculation modified to match implosion trajectory (red). Dotted lines show average ratios. (b) Measured (black), Hydra simulated (blue), and modified simulated (red) Dante flux versus time for shot N120205.
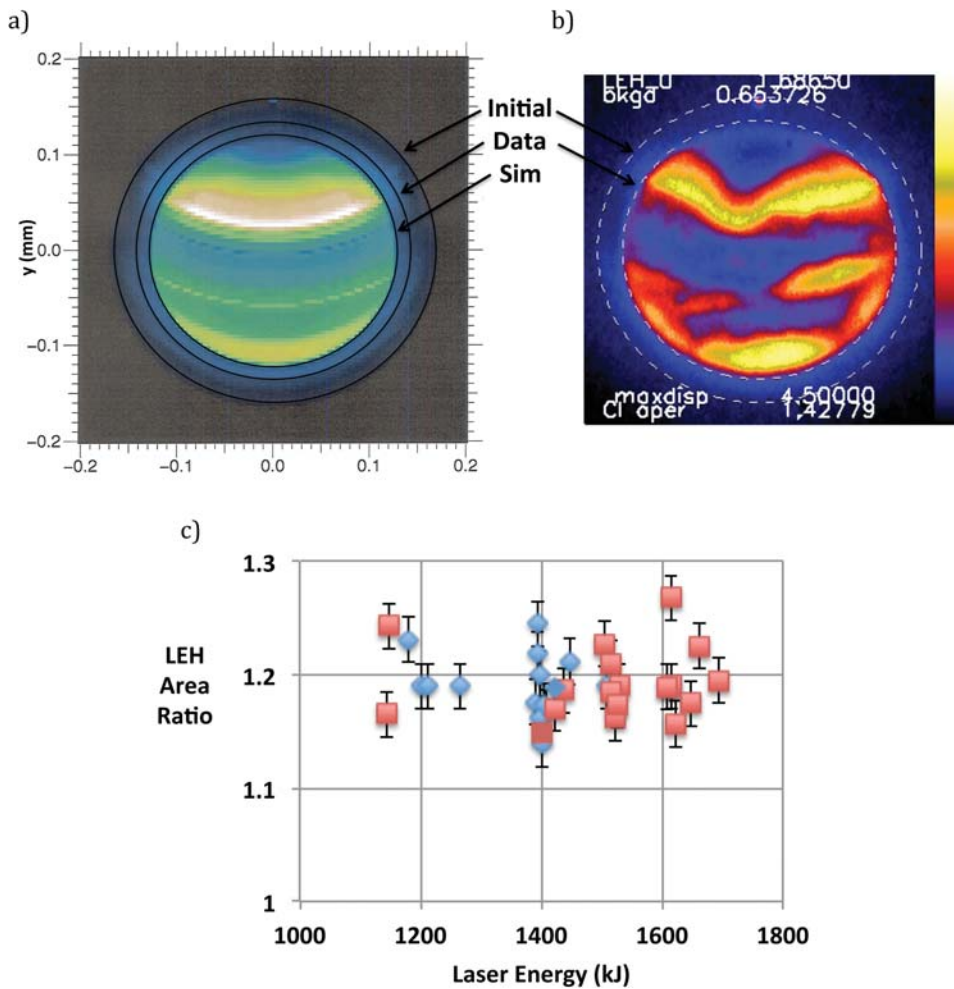
FIG. 38. Comparison of (a) 2D simulated and (b) measured >3 keV time-integrated x-ray image at 18° to hohlraum axis for a 1.4 MJ, 3 ns rise, 3.373-mm LEH in a Scale 575 hohlraum. Circles represent initial LEH size and 50% x-ray contour sizes. (c) Ratio of measured to simulated x-ray area versus incident laser energy for initially 3.373 mm (blue) and 3.101 mm diameter (red) LEHs.

bremsstrahlung emission I_{Br} to the amount of energetic electrons

$$I_{Br}[\text{keV}/\text{keV}/sr] = 6.3/4\pi \times 10^9 Z^* E_{hot}(J) \\ \times \exp(1 - h\upsilon/kT_{hot}), \quad (32)$$

where $Z^* = \langle Z^2 \rangle / \langle Z \rangle$ is the effective atomic number, E_{hot} is the energy in energetic electrons at a characteristic temperature T_{hot} of the hot electron distribution. I_{Br} scales linearly with Z since the bremsstrahlung efficiency scales as Z^2 while the electron stopping power scales as Z.

Time-integrated hard x-ray FFLEX spectra from 1.4 to 1.5 MJ, 330–420 TW hohlraums shown in Fig. 40 exhibit a 2-temperature distribution.[107] The spectrum has a component with $T_{Hot} \sim 20$ keV which is consistent with the observed SRS. There is also a "Superhot" component, with much less energy, which may be the result of $2\omega_{pe}$ processes or Raman scattering near $1/4$ n_{cr}. Electrons with energy above $\sim$170 keV can penetrate the ablator and are those most responsible for fuel preheat. Fig. 41 shows that these electrons primarily responsible for fuel preheat are being generated near the end of the pulse, at levels of 0.2–1 kJ. Since FFLEX is spatially
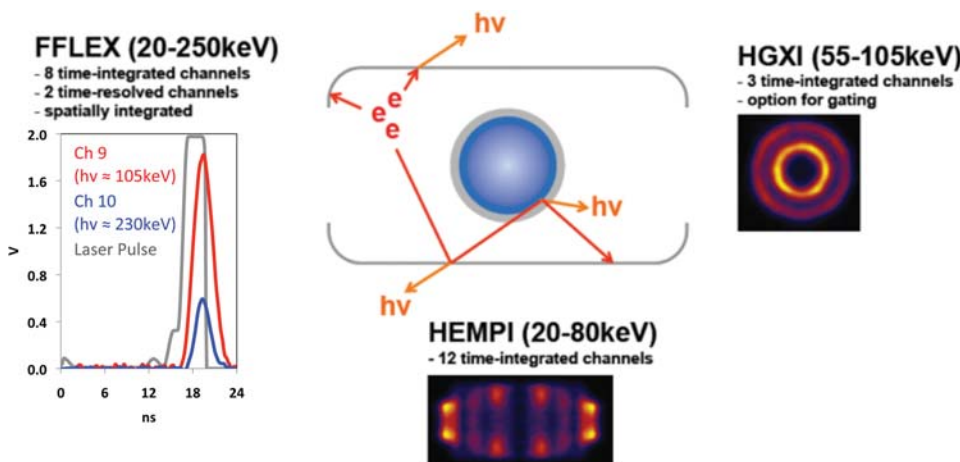

FIG. 39. Examples of hard x-ray time-resolved and imaging data collected from various lines-of-sight as a measure of hot electron induced Bremsstrahlung.

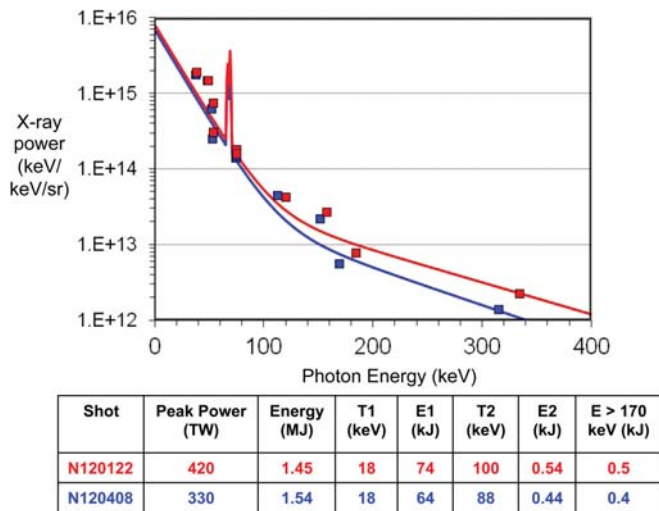| Shot	Peak Power (TW)	Energy (MJ)	T1 (keV)	E1 (kJ)	T2 (keV)	E2 (kJ)	E > 170 keV (kJ)
N120122	420	1.45	18	74	100	0.54	0.5
N120408	330	1.54	18	64	88	0.44	0.4

FIG. 40. Time-integrated hard x-ray spectra for two shots with two-temperature fits overlaid that include a contribution from Au K-alpha at 68 keV. Table lists extracted hot electron energies and temperatures of best fit.

integrating and dominated by Bremsstrahlung from the high Z hohlraum, we needed a spatially resolving hard x-ray instrument to check the fraction of hot electrons reaching the capsule.

Fig. 42(a) shows the pHXI experimental set-up and data used to infer the level of >170 keV hot electrons reaching the capsule from imaging >100 keV Bremsstrahlung. Since the pHXI Image Plate recording medium[108] and the FFLEX are absolutely calibrated and their spatially averaged signals, dominated by the hohlraum emission per Z scaling in Eq. (32) are consistent with each other per Fig. 43, the level of hot electrons reaching the capsule can be extracted from Fig. 42(b) imaged data by simple ratioing. After we first account for the fact that ≈ 15 times more electrons are necessary to yield the same bremsstrahlung emission from stopping in the CH capsule ablator ($Z^* = 5.3$) compared to stopping in Au ($Z = 79$), we infer 570 ± 250 J of >100 keV hot electrons[109] impinging on the symcap capsule driven with 1.3 MJ, 400 TW peak power shown in Fig. 42(b).

Based on simulations assuming the time-dependence of the hot electrons reaching the capsule is the same as seen on

FFLEX, we can derive the fuel adiabat increase due to hot electrons. Fully integrated simulations of the experiment that model the coupling with, stopping in, and propagation through the ablator of these energetic electrons, and subsequent stopping and heating in the DT fuel, show that less than 2% of the energy E > 100 keV absorbed in the CH ablator is absorbed in the DT ice. For better accuracy, we calculated from 1D simulations the branching ratio of electron energy deposited in the CH ablator to DT fuel as a function of electron initial energy. Convolving this with the inferred hot electron distribution shown in Fig. 43 and correcting for 2D line–of–sight effects, we derive an upper bound of hot electron energy that is absorbed in the DT fuel of 5 ± 3 J. To estimate the effect on compressibility, this energy needs to be compared to the total internal energy in the fuel. At peak power when the majority of hard x-rays are generated, the 4 successive shocks have merged, and the 0.17 mg of DT fuel is compressed to at least 2.5 g/cc, yielding 100 J for the internal energy $\sim \rho^{2/3}$ of a Fermi degenerate $\alpha = 1$ system. Since the adiabat $\alpha \approx 1.5$ after 4th shock passage in current NIC implosions, the adiabat increase due to hot electron preheat is hence $\Delta\alpha/\alpha = 5/150 = 3 \pm 2\%$. This is well below the requirement (<10%) and consistent with the specifications set for the CH point design. Furthermore, the maximum hot electron levels measured early in the pulse using truncated pulses used for early time symmetry tuning described in Sec. V B 3 are also well below specifications by orders of magnitude. The modest inferred hot electron preheating is further supported by the fact that recent fully integrated DT implosions reached fuel areal densities within 15% of the requirement for ignition and burn.

3. Optimizing early time symmetry

Figure 44(a) is a picture of a Reemit target. Reemit targets are used to optimize symmetry during the first 2 ns of the pulse by imaging soft x-ray reemission from the Bi coated sphere which replaces the standard CH capsule.[110] For times longer than the first couple of ns, ablation from the CH capsule produces plasma conditions in the hohlraum that differ from those in a hohlraum with a Bi capsule. This allows us to

a)

b)

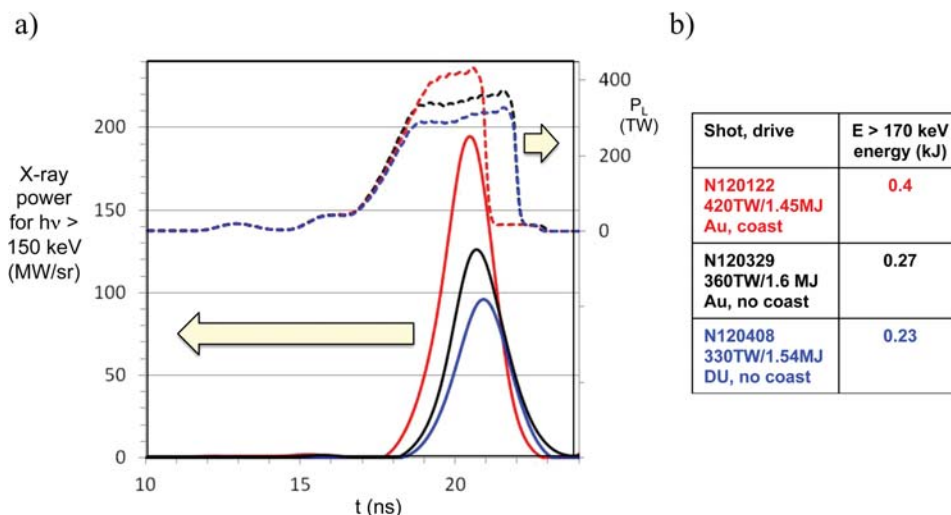| Shot, drive	E > 170 keV energy (kJ)
N120122 420TW/1.45MJ Au, coast	0.4
N120329 360TW/1.6 MJ Au, no coast	0.27
N120408 330TW/1.54MJ DU, no coast	0.23

FIG. 41. (a) Time-resolved measurements of the laser power profile (above) and of >150 keV x-rays (below) for three shots. (b) Inferred time-integrated >170 keV electrons from hard x-ray signals.
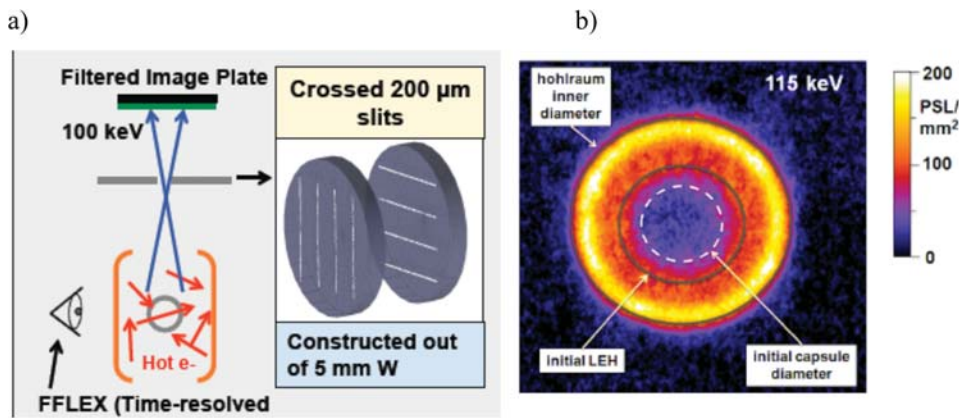
FIG. 42. (a) Experimental set-up for time-integrated moderate resolution imaging of hard (>100 keV) x-ray Bremsstrahlung emanating from the hohlraum and capsule through the top LEH. Inset shows details of 200 μm crossed-slit imager. (b) Time-integrated 115 keV image with capsule and hohlraum regions denoted.

truncate the pulse as shown in Fig. 44(b) to mitigate detector damage. But for the first couple of ns, the plasma conditions and the resultant beam propagation are the same for both capsules. To increase the sensitivity to the incoming flux asymmetry, we image the sphere at photon energies hν that are in the high energy tail of a Planckian sphere re-emission, thereby amplifying the asymmetry of the spectrally integrated incoming radiation drive by h$\nu/4kT_{reemit}$,[111] where k is the Boltzmann constant and T_{reemit} is the Bi re-emit sphere temperature, typically 85% of the hohlraum radiation temperature. This increase in sensitivity is offset, however, by the reduction in the detected photon flux at higher energies that will affect measurement accuracy. Therefore, the energy band chosen in the experiment is a compromise between the asymmetry amplification and photon flux detected. For radiation symmetry tuning at the 75 eV ignition design picket temperatures, we have chosen to perform re-emit measurements centered at 610 eV and 750 eV photon energies representing thermal asymmetry amplifications of 2.4 and 2.9, respectively.

On the right, Fig. 45 shows simulated cross-sections of fuel density profiles at bangtime for various picket P_2 drive asymmetries (0%, −12%, and −24%) after the peak cone fraction has been readjusted to provide a round core. While the core remains fairly round, the predicted fuel areal density rms variation increases from 8% to 22% to 55% as

progressively larger P_2 drive asymmetry swings are delivered during the picket. The ignition requirement of <15% rms low mode areal density variations then translates to setting P_2 to ±7.5% as shown by the horizontal box. Fig. 45 also shows typical results[112] for the inferred P_2 asymmetry vs incident inner cone fraction (defined to be at 1 ns) for re-emit targets in Scale 544 hohlraums, near peak Dante picket power. The raw data shown are taken at 900 eV photon energy and 1.3 ns, with 50–100 μm, 80–150 ps resolution over a 200 eV band-pass defined on the low end by a thin CH or Al filter and on the high end by the drop off in the Planckian reemission tail. As the inner cone fraction is increased, the images show more reemission from the waist than poles as expected. The inferred P_2 sensitivity to cone fraction matches the predicted slopes well, but is strongly offset to lower inner cone fraction relative to the baseline simulations shown as the dashed curve.

As shown by the solid line in Fig. 45, it is important to include cross beam energy transfer between the outer beams and the inner beams in modeling the required balance between inner and outer beams. The wavelength separation between the inner and outer beams is set by the symmetry requirements and LPI during the peak of the pulse. However, this wavelength also generates significant energy transfer to the inner beams during the first picket of the pulse when the beams interact in the high density LEH window blow-off. As there is essentially no loss on the inner beams because of LPI losses, the power on the inner beams must be turned down significantly during the foot of the pulse to obtain symmetry. As shown, the calculations with cross beam energy transfer still slightly overestimate the power required in the inner beams. This could be caused by the LEH window being slightly cooler and/or denser as it blows down, increasing the level of crossbeam transfer by ≈20%. However, since the calculated sensitivity to changes in the inner beam power is close to that which was observed experimentally, the playbooks generated for these experiments allowed very rapid iteration to the optimal inner beam cone fraction. The vertical dashed line shows that the optimum inner cone fraction at 1 ns for Sc 544 hohlraums has been pinpointed to 0.17 ± 0.01, applied for all subsequent Sc 544 tuning shots. Fig. 46 zooms into the region of interest and adds the Scale 575 data. Because the outer beams are moved closer to the waist of the hohlraum, the Scale 575 hohlraum requires lower fractional power in the inner beams (inner cone fraction = 0.12 at 1 ns) for a uniform illumination in the foot.
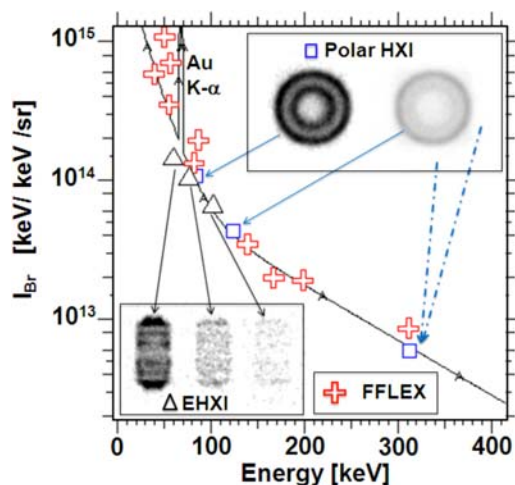

FIG. 43. Time-integrated hard x-ray spectrum measured by FFLEX (crosses), eHXI (triangles), and pHXI (squares) with overplotted two-temperature fit.
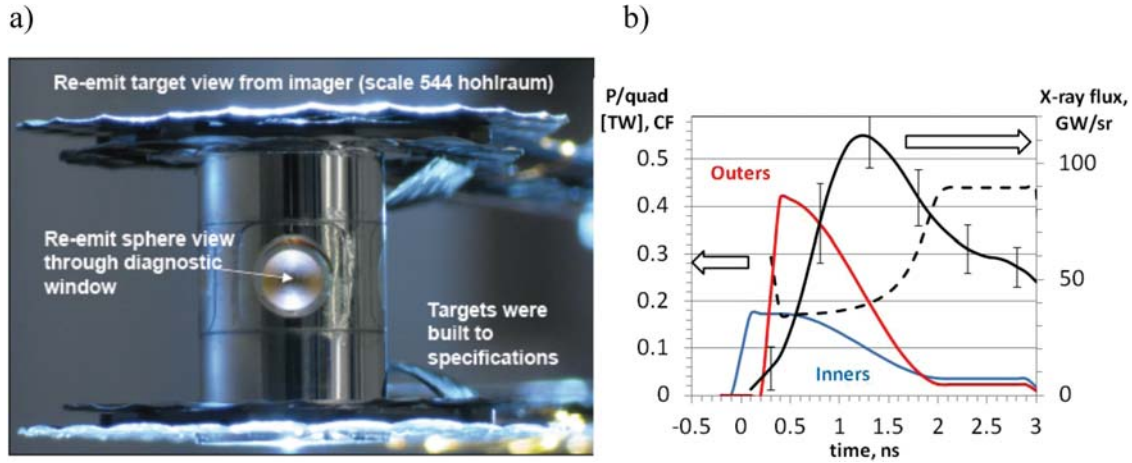
FIG. 44. (a) Reemit target picture and (b) Laser pulse (inners and outers in blue and red), inner cone fraction (dashed), and measured drive (solid black) over first 3 ns.

We note the same offset between data and simulations including crossbeam transfer.

The results have also been fitted by an analytic viewfactor model to gain more insight on the level of cross-beam transfer. We approximate the beam spots in the hohlraum with cylindrically symmetric x-ray sources. P_n/P_0 at the capsule is a sum of contributing factors from inner and outer beams as well as from the LEH given by[20,113,114]

$$\frac{P_n}{P_0} = (2n+1)\frac{\left[P_n^i S_n^i \epsilon + P_n^o S_n^o (1-\epsilon) - BP_n^{LEH} S_n^{LEH} \frac{A_{LEH}}{A_{wall}} F\right]}{(1+F)},$$

(33)

where n is mode number, P_n^x is a pure Legendre mode asymmetry at the hohlraum wall for mode n imposed by inner and outer beams as well as the LEHs, S_n^x are the corresponding smoothing factors at the capsule of mode n in a spherical hohlraum approximation, ϵ is a weighted inner/total beams power fraction, A_{LEH} is the total area of the LEHs, A_{wall} is the total wall area, and F is the ratio of the hohlraum x-ray

re-emission to laser plasma x-ray emission. The B factor in Eq. (33) is the ratio of fractional solid angles subtended by the LEH and wall at the capsule to their area ratio A_{LEH}/A_{wall}, = 0.64 and 0.74 for 5.44 mm and 5.75 mm diameter hohlraums. A_{wall} includes both the hohlraum and the high-Z capsule, assumed to have the same x-ray *albedo* α_{wall}, and excludes the area of the diagnostic windows A_{window} that have a low x-ray *albedo* ($\alpha_{window} = 0.2$). For α_{wall} defined as ratio of the re-emitted flux to incident flux, F is given by

$$F = \frac{\alpha_{wall}}{1 - \alpha_{wall} + \frac{A_{LEH} + (1-\alpha_{window})A_{window}}{A_{wall}}}$$

$$\cong \frac{\alpha_{wall}}{1 - \alpha_{wall} + \frac{A_{LEH} + A_{window}}{A_{wall}}}.$$

(34)

To include crossbeam transfer from outer to inner beams including pump depletion, we use the following coupled equations:

$$\frac{dI_i}{dx} = gI_iI_o, \quad \frac{dI_o}{dx} = -gI_iI_o, \quad \text{and} \quad I_i + I_o = I,$$

(35)

where g is the transverse averaged crossbeam gain per unit pathlength and power. $I_{i/o}$ are the incident powers of the inner/outer cones and I is the total power that is assumed conserved before and after transfer, since negligible specular
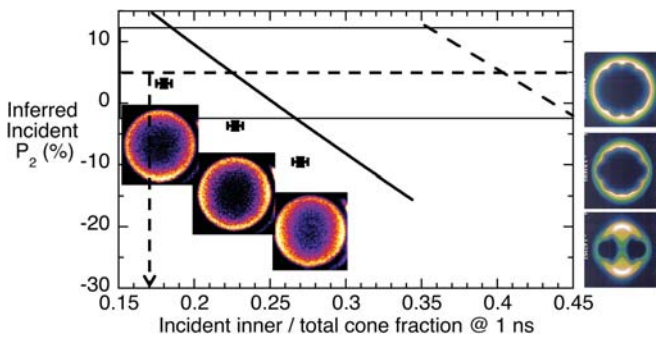

FIG. 45. Incident P_2 drive asymmetry at 1.3 ns inferred from reemission spheres for different incident inner cone fractions for 5.44 mm diameter hohlraums. Points are data, and solid and dashed lines are calculated values with and without crossbeam energy transfer. Also shown are raw data frames at 900 eV photon energy. Horizontal lines denote the ignition-tolerable −2.5% to +12.5% P_2 range. Vertical dashed line represents optimum incident cone fraction of 0.18 inferred from data. On the right are calculated cross-sections of fuel density profiles versus incident inner cone fraction after reoptimizing the peak power cone fraction to obtain best symmetry showing 8%, 22%, and 55% rms ρr variations from top to bottom image.
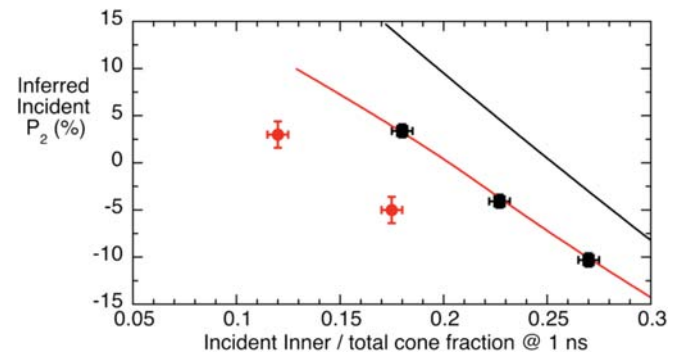

FIG. 46. Incident P_2 drive asymmetry at 1.3–1.5 ns inferred from reemission spheres for different incident inner cone fractions for both 5.44 (black) and 5.75 mm (red) diameter hohlraums. Solid lines are calculated values including crossbeam energy transfer.

reflection and backscatter losses are measured during the picket. Integrating over an effective pathlength L, the inner cone fraction CF' after transfer is related to the incident inner cone fraction $CF = I_i/I$ by

$$CF' = \frac{CFe^{gIL}}{(1 + CF(e^{gIL} - 1))}, \qquad (36)$$

$$\epsilon = \frac{(CF' - \Delta/\sin\theta_i)C_i e^{gIL}C_i\sin\theta_i[1 - \sin\theta_i(1 - \alpha_{wall})]/r_i^2}{(CF' - \Delta/\sin\theta_i)C_i\sin\theta_i\dfrac{[1 - \sin\theta_i(1 - \alpha_{wall})]}{r_i^2} + (1 - CF' - \Delta/\sin\theta_o))\sin\theta_o\dfrac{[1 - \sin\theta_o(1 - \alpha_{wall})]}{r_o^2}}, \qquad (37)$$

where $r_{i/o}$ are the distances between inner/outer cone spots and capsule center, $\theta_{i/o}$ are the average angles subtended between the line defined by the inner/outer cone spot centroids and capsule center and the hohlraum axis, Δ represents the reduction in power reaching the hohlraum wall due to fill gas absorption scaling as path length $\sim 1/\sin\theta_{i/o}$, and C_i is a normalized factor < 1 to account for reduced x-ray production of the inner beams that have a lower turning point density relative to the outer beams.

In Fig. 47, the analytic fits to the radiation-hydrodynamic simulations without crossbeam transfer when matched in slope and offset also match the data slope and offset when just adding in crossbeam transfer. The fits include the following input from simulations at the relevant 1.3 ns time: $\alpha_{wall} = 0.4$ (confirmed by earlier data[115]), hence F = 0.55, 50 μm of inward wall motion and 300 μm of outer beam refraction as confirmed by the soft x-ray LEH imager. The same three fitting parameters within 10%, $\Delta = 0.07$, $C_i = 0.2$, and G = 1.2 match both Scale 544 and Scale 575 data, as might be expected for the small changes in beam propagation path length and same LEH interaction region. The best fit weighted inner cone fractions ϵ for the Scale 544 and Scale 575 hohlraums without and with transfer are 0.04 and 0.26 and 0.04 and 0.22, respectively.
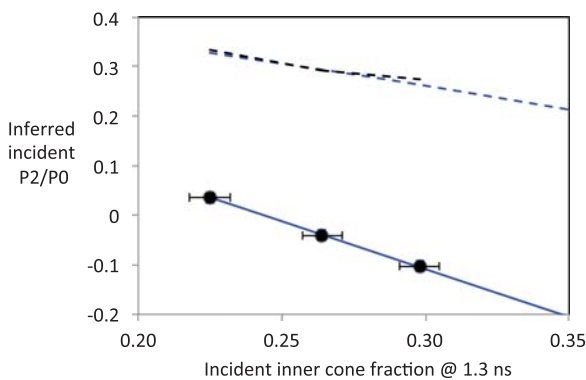

FIG. 47. Incident P_2 drive asymmetry at 1.3 ns inferred from reemission spheres for different incident inner cone fractions for 5.44 mm diameter hohlraums. Dashed lines are simulations (black) and analytic fit (blue) without crossbeam transfer. Solid blue line is the analytic fit using the same parameters as the dashed blue line except adding crossbeam transfer.

where the quantity of interest is the crossbeam gain exponent $G = gIL$.

In the simplifying limit of the laser spots being optically thick Lambertian x-ray sources, parallel to the hohlraum wall, the solid angle weighted inner beams power fraction ϵ including transfer is then given by

Just like the polar symmetry, the cores are also sensitive to azimuthal asymmetry, predominantly from the picket and peak phases. An m = 4 azimuthal asymmetry can arise from differences in crossbeam transfer, absorption, propagation, and x-ray conversion efficiency between the 23° vs 30° inner beams which principally imprint asymmetries on the waist of the capsule. The time integrated azimuthal symmetry is set by adjusting the wavelength separation between the 23° and 30° beams as discussed in the symcap section. In general, the relative powers of the incident 23° to 30° beams of the picket then have to be readjusted to avoid m = 4 symmetry swings. Fig. 48 shows the calculated sensitivity of a THD core m = 4 asymmetry to variations in the 23° inner cone fraction after symmetrizing the drive for all later parts of the pulse. A $\Delta CF_{23} = 0.2$ from optimum equates to a maximum ignition tolerable 3% m = 4 on the core.

By using a reemit target viewed through a LEH with no holes in the hohlraum waist, we can seek to optimize the azimuthal picket symmetry by varying the relative power between the 23° and 30° beams. We estimate the reemit sensitivity to m = 4 by adapting the earlier polar viewfactor model for azimuthal symmetry

$$\frac{m_4}{m_0} = \frac{\left[S_4^{23°}\epsilon^{23°} - S_4^{30°}(1 - \epsilon^{23°})\right]\epsilon}{(1 + F)}. \qquad (38)$$

Equation (38) treats the 23° and 30° beams as opposite in m = 4 phase, and the 8-fold symmetric outer beams as diluting the inner beam-induced m = 4 through the weighted inner cone fraction term ϵ. $\epsilon^{23°}$ is defined as the weighted 23° inner cone fraction relative to all inners. Differentiating and recognizing that by symmetry the m = 4 smoothing factors $S_4^{23°} = S_4^{30°}$

$$\frac{\Delta m_4}{m_0} = \frac{\left[S_4^{23°}\Delta\epsilon^{23°} + S_4^{30°}\Delta\epsilon^{23°}\right]\epsilon}{(1 + F)} = \frac{2\left[S_4^{23°}\Delta\epsilon^{23°}\right]\epsilon}{(1 + F)}. \qquad (39)$$

From the earlier polar symmetry analysis, $\epsilon = 0.22$ after transfer for these Scale 575 hohlraums. However, at the waist regions of interest for the azimuthal asymmetry, the outer beams are $\approx\sin\theta_o \approx 1/\sqrt{2}$ less effective drivers, so ϵ at the waist increases to 0.28. Plugging in $S_4^{23°} = 0.11$ and F from before = 0.55, Eq. (39) predicts 1% Δm_4 for
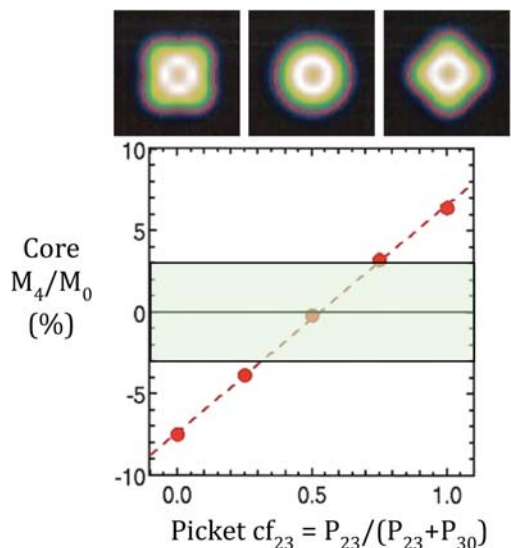
FIG. 48. Calculated THD core m = 4 versus 23° subcone fraction. Above are simulated core x-ray emission shapes for 23° subcone fractions of 0, 0.5, and 1. Green area shows ignition tolerable ±3% m = 4 range
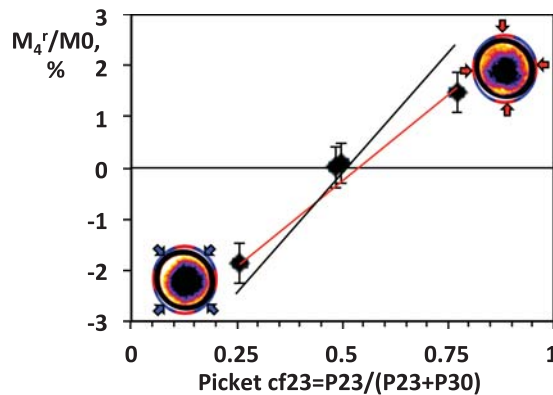

FIG. 49. Reemitted m_4 at 700 eV and 1.5 ns versus incident 23.5° cone fractions for 5.75 mm diameter hohlraums. Red line is 3D calculation including crossbeam energy transfer. Also shown are raw data frames at 700 eV photon energy.

$\Delta\varepsilon^{23°} = 0.25$, so 2.5% for an amplified reemitted Δm_4^r at $h\nu = 700$ eV. Fig. 49 shows that the data match the expected sensitivity and phase change of the dominant m = 4 mode for both the analytic model and HYDRA simulations. The data also confirmed that using matched 23° and 30° power is near optimum, and including ±0.4% error bars, well within the ignition tolerable ±1.5% reemitted m_4^r.

4. Optimizing implosion adiabat with keyhole targets

Pictures of the keyhole target used to set the shock timing and merge depth are shown in Fig. 50. The original plan used the VISAR to continuously track only the first 3 shock velocities as they overtake each other in liquid D_2 that is probed through a non-blanking quartz window (see Fig. 51(a)). The 4th shock would be timed, after first merging with the first 3 shocks in D_2, as it breaks-out of a Au witness plate[116] through either loss of VISAR reflectivity or streaked optical pyrometry (SOP).[117] Both techniques were qualified at NIF. However, shock timing technique tests at OMEGA[118] and then at NIF[119] showed that the quartz

window did not blank even at peak power levels above 400 TW, allowing the 4th shock velocity at NIF to be tracked in time as for the other lower strength shocks up to about 130 μm/ns shock velocity.

An example of 1D imaged streaked VISAR data showing fringe jumps as each successive shock is overtaken until an accelerating 4th shock is observed is shown in Fig. 51(b). As an aside, the 3 μm/ns jump in shock velocity as the first shock crosses the CH ablator/liquid D_2 interface at earlier times has been measured sufficiently accurately (to 0.6 μm/ns) that an improved EOS model[120] for this first release phase of CH has been implemented in the codes. By integrating in time the fringe jumps proportional to the leading shock velocity, we can also extract the shock merge depths. Setting the optimum shock strengths and shock merger depths to be just after the DT ice/gas interface (corresponding to ≈81 μm depth in liquid D_2) is key to maximizing the fuel density. Fig. 52(a) shows the results for 5 shots measuring and optimizing the shock speeds and merge depths by altering the foot of the pulse.[121] In just three shots, the velocities and merge depths for the first 3 shocks were set within 1.5× of their ignition tolerance to the required 0.5 μm/ns velocity and few μm depth accuracy provided by the VISAR, and reduced the calculated fuel adiabat for following DT implosions from 2 to 1.5. Reproducibility was then
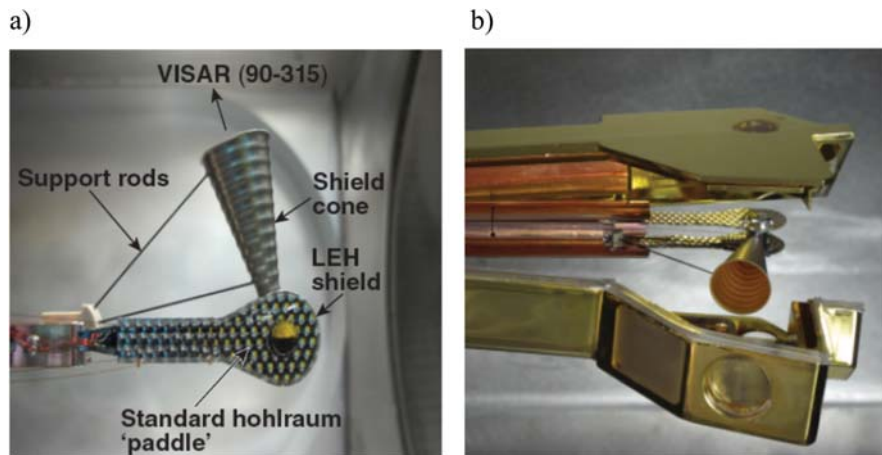

FIG. 50. (a) Picture of keyhole target with cone shield. (b) Picture of keyhole target inside partially open custom shroud with VISAR window access.
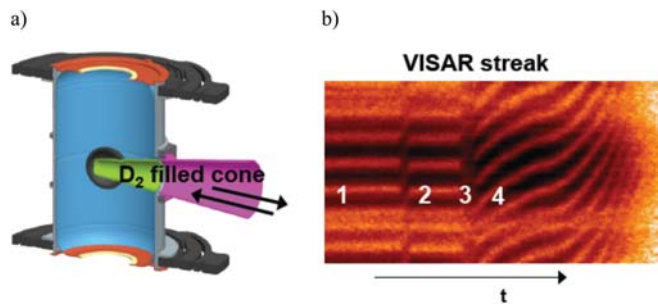
a)   b)

FIG. 51. (a) Schematic of keyhole target for shock timing showing D_2-filled re-entrant cone for VISAR access. (b) Example of streaked VISAR data from equator showing fringe jumps at successive shock overtake.

demonstrated on the 4th and 5th shots. Fig. 52(b) shows the level of pulse power profile changes required to achieve shock timing.

The rapidity in converging to near the ignition specs is a testament to the validity of the preshot playbooks developed before this campaign. These preshot calculated "playbooks," which are obtained from 2D HYDRA integrated-hohlraum simulations, provide the first order expected changes in all shock velocities, accelerations, merger times, and radii as a function of the power and time of each epoch of the laser pulseshape (initial picket, low-power trough, 2nd, 3rd, and 4th pulses). Fig. 53 shows a comparison of the measured data with several of the playbook predictions. Fig. 53(a), for example, compares the time of 1st shock breakout from the CH ablator into the D_2 fuel as a function of the laser energy in the initial picket (0–2 ns). In this case, the picket energy has been corrected for small <3% left-right picket symmetry variations that will affect a single-point shock measurement at the hohlraum waist. The measured slope is within 30% of the predicted slope, and the clear measured correlation is proof that the quoted VISAR timing accuracy of ±50 ps and laser picket energy measurement accuracy of ±1% are valid. Moreover, the variability in the delivered picket energy of ±4% shown meets the ignition variability requirement of <±5%. Shot-to-shot and side-to-side variation in picket energy has subsequently been further improved by more frequent inspection of debris accumulation on the optics. Fig. 53(b) shows a similar comparison for the 2nd shock velocity, which depends almost exclusively on the 2nd pulse laser power showing a shot-to shot variability of ±1 μm/ns (±3% of the 3-shot average), again illustrating the level of

shot-to-shot repeatability on NIF. Shock merger locations were found to follow preshot predictions very well as indicated by the example in Fig. 53(c) of the shock 3–4 merger depth (radial distance into the D_2 from the inner surface of the ablator) vs the launch time of the 4th pulse. By contrast with the other measurements, the 4th shock velocity was not observed to be in agreement with predictions as shown in Fig. 53(d) plotting the 4th shock velocity versus the 4th pulse launch time. Since the 4th shock is strongly accelerating, the measured velocity (initially observed upon merger with the 3rd shock) increases with delay time as expected with a slope within 16% of the playbook. The magnitude of the 4th shock velocity, however, is lower than the simulations by 20–25 μm/ns (≈20%). Further research is needed to understand why the 4th shock did not reach the expected velocity.

In all the above plots, the VISAR observable was strongly dominated by just one laser parameter, either because early in the pulse (Fig. 53(a)), no other dominant variable (Figs. 53(b) and 53(d)) or the other dominant variables, 3rd shock launch time, and 3rd and 4th shock strengths were not changed (Fig. 53(c)). Fig. 54 shows another set of 4 plots regarding intermediate shock merge depth sensitivities for which the observable depends on several "off-diagonal" laser parameters that must in general be corrected for per playbook slopes before the primary correlation becomes clear. For example, in Figs. 54(a) and 54(c), the merge depths have been corrected for shot-to-shot planned and random variations in the picket and trough power and second pulse launch times in translating between the raw data and corrected data. In three cases, the extracted slope sensitivities from the corrected data compare well with the predicted "playbook" slope sensitivities. Fig. 54(a) slopes compare less well, attributed to the fact that the first 2 shots at the ends of the range where the peak power was varied strongly also had large planned changes in the trough power and second shock launch time.

The expected weak sensitivity of shock timing to 2× concentration variations in ablator dopant (Fig. 55(a)), and to small variations (<2 Å) in the laser wavelength separation (Fig. 55(b)) was also checked. In particular, Fig. 55(a) shows the expected few percentage drop in 1st shock velocity during passage through a 2× more doped ablator, leading to a negligible 1–2 μm difference in first two shocks merge depth. Such verified insensitivity and repeatability over many month timescales have allowed us to eliminate some shock
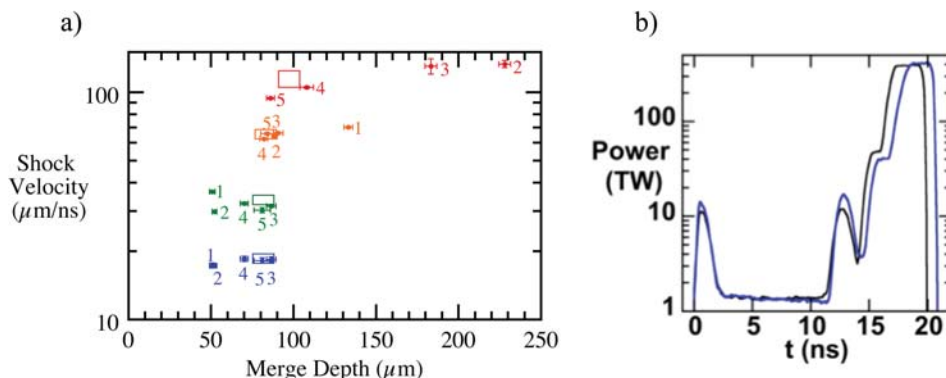
a)   b)

FIG. 52. (a) Measured (points) shock velocities and shock merge depths in liquid D_2 for 1st (blue), 2nd (green), 3rd (orange), and 4th shocks (red), labelled by chronological shot number. The ignition tolerance ranges are shown as boxes. (b) Pulseshape before (black) and after (blue) shock timing.

timing iterations when tuning symmetry mandates wavelength changes or testing mix sensitivity mandates dopant concentration changes.

Based on the lower than expected 4th shock velocity, additional tests of the impact of changes in the rate of rise to peak power pulse (see Fig. 56(a)) were then undertaken. A slower rise is predicted to be somewhat less efficient, because the shell has less volume during peak acceleration, but to be less sensitive to fluctuations in the drive during the 4th rise. Fig. 56(b) shows the expected transition from a clear 4th shock velocity jump to an accelerating compression wave as the rate of laser rise to peak power is decreased.

The effect of these variations in pulse shapes on cryogenic implosion compressibility and hot spot formation were tested on a regular basis. For example, Fig. 57(b) shows that cryolayered implosions with slower rise pulses to peak power shown in Fig. 57(a) achieve higher hot spot density for a given peak stagnation pressure, or equivalently a lower hot spot adiabat at peak compressions, closer to the conditions calculated for the CH point design. Fig. 58 shows that the measured ratio of the 10–12 MeV neutron downscattered to 13–15 MeV unscattered neutrons (DSR) that is proportional to the DT fuel areal density also shows sensitivity to the rate of rise to peak power. The DSR is plotted versus merge depth of the first 2 shocks as inferred from the relevant keyhole tuning shot. That metric, along with the 4th shock rate of rise, are predicted to be the dominant factors setting the in-flight fuel adiabat. Specifically, for a given 2nd shock merge depth in the DT implosion, the fastest (1 ns) rate of rise exhibited the lowest DSR. We also note that by extending the drive pulses as discussed in a later section, we see further increases in DSR when the merge depth is close to the optimum 81 μm, but the DSR remains low (<0.05) for nominal pulse lengths independent of shock merge depth.[122] Fig. 58 also indicates that the optimum merge depth may be set too conservatively at 81 μm, to be further checked by more implosions.

Finally, we expect the fusion yield from stagnation of the final merged shock to increase for faster rate of rises to peak power. To test this, we fill the symcaps with a 30/70 mixture of D-^{3}He to observe the 15 MeV proton yield from the D-^{3}He reaction that is sensitive to the shocked ion temperature.[123] The protons are spectrally resolved by wedge-range Al filters[124] in front of CR-39 solid-state track detectors. The shock flash protons which are predicted to be emitted 600–700 ps before bangtime when the shell is at a radius of $\approx 250 \mu m$ suffer a few MeV of slowing through a total ablator areal density of between 75 and 125 mg/cm^2 while bangtime protons range out in the >200 mg/cm^2 stagnated ablator.[125] Fig. 59 shows that the maximum proton yield increases with rate of rise to peak power. The residual variability is ascribed to fields which can deflect protons away from the wedge-range detectors. A time-of-flight particle detector[126] will be used in the future to measure the separation between shock flash and bangtime, so more meaningful shock flash total capsule areal density comparisons can be made between data and simulations.
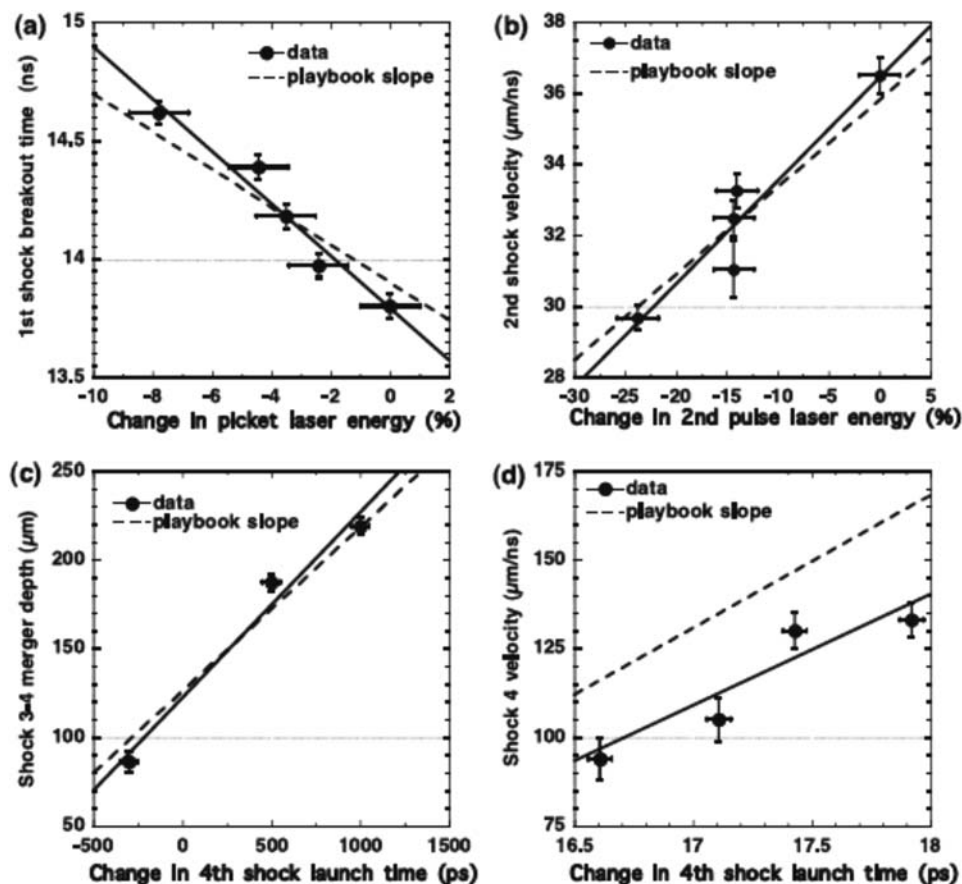

FIG. 53. Comparison of measured vs predicted shock tuning sensitivities to various adjustable laser parameters. (a) Time of 1st shock breakout into liquid D$_2$, (b) 2nd shock velocity, (c) depth of shock 3–4 merger, (d) 4th shock velocity. Solid and dashed lines are measured vs simulated slopes.
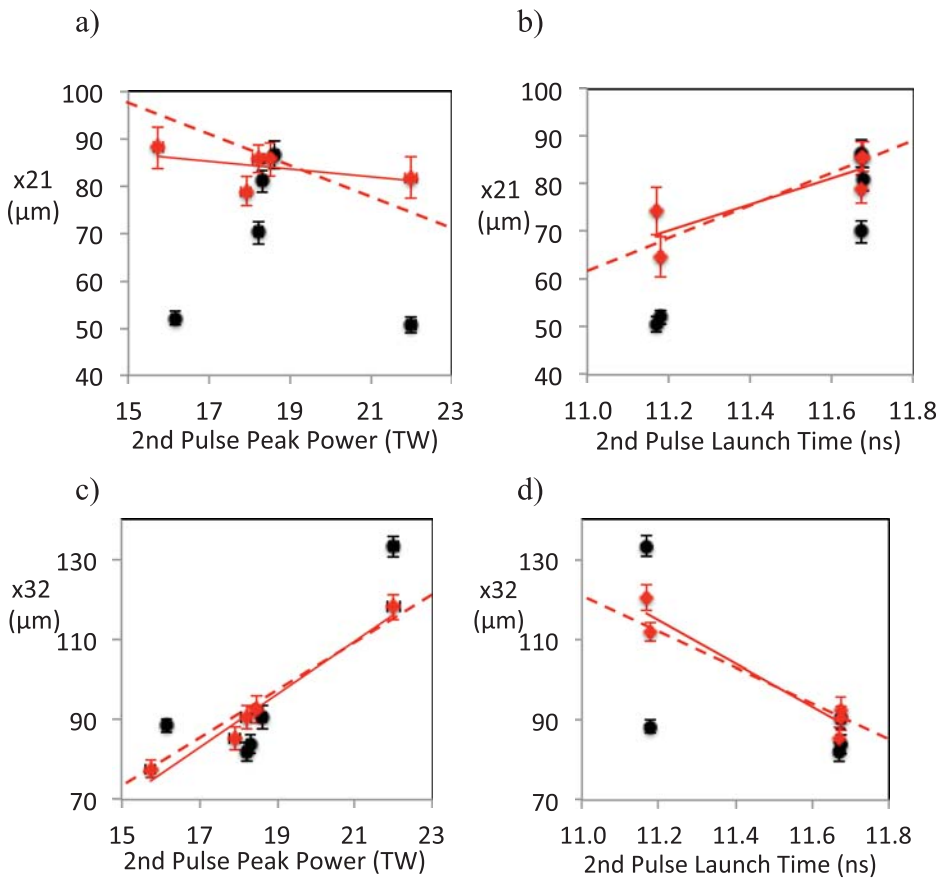
FIG. 54. Comparison of measured vs predicted shock tuning sensitivities to various adjustable laser parameters. 1st and 2nd shock merge depth vs (a) 2nd pulse peak power and (b) 2nd pulse launch time; 2nd and 3rd shock merge depth vs (c) 2nd pulse peak power and (d) 2nd pulse launch time. Black points are raw data and red points are data corrected for variations in all other laser parameters. Solid and dashed lines are measured vs simulated linear slope sensitivities.
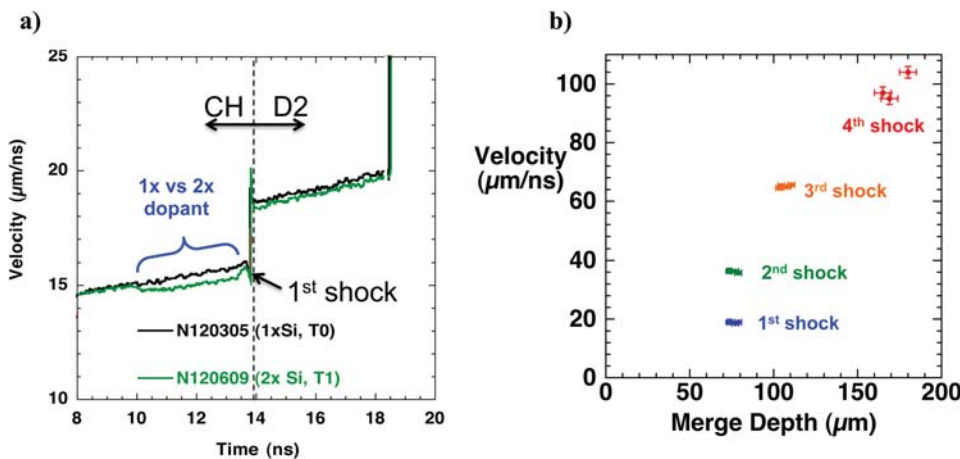

FIG. 55. (a) Measured first shock velocity in ablator and D2 comparing $1\times$ Si (black) and $2\times$ Si (green) dopant capsules driven by same laser pulse, 3 months apart. (b) Measured shock velocities and merge depths in liquid D_2 for 1st (blue), 2nd (green), 3rd (orange), and 4th shocks (red) comparing shots with 5.5 and 7.35 Å wavelength separation, corrected per playbooks for small differences in as shot capsule thickness and laser power.
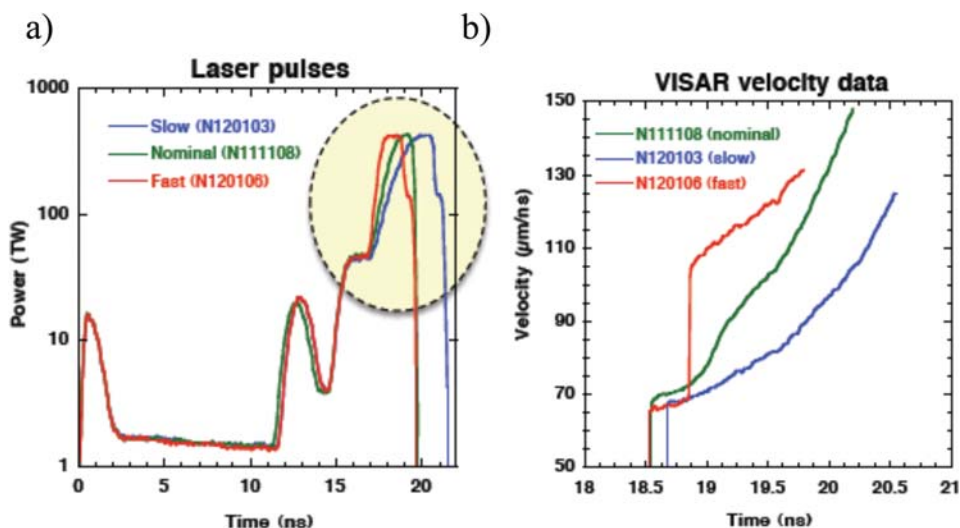

FIG. 56. (a) Comparison of three pulse power profiles used with differing slope of final rise to peak power: red (1 ns rise), green (2 ns rise), blue (3 ns rise). (b) Corresponding 3rd and 4th shock velocities measured by VISAR.
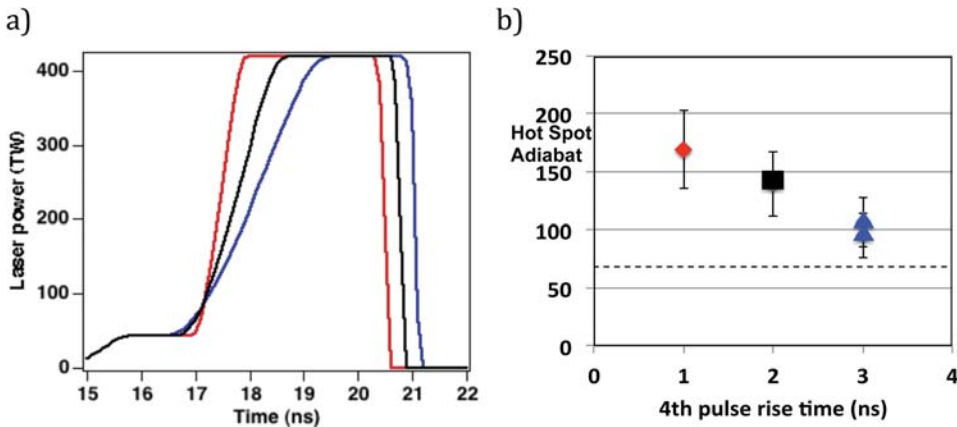
FIG. 57. (a) End of pulseshapes for 1 ns (red), 2 ns (black), and 3 ns (blue) rise to peak power. (b) Inferred hot spot adiabat vs rise time to peak power. Dashed line is ignition design requirement.

5. Implosion symmetry

Symcap targets (Fig. 60) are gas filled with an 8 mg/cc mixture of D-3He as discussed in the preceding section. They are designed for a moderate convergence ratio of 20–25. The CH ablator thickness is increased so that the shell mass is the same as that of a cryo-layered THD target. The symcaps are used to optimize radiation symmetry and also provide information on x-ray drive, LPI effects, and, indirectly, the implosion velocity from the time of peak compression. The x-ray core shape is measured by 40–90 ps gated >7 keV, 12–15$\times$ magnification, 10 μm pinhole imagers looking either through CH or high-density carbon tamped 400-600 μm-diameter diagnostic holes or through the LEH.

Fig. 61 shows the results of the P2 asymmetry inferred from the 17% x-ray contour for different wavelength separations between the 30° and outer beam cones for 1.3 MJ-class implosions. The inability to reach zero P_2 in hot spot shape in Scale 544 hohlraums with existing wavelength separations <9 Å led to a change in hohlraum geometry, specifically to 6% shorter and wider hohlraums (Scale 575). Outer spots in the Scale 575 hohlraums are closer to the waist making it possible to obtain a prolate implosion with less cross beam

transfer and a smaller wavelength separation than for a Scale 544 hohlraum. To further quantify the differential core asymmetry ΔP_{2c} due to just a change in hohlraum geometry, we can keep only the following leading partial derivatives of Eq. (33)

$$\Delta P_{2c} = -5R_C \frac{\left[P_2^i S_2^i \Delta \epsilon + \Delta P_2^o S_2^o (1-\epsilon) - \Delta B P_2^{LEH} S_2^{LEH} \frac{A_{LEH}}{A_{wall}} F \right]}{(F+1)},$$

(40)

where for a hohlraum radius R and length L: $\Delta \epsilon / \epsilon \approx -2\Delta R/R$, ΔP_2 for the outer cone spots subtending $\approx$45° to the hohlraum axis $\approx 3/2 \Delta \theta$ and $\Delta B/B = -2\Delta L/L$. R_C is the distance travelled by the shell after start of peak power, ≈ 800 μm. $\Delta R/R$ and $\Delta L/L = +6\%$ and -6% and $\Delta \theta \approx \sqrt{(\Delta R^2 + (\Delta L/2)^2)}/(R/\sin 45°) \approx 0.1$ going from Scale 544 to Scale 575 hohlraum. Per Eq. (34), F = 3 since $(1 - \alpha_{wall}) = 0.45/T_r^{0.7} t^{0.4} = 0.18$ for T_r reaching 300 eV (3 heV)[20,113] during the 3 ns-long peak and the ratio of LEH + capsule to wall area = 0.10. Including an inward wall motion based on spot imaging[127] of 400 μm which principally increases P_2^o to $\approx$0.3, while P_2^i and P_2^{LEH} remain at ≈ -0.45 and $\approx$0.95, we calculate from Eq (33) a weighted peak power inner cone fraction $\epsilon \approx 0.3$ at the relevant $P_2 = 0$ regime. Plugging in all these values, we expect the difference ΔP_{2c} in core asymmetry between the two hohlraum
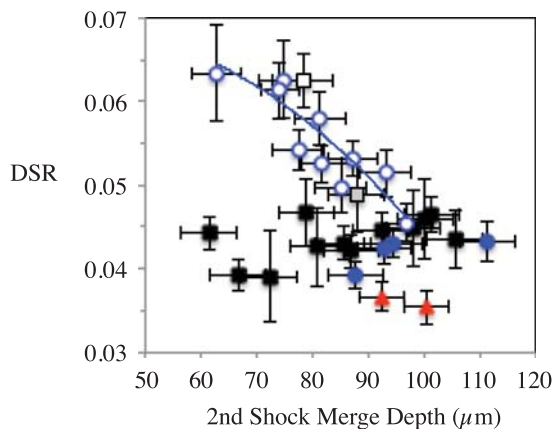

FIG. 58. Measured DSR versus inferred merge depth of first 2 shocks relative to ablator/DT ice interface based on VISAR results corrected for small differences in drive and capsule. Red triangles, black squares, and blue circles correspond to 1, 2, and 3-ns-class rise to peak power. Closed and open symbols are nominal and extended pulse cases. Blue curve is fit to extended pulse data.
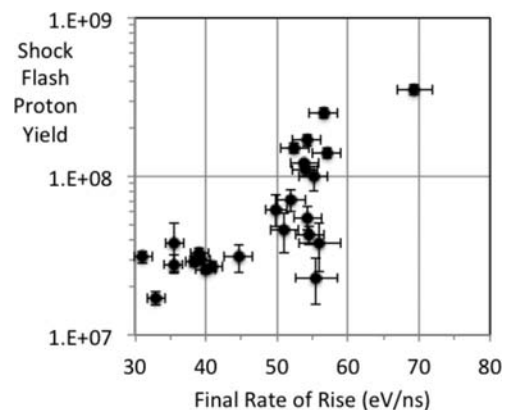

FIG. 59. Measured shock flash D-³He proton yield vs rate of radiation temperature rise to peak power as measured by Dante, for implosions driven by Scale 575 hohlraums with 3.1 mm LEH.
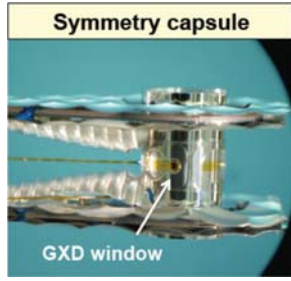
FIG. 60. Picture of a symcap target with a $400\,\mu m$ diameter CH-filled diagnostic window on the hohlraum midplane.

FIG. 62. Measured $>8\,keV$ x-ray core at peak emission for (a) Au and (b) Au-lined U hohlraum driven at same effective peak Tr.

geometries at a given wavelength setting to be $+30\,\mu m$, close to what is measured in Fig. 61. The close match also suggests crossbeam transfer was only weakly dependent on the differences in hohlraum geometry. Up until recently, to match the P_2 dependency on wavelength separation required applying an arbitrary saturation level for ion acoustic wave driven density modulations responsible for the crossbeam transfer at peak power.[128] Recent calculations have shown that ion heating[129] as a result of the many driven ion acoustic waves can detune the 3-wave resonance and may provide a natural saturation mechanism for running future simulations self-consistently.

In addition, we have compared the P_2 core symmetry of Au vs Au-lined U hohlraum implosions. Fig. 62 compares the resultant $>8\,keV$ core images at peak emission for a Au vs a Au-lined U hohlraums driven at 370 and 345 TW peak power, respectively, to reach similar peak Tr (within 0.5%) and bangtime (within 30 ps). We would expect the higher *albedo*[130] of Au-lined U hohlraums to preferentially drive the capsule equator leading to a more prolate ($+P_2$) implosion as seen; a fit to the 17% contour level gives a P_2 of -1.3 ± 0.5 and $+1.6 \pm 0.5\,\mu m$ for the Au and Au-lined U shots, respectively. For a more quantitative expectation, we start with the power balance equation

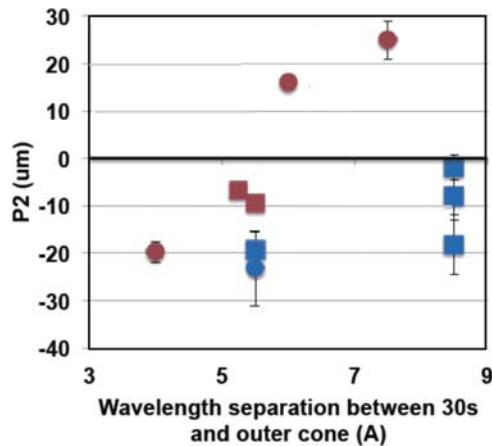$$f\eta P_L = \sigma T_r^4 [A_W(1 - a_{wall}) + A_H + A_C],\quad (41)$$

FIG. 61. Measured x-ray core P2 asymmetry at peak emission versus laser wavelength differential between inner and outer cones at 1ω for symcaps (circles) and cryogenically layered implosions (squares) in 5.75 mm (red) and 5.44 mm (blue) diameter hohlraums.
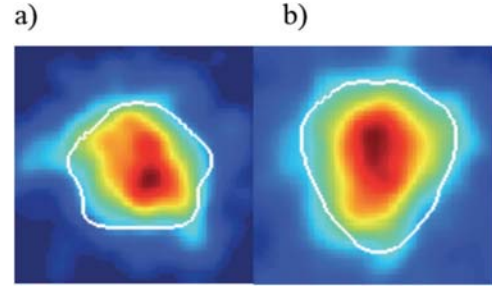
where A_W, A_H, and A_C are the hohlraum wall, LEH and average in-flight capsule areas, and P_L is the peak power. f is the fractional power absorbed measured to be the same within $\pm 1\%$ error bars. η is the x-ray conversion efficiency that we can assume will be the same for both hohlraums, since the laser only interacts with the Au liner. Hence, since all terms but P_L and α are the same for the two hohlraum cases, we can differentiate Eq. (41) as follows and rewrite in terms of the recirculating flux F factor of Eq (34):

$$\frac{dP_L}{P_L} = \frac{-d\alpha_{wall}}{(1 - \alpha_{wall}) + (A_H + A_C)/A_W} = -\frac{dF}{(F+1)}.\quad (42)$$

We first get an estimate of the zeroth order drive differences between Au and U by substituting for the applied power differential $\delta P_L/P_L = -0.07$ in Eq. (42), yielding $\delta\alpha = 0.02$, and for $F = 3$, $dF = 0.3$.

To estimate P_2 differences, we differentiate Eq (33) with respect to F

$$dP_{2c} = 5R_C \frac{\left[P_2^i S_2^i \epsilon + P_2^o S_2^o (1 - \epsilon) + BP_2^{LEH} S_2^{LEH} \frac{A_{LEH}}{A_{wall}}\right]}{(F+1)^2} dF .$$

$$(43)$$

Recognizing that near the relevant case $P_2 = 0$, $P_2^i S_2^i \epsilon + P_2^o S_2^o (1 - \epsilon) \approx BP_2^{LEH} S_2^{LEH} \frac{A_{LEH}}{A_{wall}} F$, Eq. (43) can be rewritten as

$$dP_2 = 5R_C \frac{\left[BP_2^{LEH} S_2^{LEH} \frac{A_{LEH}}{A_{wall}}\right]}{(F+1)} dF$$

$$= -5R_C \left[BP_2^{LEH} S_2^{LEH} \frac{A_{LEH}}{A_{wall}}\right] \frac{dP_L}{P_L} .\quad (44)$$

Substituting for all parameters, $R_C = 800\,\mu m$, $B = 0.74$, $P_2^{LEH} = 0.95$, $S_2^{LEH} = 0.44$, $A_{LEH}/A_{wall} = 0.05$, and $\Delta P_l/P_L = -0.07$: $dP_2 = +4\,\mu m$, close to the measured $+3\,\mu m$. Fig. 61 shows that such an offset in P_2 asymmetry should be recovered when switching to U hohlraums by only a 0.4 Å increase in cone wavelength separation.

In the same way that the wavelength shift $d\lambda_2$ between the inner and outer beams can be adjusted to control the axial P_2 symmetry, the wavelength separation $d\lambda_3$ between the 23° and 30° beams can be adjusted to control the azimuthal asymmetry. Specifically, the m_4 mode in radiation asymmetry arises
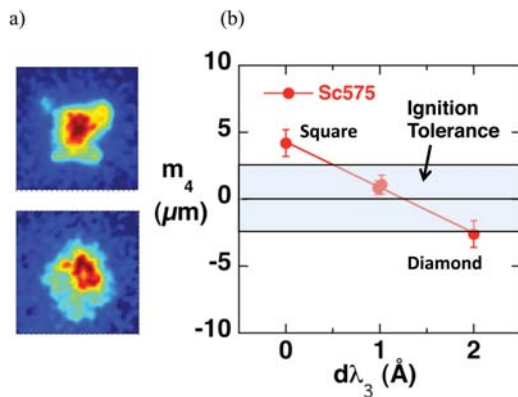
FIG. 63. (a) 8 keV x-ray core images from cryogenic DT implosions from pole view for 0, 1, and 2 Å wavelength shift at 1ω between 23.5° and 30° beams. (b) Measured m_4 amplitude at 17% contour of core images vs wavelength separation. Positive m_4 means corners of image facing 30° beam locations. Solid line is linear fit to data. Also shown is $\pm 2.5\,\mu m$ ignition-tolerable m_4 region.

because the 23° and 30° beams propagate differently. The wavelength separation between the 23° and 30° beams has been adjusted[131] to minimize m_4 in DT cryogenic implosion hot spot core shapes. Fig. 63 shows that for the scale 575 hohlraum, a 1 Å $d\lambda_3$ between the 23° and 30° beams minimizes m_4. The sign of the m_4 slope is as predicted, with the corners of the hot spot facing the beams driven harder. Fig. 64 shows the level of reproducibility between symcap x-ray core images observed from the pole that have minimized m_4. We note evidence of shadowing by the $10\,\mu m$ diameter filltube breaking the symmetry.

Following the success of the keyhole shock timing platform discussed earlier, a dual axis Visar keyhole target (Fig. 65(a)) was fielded to provide shock timing information at the capsule pole as well as the capsule waist (Fig. 65(b)) as a measure of time-dependent P_2 asymmetry during shock propagation. This was accomplished by inserting a small mirror inside the reentrant cone to redirect a fraction of the VISAR laser beam to one pole. This enabled tuning the P_2 symmetry of the first 4 shocks as well as their average velocity and timing. Fig. 66 shows that the mirrored keyhole target was utilized to check, fix and meet the ± 200 ps synchronicity requirement between the pole vs waist shock timing by decreasing the laser cone fraction in the epoch responsible for the 2nd shock by about 0.1. The difference between calculated and measured optimum cone fraction is attributed to residual uncertainty in the Au emissivity model as the hohlraum is reheated by the 2nd pulse. Figs. 67(a) and 67(b) show that the P_2 swings in implosion core symmetry were reduced by $3\times$ after optimization of the 2nd cone fraction. Figs. 67(c) and 67(d) plot the rate of change of P2 vs P2 at peak emission before and after 2nd cone fraction optimization. As expected, reducing time dependent P2 swings is required to ensure both dP2/dt and P2 approach zero simultaneously at peak emission. Three axis keyhole targets have now been developed to look for both P_4 and m_4 asymmetries. The challenge for the former is increasing the time over which mirror reflectivity remains high as unlike the current mirror seeing out the LEH, the mirror viewing at 45° will experience more hard x-ray loading from seeing the outer laser spots. This will dictate using Be mirrors in the future possessing lower x-ray absorptivity.

Based on the time-integrated and time-resolved symmetry tuning, the hot spot has been optimized to meet the ignition specification in both symcaps and cryo-layered implosions. However, cryo-layered implosions are about $5\,\mu m$ more oblate than symcaps as shown in Fig. 68. In the best performing cryo-layered implosions, Fig. 69 shows that the hot spot symmetry can meet the $<10\%$ rms out-of-round specifications for low-mode ($n < 7$) asymmetry. As discussed in a later section, this is a necessary but not sufficient requirement; we also need to ensure a suitably round in-flight shell and stagnated fuel assembly.
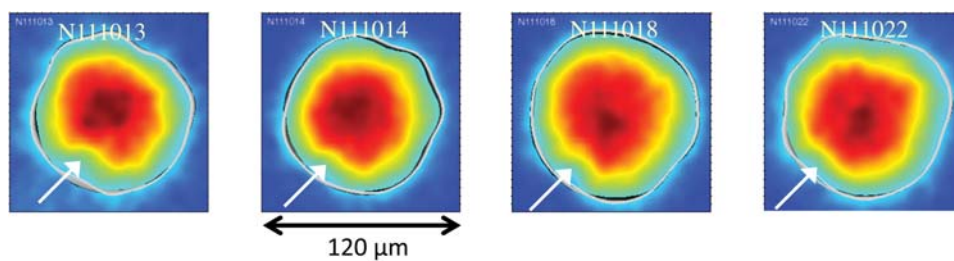

FIG. 64. Measured core x-ray emission from polar view for 4 symcap shots with original azimuthal location of filltube shown by arrows.
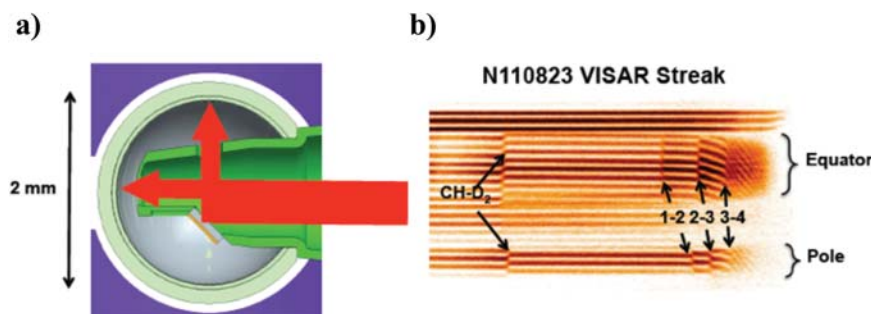

FIG. 65. (a) Schematic of dual axis VISAR geometry at capsule. (b) Example VISAR streak showing shock overtakes at fringe jumps for both equator and pole.
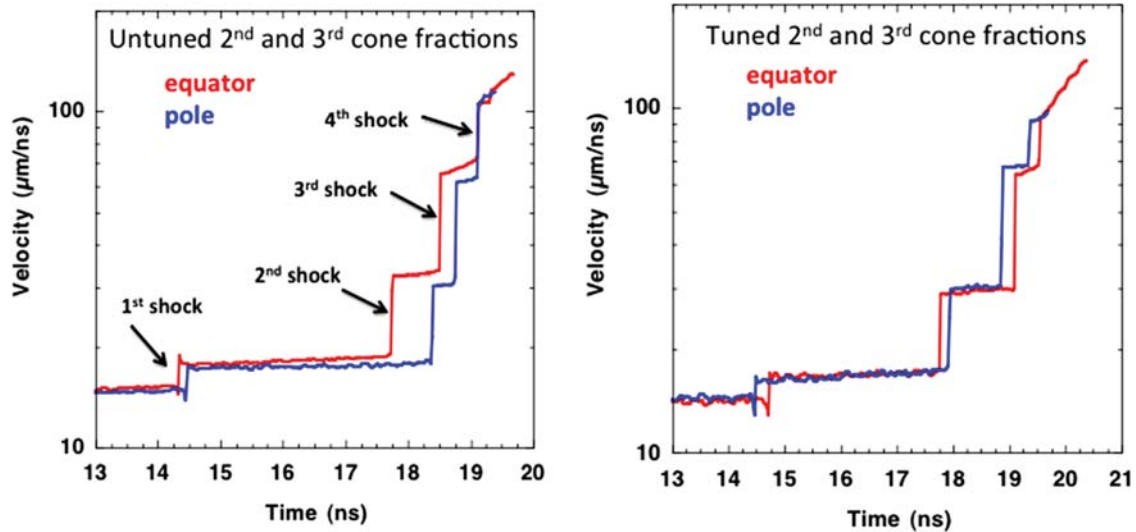
FIG. 66. Leading shock velocities measured at pole (blue) and equator (red) for (a) before and (b) after decreasing 2nd pulse inner cone fraction.
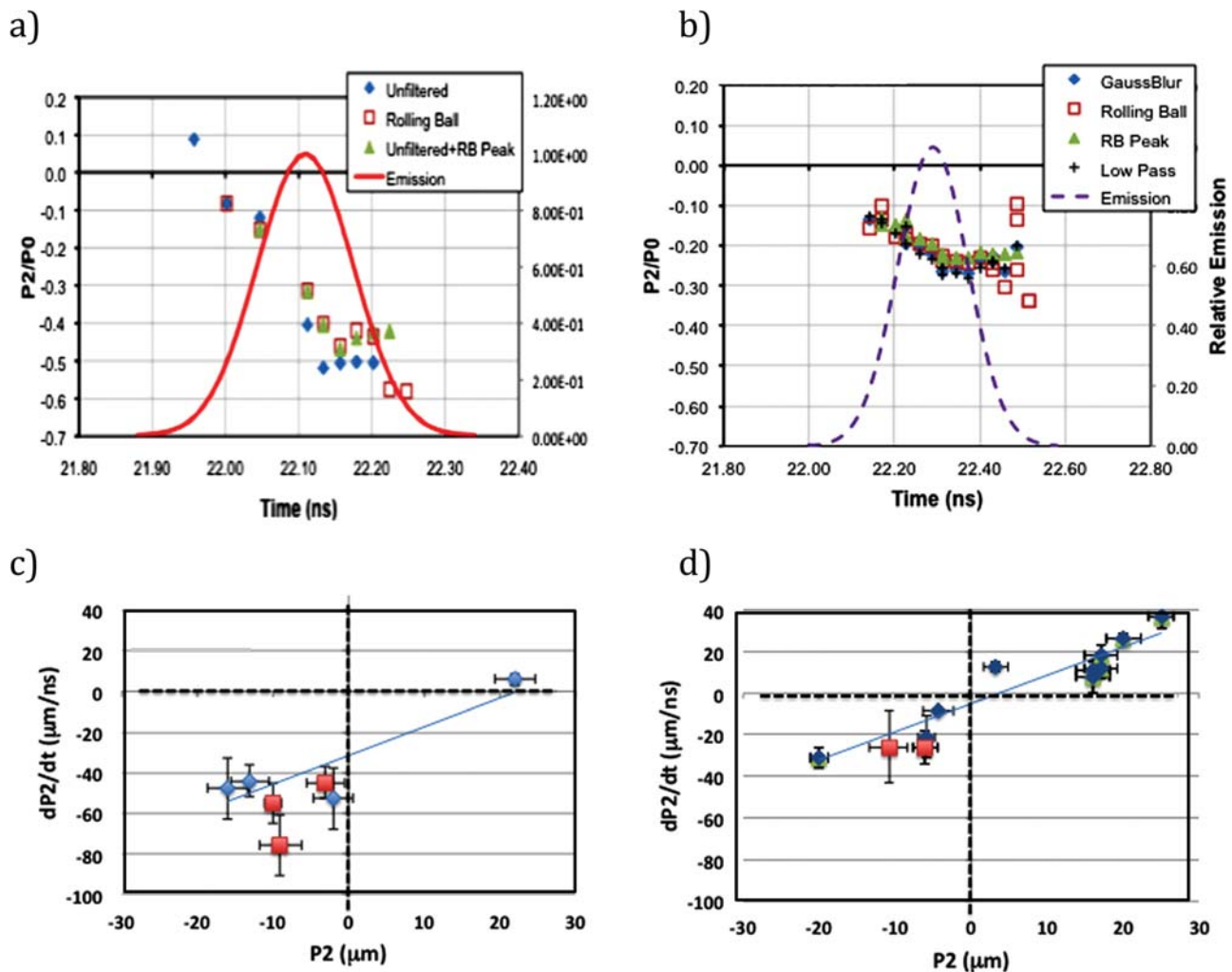

FIG. 67. Symcap x-ray core P2 asymmetry (points) and brightness (curve) vs time (a) before and (b) after tuning 2nd pulse inner cone fraction. Rate of change of P2 vs P2 at peak emission time for symcaps (blue) and cryogenic implosion cores (red) (c) before and (d) after tuning 2nd pulse inner cone fraction.
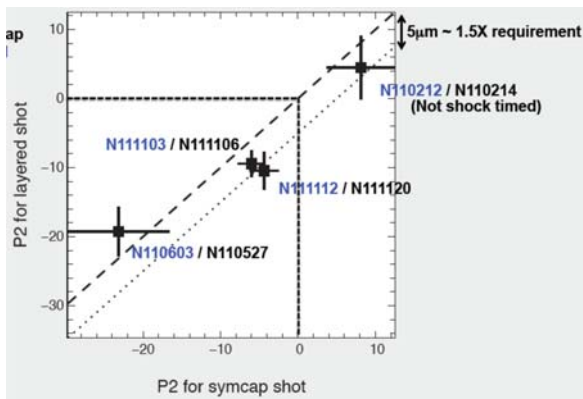
FIG. 68. Cryogenically layered vs symcap core P2 asymmetry in μm. Dashed line is identical asymmetry and dotted line is $-5\ \mu$m offset for cryogenic implosion.

6. Implosion velocity and mass remaining

Fig. 70 shows a picture of the target used to measure the trajectory, velocity, mass remaining, and thickness of the imploding ablator.[132] We use x-ray area backlighting by redirecting two of the 50° drive quads to a thin (5–15 μm) mid-Z foil driven at peak power (8–9 TW/quad) and focused by the drive continuous phase plates (CPPs) to 1-3 × 10^{15} W/cm^2. This creates He-like 2-1 resonance lines that cast a shadow of the capsule limb in-flight with up to 2 optical depths of contrast that we image with 10–25 μm-wide slits or pinholes at 9–12× magnification. To accommodate 20% increases in target scale, 2× increases in capsule dopant levels and up to 30% increases in capsule thickness since the first shot in 2009, we have transitioned from using 8 keV He-like Cu to 9 keV Zn to 10.2 keV Ge as backlighter. X-ray conversion efficiencies of 2%–0.5% are obtained by using a prepulse.[133]

Fig. 71(a) shows sample 1D gated data (90 ps resolution). The delayed trajectory of the capsule limb shown in Fig. 71(b) confirmed the late bangtimes relative to baseline simulations. The radius versus time for this Si doped capsules is best matched by driving the implosion with a peak radiation flux reduced to 85% of that calculated by the High Flux Model. As indicated in Fig. 37, the High Flux Model overestimates the measured drive by 9%–10%. The
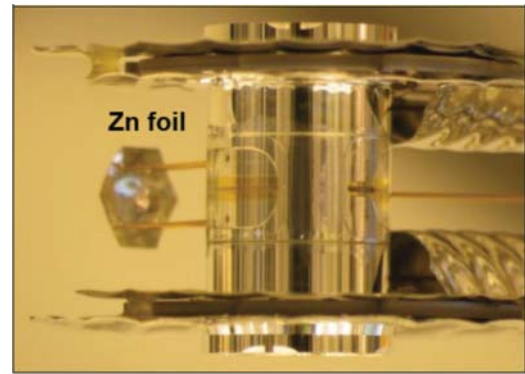

FIG. 70. The ConA hohlraum with a Zn backlighter foil suspended at the midplane at 3 mm from the hohlraum wall.

additional difference between the drive which best matches the trajectory and the measured drive could be due to a variety of effects including the impact of non Local-Thermodynamic-Equilibrium (NLTE) atomic physics in the ablator and view factor effects at the capsule.

ConA experiments prior to March 2012 used a framing camera that provided a sequence of snapshots of the capsule radius and optical depth versus time as shown in Fig. 71(a). Since March 2012, a streak camera provides a continuous record of radius and shell optical depth τ versus time, an example of which is shown in Fig. 72. In addition to the limb shadow, one sees the core stagnation emission and the explosion phase when the radiative outgoing shock reaches the outer ablation front.[134] The streak camera allows for improving temporal resolution from 90 ps to below 30 ps, hence reducing motional blurring from 25 μm to below 10 μm for more accurate late time shell density profile measurements. Several improvements have been made to the x-ray streak camera system for use on MJ-class hohlraums. First, the quantum efficiency of the streak camera photocathode to 8–10 keV photons has been improved by 10× by switching from Au to thicker (0.2 μm) CsI photocathodes matched[135] to the primary 4–6 keV electron range. Second, the streak camera has been equipped with a 4ω comb for in-situ record of the local sweep linearity and absolute timing.[136] Third,
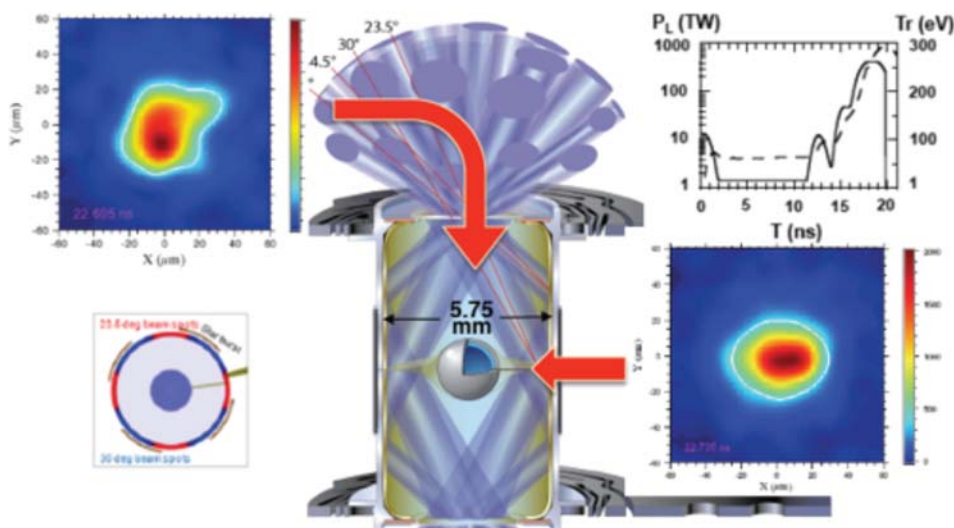

FIG. 69. Cryogenically layered implosion shots record >7 keV x-ray core images at peak emission time at the pole and equator. Inset shows typical laser power and Tr profile. Inset below the x-ray emission from the pole shows the location of the fill tube as seen from above.
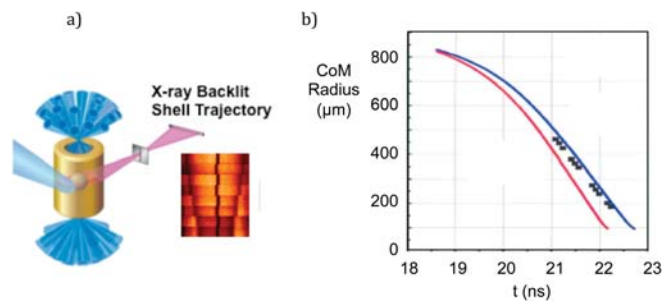
FIG. 71. (a) Schematic of x-ray radiography experimental configuration with sample gated 1D data rearranged in chronological order. (b) Measured (dots) center-of-mass of ablator versus time, baseline simulation (red curve), and simulation (blue curve) with 15% reduction in drive during the peak of the pulse.

the front end of the snout containing the imaging slit has been equipped with a 1 cm-thick Ta collimator to reduce hard x-ray background at the detector. Fourth, the residual image warp is fully characterized off-line and on-line by using backlit fiducial wires.[137]

The key implosion metric is the rocket-driven compressional pressure $P \sim \rho v^2$ at deceleration imparted to the hotspot, where ρ and v are the in-flight shell/fuel density and peak velocity. Since the ignition threshold factor (ITF) that provides a quantitative estimate for the probability of ignition is $\sim v^8$, increasing the ablation-driven rocket efficiency is important to provide margin on laser power. Specifically, since the ablation pressure[138] $P_a \sim (1-\alpha_a)T_r^4/v_{ex} \sim (1-\alpha_a)T_r^{3.5}$, reducing the ablator *albedo* α_a for fixed drive T_r is desirable. Fig. 73(a) shows that the measured terminal center-of-mass (CoM) shell velocity measured by time-resolved x-ray radiography is 15% more for Si vs Ge-doped plastic capsules driven at the same peak power. Fig. 73(b) shows that the Si K-shell absorption edge at ≈ 2 keV provides the same hard x-ray radiation preheat shielding of the inner ablator as Ge, but leads to a reduced absorption of the thermal 300 eV hohlraum spectrum between the 1.3 keV Ge L-edge and 2 keV, hence to a reduced capsule reemission or *albedo*, and a higher implosion velocity.

The x-ray radiography of symcaps was also used to confirm the trade-off between implosion velocity v and ablator mass remaining m. Mass remaining is extracted from
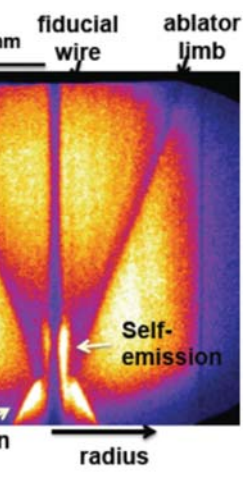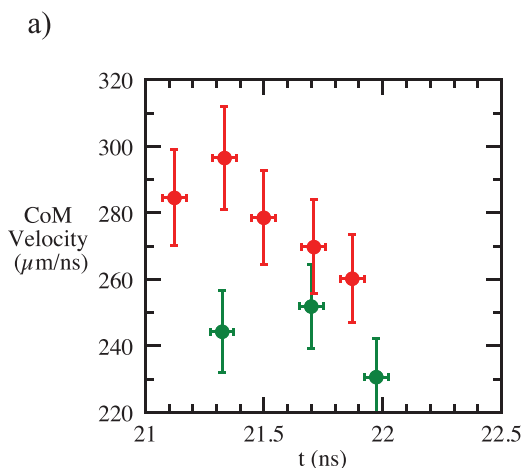

FIG. 72. Example of a 9 keV streaked radiograph of an imploding CHSi capsule with 15 μm, 40 ps resolution.

forward Abel inversions self-consistently accounting for plausible center-peaked backlighter profiles.[139] Examples of measured vs simulated transmission lineouts are shown in Fig. 74, showing the expected appearance of residual opacity from ablated Si K shell electrons when the capsule has reached <700 μm radius.

1D hydrodynamic simulations of the multishocked convergent ablators show that the capsule dynamics can be quite accurately modelled,[140,141] by the rocket equation, $v = v_{ex}\ln(m_0/m)$, where m/m_0 is the ablator mass remaining and v_{ex} is the ablator exhaust velocity $\approx \sqrt{ZkT_r/m_i} \approx 7\sqrt{T_r(eV)}$ μm/ns for fully ionized CH. Fig. 75 shows that the velocities follow the simple rocket equation with a best fit (ignoring $<4\%$ differences in peak Tr) $v_{ex} = 148$ μm/ns, comparable to the approximate value of 120 μm/ns derived for Tr $= 300$ eV. In Fig. 76, some of the data points of the previous figure are compared to simulations adjusted to match the keyhole shock timing data and the implosion radius versus time from the x-ray radiography data. The data and simulations match to within 0.5%–1% in mass remaining, within error bars, suggesting we have a good understanding of the rocket efficiency of these CH(Si) ablators.

Calculations of the convergent ablator experiments are then used to assess the velocity and mass remaining in the

FIG. 73. (a) Measured CoM terminal shell velocities for 430 TW peak power CH(Ge) (green dots) and CH(Si) (red dots) implosions. (b) Cold opacity of CH(Ge) vs CH(Si) compared to 300 eV Planckian and region of hard x-ray preheat (light red box) requiring shielding by dopant.
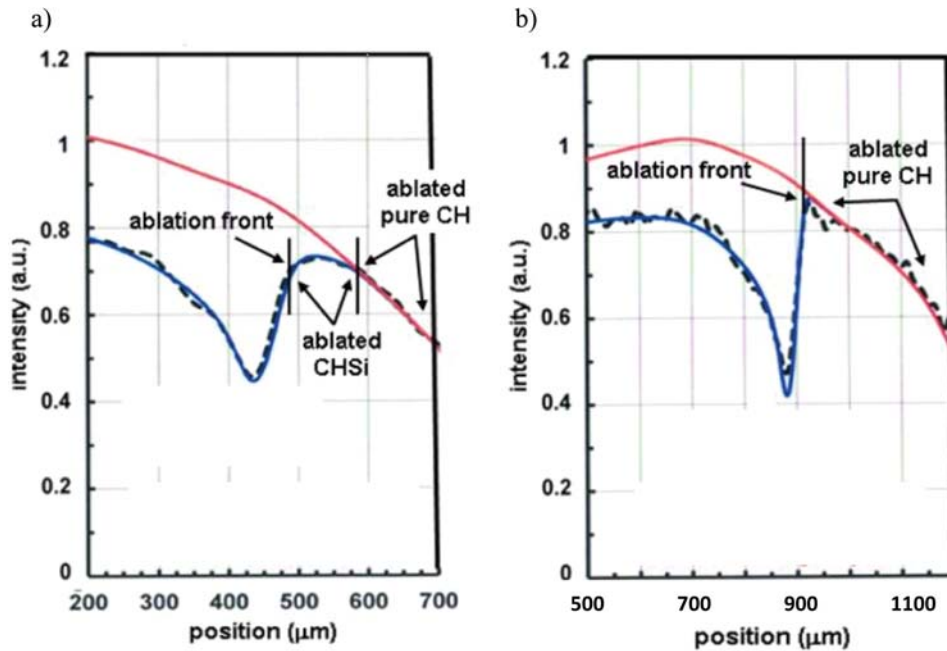
FIG. 74. Measured (black dashed) and simulated (blue solid) transmission lineouts vs radial position for capsule at (a) 470 μm when ablating into Si-doped CH and (b) 900 μm radius when still just ablating pure CH. Also shown in red is the assumed backlighter profile for best fits.

cryo-layered implosions. Fig. 77 plots the DT fuel velocities, corrected per simulation on average 12% upward from the measured CoM ablator velocities as the fuel on the inside is being propelled inward faster due to convergence, and the hotspot back pressure is less than for symcaps. The remaining ablator mass fraction has also been corrected for the fact that 0.17 mg of the initial ablator (typically 6% of the 3 mg total shell mass) is DT fuel. On average the calculated mass remaining is a bit greater than inferred, 0.01 of the initial mass, again within systematic uncertainties.

Based on the observation of more ablator decompression than expected after turn off of the laser pulse (and hence a greater, undesirable drop in shell density before deceleration), starting in March 2012 we also extended the laser peak power phase until the capsule had reached a radius of 300 μm, just before onset of deceleration, as shown in Fig. 78. Fig. 79 shows that implosions with extended "no-Coast" pulses have faster terminal CoM velocity as might be expected when keeping pressure on the ablator. Specifically, with a 0.6 ns pulse extension to keep the full drive on until a radius of 300 μm is reached, the peak implosion velocity is

increased by $12 \pm 5\%$, in agreement with simulations. It should be noted that the bangtime differential would be a poor metric of final velocity in this case; it is only 120 ps since the extra 12% burst in velocity is only applied over the last 1 ns of travel. Fig. 80 shows that implosions with extended pulses have thinner shells at peak velocity than shells which coast longer after the laser turns off. Specifically, Fig. 80 shows that an extension of 0.5 ns with all else held fixed reduced the shell thickness by 30%. "No-coast" pulses clearly result in faster, thinner, and denser imploding shells.

7. Ablator symmetry

2D x-ray radiography of the inflight ablator of a symcap was recently demonstrated using 30 μm, 80 ps resolution, 10 keV radiography at 8$\times$ magnification. For this purpose,
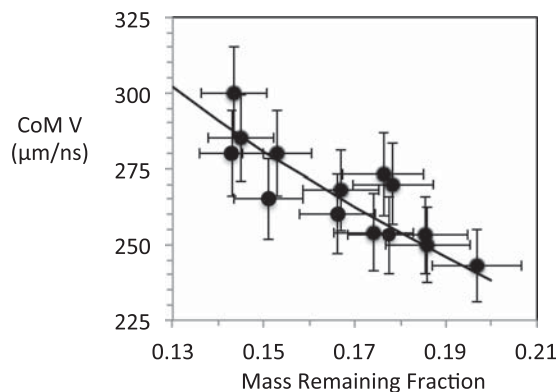

FIG. 75. Measured center-of mass velocity of symcap versus measured ablator mass remaining at a radius of 300 μm, just before deceleration.
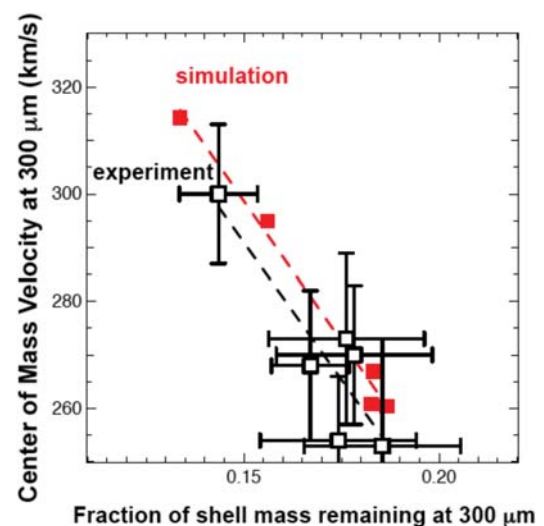

FIG. 76. Center-of-mass ablator velocity vs fraction of ablator remaining at 300 μm radius from convergent ablator data (open squares) and simulations (red closed squares).
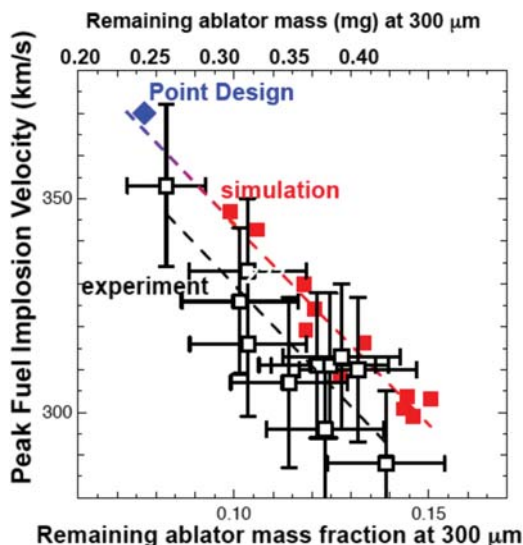
FIG. 77. Center-of-mass fuel velocity vs fraction of ablator remaining at 300 μm radius of cryogenically layered implosions (open squares) as inferred from ConA data and simulation predictions (red closed squares). Blue point is point design.

the diagnostic patches were $800 \times 800\,\mu$m. Figs, 81(a) and 81(b) show raw data 700 to 200 ps before bangtime and two single frames 350 ps apart. Unlike the 1D radiography which can be biased by polar asymmetries due to finite shell sampling, and is subject to curvature blurring and biases from any P_1 offsets between data and the viewing slot at late times when the shell is at small radii ($<300\,\mu$m), 2D data allow us to extract the profile, trajectory, shape, mass remaining, and uniformity of the ablator even after deceleration. At the latest times, the onset of core self-emission is also observed, which allows a direct comparison of any P_1 offset between shell and core.

We first consider the 1D behaviour for comparison to the earlier 1D radiography. In Fig. 82(a), the CoM and shell/gas interface P_0 time histories (extracted from the maximum slope and minimum transmission contours, respectively) show a peak CoM and interface velocity of 260 and 315 μm/ns. The faster interface velocity is attributed to convergence effects (the same reason the DT fuel velocity is expected to be faster than the CoM ablator velocity) and
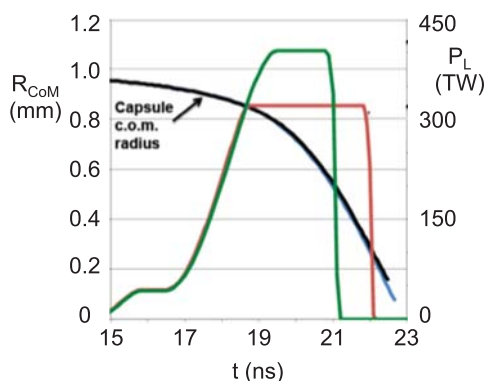

FIG. 78. End of laser pulses for nominal "coast" (green) and extended pulse "no coast" (red) implosions. Calculated center-of-mass shell radii vs time for nominal "coast" (black) and extended pulse "no coast" (blue) implosions.
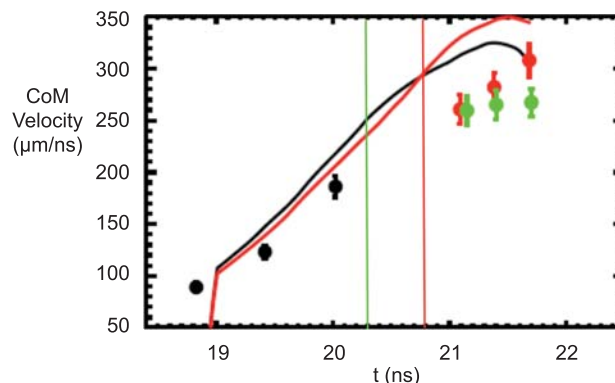

FIG. 79. Measured (dots) and simulated (curves from nominal HFM hohl-raums without the 15% drive reduction). CoM terminal shell velocities for 430 TW peak power CH(Si) implosions driven by nominal length (black and green) versus extended length pulse (red). Vertical lines show end of drive pulse. Bangtime is at 22.8 ns.

shell thickening. The mass remaining, which can now be extracted by simply area integrating the areal density (a function of transmission T and opacity κ, $= -\ln(T)/\kappa$ at each point in the image, was $0.15 \pm .015$, which when combined with the $260\,\mu$m/ns CoM velocity is consistent with the 1D Rocket Model results shown in Fig. 75. The average shell width is $\approx 30\%$ thicker than nominal calculations with the HFM, also consistent with the 1D radiography thickness results for a nominally identical shot as shown in Fig. 82(b). The combination of as expected mass remaining but thicker shell led to lower than expected peak optical depth (1 vs. 2). In the future, when we expect more compressed shells by using no-coast pulses, we would switch to a harder x-ray backlighter to maintain reasonable shell optical depth (<1.5).

Regarding 2D behavior, Fig. 83(a) shows an example Legendre moment fit to both the CoM and minimum transmission contour (the latter corresponding closely to the shell/gas interface) of a frame 300 ps before bangtime, showing a large $30 \pm 3\,\mu$m P_4 ($P_4/P_0 = 25\%$). Such a P_4 would be expected to reduce DT implosion yield by at least $2\times$, dependent on when the P_4 asymmetry is seeded. The early time history of the P_4 asymmetry will be the subject of measurements using a 3-axis keyhole. By contrast, the self-emission
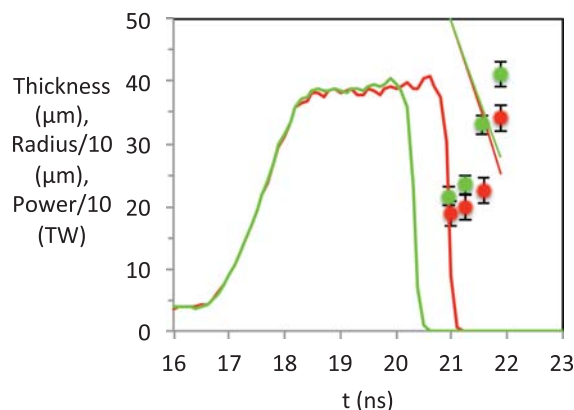

FIG. 80. Measured shell thickness (dots), shell radii and peak power laser profile for shortened (green), and nominal length main pulse (red).
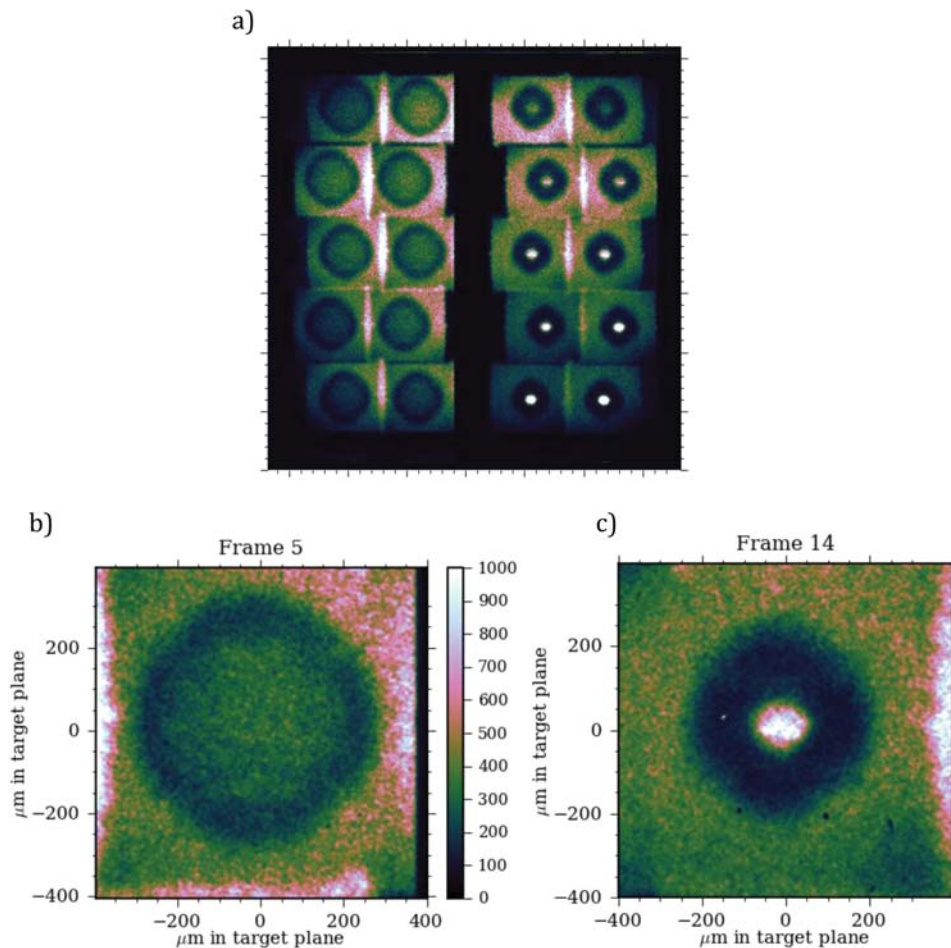
FIG. 81. (a) 2D 10 keV radiographs over a 500 ps window at peak velocity of a 223 μm-thick symcap imploded with a 1.4 MJ, 400 TW peak power pulse, 2 ns rise time. Single frames at (b) 23.67 and (c) 24.02 ns.

image exhibits only a $-1\,\mu$m P_4, consistent with simulations that show that large P_4 shell asymmetries are not expected to be transferred to center-peaked self-emission images.[142] In Fig. 83(b), the extracted interface P_4 time history shows strong P_4 growth followed by a sharp drop. Since the shell is coasting until the very last frames (i.e., at constant velocity), we cannot attribute this to classical Rayleigh-Taylor (RT) growth. One can however compare this P_4 amplitude mode growth to that expected from convergence effects in partially incompressible systems.[143–145] From the 60% shell thickening in the time observed in Fig. 82(b), we expect the P_4 amplitude to also grow by at least 60% (from 13 to 21 μm), explaining half the growth; the rest could be ballistic from velocity gradients set-up earlier. The drop in P_4 at the latest times is attributed to the arrival of the rebounding spherical shock first decelerating the parts of the shell around 45° that are closest to the center.

There is also evidence of 25% reductions in shell ρr at about 40° and 140° attributed to ablation front growth during acceleration of a ring perturbation seeded at the support tent–capsule lift-off positions. Besides biasing P_4 shape inferences both in-flight and from the hotspot, these ρr variations might lead to penetration of ablator deep into hot spot, or mix, as discussed in Sec. V B 8. Clearly, these 2D x-ray radiographs are providing a wealth of information, and for late time trajectories, will replace or check the 1D streaked x-ray radiography results that can be biased by low and mid mode asymmetries and areal density nonuniformities.

8. Mix and cold fuel asymmetry

Mix of the ablator into the fuel can result from instabilities at the ablation front and at the fuel-ablator interface. Mix becomes more of an issue as the implosion is optimized to produce higher convergence and higher compression. Mix signatures include a reduced yield and ion temperature due to radiative cooling and higher and structured x-ray brightness[146] from the hot core due to the higher Z ablator mixing into the compressed fuel. Special targets with tracer mid-Z dopants use spectroscopic signatures to measure mix.[147] Fig. 84(a) shows that the inferred CH(Ge) mix into the hotspot inferred from cryo-layered core spectra such as shown in Fig. 84(b) compared well with simulations for early implosions with non-extended pulses, and were below the ignition level threshold of 75 ng. These capsules had Ge doped ablators and were shot before the change to Si dopant in July 2011. However, these spectroscopic measurements do not pick up pure CH mix from undoped regions of the shell and should be viewed as a lower limit mix estimate. The mix mass is now routinely inferred[148] from the excess of bremsstrahlung and free-bound emission $\sim Z^2$ and $\sim Z^4$ from the compressed hotspot relative to that expected for emission from clean DT. This requires correcting for shell reabsorption from the mass remaining and core size and accounting for the electron temperature from Ross pair filter measurements of the core emission.[149] Figure 85 plots the DT yield vs inferred CH hot spot mix mass, showing the expected
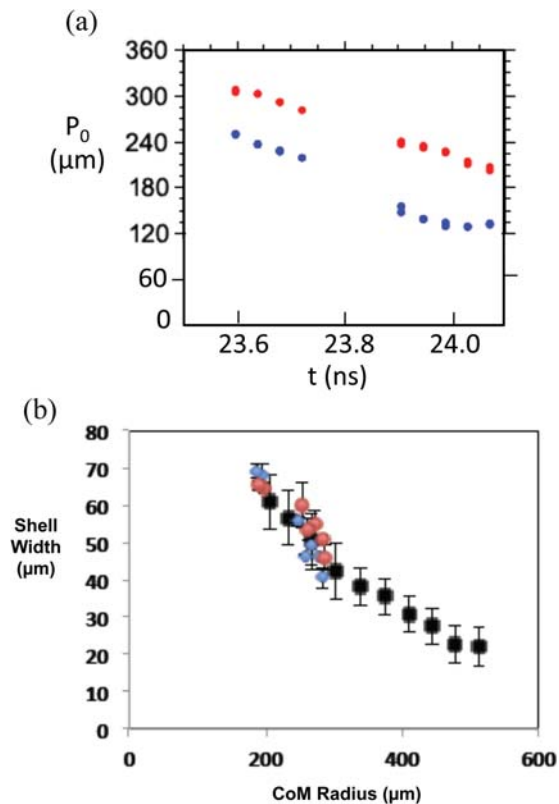
FIG. 82. (a) Center-of-mass (red points) and shell/gas interface (blue points) trajectory. (b) Inferred deconvolved width of shell vs CoM radius for a streaked 1D radiograph (black squares), gated 2D radiograph analyzed as if were 1D radiograph along equator (blue diamonds), and averaged over full 2D coverage (red circles) for nominally identical shots (N120418 and N121004).

FIG. 83. (a) Radii of Center-of-mass (blue points) and shell/gas interface (red points) vs polar angle with low mode Legendre fits for frame at 23.95 ns. 0° is top of image. (b) P4 vs P0 at shell/gas interface.

reduction in yield with increasing mix mass, attributed to radiative cooling from the higher Z mix species.

The effect of mix can also be seen in Fig. 86 where the neutron yield is plotted versus the inferred ablator mass remaining at peak velocity for the highest areal density implosions. The remaining mass is a first measure of the amount of material that instabilities at the ablation front must penetrate to mix ablator into the hot fuel. Target yields are significantly reduced for implosions with less than 0.35–0.4 mg of remaining mass. This is about 12% of the initial ablator mass. The red dashed line in Fig. 86 is the remaining mass in the ignition point design. The observed "mix cliff" occurs at a remaining mass ∼30%–40% greater than that used in the point design.

There are various possible explanations for the required increase in remaining mass in the current experiments. These include unmeasured sources of perturbation, growth rates which exceed those currently calculated, and long wavelength variations in the fuel thickness that make it easier for the ablator to penetrate through the resulting thin region. Experiments are being developed to test all of these potential issues. Improvements to the target roughness and laser power balance that could reduce the required remaining mass are also being pursued.

In addition to the mix cliff, Fig. 86 shows that yields in present experiments are ∼5× or more lower than calculated 1D yields. The solid red band shows the predictions of yields

from 1D simulations as a function of remaining mass. The simulations are for typical implosions with this ablator thickness and target size and have been adjusted to match the observed shock timing and shell trajectories as described below in Sec. V C on integrated performance of cryo-layered implosions. Understanding this difference and reducing the magnitude of the difference between experiments and simulations are important for ignition target performance. The simulations show that if the targets were performing at the calculated 1D levels of yield, alpha deposition would be significantly enhancing the yield even at these lower velocities. Fig. 87 shows that implosions which "coast" longer before deceleration have a mix cliff at lower mass remaining than the "no coast" pulses. However, these coasting shells achieve lower fuel ρr and, because they have higher implosion velocity, have even lower yield relative to calculations.

To gain insight on the dependence of mix on drive, we refer to an analytic approximation to the RT ablation front instability growth exponent fed through on acceleration to the ablator/DT fuel interface[150]

$$\gamma t = \sqrt{kg/(1 + kL)}\, t - k v_a t - k\Delta R, \quad (45)$$

where k is the perturbation wave number, g is the ablation-driven shell acceleration, L is the ablation front density scale-length, v_a is the ablation rate ∼$dm/dt/\rho$, t is the duration of acceleration, and ΔR is the in-flight ablator thickness. The first term suggests that the classical growth rate ∼$\sqrt{gt^2}$ would at first glance only depend on shell distance travelled

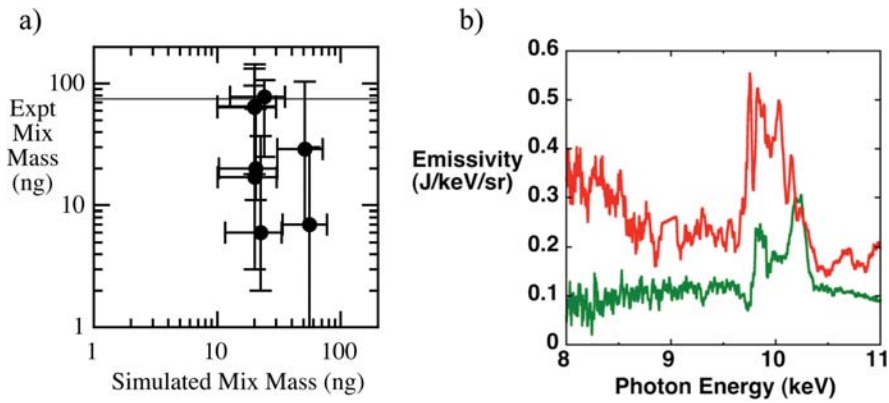FIG. 84. (a) Measured vs simulated hot spot mix mass for cryo-layered implosions based on Ge x-ray self-emission from cores driven by non-extended 2 ns rise pulses. These capsules were Ge doped ablators and were shot before the change to Si dopant in July 2011. Ignition requirement is below 75 ng line. (b) Core spectra for higher (red) and lower (green) mix cases.

$R = 1/2gt^2$ and not on the acceleration and peak power. However, if we factor in the initial shell velocity u imparted by the shocks before the acceleration phase starting at $t = 0$, then assuming for the moment a constant acceleration, R is actually $= ut + 1/2gt^2$ and hence the growth exponent $\sim \sqrt{(gt^2)} \sim \sqrt{(R - ut)}$. A higher acceleration will lead to a shorter acceleration time t, and hence larger growth rate for same distance travelled R. To quantify, we differentiate the first term of Eq. (45), and taking the limit $u \ll \sqrt{2gR}$ equivalent to assuming final implosion velocity $v \gg u$

$$\Delta\gamma t/\gamma t = (u/\sqrt{8gR})/((1 - u/\sqrt{2gR})) \, \Delta g/g. \quad (46)$$

Plugging in typical numbers derived from simulations in Eq (46): $u = -70 \, \mu m/ns$, $g = -60 \, \mu m/ns^2$, and $R = 750 \, \mu m$ leads to $\Delta\gamma t/\gamma t = 0.15 \Delta g/g$. For a 25% increase in acceleration, we expect a 4% increase in growth exponent, typically $\Delta\gamma t = 0.3$ for $\gamma t = 7$ (Growth Factor (GF) ~ 1000) and hence $\Delta GF = \exp(\Delta\gamma t) = 35\%$. One can show that this result holds even after considering growth of a fixed mode number l (i.e., k varying as $l/(R_0 - R)$ for an initial shocked shell radius R_0 at $t = 0$) and with non-constant acceleration. Solving the Rocket equation $(dm/dt)v_{ex} = mg$ for ignition relevant capsule parameters for drives with a constant foot (i.e., constant shock timing and u) but peaking at a range of temperatures T_r (i.e., range of g), one finds that $g \sim T_r^6$, a higher scaling as expected than $\sim T_r^{3.5}$ for a constant m (payload), and hence from above,

$\gamma t \sim T_r$. Moreover, since $v_a \sim T_r^3$ as peak ablation front density is almost independent of T_r per simulations, Eq. (45) shows that the classical growth rate and ablative stabilization terms have similar dependence on T_r. This in turn means ablative stabilization cannot reverse the trend of increasing growth rate with increasing power and T_r, and the RT ablation growth rates vs mode number should be self-similar as peak power varied. Figure 88 shows that is the case per simulations just varying peak power. Moreover, for the $\pm 15\%$ in peak power applied, we expect $\pm 4\%$ in peak T_r and growth exponent and hence $\pm 35\%$ in GF, matching simulation results. Figure 89 plots the inferred hot spot mix mass versus peak T_r for layered CH(Si) capsules of nominal thickness, showing that the highest drives did lead to the most mix.

An alternate metric for the performance of capsules near the mix cliff is to consider the in-flight shell width (the third term in Eq. (45)). Feedthrough of ablator perturbations at the ablator/fuel interface and the potential for hotspot mix is expected to increase with decreasing in-flight shell thickness ΔR, independent of shell density, and hence per Fig. 80 with decreasing coast time. Fig. 90 shows that the hot spot mix does also increase with thinner in-flight ablator shell thickness. The cryogenically layered ablator shell thicknesses are
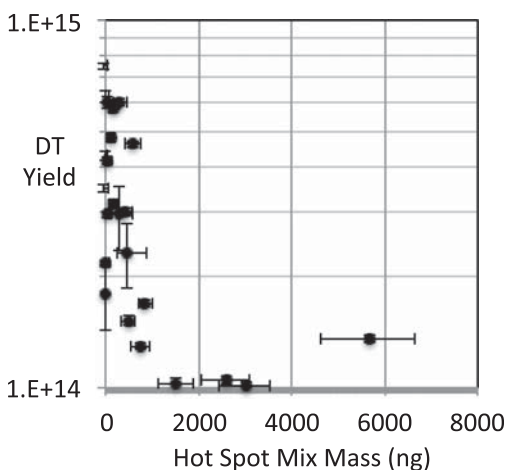
FIG. 85. Yield vs CH hot spot mix mass for cryogenic implosions driven with greater than 330 TW peak power and greater than 1.3 MJ.
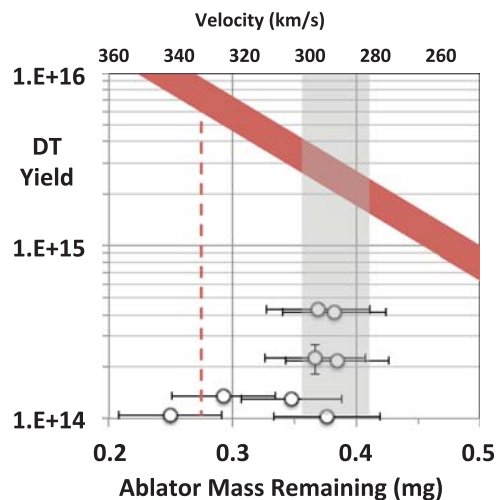
FIG. 86. Yield versus ablator mass remaining for capsules with initially 195 μm thickness driven by extended pulses of at least 300 TW peak power, 1.3 MJ total energy. Grey band denotes location of performance improvement, dashed vertical red line is the point design mass remaining value, and red sloped band is typical results from 1D simulations. Top horizontal axis gives the corresponding calculated peak implosion velocity.
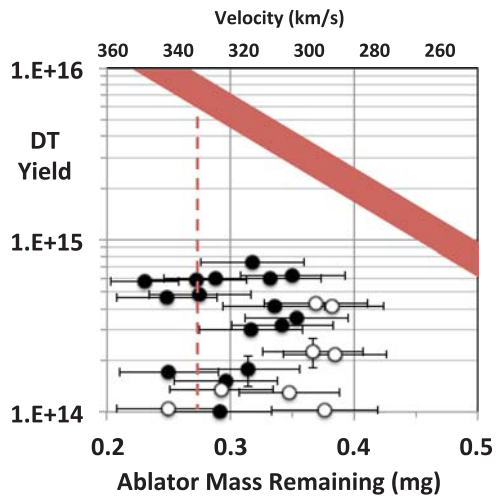
FIG. 87. Same as Fig. 86 with results from nominal "coast" implosions added as black points. Implosions which have longer coast time (shown in black) decompress before the final deceleration and appear to have a mix threshold at lower mass remaining.

inferred from the measured ablator shell widths of backlit symcap and one backlit THD implosion of similar pulse and ablator design, corrected for slight differences in drive, capsule size, and mass remaining. This scenario is also consistent with the mix cliff occurring at higher mass remaining $\sim \rho \Delta R$ for the shorter coast time implosions as shown in Fig. 87 since they are compressed to higher density. The mix cliff dependence on peak power and shell thickness, and at most weak dependence to changes in hohlraum material, Si dopant level, and rise time to peak power, suggests sensitivity to feedthrough of ablation front growth of perturbations caused by residual capsule surface roughness and dust.

Other mix hypotheses have been tested and will continue to be tested. Initially, the high levels of hydroinstability growth had been ascribed to development of a RT unstable density jump at the ablator/fuel interface due to excessive 3–5 keV x-ray preheat. This motivated switching to graded-doped ablators with twice the Si dopant level in each layer.
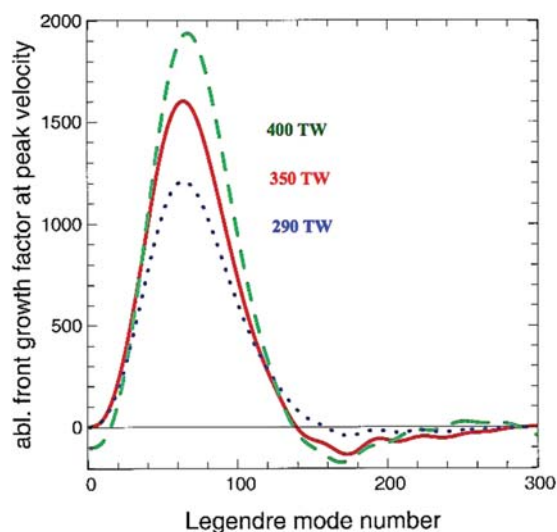
FIG. 88. Simulated ablation front growth factors at peak velocity versus perturbation mode number for three different peak powers: 400, 350, and 290 TW are dashed green, red, and dotted blue curves.
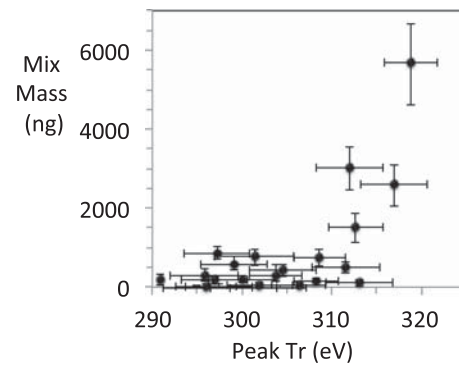
FIG. 89. Inferred hot spot mix mass versus peak radiation temperature for layered CH(Si) implosions with 195 μm nominal initial ablator thickness.

Such cryogenically layered capsules have not shown marked performance improvement so far. The reason appears to be that the most sensitive interface to preheat driven instability per simulations is the last doped/pure CH interface. By doubling the Si dopant level everywhere, less preheat reaches the last doped interface due to better shielding, offset by the fact that all but the last doped layer absorbs more of what reaches it.

To test if the small density discontinuities at the interior interfaces inherent to the baseline graded-doped ablator design could be seeding instabilities, enhanced, for example, by x-ray preheat creating unfavorable Atwood numbers, 1% and 2% uniformly Si-doped symcaps were also tested. Fig. 91 shows that for the 2% and 1% uniformly doped symcap and convergent ablator capsule, T_i dropped and mix increased significantly, more than for the graded doped-designs. Per Eq. (45), this is ascribed to increased RT growth due to a reduced ablation density scalelength from the outset caused by the higher opacity of the dopant overshadowing any growth at multiple interfaces. We also note that a 2× difference in dopant level for the graded doped design did not affect symcap performance either.

Initial tests of the performance of 20–25 μm thicker ablators have begun, driven with longer pulses and more energy to maintain "no-coast" conditions. Fig. 91 shows that the thicker symcaps driven to about the same velocity performed as well or better than the nominal thickness cases. Potentially more efficient rounded cylinder hohlraum designs
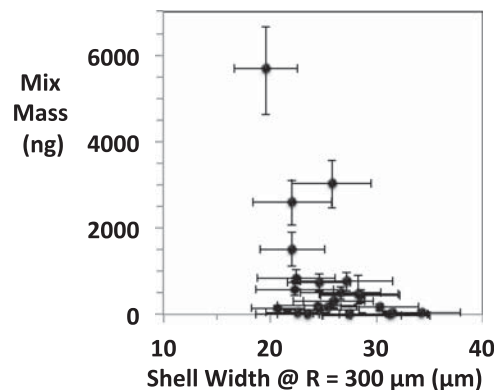
FIG. 90. Mix mass versus inferred ablator shell width at a radius of 300 μm for all >1.4 MJ DT and THD shots since June 2011.

a)   b)
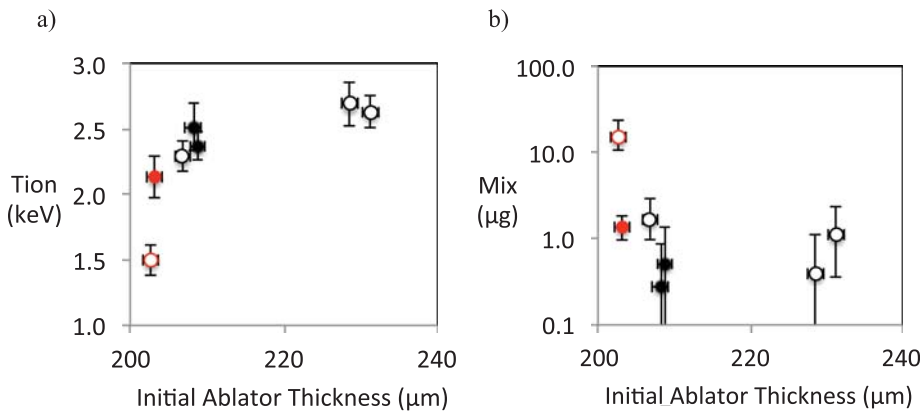
FIG. 91. (a) Tion and (b) Mix mass vs initial ablator thickness for symcaps and convergent ablator implosions driven with 3 ns-class 4th rise drives yielding <1.3 ns coast time. Black and red capsules denote graded and uniform Si-dopant, respectively. Open symbols have 2× Si dopant levels.

("rugby")[151] allowing increased clearance between capsule and hohlraum wall for the inner beams to reduce SRS and/or reduced wall area losses[152] will also be tested at NIF for improved coupling to allow for thicker capsule implosions. Finally, potentially more efficient ablators (Be[153] and high-density carbon[154]) will be tested.

A potential source of the yield deficit in implosions without obvious mix into the hot spot could still be the result of ablator mixing into the main fuel. However, the reduced yield could also result from low mode asymmetry of the cold fuel and ablator. Measurements of the isotropy of the neutron yield, the neutron down scatter spectra, and images of the down-scattered neutrons all suggest that the cold fuel likely has a higher areal density at the poles of the implosion along the axis of the hohlraum than around the equator. Another hypothesis is that mix is occurring preferentially at thin spots of the ablator and/or fuel due to non-uniformities caused for example by residual symmetry swings. Fig. 92 shows that nuclear measurements indicate that the main fuel can have quite large ρr variations even when the hot spot shape is quite round. Specifically, since ≈20% of neutrons are down-scattered on a spatially averaged basis for an average ρr of 1 g/cm^2, the 10% local variations in unscattered yield shown in Fig. 92(b) suggests there could be 50% variations in ρr averaged over ~1 steradian of the compressed fuel. This would also be consistent with the fact that the average DSR does not drop for the highest mix cases as shown in Fig. 93. By implementing 2D 10–20 keV and 100 keV Compton radiography discussed earlier, the in-flight and compressed ablator and fuel is being checked for distortions and thin spots

that could enhance mix feedthrough locally and hence increase the required spatially averaged minimum mass remaining.

A low mode asymmetry may also result in less efficient transfer of the shell kinetic energy to thermal hot spot energy and conversion of the kinetic energy to mass fuel motion instead of thermal energy as well as potentially enhancing mix as indicated above. In addition to minimizing these low mode asymmetries, further optimization of the peak power pulse shape beyond the simple variations in the rise times tested to date may also be required to achieve increased hot spot density and improved yields predicted by integrated simulations.[155]

Besides varying the peak power pulse shape, the level and length of the foot can affect mix. Specifically, seeding of the RT instability by Richtmyer-Meshkov growth during the initial shock traversal phase might be reduced by factors of 2 by altering the trough power and length, which can be tested by x-ray radiography of large preimposed perturbations[156] driven by just the foot of the NIC pulse. Finally, pulse shapes with a higher foot, designed to put the capsule on a higher in-flight adiabat,[157] might be used to reduce mix. Capsules with such pulses have increased density scalelength stabilization per Eq. (45) due to having a calculated 3× longer ablation scalelength. For example, at the peak ablation front RT growth mode l = 60 (Fig. 88), k = 0.1/μm midway in-flight and hence an increase in L from 10 to 30 μm decreases the classical growth exponent by $\sqrt{2}$, hence the l = 60 GF from 7 to 5 e-foldings, a nearly 10× reduction in growth which is a more significant decrease than possible by

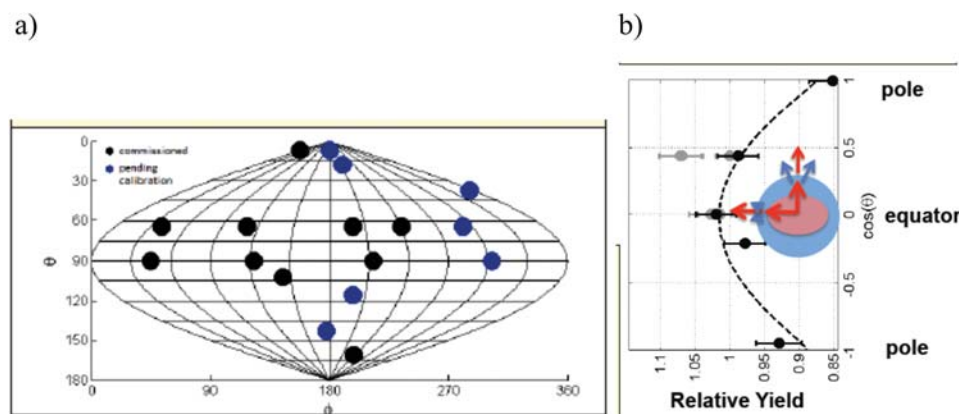a)   b)

FIG. 92. (a) Position of Zirconium Nuclear Activation Detectors arranged on the surface of the target chamber measuring primary DT neutron yield along different lines-of-sight. (b) Measured relative yield versus polar angle on one shot.
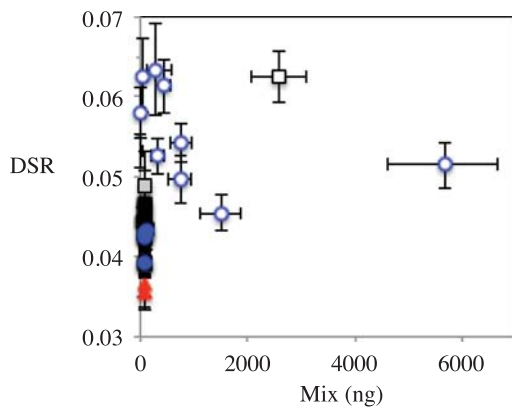
FIG. 93. Measured DSR versus inferred mix mass for DT and THD implosions. Red triangles, black squares, and blue circles correspond to 1, 2, and 3-ns-class rise to peak power. Closed and open symbols are nominal and extended pulse cases.

increasing ablation rates and/or in-flight shell thicknesses through an in-flight density drop. Experiments to directly measure the growth rate of hydrodynamic instabilities are part of the path forward following the NIC. Fig. 94 indicates the use of the keyhole geometry to obtain the growth rates in a converging geometry. This is an extension of backlighter radiography techniques utilized for a wide range of experiments on both the Nova and Omega laser.[67]

C. Integrated performance of cryo-layered implosions

As the NIC has progressed through the implosion optimization experiments described above, surrogacy issues and progress on ITFX, the GLC, and the fuel stagnation pressure are checked periodically using cryo-layered implosions.

We have developed a standardized approach to modeling the expected performance of cryo-layered implosions[158] as indicated in Fig. 95. The first step is an integrated hohlraum and capsule simulation using the high flux model described earlier. The calculation is run with the as shot laser pulse and capsule. This generates the starting point for the x-ray flux used in the capsule only simulations to follow. In the second step, the 1D radiation drive is adjusted until the calculations match the keyhole VISAR shock timing data
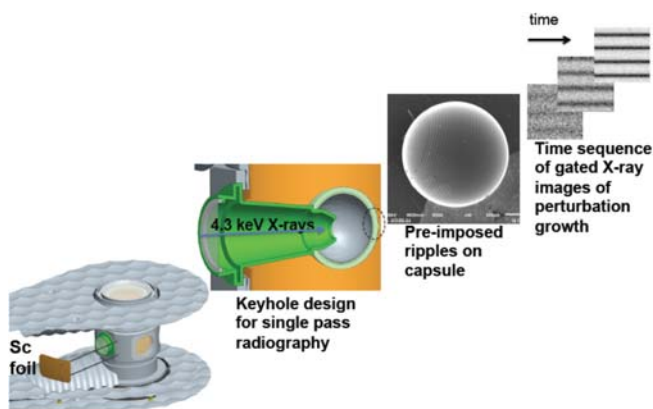

FIG. 94. Backlit radiography of an ignition target in the keyhole geometry can be used to obtain growth rates of hydrodynamic instabilities in a convergent geometry. Shown is a sequence of calculations of increasing contrast from growing 1D ripples at 3 different times.

and the convergent ablator radius versus time as indicated in the middle frame of Fig. 95. The 1D drive is applied, along with the measured surface roughness and a flux asymmetry chosen to match the hot spot shape, in 2D or 3D, to a capsule implosion calculation as indicated in the right hand frame of Fig. 95. Fig. 96(a) shows the calculated drive in an integrated hohlraum and capsule simulation, and the adjusted drive used to match the VISAR and ConA data. The peak drive must be adjusted downward by about 15% relative to the standard High Flux Model calculation of the hohlraum as described earlier. Additional multipliers earlier in the pulse are required to match the VISAR shock timing data. The middle frame in Fig. 95 shows that this procedure produces a very good match to the Keyhole VISAR shock timing data and ConA radius versus time. The calculation in Fig. 96 is for the cryo-layered implosion carried out on February 5, 2012 (N120205 using NIF date conventions year month and day YYMMDD) and the companion ConA and Keyhole experiments. Fig. 96(c) shows that the radius versus time for this implosion is well matched. Figs. 96(b) and 96(d) show that the mass remaining and shell thickness versus radius are also well matched with this drive.

The table in Fig. 97 shows that predictions with these adjusted drives do a reasonable job of matching the observed hot spot ion temperature and DSR from the NTOF data for this implosion. However, the calculation overestimates the hot spot density and pressure by $\sim 2\times$ and the yield by 3-5$\times$ depending on the details of the 2D or 3D calculations as indicated. The 2D and 3D calculations were carried out with the measured ablator and ice roughness as well as a radiation flux asymmetry chosen to match the observed shape of the hot spot. The calculations are also run with 30 ng of ablator premixed into the hot spot to represent the calculated effect of the fill tube which is not resolved in these simulations. Except where specified, the comparison of calculated performance to observed performance shown in the following figures is for calculations carried out in a similar way. Pressure and density for the experiment are estimated from the observed yield, hot spot size, burn width, and ion temperature as discussed in Sec. II. As indicated, the calculations have been run both with and without alpha deposition. The ratio of the yields is the yield amplification from alpha deposition. At the calculated 1D yields, alpha deposition for shot N120205 nearly doubles the yield while at the observed yield, the estimated yield amplification is reduced to about 15%–20%. This is not negligible but not large enough to produce a measurable change in ion temperature.

The radiation flux asymmetry applied in the calculations above consists primarily of the level of P_2 needed to match the observed hot spot shape. Throughout most of the NIC campaign, the hot spot shape provided the principal information about the symmetry of the implosion. When the imploding shell shape is nearly spherical, calculations indicate that data from the hot spot provide a reasonable representation of the symmetry of the overall implosion. However, nuclear data from the NTOFs looking in different directions, as well as the FNAD data discussed in Sec. V B 7 indicate a more complex shape to the cold compressed fuel than represented by the hot spot shape. The recent data from the 2D ConA
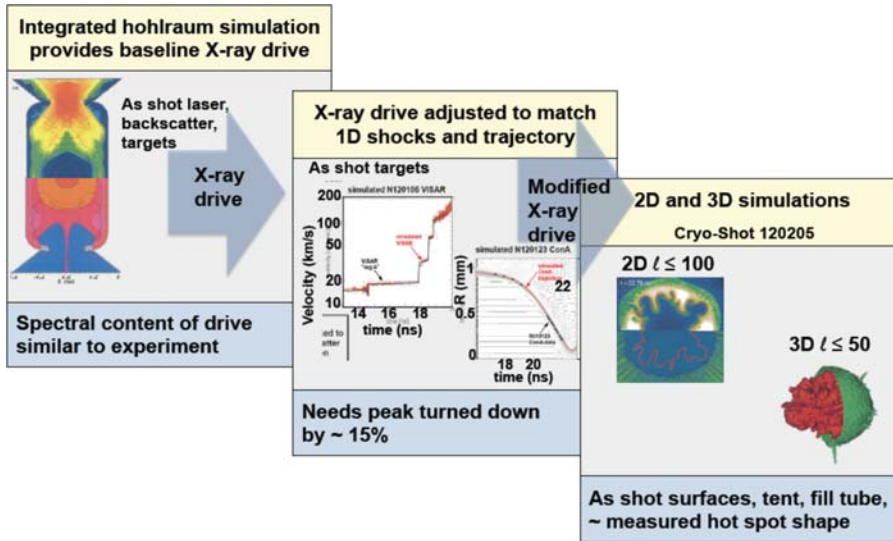
FIG. 95. Calculations of the expected performance of cryo-layered implosions follow a sequence of steps: (a) An integrated hohlraum and capsule simulation provides a starting point for the x-ray drive; (b) the drive from the integrated simulation is modified in order to match the measured VISAR shock timing data and ConA radius versus time data to provide the best 1D starting point for the implosion; (c) the 1D drive is applied, along with the measured surface roughness and hot spot shape, in 2D or 3D, to a capsule implosion calculation.

target on the shape of the imploding ablator discussed in Sec. V B 6 also indicate an implosion asymmetry not captured by the hot spot shape. When the low mode asymmetry of the imploding shell deviates substantially from a sphere, the main fuel can be far more asymmetrical, and have a far greater impact on the efficiency of the implosion than indicated by the observed hot spot shape.

Fig. 98 shows the impact of an imposed P_1 flux asymmetry on the implosion of shot N120205. Fig. 98(a) shows the 2D implosion with high mode roughness on the ablator and ice but with otherwise low levels of low mode asymmetry. This implosion achieves a peak pressure of about 150 gigabars. The implosion is nearly isobaric across the hot spot and cold fuel as shown by the axial plot of the pressure in Fig. 98(c). When a 2% P_1 is applied in the foot of the pulse, the imploded shape and pressure are little changed from the spherical case. But when a 2% P_1 is applied during the peak of the pulse, conditions in the hot spot and main fuel change dramatically.[159] The emitting hot spot remains nearly spherical and is nearly the same temperature and size as the hot spot in the spherical implosion. However, its pressure (and hot spot density) is reduced by nearly a factor of two compared to the spherical implosion. This reduced pressure is comparable to that observed in the experiment for this shot. These calculations show that large low mode asymmetry can account for the reduced pressure seen in experiments. The center of the hot spot has been displaced from the initial center of the capsule by an amount about equal to its compressed radius. Regions in the compressed main fuel achieve nearly the same peak pressures as in the spherical case but the main fuel distribution is now highly asymmetric. Without an image of the compressed main fuel, the shape of

FIG. 96. (a) Radiation temperature vs time showing the adjusted drive (red) vs standard simulation (black), (b) remaining ablator mass fraction vs radius, (c) mass averaged radius vs time, and (d) ablator thickness vs radius from data (black points) vs adjusted simulations (red curves).

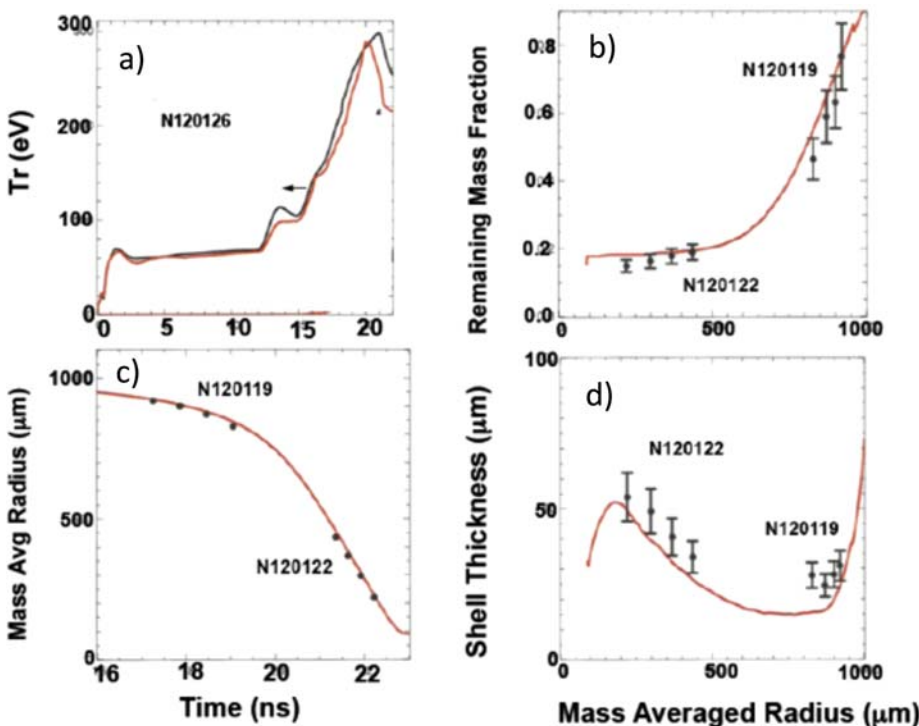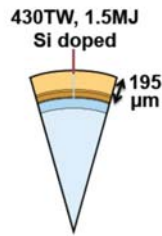|	1-D	2-D	3-D	expt.
DSR (%)	4.41	4.60	4.24	4.3±0.2
T_{ion} (keV)	2.90	2.91	3.29	3.4±0.16
HS density (g/cc)	75	82	71	44±8
HS pres. (Gbar)	195	202	175	102±20
Neutrons (no alpha deposition)	22.9	17.8	16.2	4.8 (est)
Neutrons (10^{14}) (13-15 MeV)	39.2	29.8	23.6	5.6±0.2

FIG. 97. Comparison of calculated to measured performance for DT shot N120205. The inset shows a schematic of the capsule. The calculations provide a reasonable match to the measured temperature and DSR but overestimate the hot spot density and pressure by roughly a factor of two. For a given temperature, the yield will scale roughly as the square of the hot spot density so the calculated yields are high by about that factor as well.

the hot spot is very misleading. The most compelling hot spot evidence for an applied P_1 would be the offset in the centroid of the hot spot relative to the initial centroid of the capsule. Diagnostic fiducials on the 2D ConA target are being refined to enable this measurement. As discussed in Sec. IV D 3 the ARC short pulse beamline on NIF is being developed to enable accurate Compton radiograph images of the compressed fuel. Although these low mode perturbations are quite large, and a significant fraction of the initial fuel kinetic energy remains as mass motion at the time of peak neutron production, we nonetheless find that the relationship between the calculated GLC and ITFX remains essentially unchanged from that shown in Fig. 19. This correspondence is predicted by Eq. (9). In this model, if the effective fuel kinetic energy is multiplied by a factor ε, then $P\tau$ is reduced by that factor and ITFX is reduced by $\varepsilon^{8/3}$. In the calculational data base, we would expect this to be reduced to $\varepsilon^{2.2}$ as indicated in Fig. 19. Fig. 99 shows the calculated values
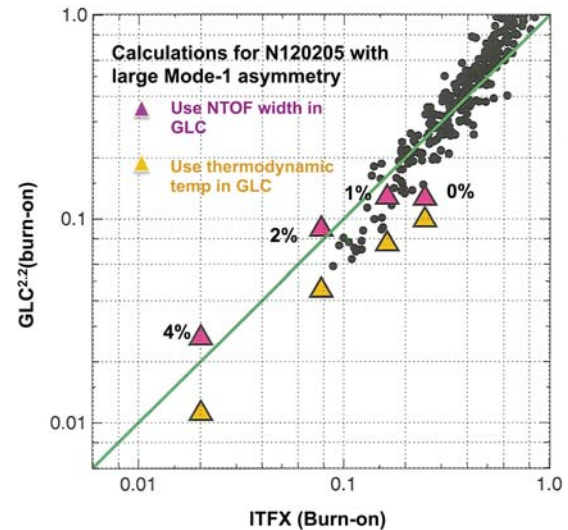
FIG. 99. Calculations with large P1 perturbations retain the relationship between GLC and ITFX even though they are far from isobaric and have substantial mass flow at peak compression. Points are shown with P1 = 0%, 1%, 2%, and 4%. Also shown are temperatures obtained from the width of the NTOF primary neutron signal and NTOF measurements whose widths have been corrected for the effects of mass flow.

of GLC and ITFX for shot N120205 with 0%, 1%, 2%, and 4% P1. Two sets of points are shown. As discussed in Sec. II, we have used the ion temperature taken from the width of the primary neutron peak as would be measured by the NTOF detectors. In general, this measurement is representative of the average thermodynamic temperature during the burn phase. However, this width can be affected by large mass motion. For the calculations with large mode 1 perturbations in Fig. 99, two sets of points are shown. One set uses the NTOF width and the other uses the thermodynamic temperature from the calculation. Since NIF has several NTOF detectors at widely spaced angles, the NTOF temperature can be corrected for the effects of low mode mass motion.
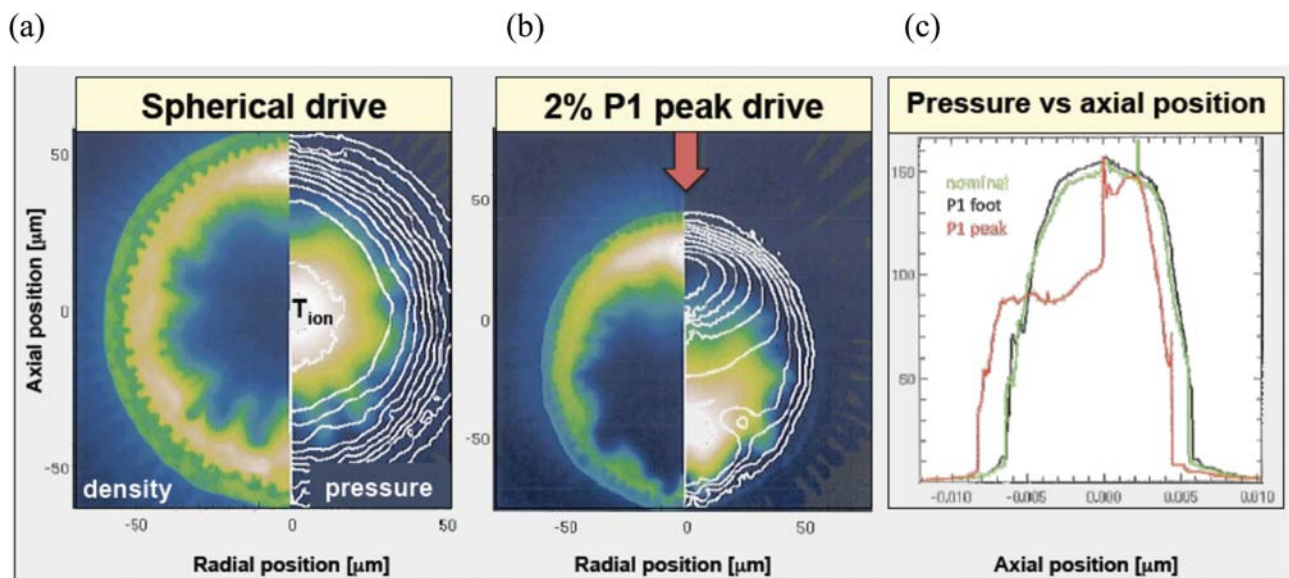
FIG. 98. (a) Calculated implosion of a cryo-layered implosion N120205 with measured surface roughness but with otherwise low levels of low mode asymmetry; (b) the same implosion with 2% P1 flux asymmetry during the peak of the pulse; (c) the axial pressure distribution (along the direction of the arrow in (b)) across the hot spot and main fuel

FIG. 100. (a) Cryo-layered target in its protective shroud. (b) Cryo-layered target showing the LEH storm window developed in 2010–11 to protect the hohlraum windows from condensation of residual chamber gas.

Fig. 100 shows a cryo-layered target and the shroud that encloses the target until just before shot time. The first cryogenic target implosion[160] was carried out on September 29, 2010 but it took the remainder of CY2010 and early 2011 to fully qualify the cryogenic target positioner (cryo-tarpos) and the target fielding configuration. One key issue that had to be resolved was the formation of tritiated hydro carbons which were produced in the fill system. These impurities resulted in low-quality layers. A second issue, that required the invention of a "storm window" on the cryo-layered target, was condensation of micron thick layers of residual target chamber gas on the windows of the hohlraum. This condensation was also an issue in the early Keyhole targets. Formation of this condensate prevented precision pulse shaping and resulted in low fuel ρr as indicated by the first 4 cryo-layered shots in Fig. 101. For these early implosions, the DSR was only about 35% of that required for ignition.

Fig. 101 shows that improved shock timing[161] along with extended pulses[162] to eliminate coasting has resulted in two discrete jumps in fuel ρr which has reached about 85% of the point design value. The first shock-timed implosions were carried out in May 2011 and the extended "no-coast" pulses were carried out in March-July 2012. Over this period of time, a variety of modifications to the capsule and hohlraum drive were tested. These variations included capsules doped with either Si or Ge. Capsules with nominal Si doping

levels (as shown in Fig. 3(b)) and 2× nominal levels were fielded. The wavelength difference between inner and outer beams as well as between the 23.5° and 30° was varied to adjust the symmetry of the hot spot. Two different size LEHs, 3.1 mm and 3.373 mm diameter, were fielded to test the LEH impact on drive and symmetry. The peak power was changed from 300 to 500 TW.[163] All of these changes had relatively little impact on the measured DSR of the imploded fuel.

An increase in ρr from improved shock timing and extended pulses should be accompanied by a decrease in core size as measured by x-rays and unscattered neutrons and in the cold fuel average radius as measured by scattered neutrons. Fig. 102 shows that the resultant cryogenic DT x-ray hot spot image sizes shows a decrease with reduced "coast time." The variations in radius in Fig, 102 and in DSR in Fig. 101 for the extended pulse cases with the shortest 0.8–1 ns coast time can be attributed to variations in shock merge depth as was shown in Fig. 58. Figs. 103(a) and 103(b) show consistency between the >8 keV x-ray and unscattered 13–15 MeV neutron images of the hot core ($P_0 = 24 \pm 2$ vs $27 \pm 4 \mu m$), while Fig. 103(c) shows, as expected, a larger cold fuel average radius ($P_0 = 35 \pm 4 \mu m$). Fig. 104 plots the measured radii vs DSR, following fairly well the expected trend of radius $\sim 1/\sqrt{\text{DSR}}$ in the limit of a thin fuel shell for fixed fuel mass. More refined analyses[164] comparing the unscattered and downscattered neutron sizes

FIG. 101. Ratio of downscattered to unscattered neutrons (DSR) and inferred fuel areal density from cryogenically layered DT implosions versus shot number for showing progression in improvement. The first vertical dashed line separates the first 4 pre shock timed implosions from the shock timed implosions. The second vertical dashed line separates the nominal length from the extended "no-coast" implosions appearing at shot 25. Band above shows point design dsr and ρr required.

FIG. 102. Mean hot spot radius from 17% x-ray contours of cryogenically layered implosions versus time interval between end of drive pulse and bangtime. As in Fig. 91, red triangles, black squares, and blue circles correspond to 1, 2, and 3-ns-class rise to peak power. Closed and open symbols are nominal and extended pulse cases.

FIG. 103. Time-integrated emission images of the core from (a) $>8\,\mathrm{keV}$ x-rays and (b) unscattered neutrons, and (c) of cold fuel from downscattered 10–12 MeV neutrons for shot N110914.

and P_2 asymmetry are now also extracting the first 2 Legendre moments of compressed cold fuel thickness and areal density. We are actively combining this neutron shape information with the angularly dependent neutron yields, x-ray yields and x-ray core shapes to reconstruct the last phases of the implosion,[22] adding in more data (such as 2D radiography) as it becomes available.
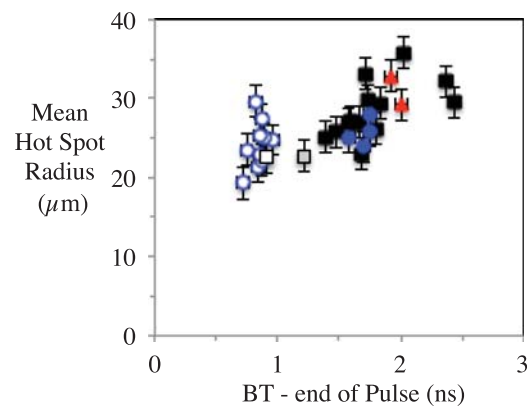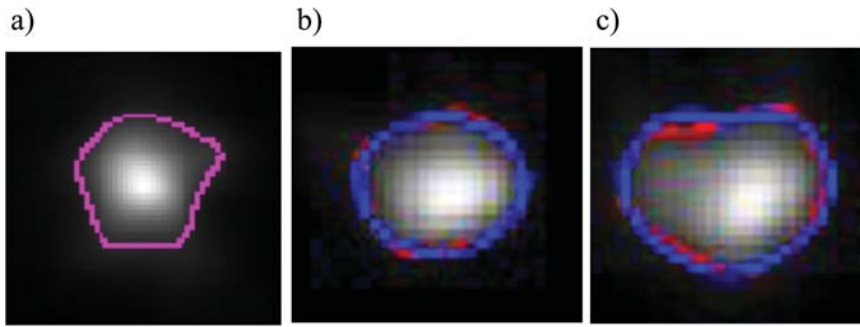
As discussed in Sec. II, progress toward the integrated performance required for ignition can be graphically represented as shown in Fig. 105. Data for all the cryo-layered implosions carried out during the NIC are incorporated in these plots. The contours drawn represent constant yield amplification as indicated. The axes for Fig. 105(a) are $P\tau$ and ion temperature T while for Fig. 105(b), the axes are Yield and DSR. The data points in the plots are color coded to indicate those that were coast vs no-coast implosions. Also indicated are the early experiments prior to the onset of precision shock timing.

As shown in Fig. 105(a), the no-coast shots have the highest value of $P\tau$ but also have the widest range of Tion. As shown in Fig. 105(b), the DSR values cluster much more closely than the yield during the various phases of the NIC campaign. Fig. 106 highlights a few of the shots that represent significant stages in the ignition campaign. Fig. 106(a) shows the evolution of experimental results in the Yield-DSR space, while Fig. 106(b) show the similar evolution in the $P\tau$-T space. Shot N100929 was the first cryo-layered implosion, carried out as a performance qualification test of the

cryogenic target positioner. As indicated above, this shot was carried out before the development of the Keyhole target platform that is needed to optimize shock timing. Shot N110603 was the first shot carried out after initial shock timing experiments. Shot N120205 was one of the best performing "coast" shots carried out after a significant effort to optimize the hot spot shape as well as the laser pulse shape, and shot N120321 was the best performing "no-coast" implosion. Fig. 106(a) shows the representative increase in DSR achieved between N100929 and the first shock timed "coast" shots and the substantial further increase in DSR obtained for no-coast pulses. Fig. 106(b) shows the $\sim 5\times$ increase in $P\tau$ achieved during the evolution of the NIC campaign. The temperatures achieved in these implosions are close to those predicted by Eq. (13). All of these shots highlighted in Fig. 106 had an inferred mix of less than an estimate of 350 ng. As shown, shot N120321 had a yield amplification near 30% with a GLC(no-burn) ~ 0.3 of that required for ignition as well as an ITFX ~ 0.07 and was the best overall performing shot in the NIC campaign. The calculated 1D and 3D yields and DSRs for a pair the shots, N120205 and N120321, is also shown in Fig. 106(a) while the predicted $P\tau$ and T are shown in Fig. 106(b). These calculations were carried out as described above.[158] The "no-coast" implosion shot N120321, which has a significantly better calculated 1D performance, is also more affected by the known 3D imperfections in the experiment. Both of these calculations predict yields in 3D that are within about a factor of 3 of the experimental measurements. The 3D calculations do not yet have an adequate representation of the perturbations from the tent supporting the capsule or of the long wavelength asymmetry of the imploding shell now being measured by the 2DConA experiments discussed above in Sec. V B 7. In addition, the 3D calculations cannot be done with a resolution needed to model the growth of short wavelength perturbations from isolated defects that are the most likely source of mix to reach the central hot spot. But for the best performing of the coast and no-coast cryo-layered implosion, the 3D calculations are converging to the observed results.

However, the large spread in yields and in the fuel ion temperatures for otherwise similar implosions is not yet predicted by the 3D calculations. This spread in yield and ion temperature can be largely explained by variability in the hot spot mix observed in these implosions. This variability is shown in Figs. 107(a) and 107(b) in which the data points are color coded by the amount of mix mass as inferred from hot spot Bremsstrahlung and free-bound emission.[148] Fig.
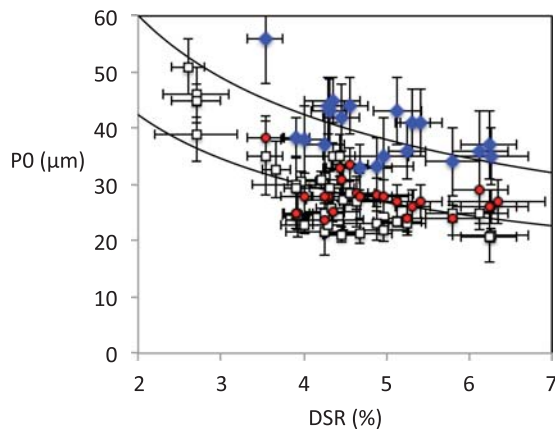

FIG. 104. Average polar size (P_0) of 17% contour of core emission as measured by imaged $>8\,\mathrm{keV}$ x-rays (open squares) and unscattered neutrons (red dots) and cold fuel as inferred from downscattered neutrons (blue diamonds) as seen from the capsule equator vs dsr inferred from the ratio of downscattered to unscattered neutrons. Curves are fits to $P_0 \sim 1/\sqrt{DSR}$.

a)

b)
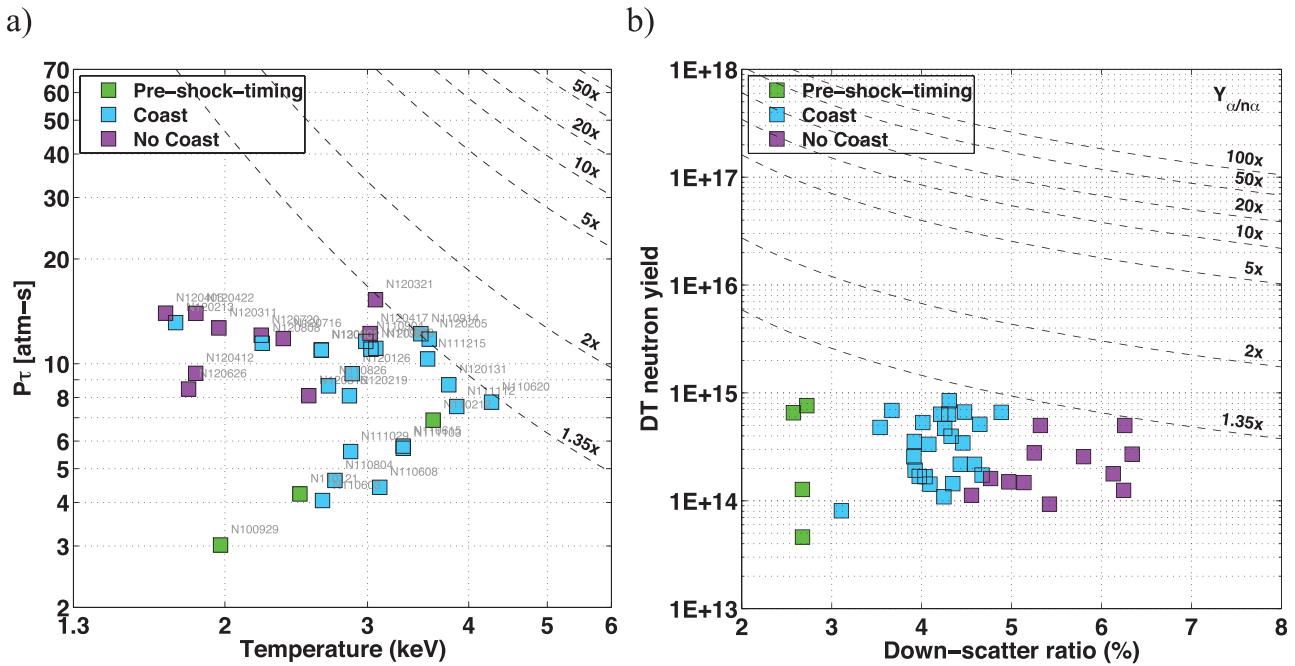
FIG. 105. Progress on the integrated performance of cryo-layered implosion shots can be represented in a space (a) of Pt vs T (GLC) or (b) Yield vs DSR (ITFX). Results are for DT implosions and the quantities listed on the axes include the effects of alpha deposition. Contours shown are lines of constant yield amplification from alpha deposition.

108 is a plot of GLC$^{2.2}$ versus ITFX which adds the data from all of the layered shots to the calculations shown in Fig. 99. As in Fig. 107, the data points are color-coded by the amount of mix. Cryo-layered experiments with less than an estimated 350 ng of mix mass have the expected relationship between GLC and ITFX. However, the enhanced radiation losses caused by hot spot mix are not incorporated in the hydrodynamic model used to develop the relationship

between GLC and ITFX and we see that the correspondence between GLC and ITFX breaks down for high levels of mix. Specifically, since Fig. 107 shows mix does not affect pressure, GLC$^{2.2}$ per Eq. (5) thus scales as $(\langle\sigma v\rangle/T^2)^{2.2} \sim T^6$ for $\langle\sigma v\rangle \sim T^{4.7}$ at the measured 2–3.5 keV ion temperatures. Hence we expect GLC$^{2.2}$ to drop by 30× as T_i drops from 3.5 to 2 keV due to radiative cooling at the highest levels of mix, as observed in Fig. 108. Fig. 108 also shows the results
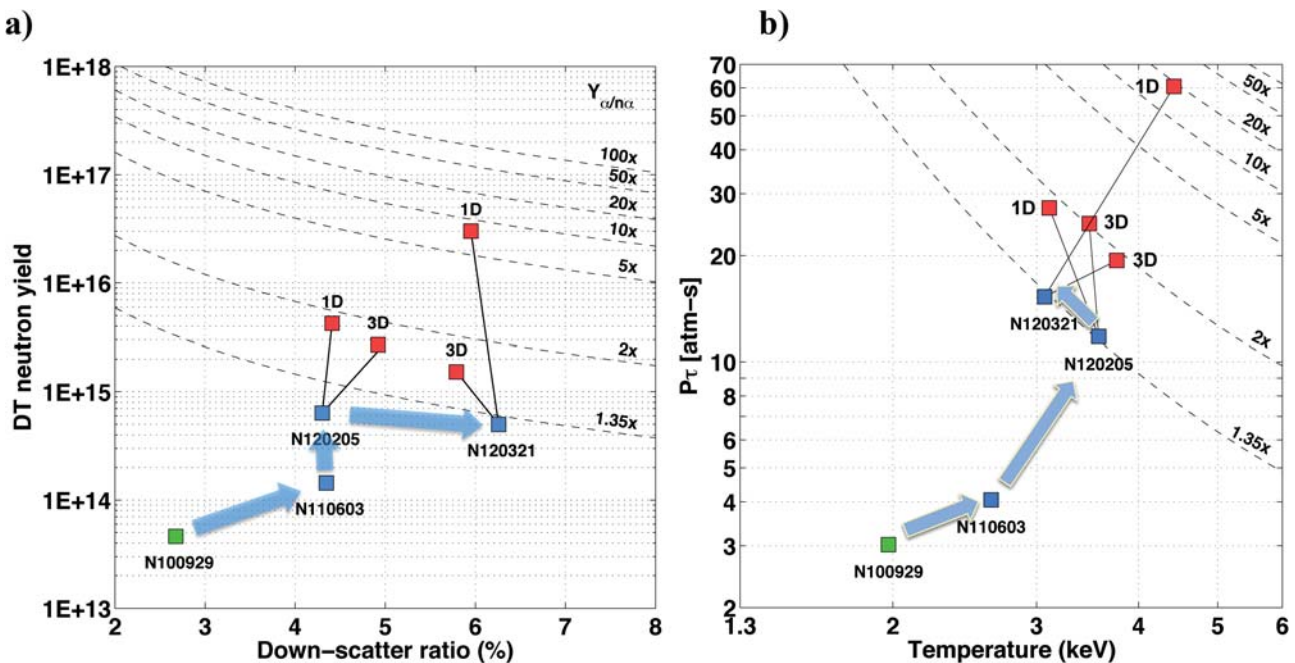
FIG. 106. (a) Key shots in Yield–DSR space illustrate the progress toward reaching the conditions required for ignition. The shots shown represent better performing experiments at each stage and are all experiments with low levels of hot spot mix. Also shown are the improvements being made in modeling the results of these experiments as the NIC campaign has developed the capability of incorporating an increasing range of 3D effects into the calculations. (b) The same shots plotted in Pτ-T space. Contours are lines of constant yield amplification from alpha heating.

a)

b)
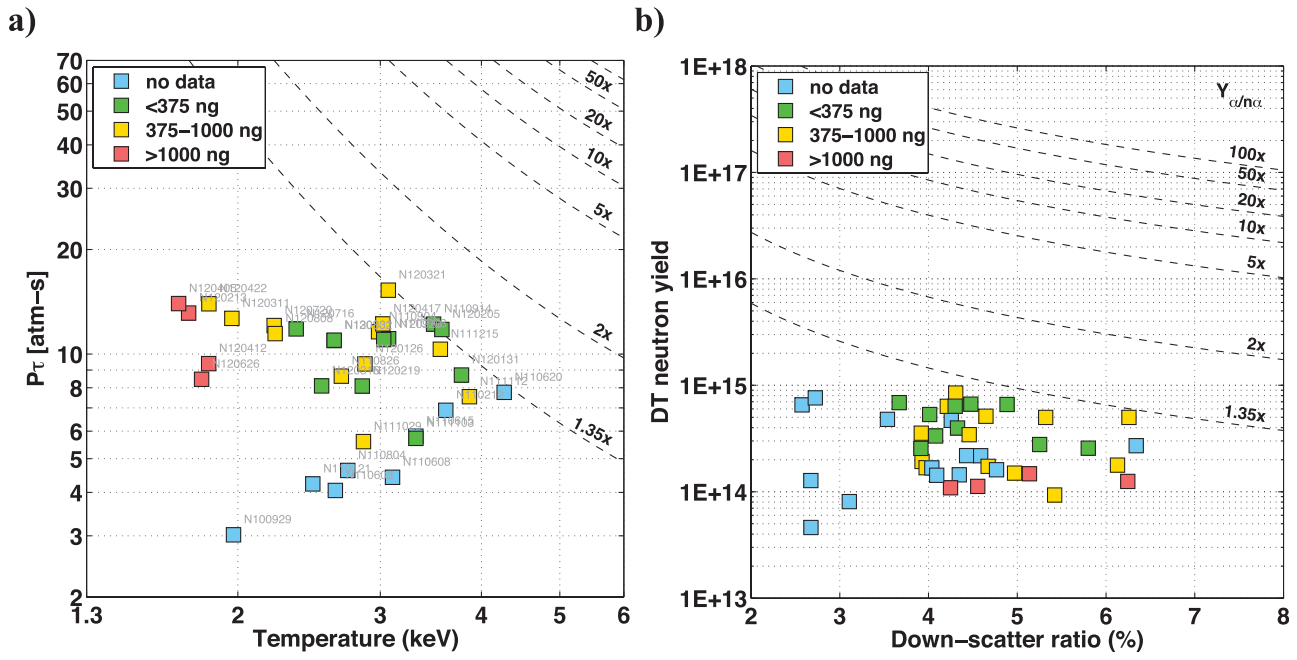
FIG. 107. A wide range of mix mass is observed in experiments in which the implosions were expected to be similar in performance. This is seen clearly in the wide range of ion temperatures resulting from radiative cooling in a plot of Pτ vs T (a) and in a wide range of yields in a plot of Yield vs DSR (b). Contours are lines of constant yield amplification from alpha heating.

of incorporating 1000 ng of mix into Hydra calculations for a subset of the implosions used to produce Fig. 99. These calculations show that the offset between ITFX and the GLC matches that seen for experiments with this level of inferred mix. In principle, ITFX can be modified to incorporate enhanced radiation losses from the hot spot. However, until that is done, the GLC is the most applicable ignition metric for implosions with substantial levels of mix.

The impact of mix on capsule performance is also shown in Fig. 109 which is a plot of yield versus ion temperature[22] for all the cryo-layered implosions. Experimental

points in Fig. 109 are also labeled by the hot spot mix mass. Calculations for several of the experiments without mix, both with and without alpha deposition are also plotted. The dashed lines indicate the expected scaling of yield with Ti from Eq. (17) if the hot spot density and burn width were unchanged. However, the hot spot density in the implosions with significant mix is seen to increase because of radiative cooling. This gives a weaker dependence of yield on hot spot temperature, as seen in the data. When the calculations are run with varying levels of pre-imposed mix in the hot spot, the calculated yield follows the observed scaling with temperature, as seen in Fig. 110, although the absolute yields
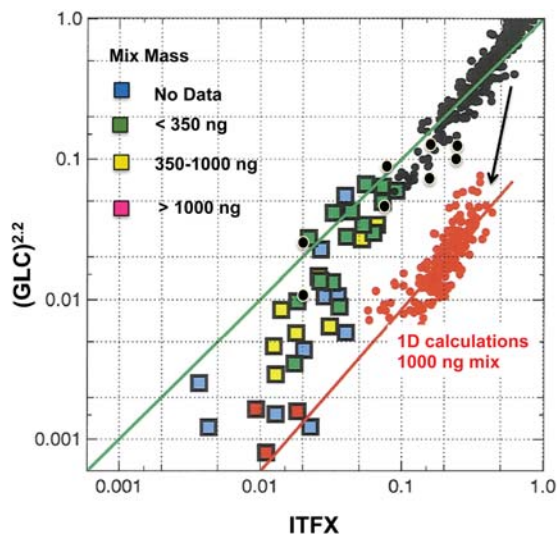
FIG. 108. The relationship between the GLC and ITFX observed in the NIC experiments with low levels of mix generally follows that expected from Hydra calculations without mix. Experiments with significant mix deviate from this relationship. Hydra calculations with mix see a similar degradation in performance and offset between GLC and ITFX to that seen in experiments with similar levels of mix.
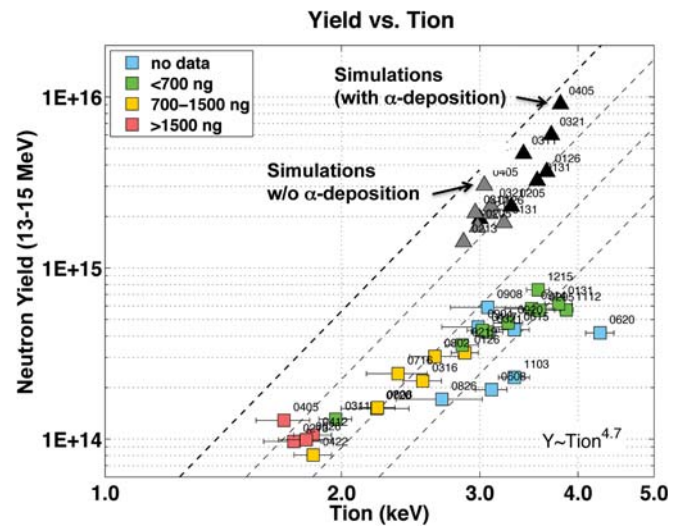
FIG. 109. Neutron yield for 50/50 DT fuel versus ion temperature. Dashed lines show expected scaling of yield versus temperature with no mix. Squares are data color-coded by level of inferred hot spot mix, triangles are from postshot simulations with (black) without (gray) alpha deposition adjusted to match shock timing and implosion velocity.

FIG. 110. Same plot as Fig. 107 adding calculations with pre-loaded hot spot mix.

FIG. 111. Same as Fig. 107 adding plausible percent level low mode asymmetries (purple triangles). Images shown are for a particular calculation of shot N120205 with P1 = 2%, P2 = −2%, and P3 = −2%.

remain factors of several higher than the experimental yields.

In current calculations, the principal sources of ablator material which reaches the hot spot are surface defects on the capsule, the fill tube, and the capsule tent support structure. Given the current level of information on capsule defects, the calculations do not predict the levels of mix inferred in these experiments or the level of variability in mix from shot to shot. However, we have only recently developed the capability for doing 4π characterization of an as-built capsule. With this new capability, we can obtain information not just about the initial capsule surface roughness but also about the dust and other defects that can accumulate during the assembly process. We do not yet know whether the increased mix mass observed is due to growth rates that are larger than calculated, to surface defects that are larger than current estimates, to variations in shell thickness which are enabling mix to penetrate more easily through thin spots, or to some other effect which is increasing the effective surface roughness. Addressing these issues will be a key focus in experiments going forward.

As discussed above, low mode asymmetry could be a major contributor to the discrepancy between the calculated and observed yields and hot spot pressures. Fig. 111 shows the impact on the calculated yield from percent level perturbations in low modes. The images shown in the figure are for the shot N120205 with $P_1 = 2\%$, $P_2 = -2\%$, and $P_3 = -2\%$. This particular choice gives agreement with observed yields, ion temperatures, and pressures as well as the hot spot size and shape. In this calculation, the effect of the P_1 and P_3 perturbations is to produce an oblate (or pancaked) implosion. As discussed above in Vb5, cryo-layered implosions in general are observed to be more pancaked than expected from the shape seen in the lower convergence symcap. The applied $P_2 = -2\%$ then generates a nearly spherical hot spot, while the fuel remains highly distorted.[159] There are various possible sources of low-mode asymmetry in the radiation flux. These include pointing errors, quad-to-quad power imbalance, and diagnostic holes as well as amplification of
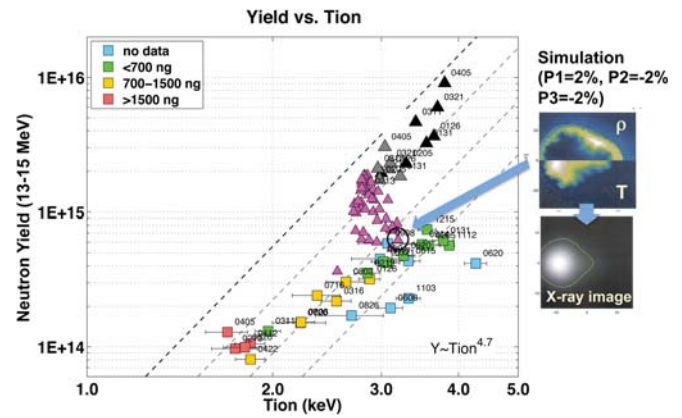
these effects due to cross beam transfer. Experiments are being modified to better quantify the presence of this type of low mode asymmetry, and experiments that apply a deliberate P1 are part of the path forward plan for the Ignition Campaign.
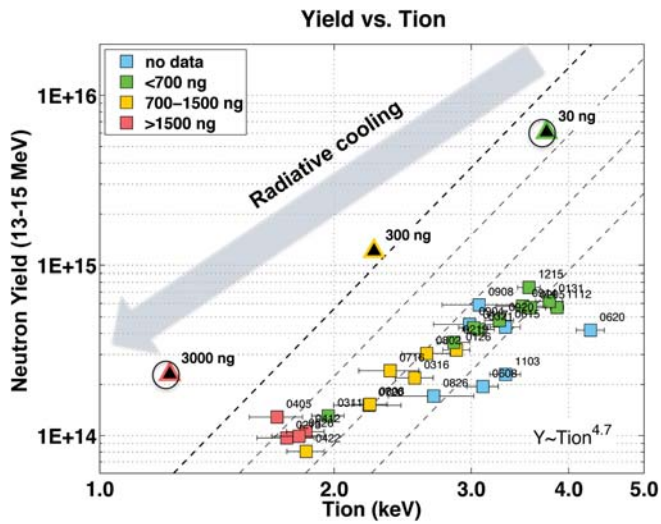
Also, as identified at the start of the ignition campaign, the P_4 component of flux asymmetry is strongly affected by the hohlraum length. As discussed in Sec. V B 6, measurements using the newly developed 2D ConA target show significant levels of P_4 (20–30 μm in the first experiment) as the shell is imploding. This data indicate that it is likely that all of the cryo-layered implosions to date have been degraded to some extent by the existence of a significant P_4 asymmetry. The impact of a P_4 asymmetry depends on when during the pulse it is generated[22] as shown in Fig. 112. A P_4 that is generated early in the pulse has time to generate significant lateral mass flow as the capsule implodes. This mass flow generates an azimuthal variation in the shell ρr as well as an azimuthal variation in the imploded radius. Changes to the hohlraum length are under way to minimize the level of P_4. If the P_4 asymmetry has a significant time dependence, it may be necessary to focus the outer beams to different locations on the hohlraum wall or change the hohlraum design to reduce the potential sources of P_4. The 3-axis keyhole target mentioned in Sec. V B 4 is part of the go-forward plan following NIC to obtain early time information on both axial and azimuthal mode 4 variations.
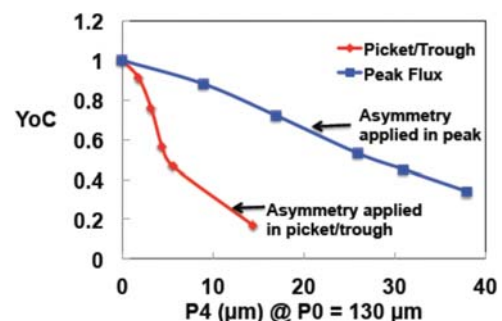
FIG. 112. Calculated YoC vs. in-flight shell shape P_4 observed at an average radius of 130 μm for P_4 asymmetry applied in the picket and trough (red curve) and peak (blue curve).

As discussed in Sec. II, the peak pressure generated in the hot spot is linearly related to the GLC for implosions on the NIC. At ignition for a NIF scale implosion, we need a hot spot pressure of ∼330 gigabars. As with ITFX, the relationship between pressure and the GLC breaks down for implosions with high levels of mix. Implosions can have enough hot spot mix to lower the ion temperature and burn rate below levels required for ignition without resulting in a drop in pressure. Nonetheless, the hot spot pressure provides information that is a very valuable complement to other ignition metrics.

Figures 113 and 114 are plots of the hot spot pressure inferred from the yield, hot spot size, ion temperature and burn width, following Eq. (7), versus the implosion velocity inferred from the companion ConA experiments. Fig. 113 is for the "coast" set of implosions for which the laser pulse ended with the capsule at a radius of about 500 μm, about half its initial radius. Fig. 114 adds the data for the "no-coast" implosions for which the laser pulse was extended until the capsule was at about 300 μm. The dashed lines indicate the approximately v^3 scaling of pressure as predicted by Eq. (21). The experiments for the "coast" implosions shown in Fig. 113 show the expected v^3 scaling of pressure seen in the Hydra simulations. However, the pressures (and hot spot densities) inferred in the experiments are about a factor of 2 lower than those in the calculations. In general, the calculations deviate from the experiments in a way that is qualitatively similar to the results shown in Fig. 97 for the shot N120205 (which is part of the data set in Fig. 113). Fig. 114 shows a similar scaling with velocity for the "no coast" implosions. The "no-coast" experiments have about 50% more pressure at a given implosion velocity than the "coast" implosions. The calculated pressures for "no coast" pulses trend above those calculated for the point design and are above those calculated for "coast" pulses. As a result, although they achieve a higher pressure, the experimentally inferred pressures for "no coast" pulses remain about a factor of two below the calculations. As discussed above, leading candidates for at least part of the observed low pressure are
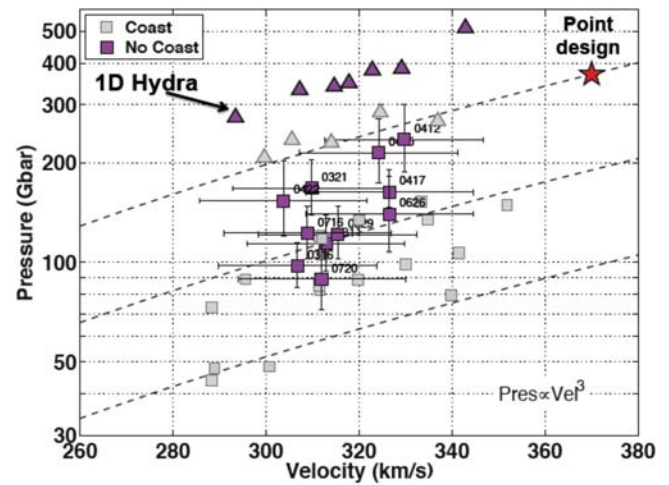
FIG. 114. Same as Fig. 113 comparing extended pulse no-coast implosion data and postshot simulations.

low mode asymmetry and hydrodynamic instability sufficiently large to cause shell breakup.

The experimentally observed pressures for the "no coast" implosions are approaching the trend line of pressure versus velocity of the point design. However, we have observed a rapid onset of mix for "no coast" implosions above a velocity of about 300 km/s, as indicated in Fig. 86. The "no-coast" shot N120321 had an observed GLC ∼ 0.3, the highest value measured during NIC experiments. That implosion had an estimated velocity just above 300 km/s based on ConA data and had relatively low levels of hot spot mix. Higher velocity "no coast" implosions driven at higher power, although achieving higher peak pressures, have had hot spot mix levels sufficient to radiatively cool the hot spot and reduce the yields. As described above in Sec. V B 7, the calculated threshold for significant levels of mix is above the point design velocity of 370 km/s. One of the key research efforts moving forward in the ignition program are experiments to provide the data needed to understand this difference and to develop a path forward to higher velocity. This path forward will include reduced low-mode asymmetry to reduce thin spots in the shell and improve the efficiency of conversion of kinetic energy into compression of the fuel, experiments to measure the growth rates for hydrodynamic instability, adjustments to the pulse to minimize growth, and improvements to the capsule and other sources of perturbations to reduce seeds for hydrodynamic instability.

VI. THE PATH FORWARD

Current evidence points to low-mode asymmetry and hydrodynamic instability as key areas of research to improve the performance of ignition experiments on the NIF and are a central focus of the Ignition Program going forward. Experiments have been identified to develop a better understanding of the 1D characteristics of the implosion. A variety of possible modifications to the hohlraums, designed to improve energetics and symmetry control, are also being pursued, as is the use of alternate ablator materials. These efforts can be summarized as follows:
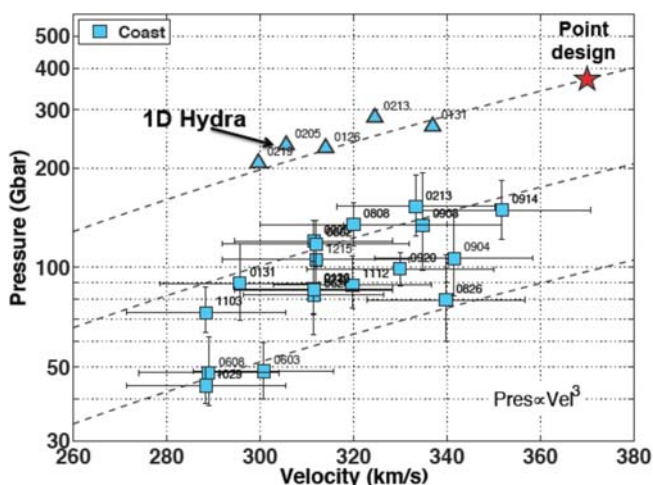

FIG. 113. Pressure vs peak implosion velocity overlaid on v^3 scaling (dashed lines), comparing nominal coast pulse data (squares) to postshot simulations (triangles) adjusted to match measured shock timing and implosion velocity. Also shown as red star are the 2D point design values.

- To better quantify and minimize the magnitude of the long spatial scale variations in the fuel shape and ρr, the ignition campaign will be exploiting the recently developed 2D radiography (the 2D ConA target) of the imploding ablator. Compton radiography[64] of the fuel at peak compression is also under development and is expected to provide images of the final state of the compressed fuel. Variations in the hohlraum length to minimize P_4 will be explored. Time dependent control of P_4 may be possible by pointing the 44° and 50° outer beams to different locations. Different hohlraum shapes which generate lower levels of P_4 will be explored. In conjunction with the development of these techniques, the campaign will implement target fabrication and laser power balance improvements designed to reduce long spatial scale perturbations in the targets as well as the symmetry of laser energy delivered to the hohlraum.

- The NIF ignition point design pulse has been chosen to minimize the effects of hydrodynamic instability at the point design velocity and fuel adiabat. However, uncertainty in DT and CH EOS as well a material properties such as thermal conductivity at the fuel ablator interface introduce significant uncertainty in the optimal pulse and target configuration needed to minimize hydro-instability growth rates. Experiments to directly measure the growth rate of hydrodynamic instabilities are a key element of the path forward. The keyhole geometry will be combined with backlit radiography, looking at the inside of an ignition capsule, to obtain the growth rates in a converging geometry. This technique will be useful to look at growth rates to imploded radii about half or less of the initial capsule radius. These experiments will cover the early time Richtmyer-Meshkov phase of instability growth, as well as acceleration of the shell to near peak velocity. Experiments similar to the 2D ConA targets, but with imposed perturbations, will be used to look at the growth of perturbations at late time.

- A goal of the NIF ignition point design has been to optimize the tradeoff between implosion velocity, fuel adiabat and mix. However, because of uncertainty in the underlying physics, the current point design parameters are likely not the optimal final choices. Calculations predict lower hydrodynamic instability growth rates for higher adiabat implosions and the ignition campaign has begun the process of designing and testing a higher adiabat implosion. Growth rate experiments will be conducted on this target as well as on the point design. The full range of targets used to optimize the NIF ignition point design, including cryo-layered implosions, will also be applied to this higher adiabat implosion. Having data for implosions with a range of fuel adiabats will help identify the optimal path to ignition.

- A number of experiments are planned to better understand and optimize the 1D performance of the NIF ignition capsules. A new 1D radiography technique, Refraction Enhanced Imaging (REI)[55] will be pursued to enable direct imaging of fuel radius and thickness versus time in cryo-layered implosions. To test the surrogacy of shock timing in standard keyhole targets, in which shocks

propagate through a cone filled with liquid deuterium, the capability of fielding keyhole targets with ignition thickness solid layers has been developed.[165] Targets are also being developed to explore the potential impact of various kinetic effects such as species separation[166] during the initial stages of shock propagation and hot spot formation, and deviations from a Maxwellian distribution of particles in the igniting fuel.

- A variety of modifications to the hohlraum are being explored. The current cylindrical hohlraum utilizes significant levels of cross-beam transfer from the outer beams to the inner beams to optimize radiation symmetry. Although we have been able to achieve the required radiation drive, increased scattering losses have come along with the required levels of cross-beam transfer. Current losses are about 15% or 200 kJ of laser energy. Hohlraums with a reduced need for cross beam transfer may have reduced LPI losses. Hohlraums with higher initial gas fill utilizing a higher picket, hohlraums with a higher-z gas fill such as neo-pentane or hohlraums with an embedded B-field to increase the temperature in the laser propagation regions, and hohlraums with larger clearance between the capsule and hohlraum waist such as one with a rugby geometry[152,167] all have potentially improved inner beam propagation and would require reduced cross beam transfer. Besides the potential energetics benefits, reduced cross-beam transfer would reduce the potential impact of quad-to-quad variations in cross-beam transfer which could contribute to random low mode asymmetry in the radiation flux. The ability to change the wavelength shift between inner and outer beams after the foot of the pulse is being explored as a way of providing greater flexibility in the use of cross beam transfer during different times in the pulse.

- Alternate ablators, such as HDC (or nano-crystalline diamond) and Be, are being developed. These ablators have potential advantages compared to CH and may provide an alternate path to ignition. HDC ablator capsules, because of their high density, have much shorter pulse lengths than CH capsules and this may enable the use of near-vacuum hohlraums with lower levels of LPI.

In the 3 yr period of experiments following completion of the NIF project, about half the time on the NIF facility was devoted to the development of a wide range of laser capabilities, facility infrastructure including the cryo-target positioner, diagnostics, and experimental target configurations required for a precision ignition campaign. Over this 3-yr period, about $1\frac{1}{2}$ yr were devoted to the experiments described above. In that short period of time, the NIC experiments came within about a factor of 3 in fuel pressure or the GLC needed for ignition. A wide range of experiments, as well as further improvements to the laser, targets, and diagnostics are now under way to develop the information needed to bridge the gap between current results and the conditions needed for ignition.

It is not possible for a Review article to capture all the latest results in a constantly evolving program such as the NIF Ignition Campaign. This review has focused on experiments from the end of the NIF project in 2009 until the end of the
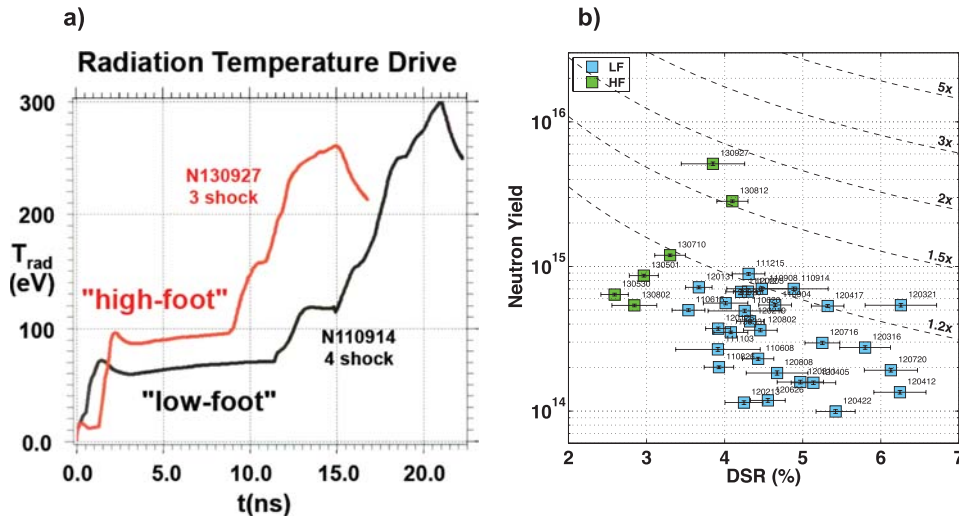
FIG. 115. (a) Comparison of a typical "low-foot" pulse used for most of the implosion experiments in the NIC campaign to a "high-foot" pulse designed for reduced hydrodynamic instability, (b) implosions using the "high-foot" pulse have achieved substantially higher yields than implosions using the "low-foot pulse." As a result, yield amplification from these implosions is now close to the alpha-dominated regime in which yield is more than doubled as a result of alpha deposition.

NIC in September 2012. Since the end of the NIC, a wide range of work following the path forward above has been carried out in the ignition campaign on NIF. One particular set of experiments that indicates the path forward summarized above is succeeding is captured in results from implosions with a slightly modified laser pulse as shown in Fig. 115(a). This "high-foot" pulse was designed to reduce hydrodynamic instability as described above. The higher initial radiation temperature in the "foot" of the pulse puts the imploding shell on a higher adiabat (about 2.3 versus 1.5 for the "low-foot") that increases ablation rates and density scale lengths in the shell. Because of the initially greater shock strength, the first shock transits the shell more quickly and the overall pulse is shortened. This change in pulse reduces hydrodynamic instability growth rates at the expense of shell compressibility. Other than this change in pulse shape, the high-foot implosions utilized the same capsule as the previous low-foot pulse and the same hohlraum geometry with a slightly higher initial gas fill. Targets with this pulse shape have gone through an initial round of implosion optimization using the same set of surrogate targets discussed above. The trade off between low adiabat for compressibility and hydrodynamic instability is one of the fundamental trade offs in ICF. Implosions using this modified pulse have achieved a factor of several increase in yield[168–171] with DSRs near the low end of those achieved with the "low-foot" pulse. Convergence ratios are about 30 for the "high-foot" instead of values closer to 40 for the "low-foot" pulse. As a result of the improved yield, as seen in Fig. 115(b), NIF implosions are now very near the point at which the yield is doubled as a result of alpha heating and the GLC(no-burn) is within about a factor of 2 of that required for ignition. In conjunction with the improved experimental performance, the simulated yields are in better correspondence with the measured yields as indicated in Fig. 116. The simulated 1D yields shown have the drive adjusted to match measured shock-timing and the measured implosion trajectory as discussed in Sec. V C. Because of this improved correspondence, we expect the calculations to be better guides for the choice of experiments going forward. As shown, the simulated yields have been within a factor of 2–3 of the measured yields as the experiments moved to higher velocity and higher

performance over a period of 5 months in 2013. To date, these implosions have not suffered from ablator mix into the hot spot as we have moved to higher velocity. As discussed above, high levels of mix were observed in the "low-foot" implosions as they were driven to higher velocity. This resulted in the rapid divergence in measured performance relative to calculations indicated in Fig. 116 for representative "low-foot" experiments. Based on the fact that the "high-foot" implosions have had low levels of mix, and the fact that techniques have been developed which will enable improvements to the low mode symmetry effects, there is clearly room for further improvement in performance.

The conclusion that the improved performance seen in cryo-layered "high-foot" implosions is due to reduction in hydrodynamic instability growth is supported by experiments carried since the end of the NIC with pre-imposed perturbations on NIF capsules in the keyhole geometry. Fig. 117 shows that these experiments have verified the reduced growth rates expected for the "high-foot" pulse
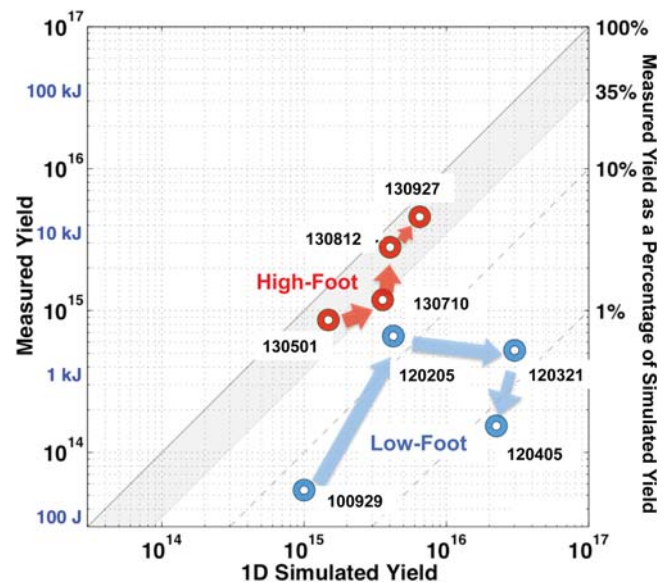

FIG. 116. Comparison of observed to simulated yield for representative "low-foot" experiments and for the recent "high-foot" shots showing the closer correspondence for the "high-foot" experiments.
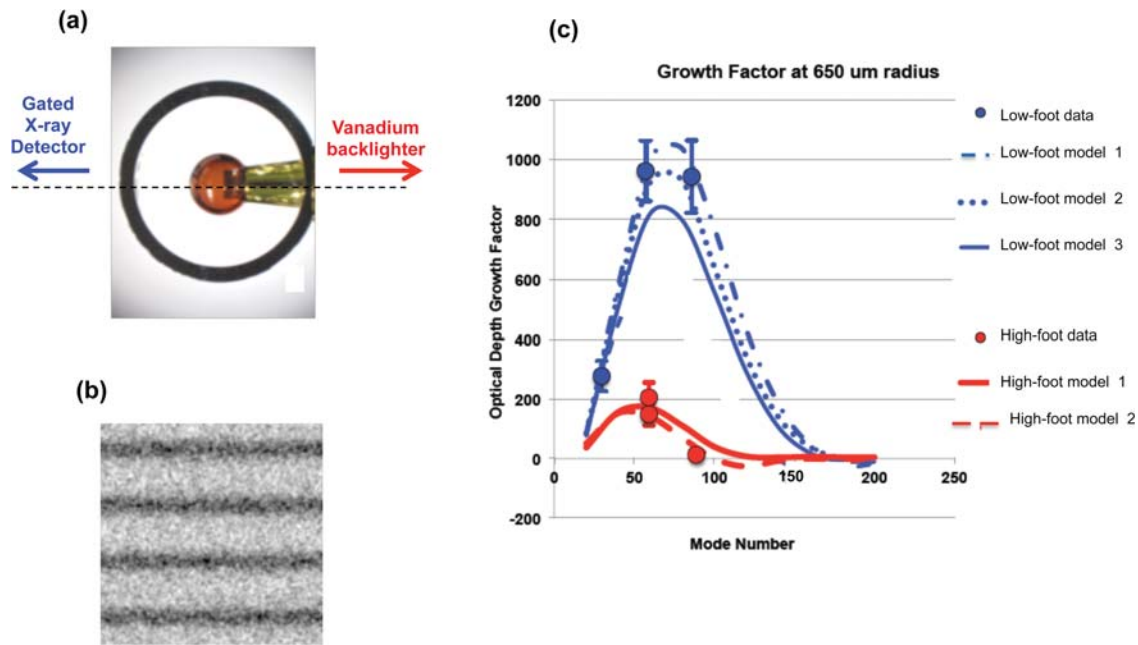
FIG. 117. Growth of hydrodynamic instabilities on NIF capsules shows the reduction expected for the high foot pulse relative to the low-foot pulse; (a) picture of the capsule with machined grooves in the keyhole geometry; (b) sample of data obtained for mode 60 (wavelength of 120 μm at the initial capsule radius of about 1100 μm) at an imploded radius of 500 μm for the low-foot pulse; (c) growth factors at a radius of 600 μm. The curves show the sensitivity to uncertainty in the modeling.

implosions.[169,172,173] As described in Sec. V B 8 and Fig. 94, perturbations are machined on the surface of a capsule into which a re-entrant cone is inserted. Fig. 117(a) shows a picture of a Si-doped CH shell attached to a re-entrant Au cone. The shell is backlit with a Vanadium backlighter and the growth of the perturbations is viewed with the GXD framing camera. These experiments obtained a sequence of images at varying radii as the capsule imploded. The initial experiments observed the growth to a radius of 500 μm. Extensions of these experiments to smaller radius, including stagnation, are planned. Data for modes 30, 60, and 90 (wavelengths of 240, 120, and 80 μm at the initial capsule radius of slightly greater than 1100 μm) were obtained. Data for mode 60 at 500 μm are shown in Fig. 117(b). The amplification in optical depth of the applied perturbations for both the low-foot and high-foot pulses is shown in Fig. 117(c) along with the calculated RT growth spectrum. The amplification of perturbations by the high-foot pulse, particularly those near mode 90 are clearly much reduced from those driven by the low-foot pulse. The calculated growth spectrum for the low-foot pulse is sensitive to both the details of the shock timing generated by the pulse and the EOS of the CH ablator. In Figure 117(c), curves 1 and 2 for the low-foot pulse show variations in the growth calculated using the same EOS for CH but using the shock timing from two different keyhole shock-timing experiments. Curves 2 and 3 utilize the same shock timing data but show the difference in growth resulting from different interpretations of the shock-hugoniot data and its implications for the EOS of a CH ablator. As indicated, growth of perturbations driven by the high-foot pulse is less sensitive to these uncertainties. Additional experiments of this type will be carried out to fill out the growth spectrum for CH and to obtain data for different pulses and different

ablators as we optimize the performance of the NIF implosions. It is likely that ignition will require a somewhat lower adiabat than that of the current "high-foot" pulse. A key challenge will be to retain favorable instability growth, or to reduce the seeds for growth, as the "high-foot" implosions are modified to achieve this lower adiabat. Calculations indicate that this is quite possible and these modified pulse shapes will be tested in future experiments.

Since the end of the NIC, experiments have begun in other categories of the path-forward, including experiments to evaluate alternate hohlraum geometries and gas fills, experiments to explore the performance of HDC as an alternate ablator, and keyhole experiments with solid DT layers instead of liquid D_2 to address surrogacy questions. The ongoing results from this work and the improved understanding of the underlying physics of ignition generated from the results will be incorporated into implosions designed to continue the recent progress toward ignition on the NIF.

ACKNOWLEDGMENTS

[1]See National Technical Information Services Document No. PB2013-110026, National Ignition Campaign Program Completion Report No. LLNL-AR-592032. Copies may be obtained from the National Technical Information Service, Springfield, VA 22161.

[2]J. D. Lindl, P. Amendt, R. L. Berger, S. G. Glendinning, S. H. Glenzer, S. W. Haan, R. L. Kauffman, O. L. Landen, and L. J. Suter, Phys. Plasmas **11**, 339 (2004).

[3]T. J. B. Collins, J. A. Marozas, K. S. Anderson, R. Betti, R. S. Craxton, J. A. Delettrez, V. N. Goncharov, D. R. Harding, F. J. Marshall, R. L.

McCrory, D. D. Meyerhofer, P. W. McKenty, P. B. Radha, A. Shvydky, S. Skupsky, and J. D. Zuegel, Phys. Plasmas **19**, 056308 (2012).

[4]E. I. Moses, J. Phys.: Conf. Ser. **112**, 012003 (2008).

[5]G. H. Miller, E. I. Moses, and C. R. Wuest, Nucl. Fusion **44**, S228 (2004).

[6]J. Meyer-ter-Vehn, Nucl. Fusion **22**, 561–566 (1982).

[7]M. D. Rosen, J. D. Lindl, and A. R. Thiessen, Laser Program Annual Report No. UCRL 50055-83 (1983), pp. 2–17 to 2–20, National Technical Information Service Document No. DE84017287. Copies may be obtained from the National Technical Information Service, Springfield, VA 22161.

[8]S. W. Haan, J. D. Lindl, D. A. Callahan, D. S. Clark, J. D. Salmonson, B. A. Hammel, L. J. Atherton, R. C. Cook, M. J. Edwards, S. Glenzer, A. V. Hamza, S. P. Hatchett, M. C. Herrmann, D. E. Hinkel, D. D. Ho, H. Huang, O. S. Jones, J. Kline, G. Kyrala, O. L. Landen, B. J. MacGowan, M. M. Marinak, D. D. Meyerhofer, J. L. Milovich, K. A. Moreno, E. I. Moses, D. H. Munro, A. Nikroo, R. E. Olson, K. Peterson, S. M. Pollaine, J. E. Ralph, H. F. Robey, B. K. Spears, P. T. Springer, L. J. Suter, C. A. Thomas, R. P. Town, R. Vesey, S. V. Weber, H. L. Wilkens, and D. C. Wilson, Phys. Plasmas **18**, 051001 (2011).

[9]W. K. Levedahl and J. D. Lindl, Nucl. Fusion **37**, 165 (1997).

[10]M. M. Basko and J. Johner, Nucl. Fusion **38**, 1779 (1998).

[11]M. C. Herrmann, M. Tabak, and J. D. Lindl, Nucl. Fusion **41**, 99 (2001).

[12]See R. Kishony and D. Shvarts, Phys. Plasmas **8**, 4925 (2001).

[13]D. S. Clark, S. W. Haan, and J. D. Salmonson, Phys. Plasmas **15**, 056305 (2008).

[14]O. L. Landen, J. Edwards, S. W. Haan, H. F. Robey, J. Milovich, B. K. Spears, S. V. Weber, D. S. Clark, J. D. Lindl, B. J. MacGowan, E. I. Moses, J. Atherton, P. A. Amendt, T. R. Boehly, D. K. Bradley, D. G. Braun, D. A. Callahan, P. M. Celliers, G. W. Collins, E. L. Dewald, L. Divol, J. A. Frenje, S. H. Glenzer, A. Hamza, B. A. Hammel, D. G. Hicks, N. Hoffman, N. Izumi, O. S. Jones, J. D. Kilkenny, R. K. Kirkwood, J. L. Kline, G. A. Kyrala, M. M. Marinak, N. Meezan, D. D. Meyerhofer, P. Michel, D. H. Munro, R. E. Olson, A. Nikroo, S. P. Regan, L. J. Suter, C. A. Thomas, and D. C. Wilson, Phys. Plasmas **18**, 051002 (2011).

[15]C. D. Zhou and R. Betti, Phys. Plasmas **15**, 102707 (2008).

[16]R. Betti, P. Y. Chang, B. K. Spears, K. S. Anderson, J. Edwards, M. Fatenejad, J. D. Lindl, R. L. McCrory, R. Nora, and D. Shvarts, Phys. Plasmas **17**, 058102 (2010); P. Y. Chang, R. Betti, B. K. Spears, K. S. Anderson, J. Edwards, M. Fatenajad, J. D. Lindl, R. L. McCrory, R. Nora, and D. Shvarts, Phys. Rev. Lett. **104**, 135002 (2010).

[17]M. J. Edwards, J. D. Lindl, B. K. Spears, S. V. Weber, L. J. Atherton, D. L. Bleuel, D. K. Bradley, D. A. Callahan, C. J. Cerjan, D. Clark, G. W. Collins, J. E. Fair, R. J. Fortner, S. H. Glenzer, S. W. Haan, B. A. Hammel, A. V. Hamza, S. P. Hatchett, N. Izumi, B. Jacoby, O. S. Jones, J. A. Koch, B. J. Kozioziemski, O. L. Landen, R. Lerche, B. J. MacGowan, A. J. MacKinnon, E. R. Mapoles, M. M. Marinak, M. Moran, E. I. Moses, D. H. Munro, D. H. Schneider, S. M. Sepke, D. A. Shaughnessy, P. T. Springer, R. Tommasini, L. Bernstein, W. Stoeffl, R. Betti, T. R. Boehly, T. C. Sangster, V. Yu. Glebov, P. W. McKenty, S. P. Regan, D. H. Edgell, J. P. Knauer, C. Stoeckl, D. R. Harding, S. Batha, G. Grim, H. W. Herrmann, G. Kyrala, M. Wilke, D. C. Wilson, J. Frenje, R. Petrasso, K. Moreno, H. Huang, K. C. Chen, E. Giraldez, J. D. Kilkenny, M. Mauldin, N. Hein, M. Hoppe, A. Nikroo, and R. J. Leeper, Phys. Plasmas **18**, 051003 (2011).

[18]J. H. Nuckolls, L. Wood, A. Thiessen, and G. B. Zimmerman, Nature **239**, 139 (1972).

[19]S. E. Koonin, Chair, Committee for the Review of the Department of Energy's Inertial Confinement Fusion Program, *Review of the Department of Energy's Inertial Confinement Fusion Program: The National Ignition Facility* (National Academy Press, Washington, DC, 1997).

[20]J. D. Lindl, Phys Plasmas **2**, 3933 (1995).

[21]S. Atzeni and J. Meyer-ter-Vehn, *The Physics of Inertial Fusion* (Oxford Science Publications, 2004), p. 32.

[22]M. J. Edwards, P. K. Patel, J. D. Lindl, B. K. Spears, S. V. Weber, L. J. Atherton, D. L. Bleue, D. K. Bradley, D. A. Callahan, C. J. Cerjan, D. S. Clark, G. W. Collins, J. E. Fair, R. J. Fortner, S. H. Glenzer, S. W. Haan, B. A. Hammel, A. V. Hamza, S. P. Hatchett, N. Izumi, B. Jacoby, O. S. Jones, J. A. Koch, B. J. Kozioziemski, O. L. Landen, R. Lerche, B. J. MacGowan, A. J. MacKinnon, E. R. Mapoles, M. M. Marinak, M. Moran, E. I. Moses, D. H. Munro, D. H. Schneider, S. M. Sepke, D. A. Shaughnessy, P. T. Springer, R. Tommasini, L. Bernstein, W. Stoeffl, R. Betti, T. R. Boehly, T. C. Sangster, V. Yu. Glebov, P. W. McKenty, S. P. Regan, D. H. Edgell, J. P. Knauer, C. Stoeckl, D. R. Harding, S. Batha,

G. Grim, H. W. Herrmann, G. Kyrala, M. Wilke, D. C. Wilson, J. Frenje, R. Petrasso, K. Moreno, H. Huang, K. C. Chen, E. Giraldez, J. D. Kilkenny, M. Mauldin, N. Hein, M. Hoppe, A. Nikroo, and R. J. Leeper, Phys. Plasmas **20**, 070501 (2013).

[23]S. W. Haan, J. Atherton, D. S. Clark, B. A. Hammel, D. A. Callahan, C. J. Cerjan, E. L. Dewald, S. Dixit, M. J. Edwards, S. Glenzer, S. P. Hatchett, D. Hicks, O. S. Jones, O. L. Landen, J. D. Lindl, M. M. Marinak, B. J. Macgowan, A. J. Mackinnon, N. B. Meezan, J. L. Milovich, D. H. Munro, H. F. Robey, J. D. Salmonson, B. K. Spears, L. J. Suter, R. P. Town, S. V. Weber, J. L. Kline, and D. C. Wilson, Fusion Sci. Technol. **63**, 67 (2013).

[24]L. M. Hively, Nucl. Technol./Fusion **3**, 199–200 (1983).

[25]P. T. Springer, C. Cerjan, R. Betti, J. A. Caggiano, M. J. Edwards, J. A. Frenje, V. Yu. Glebov, S. H. Glenzer, S. M. Glenn, N. Izumi, O. Jones, G. Kyrala, T. Ma, J. McNaney, M. Moran, D. H. Munro, S. Regan, T. C. Sangster, S. Sepke, H. Scott, R. P. J. Town, S. V. Weber, and B. Wilson, EPJ Web Conf. **59**, 04001 (2013).

[26]C. Cerjan, P. T. Springer, and S. M. Sepke, Phys. Plasmas **20**, 056319 (2013).

[27]H. Brysk, Plasma Phys. **15**, 611 (1973).

[28]B. Spears and J. Lindl, "Analysis of ICF ignition metrics" Phys. Plasmas (in preparation).

[29]C. D. Zhou and R. Betti, Phys. Plasmas **14**, 072703 (2007).

[30]B. K. Spears, S. Glenzer, M. J. Edwards, S. Brandon, D. Clark, R. P. J. Town, C. Cerjan, R. Dylla-Spears, E. Mapoles, D. Munro, J. Salmonson, S. Sepke, S. Weber, S. Hatchett, S. Haan, P. Springer, E. Moses, J. Kline, G. Kyrala, and D. Wilson, Phys. Plasmas **19**, 056316 (2012).

[31]B. A. Hammel, S. W. Haan, D. S. Clark, M. J. Edwards, S. H. Langer, M. M. Marinak, M. V. Patel, J. D. Salmonson, and H. A. Scott, High Energy Dens. Phys. **6**, 171 (2010).

[32]See http://www.sandia.gov/NNSA/ASC/ for Information on the ASC computers.

[33]G. B. Zimmerman and W. L. Kruer, Comments Plasma Phys. Controlled Fusion **2**, 51 (1975).

[34]M. M. Marinak, R. E. Tipton, O. L. Landen, T. J. Murphy, P. Amendt, S. W. Haan, S. P. Hatchett, C. J. Keane, R. McEachern, and R. Wallace, Phys. Plasmas **3**, 2070 (1996).

[35]R. L. Berger, C. H. Still, E. A. Williams, and A. B. Langdon, Phys. Plasmas **5**, 4337 (1998); C. H. Still, R. L. Berger, A. B. Langdon, D. E. Hinkel, L. J. Suter, and E. A. Williams, *ibid.* **7**, 2023 (2000); D. E. Hinkel, D. A. Callahan, A. B. Langdon, S. H. Langer, C. H. Still, and E. A. Williams, *ibid.* **15**, 056314 (2008).

[36]A. A. Hauer, L. Suter, N. Delamater, D. Ress, L. Powers, G. Magelssen, D. Harris, O. Landen, E. Lindmann, W. Hsing, D. Wilson, P. Amendt, R. Thiessen, R. Kopp, D. Phillion, B. Hammel, D. Baker, J. Wallace, R. Turner, M. Cray, R. Watt, J. Kilkenny, and J. Mack, Phys. Plasmas **2**, 2488 (1995).

[37]T. J. Murphy, J. M. Wallace, N. D. Delamater, C. W. Barnes, P. Gobby, A. A. Hauer, E. Lindman, G. Magelssen, J. B. Moore, J. A. Oertel, R. Watt, O. L. Landen, P. Amendt, M. Cable, C. Decker, B. A. Hammel, J. A. Koch, L. J. Suter, R. E. Turner, R. J. Wallace, F. J. Marshall, D. Bradley, R. S. Craxton, R. Keck, J. P. Knauer, R. Kremens, and J. D. Schnittman, Phys. Rev. Lett. **81**, 108 (1998).

[38]R. E. Turner, P. Amendt, O. L. Landen, S. G. Glendinning, P. Bell, C. Decker, B. A. Hammel, D. Kalantar, D. Lee, R. Wallace, D. Bradley, M. Cable, R. S. Craxton, R. Kremens, W. Seka, J. Schnittman, K. Thorp, T. J. Murphy, N. Delamater, C. W. Barnes, A. Hauer, G. Magelssen, and J. Wallace, Phys. Plasmas **7**, 333 (2000); R. E. Turner, P. A. Amendt, O. L. Landen, L. J. Suter, R. J. Wallace, and B. A. Hammel, *ibid.* **10**, 2429 (2003).

[39]G. A. Kyrala, S. Dixit, S. Glenzer, D. Kalantar, D. Bradley, N. Izumi, N. Meezan, O. L. Landen, D. Callahan, S. V. Weber, J. P. Holder, S. Glenn, M. J. Edwards, P. Bell, J. Kimbrough, J. Koch, R. Prasad, L. Suter, and J. Kilkenny, Rev. Sci. Instrum. **81**, 10E316 (2010); G. A. Kyrala, J. L. Kline, S. Dixit, S. Glenzer, D. Kalantar, D. Bradley, N. Izumi, N. Meezan, O. Landen, D. Callahan, S. V. Weber, J. P. Holder, S. Glenn, M. J. Edwards, J. Koch, L. J. Suter, S. W. Haan, R. P. J. Town, P. Michel, O. Jones, S. Langer, J. D. Moody, E. L. Dewald, T. Ma, J. Ralph, A. Hamza, E. Dzenitis, and J. Kilkenny, Phys. Plasmas **18**, 056307 (2011).

[40]D. H. Froula, D. Bower, M. Chrisp, S. Grace, J. H. Kamperschroer, T. M. Kelleher, R. K. Kirkwood, B. MacGowan, T. McCarville, N. Sewall, F. Y. Shimamoto, S. J. Shiromizu, B. Young, and S. H. Glenzer, Rev. Sci. Instrum. **75**, 4168 (2004).

[41]A. J. Mackinnon, T. McCarville, K. Piston, C. Niemann, G. Jones, I. Reinbachs, R. Costa, J. Celeste, G. Holtmeier, R. Griffith, R. Kirkwood,

B. MacGowan, S. H. Glenzer, and M. R. Latta, Rev. Sci. Instrum. **75**, 4183 (2004).

[42] E. L. Dewald, K. M. Campbell, R. E. Turner, J. P. Holder, O. L. Landen, S. H. Glenzer, R. L. Kauffman, L. J. Suter, M. Landon, M. Rhodes, and D. Lee, Rev. Sci. Instrum. **75**, 3759 (2004).

[43] J. W. McDonald, R. L. Kauffman, J. R. Celeste, M. A. Rhodes, F. D. Lee, L. J. Suter, A. P. Lee, J. M. Foster, and G. Slark, Rev. Sci. Instrum. **75**, 3753 (2004).

[44] M. D. Landon, J. A. Koch, S. S. Alvarez, P. M. Bell, F. D. Lee, and J. D. Moody, Rev. Sci. Instrum. **72**, 698 (2001).

[45] J. A. Oertel, R. Aragonez, T. Archuleta, C. Barnes, L. Casper, V. Fatherley, T. Heinrichs, R. King, D. Landers, F. Lopez, P. Sanchez, G. Sandoval, L. Schrank, P. Walsh, P. Bell, M. Brown, R. Costa, J. Holder, S. Montelongo, and N. Pederson, Rev. Sci. Instrum. **77**, 10E308 (2006).

[46] N. Delamater, G. Magelssen, and A. Hauer, Phys. Rev. E **53**, 5241 (1996).

[47] N. Delamater, P. Bradley, G. Magelssen, and D. Wilson, Rev. Sci. Instrum. **77**, 10E302 (2006).

[48] P. M. Celliers, D. K. Bradley, G. W. Collins, D. G. Hicks, T. R. Boehly, and W. J. Armstrong, Rev. Sci. Instrum. **75**, 4916 (2004); R. M. Malone, J. R. Bower, G. A. Capelle, J. R. Celeste, P. M. Celliers, B. C. Frogget, R. L. Guyton, M. I. Kaufman, G. A. Lare, T. L. Lee, B. J. MacGowan, S. Montelongo, E. W. Ng, T. L. Thomas, Jr., T. W. Tunnell, and P. W. Watts, Proc. SPIE **5523**, 148 (2004).

[49] D. H. Munro, P. M. Celliers, G. W. Collins, D. M. Gold, L. B. Da Silva, S. W. Haan, R. C. Cauble, B. A. Hammel, and W. W. Hsing, Phys. Plasmas **8**, 2245 (2001).

[50] T. R. Boehly, D. G. Hicks, P. M. Celliers, T. J. B. Collins, R. Earley, J. H. Eggert, D. Jacobs-Perkins, S. J. Moon, E. Vianello, D. D. Meyerhofer, and G. W. Collins, Phys. Plasmas **11**, L49 (2004).

[51] H. F. Robey, D. H. Munro, B. K. Spears, M. M. Marinak, O. S. Jones, M. V. Patel, S. W. Haan, J. D. Salmonson, O. L. Landen, T. R. Boehly, and A. Nikroo, J. Phys.: Conf. Ser. **112**, 022078 (2008).

[52] D. G. Hicks, B. K. Spears, D. G. Braun, R. E. Olson, C. M. Sorce, P. M. Celliers, G. W. Collins, and O. L. Landen, Rev. Sci. Instrum. **81**, 10E304 (2010); D. G. Hicks, B. K. Spears, D. G. Braun, P. M. Celliers, G. W. Collins, O. L. Landen, and R. E. Olson, Phys. Plasmas **17**, 102703 (2010).

[53] B. Spears, D. Hicks, C. Velsko, M. Stoyer, H. Robey, D. Munro, S. Haan, O. Landen, A. Nikroo, and H. Huang, J. Phys.: Conf. Ser. **112**, 022003 (2008).

[54] R. E. Olson, M. Geissel, J. W. Kellogg, D. G. Hicks, B. K. Spears, J. P. Holder, O. L. Landen, G. R. Bennett, A. D. Edens, B. W. Atherton, and R. J. Leeper, Rev. Sci. Instrum. **79**, 10E913 (2008).

[55] J. A. Koch, O. L. Landen, B. J. Kozioziemski, N. Izumi, E. L. Dewald, J. D. Salmonson, and B. A. Hammel, J. Appl. Phys. **105**, 113112 (2009); J. A. Koch, O. L. Landen, L. J. Suter, L. P. Masse, D. S. Clark, S. Ross, A. J. Mackinnon, N. B. Meezan, C. A. Thomas, and Y. Ping, Appl. Opt. **52**, 3538 (2013); J. A. Koch, O. L. Landen, L. J. Suter, and L. P. Masse, J. Opt. Soc. Am. A **30**, 1460 (2013).

[56] Y. Ping, O. L. Landen, D. G. Hicks, J. A. Koch, R. Wallace, C. Sorce, B. A. Hammel, and G. W. Collins, JINST **6**, P09004 (2011).

[57] C. Cherfils, S. G. Glendinning, D. Galmiche, B. A. Remington, A. L. Richard, S. Haan, R. Wallace, N. Dague, and D. H. Kalantar, Phys. Rev. Lett. **83**, 5507 (1999); S. G. Glendinning, J. Colvin, S. W. Haan, D. H. Kalantar, O. L. Landen, M. M. Marinak, B. A. Remington, R. Wallace, C. Cherfils, N. Dague, L. Divol, D. Galmiche, and A. L. Richard, Phys. Plasmas **7**, 2033 (2000).

[58] V. A. Smalyuk, S. X. Hu, J. D. Hager, J. A. Delettrez, D. D. Meyerhofer, T. C. Sangster, and D. Shvarts, Phys. Rev. Lett. **103**, 105001 (2009); Phys Plasmas **16**, 112701 (2009).

[59] B. A. Hammel, H. A. Scott, S. P. Regan, C. Cerjan, D. S. Clark, M. J. Edwards, R. Epstein, S. H. Glenzer, S. W. Haan, N. Izumi, J. A. Koch, G. A. Kyrala, O. L. Landen, S. H. Langer, K. Peterson, V. A. Smalyuk, L. J. Suter, and D. C. Wilson, Phys. Plasmas **18**, 056310 (2011); S. P. Regan, R. Epstein, B. A. Hammel, L. J. Suter, J. Ralph, H. Scott, M. A. Barrios, D. K. Bradley, D. A. Callahan, C. Cerjan, G. W. Collins, S. N. Dixit, T. Doeppner, M. J. Edwards, D. R. Farley, S. Glenn, S. H. Glenzer, I. E. Golovkin, S. W. Haan, A. Hamza, D. G. Hicks, N. Izumi, J. D. Kilkenny, J. L. Kline, G. A. Kyrala, O. L. Landen, T. Ma, J. J. MacFarlane, R. C. Mancini, R. L. McCrory, N. B. Meezan, D. D. Meyerhofer, A. Nikroo, K. J. Peterson, T. C. Sangster, P. Springer, and R. P. J. Town, *ibid.* **19**, 056307 (2012).

[60] J. M. Gostic, D. A. Shaughnessy, K. T. Moore, I. D. Hutcheon, P. M. Grant, and K. J. Moody, Rev. Sci. Instrum. **83**, 10D904 (2012).

[61] D. H. Kalantar, S. W. Haan, B. A. Hammel, C. J. Keane, O. L. Landen, and D. H. Munro, Rev. Sci. Instrum. **68**, 814 (1997).

[62] F. J. Marshall, P. W. McKenty, J. A. Delettrez, R. Epstein, J. P. Knauer, V. A. Smalyuk, J. A. Frenje, C. K. Li, R. D. Petrasso, F. H. Seguin *et al.*, Phys. Rev. Lett. **102**, 185004 (2009).

[63] M. A. Barrios, K. B. Fournier, S. P. Regan, O. Landen, Y. P. Opachich, K. Widmann, M. May, S. F. Khan, D. K. Bradley, and G. W. Collins, High Energy Dens. Phys. **9**, 626 (2013).

[64] R. Tommasini, S. P. Hatchett, D. S. Hey, C. Iglesias, N. Izumi, J. A. Koch, O. L. Landen, A. J. MacKinnon, C. Sorce, J. A. Delettrez, V. Yu. Glebov, T. C. Sangster, and C. Stoeckl, Phys. Plasmas **18**, 056309 (2011).

[65] D. R. Farley, N. Izumi, and O. L. Landen, Nucl. Instrum. Methods Phys. Res. A **705**, 17 (2013).

[66] S. H. Glenzer, D. A. Callahan, A. J. MacKinnon, J. L. Kline, G. Grim, E. T. Alger, R. L. Berger, L. A. Bernstein, R. Betti, D. L. Bleuel, T. R. Boehly, D. K. Bradley, S. C. Burkhart, R. Burr, J. A. Caggiano, C. Castro, D. T. Casey, C. Choate, D. S. Clark, P. Celliers, C. J. Cerjan, G. W. Collins, E. L. Dewald, P. DiNicola, J. M. DiNicola, L. Divol, S. Dixit, T. Döppner, R. Dylla-Spears, E. Dzenitis, M. Eckart, G. Erbert, D. Farley, J. Fair, D. Fittinghoff, M. Frank, L. J. A. Frenje, S. Friedrich, D. T. Casey, M. Gatu Johnson, C. Gibson, E. Giraldez, V. Glebov, S. Glenn, N. Guler, S. W. Haan, B. J. Haid, B. A. Hammel, A. V. Hamza, C. A. Haynam, G. M. Heestand, M. Hermann, H. W. Hermann, D. G. Hicks, D. E. Hinkel, J. P. Holder, D. M. Holunda, J. B. Horner, W. W. Hsing, H. Huang, N. Izumi, M. Jackson, O. S. Jones, D. H. Kalantar, R. Kauffman, J. D. Kilkenny, R. K. Kirkwood, J. Klingmann, T. Kohut, J. P. Knauer, J. A. Koch, B. Kozioziemki, G. A. Kyrala, A. L. Kritcher, J. Kroll, K. La Fortune, L. Lagin, O. L. Landen, D. W. Larson, D. LaTray, R. J. Leeper, S. Le Pape, J. D. Lindl, R. Lowe-Webb, T. Ma, J. McNaney, A. G. MacPhee, T. N. Malsbury, E. Mapoles, C. D. Marshall, N. B. Meezan, F. Merrill, P. Michel, J. D. Moody, A. S. Moore, M. Moran, K. A. Moreno, D. H. Munro, B. R. Nathan, A. Nikroo, R. E. Olson, C. D. Orth, A. E. Pak, P. K. Patel, T. Parham, R. Petrasso, J. E. Ralph, H. Rinderknecht, S. P. Regan, H. F. Robey, J. S. Ross, M. D. Rosen, R. Sacks, J. D. Salmonson, R. Saunders, J. Sater, C. Sangster, M. B. Schneider, F. H. Séguin, M. J. Shaw, B. K. Spears, P. T. Springer, W. Stoeffl, L. J. Suter, C. A. Thomas, R. Tommasini, R. P. J. Town, C. Walters, S. Weaver, S. V. Weber, P. J. Wegner, P. K. Whitman, K. Widmann, C. C. Widmayer, C. H. Wilde, D. C. Wilson, B. Van Wonterghem, B. J. MacGowan, L. J. Atherton, M. J. Edwards, and E. I. Moses, Phys Plasmas **19**, 056318 (2012).

[67] S. Glenn, J. Koch, D. K. Bradley, N. Izumi, P. Bell, J. Holder, G. Stone, R. Prasad, A. MacKinnon, P. Springer, O. L. Landen, and G. Kyrala, Rev. Sci. Instrum. **81**, 10E539 (2010).

[68] N. Izumi, G. Stone, C. Hagmann, C. Sorce, D. K. Bradley, M. Moran, O. L. Landen, P. Springer, W. Stoeffl, R. Tommasini, H. W. Hermann, G. A. Kyrala, V. Y. Glebov, J. Knauer, T. C. Sangster, and J. A. Koch, J. Phys.: Conf. Ser. **244**, 032048 (2010); N. Izumi, C. Hagmann, G. Stone, D. Hey, S. Glenn, A. Conder, A. Teruya, C. Sorce, R. Tommasini, W. Stoeffl, O. L. Landen, H. W. Herrmann, G. A. Kyrala, R. Bahukutumbi, V. Y. Glebov, T. C. Sangster, M. Eckart, A. J. Mackinnon, J. A. Koch, D. K. Bradley, and P. Bell, Rev. Sci. Instrum. **81**, 10E515 (2010).

[69] J. A. Koch, S. W. Haan, and R. C. Mancini, J. Quantum Spectrosc. Radiat. Transfer **88**, 433 (2004); T. Ma, N. Izumi, R. Tommasini, D. K. Bradley, P. Bell, C. J. Cerjan, S. Dixit, T. Döppner, O. Jones, J. L. Kline, G. Kyrala, O. L. Landen, S. LePape, A. J. Mackinnon, H.-S. Park, P. K. Patel, R. R. Prasad, J. Ralph, S. P. Regan, V. A. Smalyuk, P. T. Springer, L. Suter, R. P. J. Town, S. V. Weber, and S. H. Glenzer, Rev. Sci. Instrum. **83**, 10E115 (2012); N. Izumi, T. Ma, M. Barrios, L. R. Benedetti, D. Callahan, C. Cerjan, J. Edwards, S. Glenn, S. Glenzer, J. Kilkenny, J. Kline, G. Kyrala, O. L. Landen, S. Regan, L. Suter, R. Tommasini, R. Town, A. J. Mackinnon, P. Bell, and D. K. Bradley, *ibid.* **83**, 10E121 (2012).

[70] P. M. Bell, D. K. Bradley, J. D. Kilkenny, A. Conder, C. Cerjan, C. Hagmann, D. Hey, N. Izumi, J. Moody, A. Teruya, J. Celeste, J. Kimbrough, H. Khater, M. J. Eckart, and J. Ayers, Rev. Sci. Instrum. **81**, 10E540 (2010).

[71] S. R. Nagel, T. J. Hilsabeck, P. M. Bell, D. K. Bradley, M. J. Ayers, M. A. Barrios, B. Felker, R. F. Smith, G. W. Collins, O. S. Jones, J. D. Kilkenny, T. Chung, K. Piston, K. S. Raman, B. Sammuli, J. D. Hares, and A. K. L. Dymoke-Bradshaw, Rev. Sci. Instrum. **83**, 10E116 (2012).

[72] E. Loomis, G. Grim, C. Wilde, D. C. Wilson, M. Wilke, J. Finch, G. Morgan, I. Tregillis, and D. Clark, J. Phys.: Conf. Ser. **244**, 032051 (2010); F. E. Merrill, D. Bower, R. Buckles, D. D. Clark, C. R. Danly, O.

B. Drury, J. M. Dzenitis, V. E. Fatherley, D. N. Fittinghoff, R. Gallegos, G. P. Grim, N. Guler, E. N. Loomis, S. Lutz, R. M. Malone, D. D. Martinson, D. Mares, D. J. Morley, G. L. Morgan, J. A. Oertel, I. L. Tregillis, P. L. Volegov, P. B. Weiss, C. H. Wilde, and D. C. Wilson, Rev. Sci. Instrum. **83**, 10D317 (2012).

[73]D. C. Wilson, W. C. Mead, L. Disdier, M. Houry, J.-L. Bourgade, and T. J. Murphy, Nucl. Instrum. Methods Phys. Res. A **488**, 400 (2002).

[74]J. A. Frenje, R. Bionta, E. J. Bond, J. A. Caggiano, D. T. Casey, C. Cerjan, J. Edwards, M. Eckart, D. N. Fittinghoff, S. Friedrich, V. Yu. Glebov, S. Glenzer, G. Grim, S. Haan, R. Hatarik, S. Hatchett, M. Gatu Johnson, O. S. Jones, J. D. Kilkenny, J. P. Knauer, O. Landen, R. Leeper, S. Le Pape, R. Lerche, C. K. Li, A. Mackinnon, J. McNaney, F. E. Merrill, M. Moran, D. H. Munro, T. J. Murphy, R. D. Petrasso, R. Rygg, T. C. Sangster, F. H. Seguin, S. Sepke, B. Spears, P. Springer, C. Stoeckl, and D. C. Wilson, Nucl. Fusion **53**, 043014 (2013).

[75]Z. A. Ali, V. Y. Glebov, M. Cruz, T. Duffy, C. Stoeckl, S. Roberts, T. C. Sangster, R. Tommasini, A. Throop, M. Moran, L. Dauffy, and C. Horsefield, Rev. Sci. Instrum. **79**, 10E527 (2008); V. Y. Glebov, D. D. Meyerhofer, T. C. Sangster, C. Stoeckl, S. Roberts, C. A. Barrera, J. R. Celeste, C. J. Cerjan, L. S. Dauffy, D. C. Eder, R. L. Griffith, S. W. Haan, B. A. Hammel, S. P. Hatchett, N. Izumi, J. R. Kimbrough, J. A. Koch, O. L. Landen, R. A. Lerche, B. J. MacGowan, M. J. Moran, E. W. Ng, T. W. Phillips, P. M. Song, R. Tommasini, B. K. Young, S. E. Caldwell, G. P. Grim, S. C. Evans, J. M. Mack, T. J. Sedillo, M. D. Wilke, D. Casey, J. A. Frenje, C. K. Li, R. D. Petrasso, F. H. Sequin, J. L. Bourgade, L. Disdier, M. Houry, I. Lantuejoul, O. Landoas, G. A. Chandler, G. W. Cooper, R. J. Leeper, R. E. Olson, C. L. Ruiz, M. A. Sweeney, S. P. Padalino, C. Horsfield, and B. A. Davis, *ibid.* **77**, 10E715 (2006); V. Y. Glebov, C. Stoeckl, T. C. Sangster, S. Roberts, R. A. Lerche, and G. J. Schmid, IEEE Trans. Plasma Sci. **33**, 70–76 (2005); V. Y. Glebov, C. Stoeckl, T. C. Sangster, S. Roberts, G. J. Schmid, R. A. Lerche, and M. J. Moran, Rev. Sci. Instrum. **75**, 3559 (2004); G. J. Schmid, R. L. Griffith, N. Izumi, J. A. Koch, R. A. Lerche, M. J. Moran, T. W. Phillips, R. E. Turner, V. Y. Glebov, T. C. Sangster, and C. Stoeckl, *ibid.* **74**, 1828–1831 (2003); M. Gatu Johnson, J. A. Frenje, D. T. Casey, C. K. Li, F. H. Séguin, R. Petrasso, R. Ashabranner, R. M. Bionta, D. L. Bleuel, E. J. Bond, J. A. Caggiano, A. Carpenter, C. J. Cerjan, T. J. Clancy, T. Doeppner, M. J. Eckart, M. J. Edwards, S. Friedrich, S. H. Glenzer, S. W. Haan, E. P. Hartouni, R. Hatarik, S. P. Hatchett, O. S. Jones, G. Kyrala, S. Le Pape, R. A. Lerche, O. L. Landen, T. Ma, A. J. MacKinnon, M. A. McKernan, M. J. Moran, E. Moses, D. H. Munro, J. McNaney, H. S. Park, J. Ralph, B. Remington, J. R. Rygg, S. M. Sepke, V. Smalyuk, B. Spears, P. T. Springer, C. B. Yeamans, M. Farrell, D. Jasion, J. D. Kilkenny, A. Nikroo, R. Paguio, J. P. Knauer, V. Yu. Glebov, T. C. Sangster, R. Betti, C. Stoeckl, J. Magoon, M. J. Shoup III, G. P. Grim, J. Kline, G. L. Morgan, T. J. Murphy, R. J. Leeper, C. L. Ruiz, G. W. Cooper, and A. J. Nelson, *ibid.* **83**, 10D308 (2012).

[76]J. A. Frenje, D. T. Casey, C. K. Li, F. H. Seguin, R. D. Petrasso, V. Y. Glebov, P. B. Radha, T. C. Sangster, D. D. Meyerhofer, S. P. Hatchett, S. W. Haan, C. J. Cerjan, O. L. Landen, K. A. Fletcher, and R. J. Leeper, Phys. Plasmas **17**, 056311 (2010).

[77]D. T. Casey, J. A. Frenje, M. Gatu Johnson, F. H. Séguin, C. K. Li, R. D. Petrasso, V. Yu. Glebov, J. Katz, J. Magoon, D. D. Meyerhofer, T. C. Sangster, M. Shoup, J. Ulreich, R. C. Ashabranner, R. M. Bionta, A. C. Carpenter, B. Felker, H. Y. Khater, S. LePape, A. MacKinnon, M. A. McKernan, M. Moran, J. R. Rygg, M. F. Yeoman, R. Zacharias, R. J. Leeper, K. Fletcher, M. Farrell, D. Jasion, J. Kilkenny, and R. Paguio, Rev. Sci. Instrum. **84**, 043506 (2013).

[78]M. Gatu Johnson, D. T. Casey, J. A. Frenje, C.-K. Li, F. H. Seguin, R. D. Petrasso, R. Ashabranner, R. Bionta, S. LePape, M. McKernan, A. Mackinnon, J. D. Kilkenny, J. Knauer, and T. C. Sangster, Phys. Plasmas **20**, 042707 (2010).

[79]D. L. Bleuel, C. B. Yeamans, L. A. Bernstein, R. M. Bionta, J. A. Caggiano, D. T. Casey, G. W. Cooper, O. B. Drury, J. A. Frenje, C. A. Hagmann, R. Hatarik, J. P. Knauer, M. Gatu Johnson, K. M. Knittel, R. J. Leeper, J. M. McNaney, M. Moran, C. L. Ruiz, and D. H. G. Schneider, Rev. Sci. Instrum. **83**, 10D313 (2012).

[80]B. Singh, Nuclear Data Sheets for A = 89, Vol. 85, 1, 101 (1998); H. Junde, Nuclear Data Sheets for A = 6, Vol. 9, 366 (2000).

[81]H. W. Herrmann, N. Hoffman, D. C. Wilson, W. Stoeffl, L. Dauffy, Y. H. Kim, A. McEvoy, C. S. Young, J. M. Mack, C. J. Horsfield, M. Rubery, E. K. Miller, and Z. A. Ali, Rev. Sci. Instrum. **81**, 10D333 (2010).

[82]S. H. Glenzer, B. J. MacGowan, P. Michel, N. B. Meezan, L. J. Suter, S. N. Dixit, J. L. Kline, G. A. Kyrala, D. K. Bradley, D. A. Callahan, E. L. Dewald, L. Divol, E. Dzenitis, M. J. Edwards, A. V. Hamza, C. A. Haynam, D. E. Hinkel, D. H. Kalantar, J. D. Kilkenny, O. L. Landen, J. D. Lindl, S. LePape, J. D. Moody, A. Nikroo, T. Parham, M. B. Schneider, R. P. J. Town, P. Wegner, K. Widmann, P. Whitman, B. K. F. Young, B. Van Wonterghem, L. J. Atherton, and E. I. Moses, Science **327**, 1228 (2010).

[83]N. B. Meezan, L. J. Atherton, D. A. Callahan, E. L. Dewald, S. Dixit, E. G. Dzenitis, M. J. Edwards, C. A. Haynam, D. E. Hinkel, O. S. Jones, O. Landen, R. A. London, P. A. Michel, J. D. Moody, J. L. Milovich, M. B. Schneider, C. A. Thomas, R. P. J. Town, A. L. Warrick, S. V. Weber, K. Widmann, S. H. Glenzer, L. J. Suter, B. J. MacGowan, J. L. Kline, G. A. Dyrala, and A. Nikroo, Phys. Plasmas **17**, 056304 (2010).

[84]J. D. Lindl, L. J. Atherton, P. A. Amendt, S. Batha, P. Bell, R. L. Berger, R. Betti, D. L. Bleuel, T. R. Boehly, D. K. Bradley, D. G. Braun, D. A. Callahan, P. M. Celliers, C. J. Cerjan, D. S. Clark, G. W. Collins, R. C. Cook, E. L. Dewald, L. Divol, S. N. Dixit, E. Dzenitis, M. J. Edwards, J. E. Fair, R. J. Fortner, J. A. Frenje, V. Yu. Glebov, S. H. Glenzer, G. Grim, S. W. Haan, A. V. Hamza, B. A. Hammel, D. R. Harding, S. P. Hatchett, C. A. Haynam, M. C. Herrmann, D. G. Hicks, D. E. Hinkel, D. D. Ho, N. Hoffman, H. Huang, N. Izumi, B. Jacoby, O. S. Jones, D. H. Kalantar, R. Kauffman, J. D. Kilkenny, R. K. Kirkwood, J. L. Kline, J. P. Knauer, J. A. Koch, B. J. Kozioziemski, G. A. Kyrala, K. La Fortune, O. L. Landen, D. Larson, R. Lerche, S. Le Pape, R. London, B. J. MacGowan, A. J. MacKinnon, T. N. Malsbury, E. R. Mapoles, M. M. Marinak, P. W. McKenty, N. Meezan, D. D. Meyerhofer, P. Michel, J. Milovich, J. D. Moody, M. Moran, K. A. Moreno, E. I. Moses, D. H. Munro, A. Nikroo, R. E. Olson, T. Parham, R. W. Patterson, K. Peterson, R. Petrasso, S. M. Pollaine, J. E. Ralph, S. P. Regan, H. F. Robey, M. D. Rosen, R. Sacks, J. D. Salmonson, T. C. Sangster, S. M. Sepke, D. H. Schneider, M. B. Schneider, M. Shaw, B. K. Spears, P. T. Springer, C. Stoeckl, L. J. Suter, C. A. Thomas, R. Tommasini, R. P. Town, B. M. VanWonterghem, R. Vesey, S. V. Weber, P. J. Wegner, K. Widman, C. C. Widmayer, M. Wilke, H. L. Wilkens, E. A. Williams, D. C. Wilson, and B. K. Young, Nucl. Fusion **51**, 094024 (2011).

[85]P. Michel, S. H. Glenzer, L. Divol, D. K. Bradley, D. Callahan, S. Dixit, S. Glenn, D. Hinkel, R. K. Kirkwood, J. L. Kline, W. L. Kruer, G. A. Kyrala, S. Le Pape, N. B. Meezan, R. Town, K. Widmann, E. A. Williams, B. J. MacGowan, J. L. Lindl, and L. J. Suter, Phys. Plasmas **17**, 056305 (2010).

[86]R. K. Kirkwood, J. D. Moody, J. Kline, E. Dewald, S. Glenzer, L. Divol, P. Michel, D. Hinkel, R. Berger, E. Williams, J. Milovich, L. Yin, H. Rose, B. MacGowan, O. Landen, M. Rosen, and J. Lindl, Plasma Phys. Controlled Fusion **55**, 103001 (2013).

[87]H. A. Scott and S. B. Hansen, High Energy Dens. Phys. **6**, 39 (2010).

[88]C. A. Iglesias and B. G. Wilson, J. Quantum Spectrosc. Radiat. Transfer **52**, 127 (1994).

[89]L. Suter, S. Hansen, M. Rosen, P. Springer, and S. Haan, in *Atomic Processes in Plasmas*, edited by K. B. Fournier (American Institute of Physics, New York, 2009), p. 3; Y. T. Lee, J. Quantum Spectrosc. Radiat. Transfer **38**, 131 (1987).

[90]G. Schurtz, S. Gary, S. Hulin, C. Chenais-Popovics, J.-C. Gauthier, F. Thais, J. Breil, F. Durut, J.-L. Feugeas, P.-H. Maire, P. Nicolaï, O. Peyrusse, C. Reverdin, G. Soullié, V. Tikhonchuk, B. Villette, and C. Fourment, Phys. Rev. Lett. **98**, 095002 (2007);

[91]G. P. Schurtz, P. D. Nicolai, and M. Busquet, Phys. Plasmas **7**, 4238 (2000).

[92]E. L. Dewald, M. Rosen, S. H. Glenzer, L. J. Suter, F. Girard, J. P. Jadaud, J. Schein, C. Constantin, F. Wagon, G. Huser, P. Neumayer, and O. L. Landen, Phys. Plasmas **15**, 072706 (2008).

[93]M. D. Rosen, H. A. Scott, D. E. Hinkel, E. A. Williams, D. A. Callahan, R. P. J. Town, L. Divol, P. A. Michel, W. L. Kruer, L. J. Suter, R. A. London, J. A. Harte, and G. B. Zimmerman, High Energy Dens. Phys. **7**, 180 (2011).

[94]J. L. Kline, S. H. Glenzer, R. E. Olson, L. J. Suter, K. Widmann, D. A. Callahan, S. N. Dixit, C. A. Thomas, D. E. Hinkel, E. A. Williams, A. S. Moore, J. Celeste, E. Dewald, W. W. Hsing, A. Warrick, J. Atherton, S. Azevedo, R. Beeler, R. Berger, A. Conder, L. Divol, C. A. Haynam, D. H. Kalantar, R. Kauffman, G. A. Kyrala, J. Kilkenny, J. Liebman, S. Le Pape, D. Larson, N. B. Meezan, P. Michel, J. Moody, M. D. Rosen, M. B. Schneider, B. Van Wonterghem, R. J. Wallace, B. K. Young, O. L. Landen, and B. J. MacGowan, Phys. Rev. Lett. **106**, 085003 (2011);

[95]R. E. Olson, L. J. Suter, J. L. Kline, D. A. Callahan, M. D. Rosen, S. N. Dixit, O. L. Landen, N. B. Meezan, J. D. Moody, C. A. Thomas, A. Warrick, K. Widmann, E. A. Williams, and S. H. Glenzer, Phys. Plasmas **19**, 053301 (2012).

[96]S. H. Glenzer, B. J. MacGowan, N. B. Meezan, P. A. Adams, J. B. Alfonso, E. T. Alger, Z. Alherz, L. F. Alvarez, S. S. Alvarez, P. V. Amick, K. S. Andersson, S. D. Andrews, G. J. Antonini, P. A. Arnold, D. P. Atkinson, L. Auyang, S. G. Azevedo, B. N. M. Balaoing, J. A. Baltz, F. Barbosa, G. W. Bardsley, D. A. Barker, A. I. Barnes, A. Baron, R. G. Beeler, B. V. Beeman, L. R. Belk, J. C. Bell, P. M. Bell, R. L. Berger, M. A. Bergonia, L. J. Bernardez, L. V. Berzins, R. C. Bettenhausen, L. Bezerides, S. D. Bhandarkar, C. L. Bishop, E. J. Bond, D. R. Bopp, J. A. Borgman, J. R. Bower, G. A. Bowers, M. W. Bowers, D. T. Boyle, D. K. Bradley, J. L. Bragg, J. Braucht, D. L. Brinkerhoff, D. F. Browning, G. K. Brunton, S. C. Burkhart, S. R. Burns, K. E. Burns, B. Burr, L. M. Burrows, R. K. Butlin, N. J. Cahayag, D. A. Callahan, P. S. Cardinale, R. W. Carey, J. W. Carlson, A. D. Casey, C. Castro, J. R. Celeste, A. Y. Chakicherla, F. W. Chambers, C. Chan, H. Chandrasekaran, C. Chang, R. F. Chapman, K. Charron, Y. Chen, M. J. Christensen, A. J. Churby, T. J. Clancy, B. D. Cline, L. C. Clowdus, D. G. Cocherell, F. E. Coffield, S. J. Cohen, R. L. Costa, J. R. Cox, G. M. Curnow, M. J. Dailey, P. M. Danforth, R. Darbee, P. S. Datte, J. A. Davis, G. A. Deis, R. D. Demaret, E. L. Dewald, P. Di Nicola, J. M. Di Nicola, L. Divol, S. Dixit, D. B. Dobson, T. Doppner, J. D. Driscoll, J. Dugorepec, J. J. Duncan, P. C. Dupuy, E. G. Dzenitis, M. J. Eckart, S. L. Edson, J. G. Edwards, M. J. Edwards, O. D. Edwards, P. W. Edwards, J. C. Ellefson, C. H. Ellerbee, G. V. Erbert, C. M. Estes, W. J. Fabyan, R. N. Fallejo, M. Fedorov, B. Felker, J. T. Fink, M. D. Finney, L. F. Finnie, M. J. Fischer, J. M. Fisher, B. T. Fishler, J. W. Florio, A. Forsman, C. B. Foxworthy, R. M. Franks, T. Frazier, G. Frieder, T. Fung, G. N. Gawinski, C. R. Gibson, E. Giraldez, S. M. Glenn, B. P. Golick, H. Gonzales, S. A. Gonzales, M. J. Gonzalez, K. L. Griffin, J. Grippen, S. M. Gross, P. H. Gschweng, G. Gururangan, K. Gu, S. W. Haan, S. R. Hahn, B. J. Haid, J. E. Hamblen, B. A. Hammel, A. V. Hamza, D. L. Hardy, D. R. Hart, R. G. Hartley, C. A. Haynam, G. M. Heestand, M. R. Hermann, G. L. Hermes, D. S. Hey, R. L. Hibbard, D. G. Hicks, D. E. Hinkel, D. L. Hipple, J. D. Hitchcock, D. L. Hodtwalker, J. P. Holder, J. D. Hollis, G. M. Holtmeier, S. R. Huber, A. W. Huey, D. N. Hulsey, S. L. Hunter, T. R. Huppler, M. S. Hutton, N. Izumi, J. L. Jackson, M. A. Jackson, K. S. Jancaitis, D. R. Jedlovec, B. Johnson, M. C. Johnson, T. Johnson, M. P. Johnston, O. S. Jones, D. H. Kalantar, J. H. Kamperschroer, R. L. Kauffman, G. A. Keating, L. M. Kegelmeyer, S. L. Kenitzer, J. R. Kimbrough, K. King, R. K. Kirkwood, J. L. Klingmann, K. M. Knittel, T. R. Kohut, K. G. Koka, S. W. Kramer, J. E. Krammen, K. G. Krauter, G. W. Krauter, E. K. Krieger, J. J. Kroll, K. N. La Fortune, L. J. Lagin, V. K. Lakamsani, O. L. Landen, S. W. Lane, A. B. Langdon, S. H. Langer, N. Lao, D. W. Larson, D. Latray, G. T. Lau, S. Le Pape, B. L. Lechleiter, Y. Lee, T. L. Lee, J. Li, J. A. Liebman, J. D. Lindl, S. F. Locke, H. K. Loey, R. A. London, F. J. Lopez, D. M. Lord, R. R. Lowe-Webb, J. G. Lown, A. P. Ludwigsen, N. W. Lum, R. R. Lyons, T. Ma, A. J. MacKinnon, M. D. Magat, D. T. Maloy, T. N. Malsbury, G. Markham, R. M. Marquez, A. A. Marsh, C. D. Marshall, S. R. Marshall, I. L. Maslennikov, D. G. Mathisen, G. J. Mauger, M.-Y. Mauvais, J. A. McBride, T. McCarville, J. B. McCloud, A. McGrew, B. McHale, A. G. MacPhee, J. F. Meeker, J. S. Merill, E. P. Mertens, P. A. Michel, M. G. Miller, T. Mills, J. L. Milovich, R. Miramontes, R. C. Montesanti, M. M. Montoya, J. Moody, J. D. Moody, K. A. Moreno, J. Morris, K. M. Morriston, J. R. Nelson, M. Neto, J. D. Neumann, E. Ng, Q. M. Ngo, B. L. Olejniczak, R. E. Olson, N. L. Orsi, M. W. Owens, E. H. Padilla, T. M. Pannell, T. G. Parham, R. W. Patterson, Jr., G. Pavel, R. R. Prasad, D. Pendlton, F. A. Penko, B. L. Pepmeier, D. E. Petersen, T. W. Phillips, D. Pigg, K. W. Piston, K. D. Pletcher, C. L. Powell, H. B. Radousky, B. S. Raimondi, J. E. Ralph, R. L. Rampke, R. K. Reed, W. A. Reid, V. V. Rekow, J. L. Reynolds, J. J. Rhodes, M. J. Richardson, R. J. Rinnert, B. P. Riordan, A. S. Rivenes, A. T. Rivera, C. J. Roberts, J. A. Robinson, B. Robinson, S. R. Robison, O. R. Rodriguez, S. P. Rogers, M. D. Rosen, G. F. Ross, M. Runkel, A. S. Runtal, R. A. Sacks, S. F. Sailors, J. T. Salmon, J. D. Salmonson, R. L. Saunders, J. R. Schaffer, T. M. Schindler, M. J. Schmitt, M. B. Schneider, K. S. Segraves, M. J. Shaw, M. E. Sheldrick, R. T. Shelton, M. K. Shiflett, S. J. Shiromizu, M. Shor, L. L. Silva, S. A. Silva, K. M. Skulina, D. A. Smauley, B. E. Smith, L. K. Smith, A. L. Solomon, S. Sommer, J. G. Soto, N. I. Spafford, D. E. Speck, P. T. Springer, M. Stadermann, F. Stanley, T. G. Stone, E. A. Stout, P. L. Stratton, R. J. Strausser, L. J. Suter, W. Sweet, M. F. Swisher, J. D. Tappero, J. B. Tassano, J. S. Taylor, E. A. Tekle, C. Thai, C. A. Thomas, A. Thomas, A. L. Throop, G. L. Tietbohl, J. M. Tillman, R. P. J. Town, S. L. Townsend, K. L. Tribbey, D. Trummer, J. Truong, J. Vaher, M. Valadez, P. Van Arsdall, A. J. Van Prooyen, E. O. Vergel de Dios, M. D. Vergino, S. P. Vernon, J. L. Vickers, G. T. Villanueva, M. A. Vitalich, S. A. Vonhof, F. E. Wade, R. J. Wallace, C. T. Warren, A. L. Warrick, J. Watkins, S. Weaver, P. J. Wegner, M. A. Weingart, J. Wen, K. S. White, P. K. Whitman, K. Widmann, C. C. Widmayer, K. Wilhelmsen, E. A. Williams, W. H. Williams, L. Willis, E. F. Wilson, B. A. Wilson, M. C. Witte, K. Work, P. S. Yang, B. K. Young, K. P. Youngblood, R. A. Zacharias, T. Zaleski, P. G. Zapata, H. Zhang, J. S. Zielinski, J. L. Kline, G. A. Kyrala, C. Niemann, J. D. Kilkenny, A. Nikroo, B. M. Van Wonterghem, L. J. Atherton, and E. I. Moses, Phys. Rev. Lett. **106**, 085004 (2011).

[97]D. E. Hinkel, M. D. Rosen, E. A. Williams, A. B. Langdon, C. H. Still, D. A. Callahan, J. D. Moody, P. A. Michel, R. P. J. Town, R. A. London, and S. H. Langer, Phys. Plasmas **18**, 056312 (2011).

[98]O. Landen, J. Edwards, S. W. Haan, J. D. Lindl, T. R. Boehly, D. K. Bradley, D. A. Callahan, P. M. Celliers, E. L. Dewald, S. Dixit, T. Doeppner, J. Eggert, D. Farley, J. A. Frenje, S. Glenn, S. H. Glenzer, A. Hamza, B. A. Hammel, C. Haynam, K. LaFortune, D. G. Hicks, N. Hoffman, N. Izumi, O. S. Jones, J. D. Kilkenny, J. L. Kline, G. A. Kyrala, A. J. Mackinnon, J. Milovich, J. Moody, N. Meezan, P. Michel, D. H. Munro, R. E. Olson, J. Ralph, H. F. Robey, A. Nikroo, S. P. Regan, B. K. Spears, L. J. Suter, C. A. Thomas, R. Town, D. C. Wilson, B. J. MacGowan, L. J. Atherton, and E. I. Moses, EPJ Web Conf. **59**, 01003 (2013).

[99]J. D. Moody, D. J. Strozzi, L. Divol, P. Michel, H. F. Robey, S. LePape, J. Ralph, J. S. Ross, S. H. Glenzer, R. K. Kirkwood, O. L. Landen, B. J. MacGowan, A. Nikroo, and E. A. Williams, Phys. Rev. Lett. **111**, 025001 (2013).

[100]M. B. Schneider, N. B. Meezan, S. S. Alvarez, J. Alameda, S. Baker, P. M. Bell, D. K. Bradley, D. A. Callahan, J. R. Celeste, E. L. Dewald, S. N. Dixit, T. Döppner, D. C. Eder, M. J. Edwards, M. Fernandez-Perea, E. Gullikson, M. J. Haugh, S. Hau-Riege, W. Hsing, N. Izumi, O. S. Jones, D. H. Kalantar, J. D. Kilkenny, J. L. Kline, G. A. Kyrala, O. L. Landen, R. A. London, B. J. MacGowan, A. J. MacKinnon, T. J. Mccarville, J. L. Milovich, P. Mirkarimi, J. D. Moody, A. S. Moore, M. D. Myers, E. A. Palma, N. Palmer, M. J. Pivovaroff, J. E. Ralph, J. Robinson, R. Soufli, L. J. Suter, A. T. Teruya, C. A. Thomas, R. P. Town, S. P. Vernon, K. Widmann, and B. K. Young, Rev. Sci. Instrum. **83**, 10E525 (2012).

[101]N. B. Meezan, D. G. Hicks, D. A. Callahan, R. E. Olson, M. S. Schenider, C. A. Thomas, H. F. Robey, P. M. Celliers, J. L. Kline, S. N. Dixit, P. A. Michel, O. S. Jones, D. S. Clark, J. E. Ralph, T. Doeppner, A. J. MacKinnon, S. W. Haan, O. L. Landen, S. H. Glenzer, L. J. Suter, M. J. Edwards, B. J. MacGowan, J. D. Lindl, and L. J. Atherton, EPJ Conf. **59**, 02002 (2013).

[102]M. B. Schneider, O. S. Jones, N. B. Meezan, J. L. Milovich, R. P. Town, S. S. Alvarez, R. G. Beeler, D. K. Bradley, J. R. Celeste, S. N. Dixit, M. J. Edwards, M. J. Haugh, D. H. Kalantar, J. L. Kline, G. A. Kyrala, O. L. Landen, B. J. MacGowan, P. Michel, J. D. Moody, S. K. Oberhelman, K. W. Piston, M. J. Pivovaroff, L. J. Suter, A. T. Teruya, C. A. Thomas, S. P. Vernon, A. L. Warrick, K. Widmann, R. D. Wood, and B. K. Young, Rev. Sci. Instrum. **81**, 10E538 (2010).

[103]J. L. Kline, D. A. Callahan, S. H. Glenzer, N. B. Meezan, J. D. Moody, D. E. Hinkel, O. S. Jones, A. J. MacKinnon, R. Bennedetti, R. L. Berger, D. Bradley, E. L. Dewald, I. Bass, C. Bennett, M. Bowers, G. Brunton, J. Bude, S. Burkhart, A. Condor, J. M. Di Nicola, P. Di Nicola, S. N. Dixit, T. Doeppner, E. G. Dzenitis, G. Erbert, J. Folta, G. Grim, S. Glenn, A. Hamza, S. W. Haan, J. Heebner, M. Henesian, M. Hermann, D. G. Hicks, W. W. Hsing, N. Izumi, K. Jancaitis, O. S. Jones, D. Kalantar, S. F. Khan, R. Kirkwood, G. A. Kyrala, K. LaFortune, O. L. Landen, L. Lagin, D. Larson, S. Le Pape, T. Ma, A. G. MacPhee, P. A. Michel, P. Miller, M. Montincelli, A. S. Moore, A. Nikroo, M. Nostrand, R. E. Olso, A. Pak, H. S. Park, J. P. Patel, L. Pelz, J. Ralph, S. P. Regan, H. F. Robey, M. D. Rosen, J. S. Ross, M. B. Schneider, M. Shaw, V. A. Smalyuk, D. J. Strozzi, T. Suratwala, L. J. Suter, R. Tommasini, R. P. J. Town, B. Van Wonterghem, P. Wegner, K. Widmann, C. Widmayer, H. Wilkens, E. A. Williams, M. J. Edwards, B. A. Remington, B. J. MacGowan, J. D. Kilkenny, J. D. Lindl, L. J. Atherton, S. H. Batha, and E. Moses, Phys. Plasmas **20**, 056314 (2013).

[104]H.-S. Park, E. L. Dewald, S. Glenzer, D. H. Kalantar, J. D. Kilkenny, B. J. MacGowan, B. R. Maddox, J. L. Milovich, R. R. Prasad, B. A. Remington, H. F. Robey, and C. A. Thomas, Rev. Sci. Insrum. **81**, 10E519 (2010).

[105]T. Döppner, E. L. Dewald, L. Divol, C. A. Thomas, S. Burns, P. M. Celliers, N. Izumi, J. L. Kline, G. LaCaille, J. M. McNaney, R. R. Prasad, H. F. Robey, S. H. Glenzer, and O. L. Landen, Rev. Sci. Instrum. **83**, 10E508 (2012).

[106]K. A. Brueckner, Phys. Rev. Lett. **36**, 677 (1976); R. P. Drake, R. E. Turner, B. F. Lasinski *et al.*, Phys. Rev. A **40**, 3219 (1989); C. A. Thomas, Phys. Rev. E **81**, 036413 (2010).

[107]E. L. Dewald, C. Thomas, S. Hunter, L. Divol, N. Meezan, S. H. Glenzer, L. J. Suter, E. Bond, J. L. Kline, J. Celeste, D. Bradley, P. Bell, R. L. Kauffman, J. Kilkenny, and O. L. Landen, Rev. Sci. Instrum. **81**, 10D938 (2010).

[108]B. R. Maddox, H.-S. Park, B. A. Remington, N. Izumi, S. Chen, C. Chen, G. Kimminau, Z. Ali, M. J. Haugh, and Q. Ma, Rev. Sci. Instrum. **82**, 023111 (2011).

[109]T. Doeppner, C. A. Thomas, L. Divol, E. L. Dewald, P. M. Celliers, D. K. Bradley, D. A. Callahan, S. N. Dixit, J. A. Harte, S. M. Glenn, S. W. Haan, N. Izumi, G. A. Kyrala, G. LaCaille, J. K. Kline, W. L. Kruer, T. Ma, A. J. MacKinnon, J. M. McNaney, N. B. Meezan, H. F. Robey, J. D. Salmonson, L. J. Suter, G. B. Zimmerman, M. J. Edwards, B. J. MacGowan, J. D. Kilkenny, J. D. Lindl, B. M. Van Wonterghem, L. J. Atherton, E. I. Moses, S. H. Glenzer, and O. L. Landen, Phys. Rev. Lett. **108**, 135006 (2012).

[110]E. L. Dewald, J. Milovich, C. Thomas, J. Kline, C. Sorce, S. Glenn, and O. L. Landen, Phys. Plasmas **18**, 092703 (2011).

[111]E. L. Dewald, C. Thomas, J. Milovich, J. Edwards, C. Sorce, R. Kirkwood, D. Meeker, O. Jones, N. Izumi, and O. L. Landen, Rev. Sci. Instrum. **79**, 10E903 (2008).

[112]E. L. Dewald, J. Milovich, P. Michel, O. L. Landen, J. L. Kline, S. Glenn, D. H. Kalantar, L. R. Benedetti, G. A. Kyrala, L. Divol, J. Holder, K. Widmann, A. Moore, M. B. Schneider, A. Pak, C. A. Thomas, D. K. Bradley, P. Bell, M. Shaw, C. Widmayer, O. Jones, D. A. Callahan, N. B. Meezan, T. Döppner, R. P. J. Town, A. Hamza, B. Dzenitis, B. Van Wonterghem, A. J. Mackinnon, S. H. Glenzer, B. J. MacGowan, J. D. Kilkenny, M. J. Edwards, L. J. Atherton, and E. I. Moses, Phys. Rev. Lett. **111**, 235001 (2013).

[113]O. L. Landen, P. A. Amendt, L. J. Suter, R. E. Turner, S. G. Glendinning, S. W. Haan, S. M. Pollaine, B. A. Hammel, M. Tabak, M. D. Rosen, and J. D. Lindl, Phys. Plasmas **6**, 2137 (1999).

[114]M. D. Rosen, Phys. Plasmas **3**, 1803 (1996).

[115]O. S. Jones, S. H. Glenzer, L. J. Suter, R. E. Turner, K. M. Campbell, E. L. Dewald, B. A. Hammel, R. L. Kauffman, O. L. Landen, M. D. Rosen, R. J. Wallace, and F. A. Weber, Phys. Rev. Lett. **93**, 065002 (2004).

[116]H. F. Robey, T. R. Boehly, R. E. Olson, A. Nikroo, P. M. Celliers, O. L. Landen, and D. D. Meyerhofer, Phys. Plasmas **17**, 012703 (2010).

[117]R. L. Kauffman, H. N. Kornblum, D. W. Phillion, C. B. Darrow, B. F. Lasinski, L. J. Suter, A. R. Theissen, R. J. Wallace, and F. Ze, Rev. Sci. Instrum. **66**, 678 (1995).

[118]T. R. Boehly, D. Munro, P. M. Celliers, R. E. Olson, D. G. Hicks, V. N. Goncharov, G. W. Collins, H. F. Robey, S. X. Hu, J. A. Morozas, T. C. Sangster, O. L. Landen, and D. D. Meyerhofer, Phys. Plasmas **16**, 056302 (2009).

[119]H. F. Robey, T. R. Boehly, P. M. Celliers, J. H. Eggert, D. Hicks, R. F. Smith, R. Collins, M. W. Bowers, K. G. Krauter, P. S. Datte, D. H. Munro, J. L. Milovich, O. S. Jones, P. A. Michel, C. A. Thomas, R. E. Olson, S. Pollaine, R. P. J. Town, S. Haan, D. Callahan, D. Clark, J. Edwards, J. L. Kline, S. Dixit, M. B. Schneider, E. L. Dewald, K. Widmann, J. D. Moody, T. Doeppner, H. B. Radousky, A. Throop, D. Kalantar, P. DiNicola, A. Nikroo, J. J. Kroll, A. V. Hamza, J. B. Horner, S. D. Bhandarkar, E. Dzenitis, E. Alger, E. Giraldez, C. Castro, K. Moreno, C. Haynam, K. N. LaFortune, C. Widmayer, M. Shaw, K. Jancaitis, T. Parham, D. M. Holunga, C. F. Walters, B. Haid, E. R. Mapoles, J. Sater, C. R. Gibson, T. Malsbury, J. Fair, D. Trummer, K. R. Coffee, B. Burr, L. V. Berzins, C. Choate, S. J. Brereton, S. Azevedo, H. Chandrasekaran, D. C. Eder, N. D. Masters, A. C. Fisher, P. A. Sterne, B. K. Young, O. L. Landen, B. M. Van Wonterghem, B. J. MacGowan, J. Atherton, J. D. Lindl, D. D. Meyerhofer, and E. Moses, Phys. Plasma **19**, 042706 (2012).

[120]S. Hamel, L. X. Benedict, P. M. Celliers, M. A. Barrios, T. R. Boehly, G. W. Collins, T. Döppner, J. H. Eggert, D. R. Farley, D. G. Hicks, J. L. Kline, A. Lazicki, S. LePape, A. J. Mackinnon, J. D. Moody, H. F. Robey, E. Schwegler, and P. A. Sterne, Phys. Rev. B **86**, 094113 (2012).

[121]H. F. Robey, P. M. Celliers, J. L. Kline, A. J. Mackinnon, T. R. Boehly, O. L. Landen, J. H. Eggert, D. Hicks, S. Le Pape, D. R. Farley, M. W. Bowers, K. G. Krauter, D. H. Munro, O. S. Jones, J. L. Milovich, D. Clark, B. K. Spears, R. P. J. Town, S. W. Haan, S. Dixit, M. B. Schneider, E. L. Dewald, K. Widmann, J. D. Moody, T. Doeppner, H. B. Radousky, A. Nikroo, J. J. Kroll, A. V. Hamza, J. B. Horner, S. D. Bhandarkar, E. Dzenitis, E. Alger, E. Giraldez, C. Castro, K. Moreno, C.

Haynam, K. N. LaFortune, C. Widmayer, M. Shaw, K. Jancaitis, T. Parham, D. M. Holunga, C. F. Walters, B. Haid, T. Malsbury, D. Trummer, K. R. Coffee, B. Burr, L. V. Berzins, C. Choate, S. J. Brereton, S. Azevedo, H. Chandrasekaran, S. Glenzer, J. A. Caggiano, J. P. Knauer, J. A. Frenje, D. T. Casey, M. Gatu Johnson, F. H. Seguin, B. K. Young, M. J. Edwards, B. M. Van Wonterghem, J. Kilkenny, B. J. MacGowan, J. Atherton, J. D. Lindl, D. D. Meyerhofer, and E. Moses, Phys. Rev. Lett. **108**, 215004 (2012).

[122]O. L. Landen, R. Benedetti, D. Bleuel, T. R. Boehly, D. K. Bradley, J. A. Caggiano, D. A. Callahan, P. M. Celliers, C. J. Cerjan, D. Clark, G. W. Collins, E. L. Dewald, S. N. Dixit, T. Doeppner, D. Edgell, J. Eggert, D. Farley, J. A. Frenje, V. Glebov, S. M. Glenn, S. H. Glenzer, S. W. Haan, A. Hamza, B. A. Hammel, C. A. Haynam, J. H. Hammer, R. F. Heeter, H. W. Herrmann, D. G. Hicks, D. E. Hinkel, N. Izumi, M. Gatu Johnson, O. S. Jones, D. H. Kalantar, R. L. Kauffman, J. D. Kilkenny, J. L. Kline, J. P. Knauer, J. A. Koch, G. A. Kyrala, K. LaFortune, T. Ma, A. J. Mackinnon, A. J. Macphee, E. Mapoles, J. L. Milovich, J. D. Moody, N. B. Meezan, P. Michel, A. S. Moore, D. H. Munro, A. Nikroo, R. E. Olson, K. Opachich, A. Pak, T. Parham, P. Patel, H.-S. Park, R. P. Petrasso, J. Ralph, S. P. Regan, B. A. Remington, H. G. Rinderknecht, H. F. Robey, M. D. Rosen, J. S. Ross, J. D. Salmonson, T. C. Sangster, M. B. Schneider, V. Smalyuk, B. K. Spears, P. T. Springer, L. J. Suter, C. A. Thomas, R. P. J. Town, S. V. Weber, P. J. Wegner, D. C. Wilson, K. Widmann, C. Yeamans, A. Zylstra, M. J. Edwards, J. D. Lindl, L. J. Atherton, W. W. Hsing, B. J. MacGowan, B. M. Van Wonterghem, and E. I. Moses, Plasma Phys. Controlled Fusion **54**, 124026 (2012).

[123]A. B. Zylstra, J. A. Frenje, F. H. Séguin, M. J. Rosenberg, H. G. Rinderknecht, M. Gatu Johnson, D. T. Casey, N. Sinenian, M. J.-E. Manuel, C. J. Waugh, H. W. Sio, C. K. Li, R. D. Petrasso, S. Friedrich, K. Knittel, R. Bionta, M. McKernan, D. Callahan, G. W. Collins, E. Dewald, T. Döppner, M. J. Edwards, S. Glenzer, D. G. Hicks, O. L. Landen, R. London, A. Mackinnon, N. Meezan, R. R. Prasad, J. Ralph, M. Richardson, J. R. Rygg, S. Sepke, S. Weber, R. Zacharias, E. Moses, J. Kilkenny, A. Nikroo, T. C. Sangster, V. Glebov, C. Stoeckl, R. Olson, R. J. Leeper, J. Kline, G. Kyrala, and D. Wilson, Rev. Sci. Instrum. **83**, 10D901 (2012).

[124]F. H. Seguin, N. Sinenian, M. Rosenberg, A. Zylstra, M. J.-E. Manuel, H. Sio, C. Waugh, H. G. Rinderknecht, M. Gatu Johnson, J. Frenje, C. K. Li, R. Petrasso, T. C. Sangster, and S. Roberts, Rev. Sci. Instrum. **83**, 10D908 (2012).

[125]J. A. Frenje, C. K. Li, J. R. Rygg, F. H. Séguin, D. T. Casey, R. D. Petrasso, J. Delettrez, V. Yu. Glebov, S. Hatchett, B. Spears, and O. Landen, Phys. Plasmas **16**, 022702 (2009).

[126]H. G. Rinderknecht, M. Gatu Johnson, A. B. Zylstra, N. Sinenian, M. J. Rosenberg, J. A. Frenje, C. J. Waugh, C. K. Li, F. H. Sèguin, R. D. Petrasso, J. R. Rygg, J. R. Kimbrough, A. MacPhee, G. W. Collins, D. Hicks, A. Mackinnon, P. Bell, R. Bionta, T. Clancy, R. Zacharias, T. Döppner, H. S. Park, S. LePape, O. Landen, N. Meezan, E. I. Moses, V. U. Glebov, C. Stoeckl, T. C. Sangster, R. Olson, J. Kline, and J. Kilkenny, Rev. Sci. Instrum. **83**, 10D902 (2012).

[127]E. L. Dewald, O. S. Jones, O. L. Landen, L. Suter, P. Amendt, R. E. Turner, and S. Regan, Rev. Sci. Instrum. **77**, 10E310 (2006).

[128]R. P. J. Town, M. D. Rosen, P. A. Michel, L. Divol, J. D. Moody *et al.*, Phys. Plasmas **18**, 056302 (2011).

[129]P. Michel, W. Rozmus, E. A. Williams, L. Divol, R. L. Berger, R. P. J. Town, S. H. Glenzer, and D. A. Callahan, Phys. Rev. Lett. **109**, 195004 (2012); P. Michel, W. Rozmus, E. A. Williams, L. Divol, R. L. Berger, S. H. Glenzer, and D. A. Callahan, Phys. Plasmas **20**, 056308 (2013).

[130]J. Schein, O. Jones, M. Rosen, E. Dewald, S. Glenzer, J. Gunther, B. Hammel, O. Landen, L. Suter, and R. Wallace, Phys. Rev. Lett. **98**, 175003 (2007); O. S. Jones, J. Schein, M. D. Rosen, L. J. Suter, R. J. Wallace, E. L. Dewald, S. H. Glenzer, K. M. Campbell, J. Gunther, B. A. Hammel, O. L. Landen, C. M. Sorce, R. E. Olson, G. A. Rochau, H. L. Wilkins, J. L. Kaae, J. D. Kilkenny, A. Nikroo, and S. P. Regan, Phys. Plasmas **14**, 056311 (2007).

[131]P. Michel, L. Divol, R. P. J. Town, M. D. Rosen, D. A. Callahan, N. B. Meezan, M. B. Schneider, G. A. Kyrala, J. D. Moody, E. L. Dewald, K. Widmann, E. Bond, J. L. Kline, C. A. Thomas, S. Dixit, E. A. Williams, D. E. Hinkel, R. L. Berger, O. L. Landen, M. J. Edwards, B. J. MacGowan, J. D. Lindl, C. Haynam, L. J. Suter, S. H. Glenzer, and E. Moses, Phys. Rev. E **83**, 046409 (2011); J. D. Moody, P. Michel, L. Divol, R. L. Berger, E. Bond, D. K. Bradley, D. A. Callahan, E. L. Dewald, S. Dixit, M. J. Edwards, S. Glenn, A. Hamza, C. Haynam, D. E. Hinkel, N. Izumi, O. Jones, J. D. Kilkenny, R. K. Kirkwood, W. L. Kruer,

O. L. Landen, S. LePape, J. D. Lindl, B. J. MacGowan, N. B. Meezan, M. D. Rosen, M. B. Schneider, D. J. Strozzi, L. J. Suter, C. A. Thomas, R. P. J. Town, K. Widmann, E. A. Williams, L. J. Atherton, S. H. Glenzer, E. I. Moses, J. L. Kline, G. A. Kyrala, and A. Nikroo, Nat. Phys. **8**, 344 (2012).

[132]D. G. Hicks, N. B. Meezan, E. L. Dewald, A. J. Mackinnon, R. E. Olson, D. A. Callahan, T. Doeppner, L. R. Benedetti, D. K. Bradley, P. M. Celliers, D. S. Clark, P. Di Nicola, S. N. Dixit, E. G. Dzenitis, J. E. Eggert, D. R. Farley, J. A. Frenje, S. M. Glenn, S. H. Glenzer, A. V. Hamza, R. F. Heeter, J. P. Holder, N. Izumi, D. H. Kalantar, S. F. Khan, J. L. Kline, J. J. Kroll, G. A. Kyrala, T. Ma, A. G. MacPhee, J. M. McNaney, J. D. Moody, M. J. Moran, B. R. Nathan, A. Nikroo, Y. P. Opachich, R. D. Petrasso, R. R. Prasad, J. E. Ralph, H. F. Robey, H. G. Rinderknecht, J. R. Rygg, J. D. Salmonson, M. B. Schneider, N. Simanovskaia, B. K. Spears, R. Tommasini, K. Widmann, A. B. Zylstra, G. W. Collins, O. L. Landen, J. D. Kilkenny, W. W. Hsing, B. J. MacGowan, L. J. Atherton, and M. J. Edwards, Phys. Plasmas **19**, 122702 (2012).

[133]D. Babonneau, M. Primout, F. Girard, J.-P. Jadaud, M. Naudy, B. Villette, S. Depierreux, C. Blancard, G. Faussurier, K. B. Fournier, L. Suter, R. Kauffman, S. Glenzer, M. C. Miller, J. Gruün, and J. Davis, Phys. Plasmas **15**, 092702 (2008).

[134]A. Pak, L. Divol, G. Gregori, S. Weber, J. Atherton, R. Bennedetti, D. K. Bradley, D. Callahan, E. Dewald, T. Doeppner, M. J. Edwards, S. Glenn, D. Hicks, N. Izumi, O. Jones, S. F. Khan, J. Kilkenny, J. L. Kline, G. A. Kyrala, J. Lindl, O. L. Landen, S. LePape, T. Ma, A. MacPhee, B. J. MacGowan, A. J. Mackinnon, L. Masse, N. B. Meezan, J. D. Moody, E. Moses, R. E. Olson, J. E. Ralph, H. S. Park, B. A. Remington, J. S. Ross, R. Tommasini, R. P. J. Town, Y. Smalyuk, S. H. Glenzer, W. W. Hsing, H. F. Robey, G. P. Grim, L. J. A. Frenje, D. T. Casey, and M. G. Johnson, Phys. Plasmas **20**, 056315 (2013).

[135]T. Boutboul, A. Akkerman, A. Gibrekhterman, A. Breskin, and R. Chechik, J. Appl. Phys. **86**, 5841 (1999); O. L. Landen, P. M. Bell, J. W. McDonald, H.-S. Park, F. Weber, J. D. Moody, M. E. Lowry, and R. E. Stewart, Rev. Sci. Instrum. **75**, 4037 (2004).

[136]Y. P. Opachich, N. Palmer, D. Homoelle, B. Hatch, P. Bell, D. Bradley, D. Kalantar, D. Browning, J. Zuegel, and O. Landen, Rev. Sci. Instrum. **83**, 10E123 (2012).

[137]Y. P. Opachich, D. H. Kalantar, A. G. MacPhee, J. P. Holder, J. R. Kimbrough, P. M. Bell, D. K. Bradley, B. Hatch, G. Brienza-Larsen, C. Brown, C. G. Brown, D. Browning, M. Charest, E. L. Dewald, M. Griffin, B. Guidry, M. J. Haugh, D. G. Hicks, D. Homoelle, J. J. Lee, A. J. Mackinnon, A. Mead, N. Palmer, B. H. Perfect, J. S. Ross, C. Silbernagel, and O. Landen, Rev. Sci. Instrum. **83**, 125105 (2012).

[138]R. E. Olson, G. A. Rochau, O. L. Landen, and R. J. Leeper, Phys. Plasmas **18**, 032706 (2011).

[139]R. E. Olson, D. G. Hicks, N. B. Meezan, J. A. Koch, and O. L. Landen, Rev. Sci. Instrum. **83**, 10D310 (2012).

[140]Y. Saillard, Nucl. Fusion **46**, 1017 (2006).

[141]N. B. Meezan, A. J. Mackinnon, D. G. Hicks, E. L. Dewald, R. Tommasini, S. Le Pape, T. Doeppner, T. Ma, D. R. Farley, D. A. Kalantar, D. A. Callahan, H. F. Robey, C. A. Thomas, S. T. Prisbrey, O. S. Jones, J. L. Milovich, D. S. Clark, M. B. Schneider, A. S. Moore, K. Widmann, J. A. Koch, J. D. Salmonson, K. P. Opachich, L. R. Benedetti, S. F. Khan, A. G. MacPhee, S. M. Glenn, D. K. Bradley, E. G. Dzenitis, B. R. Nathan, J. J. Kroll, A. V. Hamza, S. N. Dixit, L. J. Atherton, O. L. Landen, W. W. Hsing, L. J. Suter, M. J. Edwards, B. J. MacGowan, and E. I. Moses, Phys. Plasmas **20**, 056311 (2013).

[142]R. H. H. Scott, D. S. Clark, D. K. Bradley, D. A. Callahan, M. J. Edwards, S. W. Haan, O. S. Jones, B. K. Spears, M. M. Marinak, R. P. J. Town, P. A. Norreys, and L. J. Suter, Phys. Rev. Lett. **110**, 075011 (2013).

[143]M. S. Plesset, J. Appl. Phys. **25**, 96 (1954).

[144]R. Epstein, Phys. Plasmas **11**, 5114 (2004).

[145]W. W. Hsing and N. M. Hoffman, Phys. Rev. Lett. **78**, 3876 (1997).

[146]M. A. Barrios, S. P. Regan, L. J. Suter, S. Glenn, L. R. Benedetti, D. K. Bradley, G. W. Collins, R. Epstein, B. A. Hammel, G. A. Kyrala, N. Izumi, T. Ma, H. Scott, and V. A. Smalyuk, Phys. Plasmas **20**, 072706 (2013).

[147]S. P. Regan, R. Epstein, B. A. Hammel, L. J. Suter, H. Scott, M. A. Barrios, D. K. Bradley, D. A. Callahan, C. Cerjan, G. W. Collins, S. N. Dixit, T. Döppner, M. J. Edwards, D. R. Farley, K. B. Fournier, S. Glenn, S. H. Glenzer, I. E. Golovkin, S. W. Haan, A. Hamza, D. G. Hicks, N. Izumi, O. S. Jones, J. D. Kilkenny, J. L. Kline, G. A. Kyrala, O. L.

Landen, T. Ma, J. J. MacFarlane, A. J. MacKinnon, R. C. Mancini, R. L. McCrory, N. B. Meezan, D. D. Meyerhofer, A. Nikroo, H.-S. Park, J. Ralph, B. A. Remington, T. C. Sangster, V. A. Smalyuk, P. T. Springer, and R. P. J. Town, Phys. Rev. Lett. **111**, 045001 (2013).

[148]T. Ma, P. K. Patel, N. Izumi, P. T. Springer, M. H. Key, L. J. Atherton, L. R. Benedetti, D. K. Bradley, D. A. Callahan, P. M. Celliers, C. J. Cerjan, D. S. Clark, E. L. Dewald, S. N. Dixit, T. Doeppner, D. H. Edgell, R. Epstein, S. Glenn, G. Grim, S. W. Haan, B. A. Hammel, D. Hicks, W. W. Hsing, O. S. Jones, S. F. Khan, J. D. Kilkenny, J. L. Kline, G. A. Kyrala, O. L. Landen, S. Le Pape, B. J. MacGowan, A. J. Mackinnon, A. G. MacPhee, N. B. Meezan, J. D. Moody, A. Pak, T. Parham, H.-S. Park, J. E. Ralph, S. P. Regan, B. A. Remington, H. F. Robey, J. S. Ross, B. K. Spears, V. Smalyuk, L. J. Suter, R. Tommasini, R. P. Town, S. V. Weber, J. D. Lindl, M. J. Edwards, S. H. Glenzer, and E. I. Moses, Phys. Rev. Lett. **111**, 085004 (2013).

[149]T. Ma, N. Izumi, R. Tommasini, D. K. Bradley, P. Bell, C. J. Cerjan, S. Dixit, T. Doppner, O. Jones, J. L. Kline, G. Kyrala, O. L. Landen, S. Le Pape, A. J. Mackinnon, H.-S. Park, P. K. Patel, R. R. Prasad, J. Ralph, S. P. Regan, V. A. Smalyuk, P. T. Springer, L. Suter, R. P. J. Town, S. V. Weber, and S. H. Glenzer, Rev. Sci. Instrum. **83**, 10E115 (2012).

[150]R. Betti, V. N. Goncharov, R. L. McCrory, and C. P. Verdon, Phys. Plasmas **5**, 1446 (1998).

[151]M. Vandenboomgaerde, J. Bastian, A. Casner, D. Galmiche, J.-P. Jadaud, S. Laffite, S. Liberatore, G. Malinie, and F. Philippe, Phys. Rev. Lett. **99**, 65004 (2007); C. Cherfils-Clérouin, C. Boniface, M. Bonnefille, E. Dattolo, D. Galmiche, P. Gauthier, J. Giorla, S. Laffite, S. Liberatore, P. Loiseau, G. Malinie, L. Masse, P. E. Masson-Laborde, M. C. Monteil, F. Poggi, P. Seytor, F. Wagon, and J. L. Willien, Plasma Phys. Controlled Fusion **51**, 124018 (2009).

[152]F. Philippe, A. Casner, T. Caillaud, O. Landoas, M. C. Monteil, S. Liberatore, H. S. Park, P. Amendt, H. Robey, C. Sorce, C. K. Li, F. Seguin, M. Rosenberg, R. Petrasso, V. Glebov, and C. Stoeckl, Phys. Rev. Lett. **104**, 035004 (2010); H. F. Robey, P. Amendt, H.-S. Park, R. P. J. Town, J. L. Milovich, T. Döppner, D. E. Hinkel, R. Wallace, C. Sorce, D. J. Strozzi, F. Philippe, A. Casner, T. Caillaud, O. Landoas, S. Liberatore, M.-C. Monteil, F. Séguin, M. Rosenberg, C. K. Li, R. Petrasso, V. Glebov, C. Stoeckl, A. Nikroo, and E. Giraldez, Phys. Plasmas **17**, 056313 (2010).

[153]D. C. Wilson, P. A. Bradley, N. M. Hoffman, F. J. Swenson, D. P. Smitherman, R. E. Chrien, R. W. Margevicius, D. J. Thoma, L. R. Foreman, J. K. Hoffer, S. Robert Goldman, S. E. Caldwell, T. R. Dittrich, S. W. Haan, M. M. Marinak, S. M. Pollaine, and J. J. Sanchez, Phys. Plasmas **5**, 1953 (1998).

[154]J. Biener, P. B. Mirkarimi, J. W. Tringe, S. L. Baker, Y. Wang, S. O. Kucheyev, N. E. Teslich, K. J. J. Wu, A. V. Hamza, C. Wild, E. Woerner, P. Koidl, K. Bruehne, and H.-J. Fecht, Fusion Sci. Technol. **49**, 737 (2006).

[155]O. S. Jones, C. J. Cerjan, M. M. Marinak, J. L. Milovich, H. F. Robey, P. T. Springer, L. R. Benedetti, D. L. Bleuel, E. J. Bond, D. K. Bradley, D. A. Callahan, J. A. Caggiano, P. M. Celliers, D. S. Clark, S. M. Dixit, T. Doppner, R. J. Dylla-Spears, E. G. Dzenitis, D. R. Farley, S. M. Glenn, S. H. Glenzer, S. W. Haan, B. J. Haid, C. A. Haynam, D. G. Hicks, B. J. Kozioziemski, K. N. LaFortune, O. L. Landen, E. R. Mapoles, A. J. MacKinnon, J. M. McNaney, N. B. Meezan, P. A. Michel, J. D. Moody, M. J. Moran, D. H. Munro, M. V. Patel, T. G. Parham, J. D. Sater, S. M. Sepke, B. K. Spears, R. P. J. Town, S. V. Weber, K. Widmann, C. C. Widmayer, E. A. Williams, L. J. Atherton, M. J. Edwards, J. D. Lindl, B. J. MacGowan, L. J. Suter, R. E. Olson, H. W. Herrmann, J. L. Kline, G. A. Kyrala, D. C. Wilson, J. Frenje, T. R. Boehly, V. Glebov, J. P. Knauer, A. Nikroo, H. Wilkens, and J. D. Kilkenny, Phys. Plasmas **19**, 056315 (2012).

[156]E. N. Loomis, D. Braun, S. H. Batha, C. Sorce, and O. L. Landen, Phys. Plasmas **18**, 092702 (2011); **19**, 122703 (2012).

[157]J. P. Knauer, K. Anderson, R. Betti, T. J. B. Collins, V. N. Goncharov, P. W. McKenty, D. D. Meyerhofer, P. B. Radha, S. P. Regan, T. C. Sangster, V. A. Smalyuk, J. A. Frenje, C. K. Li, R. D. Petrasso, and F. H. Séguin, Phys. Plasmas **12**, 056306 (2005).

[158]D. S. Clark, D. E. Hinkel, D. C. Eder, O. S. Jones, S. W. Haan, B. A. Hammel, M. M. Marinak, J. L. Milovich, H. F. Robey, L. J. Suter, and R. P. J. Town, Phys. Plasmas **20**, 056318 (2013).

[159]B. K. Spears *et al.*, "Impacts of low mode perturbations on implosion performance," Phys. Plasmas (unpublished).

[160]S. H. Glenzer, B. K. Spears, M. J. Edwards, E. T. Alger, R. L. Berger, D. L. Bleuel, D. K. Bradley, J. A. Caggiano, D. A. Callahan, C. Castro, D. T.

Casey, C. Choate, D. S. Clark, C. J. Cerjan, G. W. Collins, E. L. Dewald, J. G. Di Nicola, P. Di Nicola, L. Divol, S. N. Dixit, T. Doppner, R. Dylla-Spears, E. G. Dzenitis, J. E. Fair, L. J. A. Frenje, M. Gatu-Johnson, E. Giraldez, V. Glebov, S. M. Glenn, S. W. Haan, B. A. Hammel, S. P. Hatchett II, C. A. Haynam, R. F. Heeter, G. M. Heestand, H. W. Herrmann, D. G. Hicks, D. M. Holunga, J. B. Horner, H. Huang, N. Izumi, O. S. Jones, D. H. Kalantar, J. D. Kilkenny, R. K. Kirkwood, J. L. Kline, J. P. Knauer, B. Kozioziemski, A. L. Kritcher, J. J. Kroll, G. A. Kyrala, K. N. LaFortune, O. L. Landen, D. W. Larson, R. J. Leeper, S. Le Pape, J. D. Lindl, T. Ma, A. J. Mackinnon, A. G. MacPhee, E. Mapoles, P. W. McKenty, N. B. Meezan, P. Michel, J. L. Milovich, J. D. Moody, A. S. Moore, M. Moran, K. A. Moreno, D. H. Munro, B. R. Nathan, A. Nikroo, R. E. Olson, C. D. Orth, A. Pak, P. K. Patel, T. Parham, R. Petrasso, J. E. Ralph, H. Rinderknecht, S. P. Regan, H. F. Robey, J. S. Ross, J. D. Salmonson, C. Sangster, J. Sater, M. B. Schneider, F. H. SôČeguin, M. J. Shaw, M. J. Shoup, P. T. Springer, W. Stoeffl, L. J. Suter, C. A. Thomas, R. P. J. Town, C. Walters, S. V. Weber, P. J. Wegner, C. Widmayer, P. K. Whitman, K. Widmann, D. C. Wilson, B. M. Van Wonterghem, B. J. MacGowan, L. J. Atherton, and E. I. Moses, Plasma Phys. Controlled Fusion **54**, 045013 (2012).

[161] A. J. Mackinnon, J. L. Kline, S. N. Dixit, S. H. Glenzer, M. J. Edwards, D. A. Callahan, N. B. Meezan, S. W. Haan, J. D. Kilkenny, T. Doeppner, D. R. Farley, J. D. Moody, J. E. Ralph, B. J. MacGowan, O. L. Landen, H. F. Robey, T. R. Boehly, P. M. Celliers, J. H. Eggert, K. Krauter, G. Frieders, G. F. Ross, D. G. Hicks, R. E. Olson, S. V. Weber, B. K. Spears, J. D. Salmonsen, P. Michel, L. Divol, B. Hammel, C. A. Thomas, D. S. Clark, O. S. Jones, P. T. Springer, C. J. Cerjan, G. W. Collins, V. Y. Glebov, J. P. Knauer, C. Sangster, C. Stoeckl, P. McKenty, J. M. McNaney, R. J. Leeper, C. L. Ruiz, G. W. Cooper, A. G. Nelson, G. G. A. Chandler, K. D. Hahn, M. J. Moran, M. B. Schneider, N. E. Palmer, R. M. Bionta, E. P. Hartouni, S. LePape, P. K. Patel, N. Izumi, R. Tommasini, E. J. Bond, J. A. Caggiano, R. Hatarik, G. P. Grim, F. E. Merrill, D. N. Fittinghoff, N. Guler, O. Drury, D. C. Wilson, H. W. Herrmann, W. Stoeffl, D. T. Casey, M. G. Johnson, J. A. Frenje, R. D. Petrasso, A. Zylstra, H. Rinderknecht, D. H. Kalantar, J. M. Dzenitis, P. Di Nicola, D. C. Eder, W. H. Courdin, G. Gururangan, S. C. Burkhart, S. Friedrich, D. L. Blueuel, I. A. Bernstein, M. J. Eckart, D. H. Munro, S. P. Hatchett, A. G. Macphee, D. H. Edgell, D. K. Bradley, P. M. Bell, S. M. Glenn, N. Simanovskaia, M. A. Barrios, R. Benedetti, G. A. Kyrala, R. P. J. Town, E. L. Dewald, J. L. Milovich, K. Widmann, A. S. Moore, G. LaCaille, S. P. Regan, L. J. Suter, B. Felker, R. C. Ashabranner, M. C. Jackson, R. Prasad, M. J. Richardson, T. R. Kohut, P. S. Datte, G. W. Krauter, J. J. Klingman, R. F. Burr, T. A. Land, M. R. Hermann, D. A. Latray, R. L. Saunders, S. Weaver, S. J. Cohen, L. Berzins, S. G. Brass, E. S. Palma, R. R. Lowe-Webb, G. N. McHalle, P. A. Arnold, L. J. Lagin, C. D. Marshall, G. K. Brunton, D. G. Mathisen, R. D. Wood, J. R. Cox, R. B. Ehrlich, K. M. Knittel, M. W. Bowers, R. A. Zacharias, B. K. Young, J. P. Holder, J. R. Kimbrough, T. Ma, K. N. La Fortune, C. C. Widmayer, M. J. Shaw, G. V. Erbert, K. S. Jancaitis, J. M. DiNicola, C. Orth, G. Heestand, R. Kirkwood, C. Haynam, P. J. Wegner, P. K. Whitman, A. Hamza, E. G. Dzenitis, R. J. Wallace, S. D. Bhandarkar, T. G. Parham, R. Dylla-Spears, E. R. Mapoles, B. J. Kozioziemski, J. D. Sater, C. F. Walters, B. J. Haid, J. Fair, A. Nikroo, E. Giraldez, K. Moreno, B. Vanwonterghem, R. L. Kauffman, S. Batha, D. W. Larson, R. J. Fortner, D. H. Schneider, J. D. Lindl, R. W. Patterson, L. J. Atherton, and E. I. Moses, Phys. Rev. Lett. **108**, 215005 (2012).

[162] H. F. Robey, B. J. MacGowan, O. L. Landen, K. N. LaFortune, C. Widmayer, P. M. Celliers, J. D. Moody, J. S. Ross, J. Ralph, S. LePape, B. K. Spears, S. W. Haan, D. Clark, J. D. Lindl, and M. J. Edwards, Phys. Plasmas **20**, 052707 (2013).

[163] V. A. Smalyuk, L. J. Atherton, L. R. Benedetti, R. Bionta, D. Bleuel, E. Bond, D. K. Bradley, J. Caggiano, D. A. Callahan, D. T. Casey, P. M. Celliers, C. J. Cerjan, D. Clark, E. L. Dewald, S. N. Dixit, T. Döppner, D.

H. Edgell, M. J. Edwards, J. Frenje, M. Gatu-Johnson, V. Y. Glebov, S. Glenn, S. H. Glenzer, G. Grim, S. W. Haan, B. A. Hammel, E. P. Hartouni, R. Hatarik, S. Hatchett, D. G. Hicks, W. W. Hsing, N. Izumi, O. S. Jones, M. H. Key, S. F. Khan, J. D. Kilkenny, J. L. Kline, J. Knauer, G. A. Kyrala, O. L. Landen, S. Le Pape, J. D. Lindl, T. Ma, B. J. MacGowan, A. J. Mackinnon, A. G. MacPhee, J. McNaney, N. B. Meezan, J. D. Moody, A. Moore, M. Moran, E. I. Moses, A. Pak, T. Parham, P. H.-S. Park, K. Patel, R. Petrasso, J. E. Ralph, S. P. Regan, B. A. Remington, H. F. Robey, J. S. Ross, B. K. Spears, P. T. Springer, L. J. Suter, R. Tommasini, R. P. Town, S. V. Weber, and K. Widmann, Phys. Rev. Lett. **111**, 215001 (2013).

[164] G. Grim, N. Guler, F. Merrill, G. Morgan, C. Danly, P. Volegov, C. Wilde, D. Wilson, D. Clark, D. Hinkel, O. Jones, K. Raman, N. Izumi, D. Fittinghoff, and O. Drury, Phys. Plasmas **20**, 056320 (2013).

[165] H. F. Robey, J. D. Moody, P. M. Celliers, S. Ross, J. Ralph, S. Le Pape, L. F. Berzak-Hopkins, T. Parham, J. Sater, E. R. Mapoles, D. M. Holunga, C. F. Walters, B. Haid, B. Kozioziemski, K. G. Krauter, G. Frieders, G. Ross, M. W. Bowers, D. Strozzi, B. R. Nathan, B. E. Yoxall, A. V. Hamza, S. D. Bhandarkar, B. K. Young, B. M. Van Wonterghem, L. J. Atherton, O. L. Landen, M. J. Edwards, and T. R. Boehly, Phys. Rev. Lett. **111**, 065003 (2013).

[166] P. Amendt, O. L. Landen, H. F. Robey, C. K. Li, and R. D. Petrasso, Phys. Rev. Lett. **105**, 115005 (2010).

[167] P. A. Amendt, C. Cerjan, A. Hamza, D. E. Hinkel, J. L. Milovich, H.-S. Park, and H. F. Robey, Phys. Plasmas **15**, 012702 (2008).

[168] O. A. Hurricane, D. A. Callahan, D. T. Casey, P. Celliers, C. Cerjan, E. L. Dewald, T. R. Dittrich, T. Doppner, D. E. Hinkel, L. F. Berzak Hopkins, J. L. Kline, S. LePape, T. Ma, A. G. MacPhee, J. L. Milovich, A. E. Pak, P. K. Patel, H.-S. Park, B. A. Remington, J. D. Salmonson, P. T. Springer, and R. Tommasini, Nature **506**, 343 (2014).

[169] O. A. Hurricane, "The high-foot campaign on the National Ignition Facility," Bull. Am, Phys. Soc. **58**(16), 279 (2013); O. A. Hurricane, "The high-foot campaign on the National Ignition Facility," Phys. Plasmas (unpublished).

[170] T. R. Dittrich, O. A. Hurricane, D. A. Callahan, E. L. Dewald, T. Doeppner, D. E. Hinkel, L. F. Berzak Hopkins, J. L. Kline, S. Le Pape, T. Ma, J. L. Milovich, J. C. Moreno, P. K. Patel, H.-S. Park, B. A. Remington, and J. D. Salmonson, Phys. Rev. Lett. **112**, 055002 (2014).

[171] H.-S. Park, O. A. Hurricane, D. A. Callahan, D. T. Casey, E. L. Dewald, T. R. Dittrich, T. Döppner, D. E. Hinkel, L. F. Berzak Hopkins, S. Le Pape, T. Ma, P. K. Patel, B. A. Remington, H. F. Robey, J. D. Salmonson, and J. L. Kline, Phys. Rev. Lett. **112**, 055001 (2014).

[172] V. A. Smalyuk, D. T. Casey, D. S. Clark, M. J. Edwards, S. W. Haan, A. Hamza, D. E. Hoover, W. W. Hsing, O. Hurricane, J. D. Kilkenny, J. Kroll, O. L. Landen, A. Moore, J. L. Peterson, K. Raman, B. A. Remington, H. F. Robey, S. V. Weber, and K. Widmann, "First measurements of hydrodynamic instability growth in indirectly driven implosions at the National Ignition Facility," Phys. Rev. Lett. (submitted); V. A. Smalyuk, M. Barrios, J. A. Caggiano, D. T. Casey, C. J. Cerjan, D. S. Clark, M. J. Edwards, J. A. Frenje, M. Gatu-Johnson, V. Y. Glebov, G. Grim, S. W. Haan, B. A. Hammel, A. Hamza, W. W. Hsing, O. Hurricane, J. D. Kilkenny, J. L. Kline, J. P. Knauer, O. L. Landen, J. D. Lindl, T. Ma, J. M. McNaney, M. Mintz, A. Moore, A. Nikroo, T. Parham, J. L. Peterson, R. Petrasso, L. Pickworth, J. E. Pino, K. Raman, S. P. Regan, B. A. Remington, H. F. Robey, D. P. Rowley, D. B. Sayre, R. E. Tipton, S. V. Weber, K. Widmann, D. C. Wilson, and C. B. Yeamans, "Hydrodynamic instability growth and mix experiments at the National Ignition Facility," Phys. Plasmas (to be published).

[173] K. Raman, V. A. Smalyuk, D. T. Casey, S. W. Haan, B. A. Hammel, O. Hurricane, and H.-S. Park, "Design of an experiment to measure hydrodynamic instability frowth in ICF capsules at the National Ignition Facility," Bull. Am. Phys. Soc. **58**(16), 371 (2013), No. YO4-10.